BIOELECTRICAL DYNAMICS OF THE ENTORHINAL CORTEX

A Dissertation
Presented to
The Academic Faculty

by

Nathaniel James Killian

In Partial Fulfillment
of the Requirements for the Degree
Doctor of Philosophy in the
Interdisciplinary Bioengineering program
Department of Biomedical Engineering

Georgia Institute of Technology
Emory University
August 2013

BIOELECTRICAL DYNAMICS OF THE ENTORHINAL CORTEX

Approved by:

Dr. Steve M. Potter, Advisor
School of Biomedical Engineering
Georgia Institute of Technology

Dr. Elizabeth A. Buffalo, Co-Advisor
Department of Neurology
Emory University School of Medicine

Dr. Michelle C. LaPlaca
School of Biomedical Engineering
Georgia Institute of Technology

Dr. Robert C. Liu
Department of Biology
Emory University

Dr. Garrett B. Stanley
School of Biomedical Engineering
Georgia Institute of Technology

Date Approved: April 26, 2013

To Mom, Dad, and Kate, for your loving support.

ACKNOWLEDGMENTS

First and foremost, I want to thank the fantastic people who worked behind the scenes to support this work. I thank my parents for always supporting my interests and for bearing with me while I've been away in Georgia. And I could not have completed this work without the amazing support of my beautiful fiancée, Kate.

There have been some hills, but I have been lucky to have had a relatively straightforward path. I came to the Georgia Tech Bioengineering program in 2007 and was intrigued by the Steve Potter's novel methods for closed-loop control of the outputs of an isolated neuronal network over many days. I was also impressed by the group of faculty in the collaborative NeuroLab -it was clear that I would have no trouble finding an interesting project. The research combined with the excellent curriculum including the NSF IGERT program in Hybrid Neural Microsystems convinced me that Georgia Tech was the right decision.

In the summer of my first year, I rotated in Beth Buffalo's lab at Yerkes National Primate Center at Emory University. I was fortunate to receive excellent guidance and training from Beth, Megan Jutras, and Mike Jutras. We thought that studying learning and memory *in vivo* in Beth's lab combined with studying learning and memory *in vitro* in Steve's lab would make a complementary combination. As it goes in science, not everything went as planned and I spent most of my time in the Buffalo lab. Despite it not being obvious how the work in different labs would be connected, I benefited greatly from this collaboration. Being involved in labs with distinct perspectives, learning many different techniques, and discussing with people having a range of backgrounds and experiences has been a true privilege and these ever-present pillars have elevated this research.

Over the years I have greatly enjoyed meeting with, discussing with, and generally solving problems with Beth. Her commitment to the success of the lab and its members is extraordinary. Through working with Beth I have gained critical thinking and analysis skills and invaluable training in presenting research, grant writing, and networking.

Working with Steve has been great. He has been very supportive and committed to the success of the lab. He has an unmatched ability to be excited about seemingly any topic in science and this infuses the rest of the lab with the same excitement and a feeling of confidence that we can achieve useful outcomes for the rest of the world in both science and engineering.

Part of this research was funded by a grant to Jelena Vukasinovic and microPerfusions, Inc. I had the pleasure to work with Jelena and Varad Vernekar on the development of a novel device for electrical interfacing and sustenance of brain tissue. Working as a team with these two seasoned experts has been very rewarding and I hope to do them justice by retaining and using the knowledge they have imparted.

The faculty and staff in the Bioengineering program, the Biomedical Engineering department at Georgia Tech and Emory, and the staff at Yerkes Research Center have been graciously helpful with ensuring that I meet program requirements and receive my allowances. I am especially grateful for their help with the processing f subcontracts from Emory. They are, among others: Alyceson Andrews, Amber Burris, Andrés García, Sally Gerrish, Chris Ruffin, Shannon Sullivan, Rita Thomas, Sandra Wilson, and Janis Wright.

I would like to thank the labmates that I have had over the past 6 years for the discussions, advice, and friendships that have helped me to make progress: Doug Bakkum, Jeff Bingham, Alex Calhoun, Zenas Chao, Sharanya Desai, Ming-fai Fong, Chad Hales, Megan Jutras, Michael Jutras, Laura Kakalios, Seth Koenig, Michelle Kuykendal, Neal

Laxpati, Dustin Li, Frank Lin, Miriam Meister, Jon Newman, John Rolston, Jim Ross, Drew Solyst, Kiril Staikov, Sarah Steinmetz, Keith Van Antwerp, Varad Vernekar, Riley Zeller-Townson, and Yixiao Zhou.

My thesis committee members, Michelle LaPlaca, Robert Liu, and Garrett Stanley, have provided invaluable insight, comments, and suggestions that have helped to guide my work. I have a tremendous amount of gratitude for my advisors, Beth Buffalo and Steve Potter, for their shaping and guidance. They have been excellent mentors in scientific research and sincerely care about their students' well-being and future endeavors. The confidence and trust that Beth and Steve have placed in me has provided the freedom to create this work and to develop my skills as a researcher.

Finally, this research could not have been performed without fellowship and grant support. Funding was provided by the National Institute of Mental Health, R01MH093807 and R01MH080007, the National Center for Research Resources P51RR165 and the Office of Research Infrastructure Programs/OD P51OD11132 to Elizabeth Buffalo. Support was also provided by a NAKFI (National Academies/Keck Futures Initiative) Smart Prosthetics grant to Steve M. Potter. The NSF IGERT program provided support for the first two years of my studies (DGE-0333411). GRA support was also provided by NIH RNS065543 to microPerfusions, Inc.

TABLE OF CONTENTS

LIST OF TABLES

LIST OF FIGURES

LIST OF SYMBOLS AND ABBREVIATIONS

A

AD ..... Alzheimer's Disease
AVMA ..... American Veterinary Medical Association
AWG ..... American Wire Gauge

B

B ..... Group of Significant Border Score Cells
BNC ..... Bayonet Neill-Concelman

C

CAD ..... Computer-Aided Design
CNC ..... Computer Numerical Control
CRT ..... Cathode Ray Tube

D

DBS ..... Deep-Brain Stimulation
DG ..... Dentate Gyrus

E

EC ..... Entorhinal Cortex

F

FFT ..... Fast Fourier Transform

G

G ..... Group of Grid Cells
GC ..... Granger Causality
GUI ..... Graphical User Interface

H

HPC ..... Hippocampus

I

IA ..... InterAural
iCSD ..... Inverse Current Source Density
ID ..... Inner Diameter
IW ..... Animal initials

L

LEC ..... Lateral Entorhinal Cortex
LFP ..... Local Field Potential

M

MAP2 ..... Microtubule-Associated Protein 2
MEA ..... Multi-Electrode Array
MEC ..... Medial Entorhinal Cortex
MP ..... Animal initials
MR ..... Memory Responsive

MRI .....Magnetic Resonance Imaging

O

OD..... Outer Diameter

P

PB .....Phosphate Buffer
PCA.....Principal Components Analysis
PH.....Parahippocampal cortex
pMEA..... perforated Multi-Electrode Array
PR..... Perirhinal Cortex

R

RMSE.....Root-Mean-Square Error
rs .....Rhinal Sulcus

S

SEM .....Standard Error of the Mean

T

TH/TF ..... Areas TH and TF of the parahippocampal cortex
TT..... Animal initials

U

UVC.....Ultraviolet-C (germicidal)

V

VPLT .....Visual Preferential Looking Task
VR.....Visually Responsive

SUMMARY

The entorhinal cortex (EC) in the medial temporal lobe plays a critical role in memory formation and is implicated in several neurological diseases including temporal lobe epilepsy and Alzheimer's disease. Despite the known importance of this brain region, little is known about the normal bioelectrical activity patterns of the EC in awake, behaving primates. In order to develop effective therapies for diseases affecting the EC, we must first understand its normal properties. To contribute to our understanding of the EC, I monitored the activity of individual neurons and populations of neurons in the EC of rhesus macaque monkeys during free-viewing of photographs using electrophysiological techniques. The results of these experiments help to explain how primates can form memories of, and navigate through, the visual world.

These experiments revealed neurons in the EC that represent visual space with triangular grid receptive fields and other neurons that prefer to fire near image borders. These properties are similar to those previously described in the rodent EC, but here the neuronal responses relate to viewing of remote space as opposed to representing the physical location of the animal. The representation of visual space may be aided by another EC neuron type that was discovered, free-viewing saccade direction cells, neurons that signaled the direction of upcoming saccades. Such a signal could be used by other cells to prepare to fire according to the future gaze location. Many of these spatially-responsive neurons also represented memory for images, suggesting that they may be useful for associating items with their locations.

I also examined the neuronal circuitry of recognition memory for visual stimuli in the EC, and I found that population synchronization within the gamma-band (30-140 Hz) in superficial layers of the EC was modulated by stimulus novelty, while the strength of

memory formation modulated gamma-band synchronization in the deep layers and in layer III. Furthermore, the strength of connectivity in the gamma-band between different layers was correlated with the strength of memory formation, with deep to superficial power transfer being correlated with stronger memory formation and superficial to deep transfer correlated with weaker memory formation. These findings support several previous investigations of hippocampal-entorhinal connectivity in the rodent and advance our understanding of the functional circuitry of the medial temporal lobe memory system.

Finally, I explored the design of a device that could be used to investigate properties of brain tissue *in vitro*, potentially aiding in the development of treatments for disorders of the EC and other brain structures. We designed, fabricated, and validated a novel device for long-term maintenance of thick brain slices and 3-dimensional dissociated cell cultures on a perforated multi-electrode array. To date, most electrical recordings of thick tissue preparations have been performed by manually inserting electrode arrays. This work demonstrates a simple and effective solution to this problem by building a culture perfusion chamber around a planar perforated multi-electrode array. By making use of interstitial perfusion, the device maintained the thickness of tissue constructs and improved cellular survival as demonstrated by increased firing rates of perfused slices and 3-D cultures, compared to unperfused controls. To the best of our knowledge, this is the first thick tissue culture device to combine forced interstitial perfusion for long-term tissue maintenance and an integrated multi-electrode array for electrical recording and stimulation.

CHAPTER 1

INTRODUCTION

Much of my research that is described in this thesis has focused on understanding the entorhinal cortex (EC). The EC is shown in cyan in Figure 1.1 as part of the medial temporal lobe (MTL) memory system. The EC is positioned as a hub for communication between the neocortex and the hippocampus (HPC). The MTL plays a critical role in formation of declarative memory, memory for facts and events. This was first learned after patient H.M. had most of his medial temporal lobes surgically resected, a procedure that resulted in severe anterograde amnesia (Corkin, 2002). Recent controlled examinations of lesions of the entorhinal cortex have supported the idea that the EC is important for declarative learning and memory: lesions can impair recognition memory for objects (Leonard et al., 1995), relational memory for pairs of items and arrangements of items (Buckmaster et al., 2004), and learning and memory of spatial locations (Steffenach et al., 2005). The importance of the EC has also been demonstrated through studies of human diseases. In particular, the EC and adjacent cortices are the site of initial morphological degradation in Alzheimer's disease (AD) (Braak and Braak, 1996), a disease that causes impaired learning and memory of visuospatial relationships (Sahakian et al., 1988). Despite the known pathological results of EC damage, little is known about the normal bioelectrical activity patterns of the EC in awake, behaving primates. In order to develop effective therapies for AD and other disorders affecting the EC, we must first understand its normal properties.

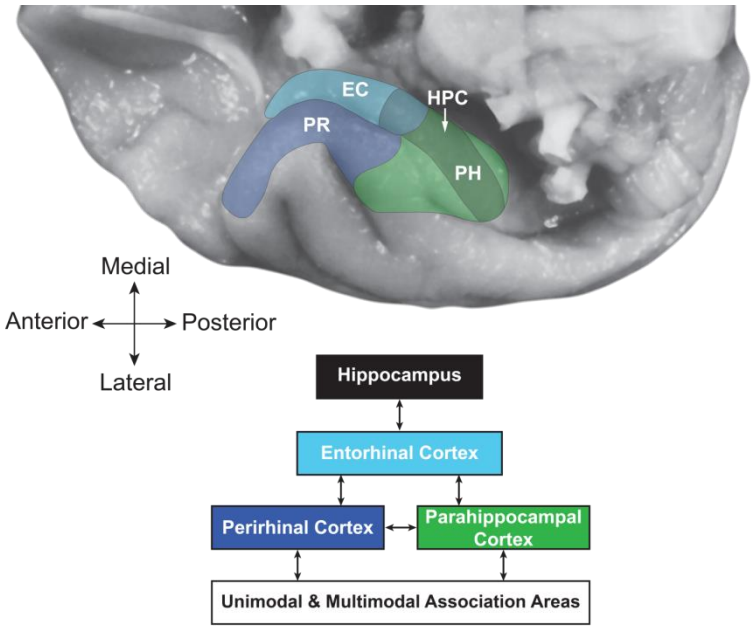

Figure 1.1 | The medial temporal lobe (MTL) memory system. The research in this thesis is focused on understanding the entorhinal cortex (EC). The EC is part of the medial temporal lobe memory system, much of which is shown here (the shaded regions). The EC is on the ventromedial surface of the temporal lobe as labeled in the photograph at the top of the ventral side of one hemisphere of the brain of a macaque monkey. The EC is a hub for communication between the hippocampus (HPC; deeper than the EC, beneath the parahippocampal and entorhinal cortices) and the neocortex. The parahippocampal (PH) and perirhinal (PR) cortices provide most of the input to the EC. Unimodal and polymodal association cortices project to PR and PH. All connections are bidirectional. Parts of this figure were inspired by and adapted, with permission, from Suzuki 1999 and Suzuki and Amaral, 1994a.

The entorhinal cortex is a 6-layered cortical region on the ventromedial surface of the brain, defined laterally by the rhinal sulcus, in the anterior part of the medial temporal lobe (Figure 1.1). Much of the input to the EC is visual in nature; the EC is included in a well-known hierarchical map of connections in the visual system as the second to last stop for signals from the retina, with the last stop being the hippocampus (Felleman and Van Essen, 1991). The EC receives most of this visual input through the perirhinal cortex and parahippocampal cortex. The EC layers that receive this input then project to the hippocampus (Suzuki and Amaral, 1994; Witter and Amaral, 1991). The hippocampus projects back to the EC and the EC projects back to the same regions that projected to it.

With complicated connectivity and with the EC being near the top of the proposed

visual hierarchy it is of course very difficult to speculate on the properties of EC neurons based on their connectivity alone. However, we have learned some important details about the EC and the hippocampus that were useful in guiding this work. It is known that neurons in the hippocampus of both rodents and primates can represent egocentric (body-based) and allocentric (world-based) locations in physical space (O'Keefe and Dostrovsky, 1971; Rolls, 1999). The hippocampus is adjacent to the EC in both rodents and primates and because neurons in the EC are strongly connected to the hippocampus, many researchers expected that they would also show activity related to spatial variables. Researchers including principally Edvard and May-Britt Moser have recently shown that indeed the EC has well-defined spatial responses (Fyhn et al., 2004; Hafting et al., 2005; Solstad et al., 2008). I drew an analogy to the spatial responses observed in rodents and hypothesized that, because primates are more visually-driven than rodents, we might observe the same types of responses in a visual context. In this thesis, I present results demonstrating that individual neurons in the EC represent visual space through spiking activity in ways that, for the first time, create a strong connection to work in rodents that may permit synergistic understanding of the EC across rodent and primate models. Considering populations of these neurons, within the EC, there are well-defined laminar groups of neurons. There is a growing body of evidence supporting the idea that different cortical layers can subserve distinct cognitive functions. In this thesis, I describe laminar differences in functional connectivity within the EC during memory formation and recognition. These discoveries were made through analyses of extracellular neuronal activity (action potentials and field potentials) recorded from the EC of macaque monkeys performing a visual memory task. After presenting these results that further our understanding of bioelectrical dynamics of the EC, I turn to how this knowledge might be used to develop treatments for diseases involving the EC. This is done through the

design of a novel microfluidic-microelectronic – brain tissue interfacing system, which could potentially be used as a long-term *in vitro* testbed for therapies targeting the EC, therapies that might utilize our knowledge of properties of the EC.

Some correlates of EC integrity and our current understanding of the EC

The EC appears to be of critical importance in Alzheimer's disease (AD), the most common neurodegenerative disease for which palliative care is the only effective form of treatment (Goedert and Spillantini, 2006). The EC is the first brain region to degenerate in AD and, as the disease progresses, the EC and the hippocampus are the most heavily damaged regions (Braak and Braak, 1996). The morphological implication of the EC in AD is consistent with results from behavioral testing in patients with AD and in monkeys with EC lesions (Sahakian et al., 1988; Buckmaster et al., 2004), namely impaired spatial learning and memory. These results suggest that neurons in the primate EC are encoding information about the locations of items in space and the relationship among these items. This warrants further study of the active properties of the primate EC in order to understand how visuospatial information is encoded. There is a wealth of knowledge of the properties of the rodent EC and hippocampus, as these structures are easily accessed in rodents (Moser et al., 2008). It has also been established that neurons in the rodent EC and hippocampus as well as the primate hippocampus represent space through spiking inhomogeneities, meaning they prefer to fire at one or more locations in space (O'Keefe and Dostrovsky, 1971; Rolls, 1999; Hafting et al., 2005). Neuronal activity in the hippocampus has previously been found to be related to not only visual space but also to the strength of visual memory formation in rhesus macaques (*Macaca mulatta*) (Jutras et al., 2009; Jutras and Buffalo, 2010). Overall there has been relatively little study of the EC and hippocampus in primates, due in large part to the difficulty in accessing these deep brain structures, but we have gained some important

information from studies in clinical settings. Temporal lobe epilepsy often involves the EC as has been shown clinically and in animal models (Bragin et al., 2002; Bartolomei et al., 2005; Kumar and Buckmaster, 2006). The primate EC has been studied in epilepsy patients performing studies alongside neurosurgical procedures aimed at localizing the source of seizures (Kreiman et al., 2002; Gelbard-Sagiv et al., 2008; Knake et al., 2007; Bragin et al., 2002; Ison et al., 2011; Chan et al., 2011; Jacobs et al., 2010). These studies have revealed interesting but fragmented information about the EC and there is the inherent limitation that the tissue being studied has pathological properties. Furthermore, these experiments can only be performed in patients with both pharmacologically-intractable epilepsy and seizures likely originating near the EC; data from the human EC are relatively rare. From the data that have been collected, there appear to be spatial responses that are localized to the EC. For example, one study including recordings from 13 patients found a significant proportion of cells in the EC that responded to particular paths during movement around the outside of a virtual square track (Jacobs et al., 2010). Interestingly, these neurons were discovered in stationary patients navigating a virtual environment using only visual input, suggesting that visual space may itself be encoded by the entorhinal cortex.

Visual space and the primate entorhinal cortex

A surprising example of the vagueness of our knowledge of the primate hippocampal formation (CA1-CA4 - hippocampus proper, dentate gyrus, subicular complex, and entorhinal cortex) is that we still do not know if there are true 'place cells' in the primate hippocampus. Place cells are neurons that encode body location at a single restricted region of space and were first discovered in the rat hippocampus in 1971 (O'Keefe and Dostrovsky, 1971). See the top of Figure 1.2 for a more detailed description of place cells. Experiments in primates have attempted to identify place cells, but have not clearly identified neurons that

respond exclusively to the location of the animal's body in real (not virtual) physical space (Tamura et al., 1992; Matsumura et al., 1999; Georges-François et al., 1999; Dale et al., 2003). A basic reason for our limited knowledge is the difficultly inherent in recording from deep brain structures in moving primates. Such experiments are difficult because they require (1) a tethered or wireless recording apparatus that (2) also does little damage to the brain during movement of the animal. However, the work of Dr. Edmund Rolls and colleagues demonstrated that recording from a moving primate may not be necessary. Their studies examined how eye position over a wide range of space causes changes in firing rate in the hippocampal formation (Georges-François et al., 1999; Rolls et al., 1998). In experiments where body, head, and eye movements were monitored, they found a population of cells in the macaque hippocampus that represented where the monkey was looking, and not exclusively where the monkey was located or oriented (Figure 1.2, bottom). These allocentric 'spatial view cells' may be the primate analog to the place cells of rodents and bats (Ulanovsky and Moss, 2007; O'Keefe and Dostrovsky, 1971). The spatial view cell experiments were performed with relatively limited spatial sampling of eye position; they recorded eye position over a wide range of space, but typically in limited detail at restricted locations in space. Other studies have examined neuronal responses related to simpler eye position signals, such as saccades to a limited number of locations (Siegel et al., 2003; Pesaran et al., 2010). However, the experiments in this thesis represent some of the first studies examining neuronal responses related to specific eye positions in a free-viewing task in fine spatial detail over many degrees of visual angle (Chapters 2 and 3).

A functional class of neuron similar to place cells called 'grid cells' was discovered in the EC of rats by Hafting et al. in 2005, see Figure 1.3. These cells represent not just one location like place cells, but presumably an unlimited number of locations at the nodes of a

triangular grid in any given environment. The prevailing theory is that this generic representation is useful for spatial computations such as path integration and that these cells may be an ingredient in the generation of place cell firing patterns, permitting computation of location 'on-the-fly' (McNaughton et al., 2006).

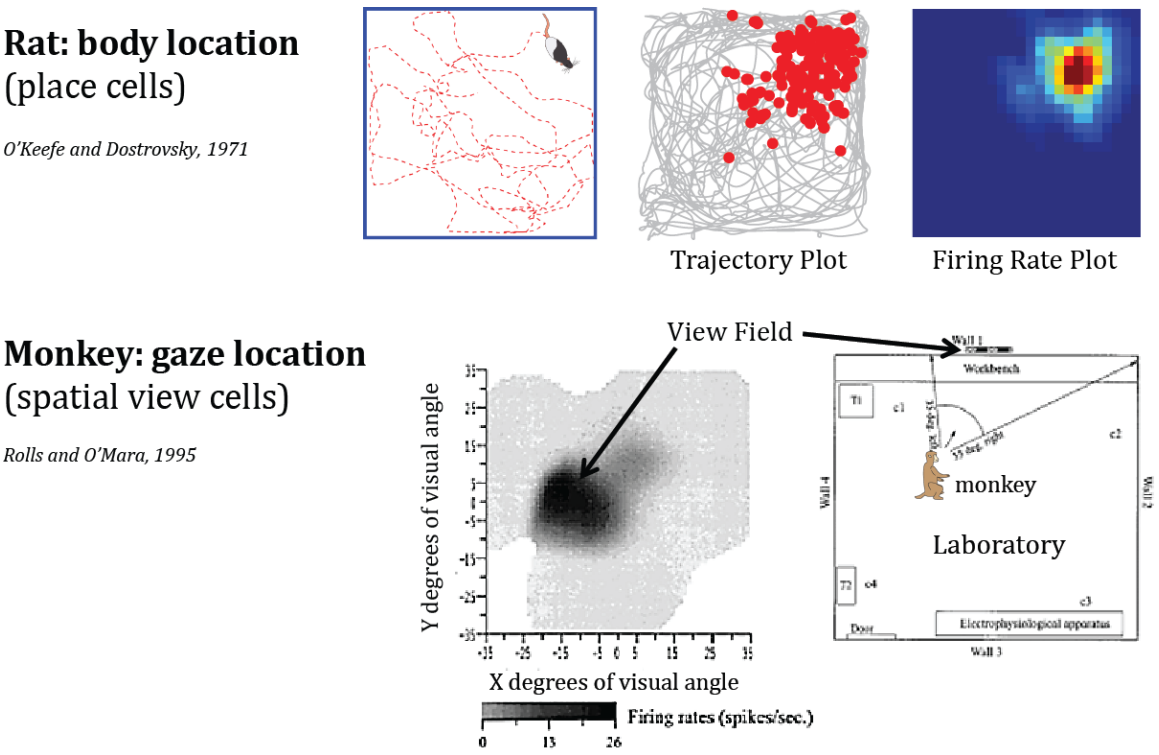

Figure 1.2 | Spatial representation in the hippocampus of rats and monkeys. Top: Recordings from the rodent hippocampus have identified place cells. Place cells are neurons in the rat hippocampus that will fire spikes when the rat moves through a particular location of an environment such as the square enclosure depicted here. Thus these are egocentric responses that make use of proximal cues. This can be seen in the movement trajectory, with red dots representing spikes in the place field, and also in the corresponding heat map of firing rate (redder locations correspond to higher firing rates). These cells were first discovered by John O'Keefe in 1971. **Bottom:** Interestingly, pure place cells have yet to be reported in primates. Studies that have been performed in monkeys have, however, identified 'view cells'. Rolls and colleagues performed experiments with monkeys walking around a laboratory, but did not find any place cells. They did, however, find cells that had increased firing rate when the monkey viewed a restricted region of external space. They called these cells 'spatial view cells'. The view field for an example spatial view cell is shown here when viewed from one particular body and head position. It's important to note that these view fields are independent of the position of the monkey and are anchored to external landmarks; in contrast to the *typical* description of place cells, these neurons have allocentric responses and use distal cues. After the discovery of place cells, researchers began investigating the structure adjacent to the hippocampus that provides most of the hippocampal input, the entorhinal cortex. Portions of this figure were reproduced, with permission, from Koenig et al., 2011 and Georges-François et al., 1999.

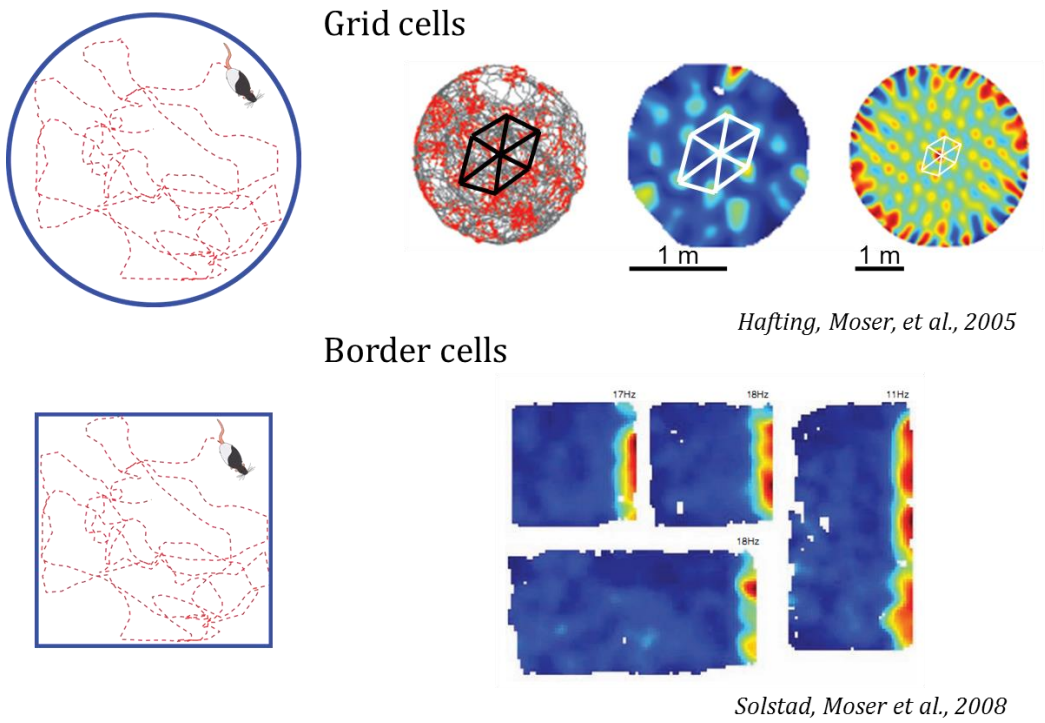

Figure 1.3 | Spatial representation in the rodent EC. Recordings from the rodent EC have defined spatial representations that are distinctly different from place cells. **Top:** In 2005, Hafting et al. discovered that many entorhinal cortex neurons fired spikes when the rat moved over the nodes of a triangular grid and these cells have since been referred to as 'grid cells'. We can see this pattern in the trajectory plot, firing rate map, and autocorrelation for one example unit recorded from a rat moving about a circular enclosure. The autocorrelation aids in quantifying periodicity and has double the spatial scale. Here I've highlighted one hexagonal portion of the triangular grid on the three characteristic plots. **Bottom:** In 2008, cells that preferentially fired spikes near environment borders, 'border cells', were discovered by the Moser group. Firing rate maps for a border cell are shown here. These cells have increased firing rate near one or more walls of the environment and if you move the wall, then the cell will continue to fire along that wall. It's thought that these firing patterns help organize information in service of memory processes: grid cells tile space and border cells anchor representations to landmarks. And more generally, these cells may help in navigating an environment by providing information about the animal's local position and position with respect to landmarks. Portions of this figure were modified, with permission, from Hafting et al., 2005 and Solstad et al., 2008.

In this thesis, I fill a gap in knowledge by describing the properties of EC neurons in monkeys that are freely exploring photographs presented on a computer monitor. In particular, similar to the properties of hippocampal spatial view cells, I found neurons in the EC that represent the visual field in a consistent and periodic manner, analogous to grid cells in rodents, but in a visual context. The known and new functional neuron types that represent different spatial features in the entorhinal cortex and hippocampus are summarized

in Figure 1.4. The results of the experiments in this thesis suggest particular neuronal computations that could be used to associate visual identities with the location in space where they were seen (Figure 1.5).

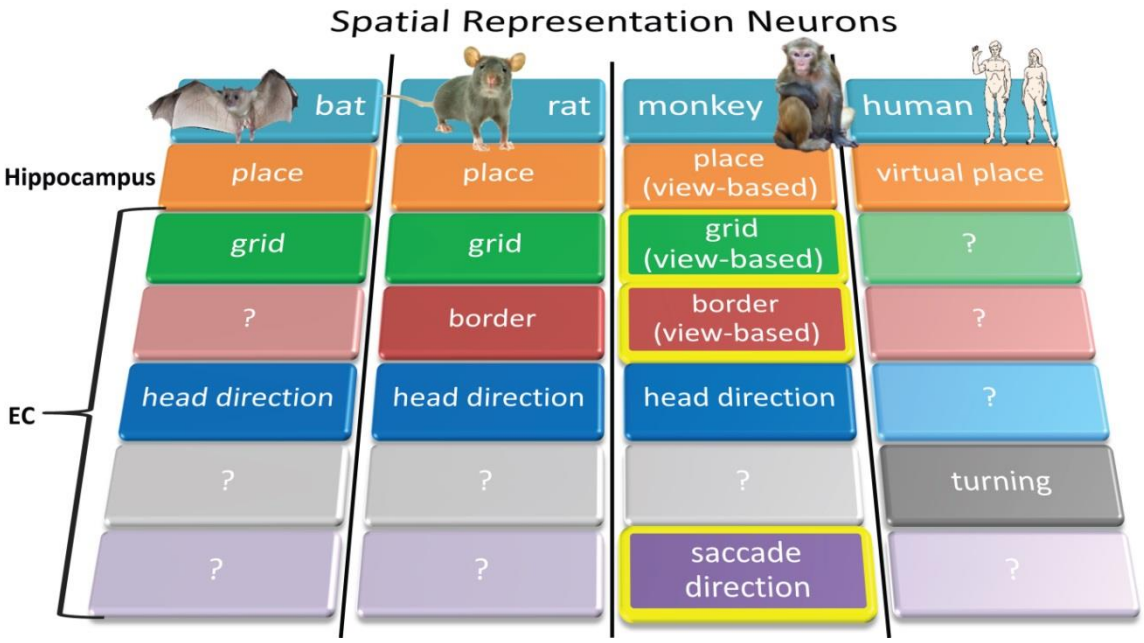

Figure 1.4 | Neurons in the hippocampal formation that represent space. Neurons that represent spatial locations or spatial relationships have been found in the hippocampus and entorhinal cortex of mammalian species from bats to humans. The table here gives an overview of functional neuron types (vertical axis) that have been identified in various species (horizontal axis). Neurons that have not been found are indicated with a '?'. There is much left to be discovered in the EC of primates (monkeys and humans). One particular representation, that of grid cells, has been found in the bat and rodent entorhinal cortices, but has yet to be described in primates. In this thesis, I provide the first direct evidence for the existence of grid cells as well as border cells in primates (Chapter 2). Additionally, I describe a novel type of cell in the EC, saccade direction cells (Chapter 3). The newly discovered functional neuron types are highlighted with a yellow border.

Figure 1.5 | Cartoon of visual representations in the MTL. Left: Visual grid cells may perform a spatial computation to create a coordinate system that is independent of content but could be used in conjunction with item-specific responses to associate items with places and/or distances. **Middle:** Spatial view cells in the hippocampus with single firing fields (Rolls and O'Mara, 1995) provide a spatially-localized association of items and places (e.g. the ox on the beach). **Right:** Landmarks may be encoded by border cells in the EC for alignment of other representations during recall of memories and for consistent encoding with repeat visits to and different perspectives of the same environment (e.g. the border between the water and the mountain).

Laminar properties of entorhinal cortex activity

Understanding how individual neurons represent visual information is more useful if we know how neuronal units are connected and interact as populations. Because of its anatomical connectivity, the EC is well-positioned to play a critical role in hippocampal-cortical interaction. See Figure 1.6 for a pictorial overview of connections involving the EC. Superficial layers of the EC receive processed multisensory information and provide the main cortical input to the hippocampus, while deep layers of the EC receive output from the hippocampus and provide feedback to other cortical areas. Furthermore, there is also a growing body of evidence supporting the idea that different cortical layers may be useful for distinct cognitive functions (Sun and Dan, 2009; Buffalo et al., 2011; Takeuchi et al., 2011). I endeavored to understand what neurons in the different layers of the EC do and how they are connected when the EC is functioning normally.

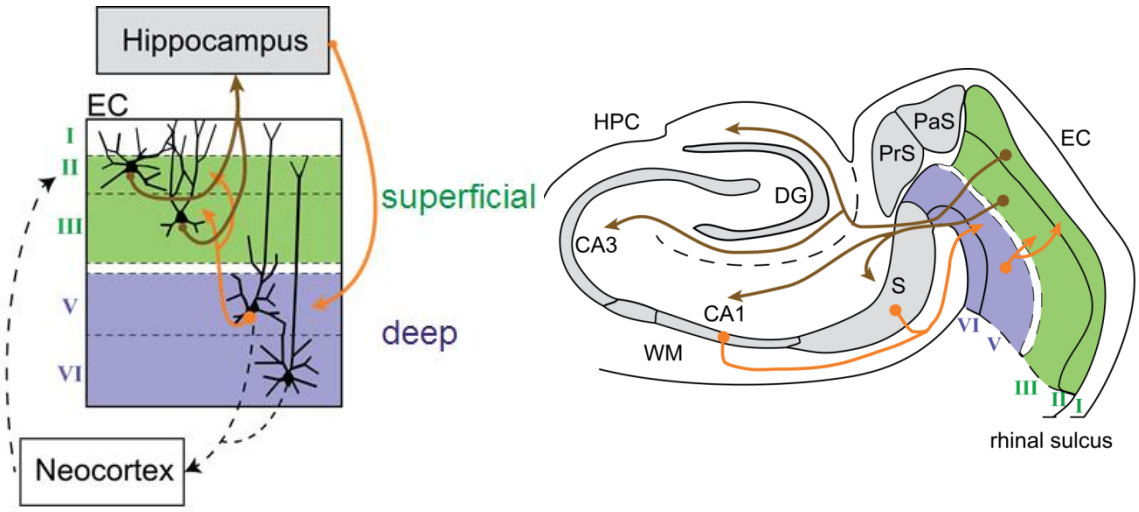

Figure 1.6 | Laminar organization of connections involving the EC. The diagram on the left describes projections to and from the EC and the diagram on the right describes the same connections but drawn on top of a transverse rodent brain slice with anatomical details introduced (note that these connections are the same in monkeys). The coloration and notation for both diagrams is consistent and they are best understood when viewed as a pair. Superficial layers (I-III; green) and deep layers (V, VI; purple) have distinct connections with the HPC and neocortex. Cortical input primarily reaches the superficial layers of the EC, which in turn project to the HPC (brown), which projects to the deep layers of the EC (orange), and the EC projects back to the same cortical regions that project to it. The deep layers also send feedback to superficial layers of the EC (orange). DG, dentate gyrus; PrS, presubiculum; PaS, parasubiculum; S, subiculum; WM, white matter. Portions of this figure were modified, with permission, from Witter and Moser, 2006.

In Chapter 4, I present results from an exploration of population activity in the EC with respect to individual layers and combinations of layers. The analyses were performed by examining both spiking activity and local field potentials (LFPs), potentials generated by regions with hundreds to thousands of neurons. The signals were recorded with arrays that had 30 micron diameter recording sites spaced at 150 microns on a 10 centimeter long shaft mounted on a tungsten microelectrode (the 'Axial Array' from NeuroNexus and FHC, Inc.; Appendix A, B). Similar electrode arrays, colloquially known as 'silicon probes' or 'Michigan probes', have been used for many years at shallow depths, but long and thin arrays for deep multi-electrode penetration are a recent development and successful implementation increased the relative yield and accuracy of the neuronal recordings (Figure 1.7). These recording devices permitted the recording from all layers of the entorhinal cortex with

accurate layer estimates made with the aid of current source density (CSD) analysis. CSD analysis makes use of 3 or more electrodes with exactly-known spacing. Most recordings from the primate EC to date have been performed with individual microelectrodes, thus no attempt was made to estimate the layers that were recorded from in most of these studies (Suzuki et al., 1997; Naya and Suzuki, 2011; Jacobs et al., 2010).

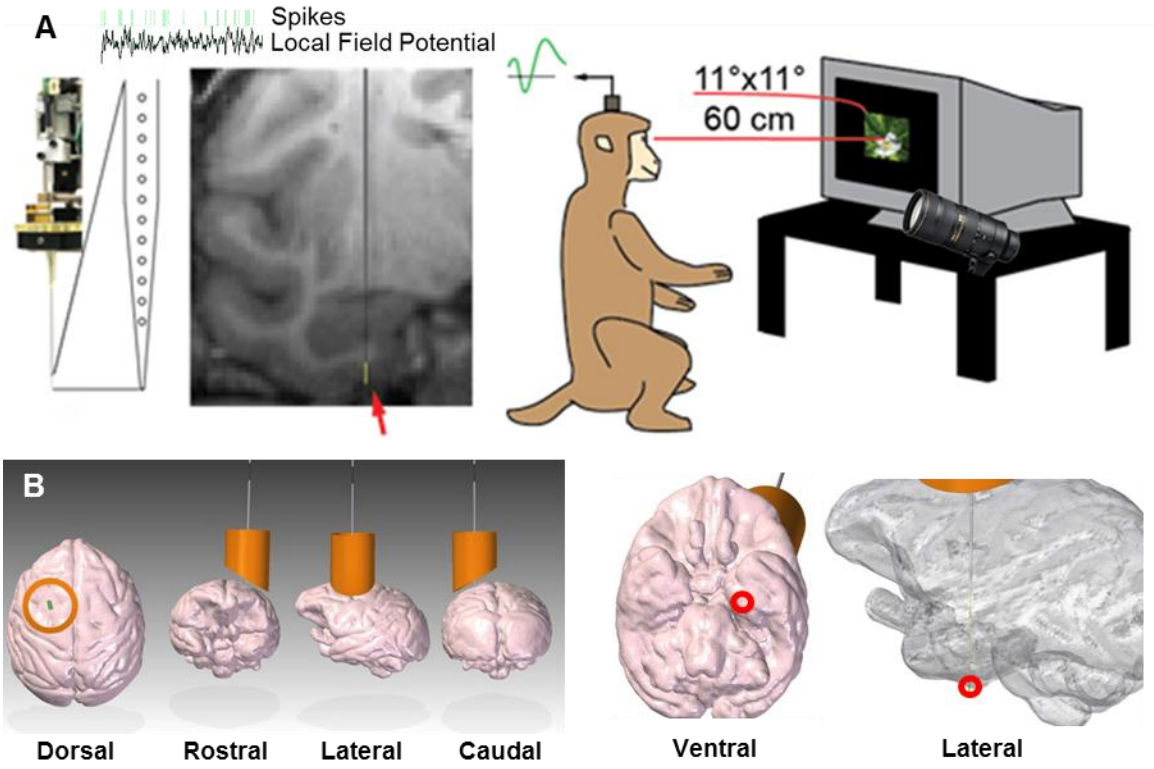

Figure 1.7 | Visualization of recording location with 3-D model macaque brain. A. I performed extracellular recordings of spikes and local field potentials from the entorhinal cortex of monkeys using a 12-contact electrode array inserted into the brain each recording session. The monkeys performed a visual recognition memory task. In this task, images are presented on a computer screen and the monkeys are allowed to freely explore the images while their gaze location is tracked with an infrared camera (placed near the monitor). **B.** Multiple views of the recording chamber (orange), recording probe, and guide tube (thin gray structure) positioned on a model macaque brain. Ventral and lateral views with the approximate final probe position in the entorhinal cortex indicated by red circles. The probe can be seen through the transparent model on the far right.

It has previously been shown that many EC neurons respond with changes in firing rate to incoming visual information, and many of these neurons have enhanced or suppressed responses to repeated image presentations (Suzuki et al., 1997; Xiang and Brown, 1998). I found that these firing rate changes were synchronized within the EC at predictable latencies to stimulus presentation and differed with respect to laminar location. Additionally, I found separate population synchronization patterns associated with encoding and recognition responses. Different synchronization patterns may represent separate modes of information transfer (Jutras et al., 2009; Buffalo et al., 2011; Colgin et al., 2009). I used the time-frequency decomposition of the LFPs to describe these properties. The activity patterns may reflect communication across layers of the EC. To address this issue, I performed analyses using a connectivity measure called Granger causality to assess the strength, frequency, and direction of signal transfer across layers (Granger, 1969; Geweke, 1982). Using the Visual Preferential Looking Task (VPLT) (Jutras and Buffalo, 2010; Wilson and Goldman-Rakic, 1994; Manns et al., 2000), I related these activity patterns to recognition memory processes and characterized beneficial and detrimental patterns. Owing to the uniquely segregated connectivity with the hippocampus, I hypothesized that the EC would show layer-specific differences in activity related to memory formation and recognition. Indeed, I found strong activity patterns in the EC that were related to different phases of visual stimulus encoding and recognition as well as to the strength of memory formation.

Potential applications to clinical devices and a novel *in vitro* testbed

As previously described, the EC has been shown to be critically involved in many diseases including epilepsy and AD. Yet we know very little about the EC and to the best of my knowledge there are no existing therapies that specifically target the EC to treat diseases.

The work described in this thesis lays a foundation of knowledge of the primate EC and thus is a starting position for the development of novel therapies. There are many potential routes for the development of such therapies. In this thesis, I chose to explore one avenue: long-term *in vitro* testing on large sections of explanted tissue.

Stimulation of the EC in human epilepsy patients has been shown to enhance memory for locations in space (Suthana et al., 2012). However, the stimulation parameters in the study of Suthana et al. were not tuned, but were instead borrowed from deep-brain stimulation (DBS) studies with parameters shown to be safe in humans (Velasco et al., 2001; Boon et al., 2007). Stimulation that restores the desired spatiotemporal activity patterns, such as those characterized in this thesis, might be more effective (Berger et al., 2011). Development of therapies would be accelerated by an *in vitro* testbed that permits bi-directional electrical interfacing to optimize stimulation parameters. Current *in vitro* approaches are useful for understanding brain function, but because of limitations in tissue size and culturing duration, are rarely used as development platforms for clinically-viable brain-machine interfaces. A microfluidic-microelectronic – brain tissue interfacing system was designed and validated to overcome these limitations. See Figure 1.8 for an overview of the device. The device and its capabilities are described in Chapter 5. The research in Chapter 5 built upon previous work on thick tissue slices cultured in perfusion chambers (Rambani et al., 2009). A novel perfusion chamber was developed and integrated with a thin perforated microelectrode array (pMEA) to allow electrical interfacing with thick neuronal tissue sections. This device represents the first bi-directional multi-electrode array interface for interstitially perfused tissue. Such tissue can be cultured to be more like what is seen *in vivo* compared to thin slices and monolayer cultures typically used with these electrode arrays because of the ability to maintain many cell layers in a thick (≥500 μm) brain slice.

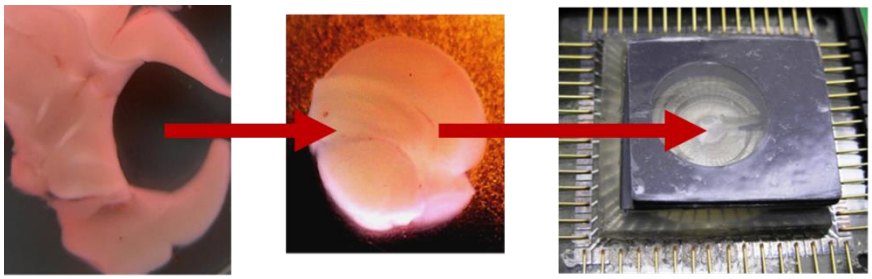

Figure 1.8 | Diagram of usage procedure for the thick brain slice testbed. A desired brain slice is obtained and cut to fit in the testbed. Here a 1 mm thick circular section with a 4.5 mm diameter was taken from a juvenile rat brain and it contains portions of the hippocampus, neocortex, and thalamus. The testbed provides interstitial perfusion of the tissue and bi-directional electrical interfacing through 60 electrodes.

CHAPTER 2

A MAP OF VISUAL SPACE IN THE ENTORHINAL CORTEX[1]

Place-modulated activity of neurons in the hippocampal formation presents a means to organize contextual information in the service of memory formation and recall (Dale et al., 2003; Moser et al., 2008). In particular, grid cells and border cells have been observed in the entorhinal cortex (EC) of rats and bats (Yartsev et al., 2011; Hafting et al., 2005; Solstad et al., 2008), but have yet to be described in single units in primates. Here, I examined spatial representations in the EC of head-fixed monkeys performing a free-viewing visual memory task (Jutras et al., 2009; Jutras and Buffalo, 2010). Individual neurons were identified in the primate EC that emitted action potentials when the monkey fixated multiple discrete locations in the visual field across the presentation of up to hundreds of novel images. These firing fields possess spatial periodicity similar to a triangular tiling with a corresponding well-defined hexagonal structure in the spatial autocorrelation. Further, these neurons demonstrated theta-band oscillatory activity and changing spatial scale as a function of distance from the rhinal sulcus, which is consistent with previous findings in rodents (Hafting et al., 2005, 2008; Koenig et al., 2011; Brandon et al., 2011). A separate group of cells in the EC preferentially fired when parts of the stimulus bounds were viewed, similar to rat border cells (Solstad et al., 2008). These spatial representations may provide a framework to anchor the encoding of stimulus content in a complex visual scene. Together, my results

---

[1] Adapted from: Killian, N. J., Jutras, M. J., and Buffalo, E. A. (2012). A map of visual space in the primate entorhinal cortex. *Nature*.

provide a direct demonstration of grid cells in the primate and suggest that EC neurons encode space during visual exploration, even without locomotion.

Introduction

The primate hippocampus has been shown to represent both egocentric spatial information, with cells responding to self-motion and head-direction information, as well as allocentric spatial information, with cells firing spikes in response to place 'out there' (Dale et al., 2003; Rolls, 1999; Tamura et al., 1992; Ono et al., 1993; Robertson et al., 1999). The presence of allocentric spatial view cells, analogous to rodent place cells, suggests that the primate entorhinal cortex (EC) may also represent space independent of the position of the animal. Indeed, the nonretinocentric, bilateral receptive fields of primate EC neurons allow for the possibility of regular and allocentric spatial firing within the EC (Suzuki et al., 1997). To examine spatial representations in the primate hippocampal formation, I recorded the activity of 223 neurons from the EC of two monkeys performing a free-viewing visual recognition memory task, the Visual Preferential Looking Task (VPLT) (Jutras et al., 2009; Jutras and Buffalo, 2010). I also analyzed data collected from 119 neurons in the hippocampus of two monkeys by Michael Jutras (Jutras and Buffalo, 2010). In this task, novel images were each presented twice on a computer monitor with a fixed reference frame and gaze location was recorded simultaneously with neuronal data. Images consisted of photographs that contained a wide variety of elements including abstract art, animals, landscapes, and people (Figure 2.1a). On average, EC neurons gave enhanced responses to stimulus presentation and many demonstrated a reduced firing rate for repeat presentations, consistent with previous findings of repetition suppression[2] (Suzuki et al., 1997). Neurons in

[2] Repetition suppression is described in the Results section and Figure 2.6.

the hippocampus exhibited a more diverse range of suppressed and excited visual and recognition responses (Jutras and Buffalo, 2010). All of these responses were contained within the analyzed data; I included data segments in the analyses if and only if the monkey was actively exploring an image on the screen (prestimulus fixation periods and viewing outside of the image bounds were not included). The monkeys explored the static images with a dynamic sequence of fixations. Their eyes moved around an image, extracting information about features of interest to them.

In the rat EC, grid cells are found exclusively in the medial EC (MEC). Spatial and visual input to the EC is topographically organized such that spatial information reaches the MEC via input from the postrhinal cortex (parahippocampal cortex areas TF/TH in primates) cortex, while visual object information reaches lateral EC (LEC) via the perirhinal cortex (Witter et al., 2000). In monkeys, roughly the posterior half of the EC receives visuospatial information from parahippocampal cortex (TF/TH), retrosplenial cortex, and presubiculum, while the anterior half receives visual object information from the perirhinal cortex (Insausti and Amaral, 2008). Projections from EC to the hippocampus also have a similar anatomical organization in rats and monkeys, but the anatomical axes are oriented differently. Anterior EC in the monkey and LEC in the rat project to the region around the border between CA1 and subiculum, while posterior EC in the monkey and MEC in the rat project to proximal CA1 and distal subiculum. In addition, there is a lateral to medial gradient of projections in the monkey such that cells located in lateral EC project to posterior levels of the hippocampus while cells located in medial EC project to more anterior regions of the hippocampus (Witter and Amaral, 1991; Canto et al., 2008). This is similar to the gradient observed in the rat EC where dorsal EC projects more to septal hippocampus while ventral EC projects to temporal levels of the hippocampus. Based on the topography of

these inputs, it is expected that the rat MEC and LEC correspond to posterior and anterior EC, respectively, in monkeys.

The spatial firing fields of grid cells can be thought of as representing the nodes of a triangular grid, and it follows that the spatial autocorrelation of the firing rate map should have a well-defined hexagon surrounding a central peak. A gridness score has been used to quantify the strength of 60° rotational symmetry that leads to this hexagonal structure (Sargolini et al., 2006; Brandon et al., 2011). Other symmetry patterns may exist (Krupic et al., 2012), but here I only examined 60° rotational symmetry.

Results

The gridness of all recorded units was evaluated (Figure 2.1, Figure 2.2) and surrogate data were used to determine significant gridness scores. Grid cells were classified as those having a gridness score above the 95th percentile of the scores for 100 time-shifted permutations of the spike timings (see Methods). The number of grid cells identified in the posterior EC, (23/193, 11.9%) was significantly greater than that expected by chance (p < 0.0001, $\chi^2(19.4,1)$) (Figure 2.1c,e). The remaining 88% of neurons appear to be participating in an array of different computations (e.g. border cells and memory cells to be described in this chapter and saccade-direction cells described in Chapter 3). Importantly, the spatial density of gaze location did not produce high gridness scores (Figure 2.3b), and across the population, the grid scores for EC grid cells were consistently higher than grid scores calculated for eye movements (p < 1x10-8 Wilcoxon rank-sum test; Figure 2.1d).

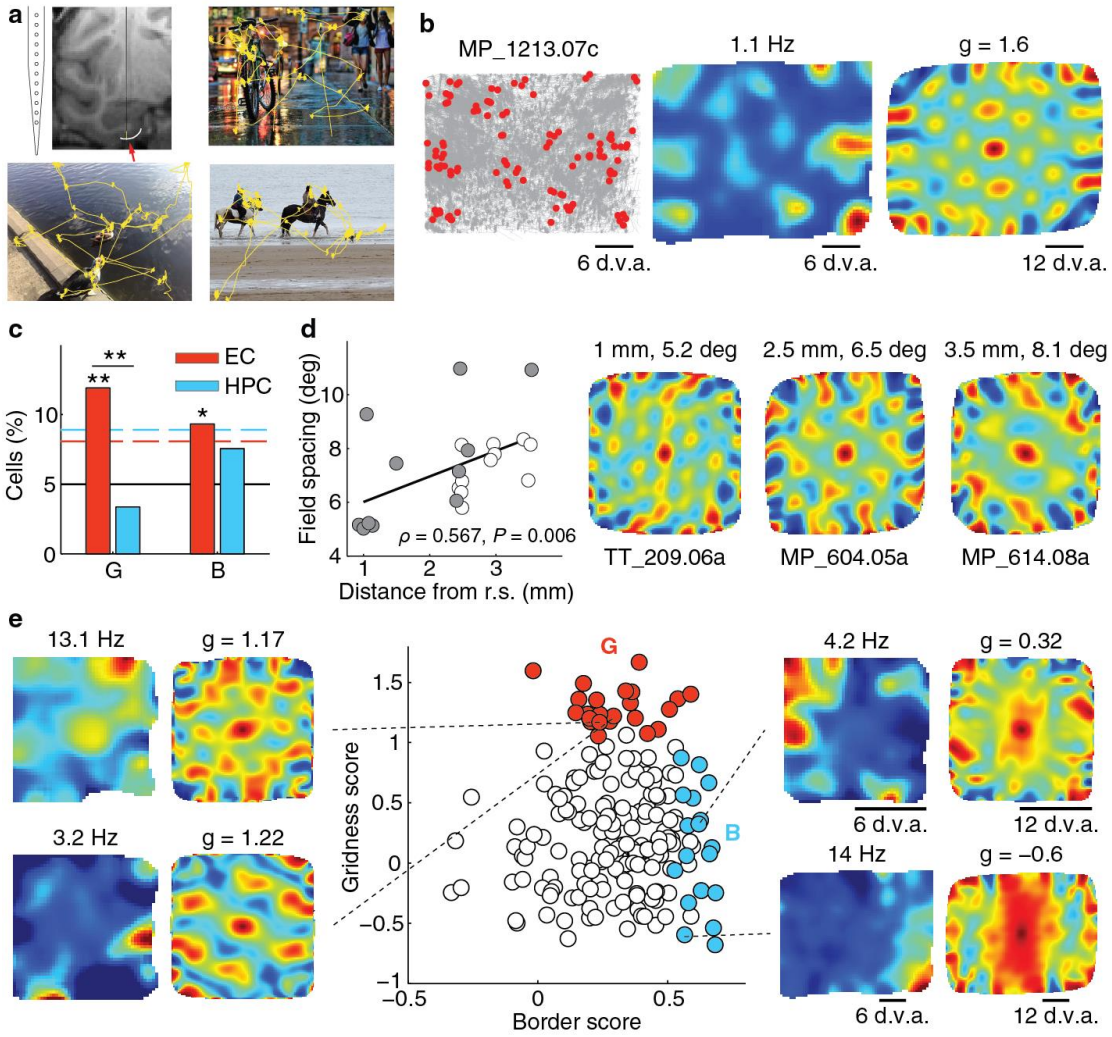

Figure 2.1 | Spatial representation in the primate entorhinal cortex. a. Linear electrode array placed in the entorhinal cortex (red arrow). 10-second scan paths are shown in yellow. **b.** An example of a grid cell. Left: plots of eye position (gray) and spikes (red) reveal non-uniform spatial density of spiking. Monkey name and unit number are indicated at the top. Middle: spatial firing rate maps show multiple distinct firing fields. The maximum of the rate map (red) is given at the top. Right: the spatial periodicity of the firing fields is seen with spatial autocorrelations. The color scale limits are ±1 (blue-red), the maximum correlation magnitude, with green being 0 correlation. g = gridness score, dva = degrees of visual angle. **c.** Percentages of cells in the EC and HPC with a significantly high gridness score (G), or border score (B). The black line shows the 5% chance level, the dashed lines represent the 95% confidence level; $^{*}p < 0.05$, $^{**}p < 0.01$. **d.** Grid cell spacing increased with distance from the rhinal sulcus. Open and closed circles identify the grid cells from each of the two monkeys. Right: autocorrelations for representative grid cells recorded at different locations medial to the rhinal sulcus. **e.** Gridness and border scores are plotted for all cells recorded in the posterior EC (N = 193; red: cells with significant gridness scores, N = 23; blue: cells with significant border scores, N = 18).

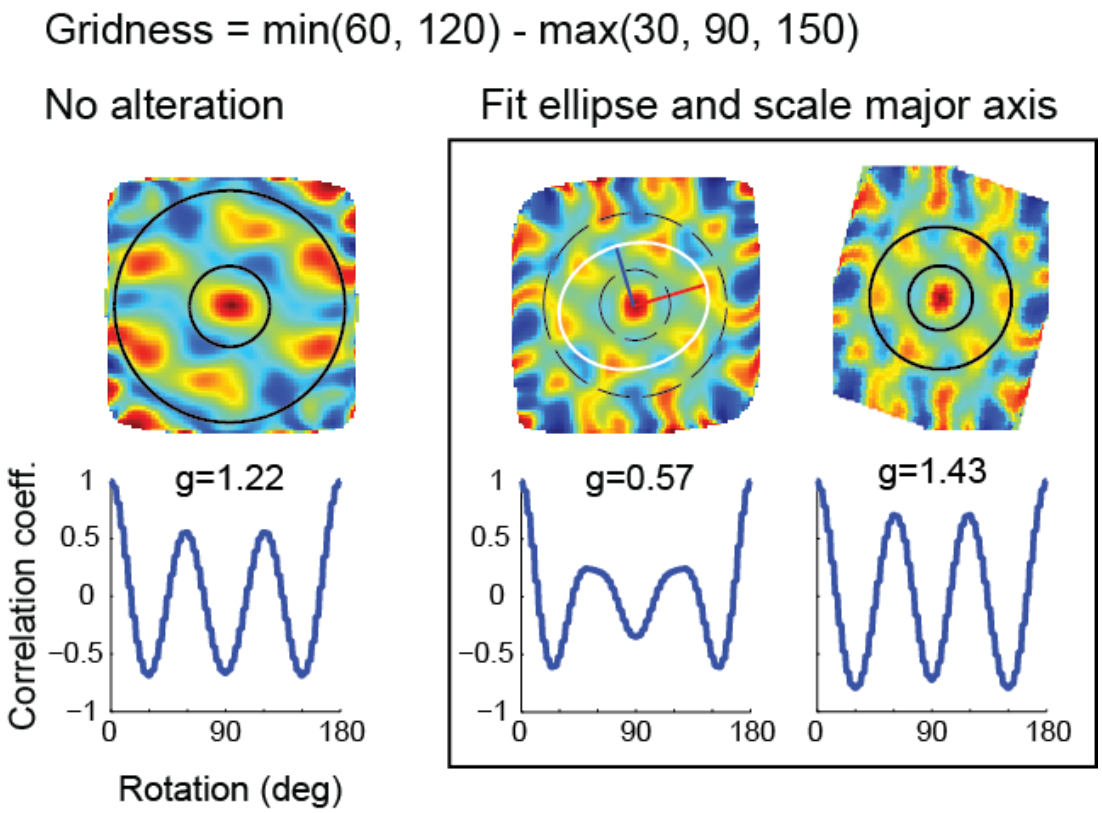

Figure 2.2 | Gridness score calculation. Grid cells were classified using a gridness score (Sargolini et al., 2006; Brandon et al., 2011). An annulus was fit around the six peaks nearest to the center peak of the spatial autocorrelation and the rotational correlation was calculated at 30, 60, 90, 120, and 150 degrees. The minimum correlation coefficient from rotations of 60 and 120 degrees and the maximum correlation coefficient from rotations of 30, 90, and 150 degrees were identified, and the gridness score was equal to the minimum correlation coefficient of the set of values at 60 and 120 degrees minus the maximum correlation coefficient of the set of values at 30, 90, and 150 degrees. The inner radius of the annulus was determined as half of the mean of the distance to the six nearest peaks and the outer radius was varied from 2 bins (see Table 2.1) past the inner radius to the outer edge of the autocorrelation, taking the best resulting score. The score was calculated without scaling and by an ellipse fit-and-scale method like that used in Brandon et al., 2011, to compute gridness for grids that have some ellipticity. As shown in the example at the right, ellipticity causes firing fields of outer rings to enter into the annulus, increasing the correlation at 90 degrees and thus decreasing the gridness score. The minor axis of an ellipse was solved for after specifying the far peak as the major axis. After determining the ellipse axes, the autocorrelation image was scaled along the major axis so that the ellipse became a circle. The higher of the two calculated gridness scores was used for each actual or surrogate autocorrelation image.

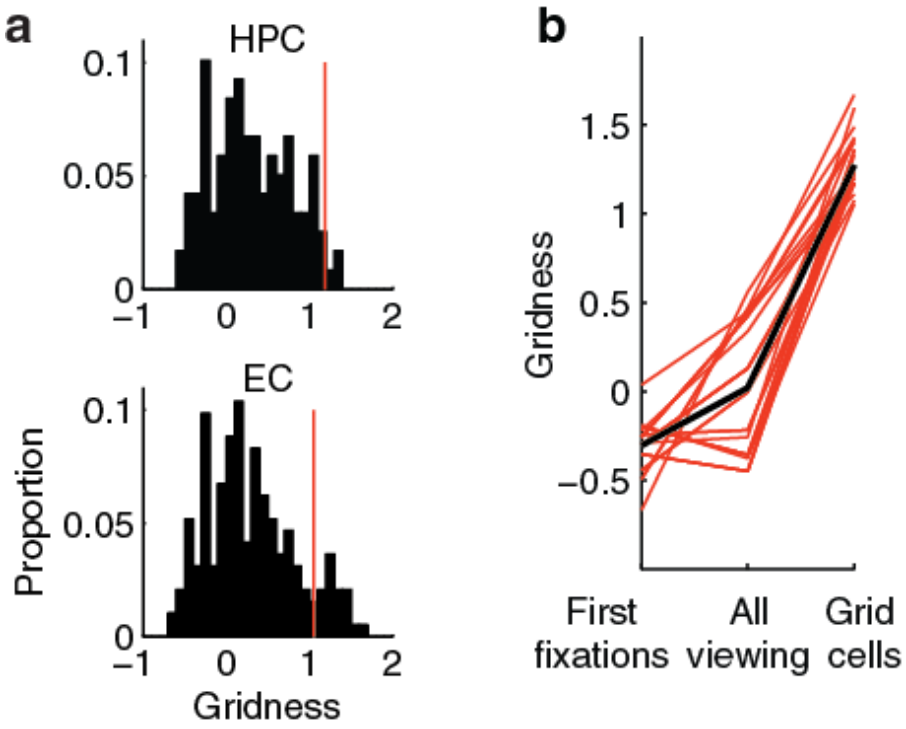

Figure 2.3 | Gridness scores. a. Distribution of gridness scores for entorhinal cortex (EC) (N = 193) and hippocampus (HPC) (N = 119) neurons, cells with significant gridness scores lay to the right of the red lines (the smallest of the significant grid scores for each group). The variances of EC and HPC gridness scores were not significantly different (Levene's test, $F(1,310) = 0.51$, $p = 0.48$). **b.** Shown are the gridness scores for the autocorrelations of initial fixation and aggregate viewing distributions for all grid cells (N = 23). For all grid cells, viewing patterns had lower gridness scores than the actual gridness scores. The black line represents the average gridness scores.

Because these analyses were computed across presentations of multiple complex stimuli, these data suggest that the grid cell representation is not specific to stimulus content. In order to explicitly address this, I examined the reliability of these representations by comparing the rate maps generated from the first and second halves of each session. There was a significant positive correlation between these firing rate maps across the population of grid cells ($p < 0.05$, N = 23, sign test), which suggests that these representations are stable and stimulus-independent (Figure 2.4). Future studies could be performed with images of varying global scales and containing objects on varying scales to determine if how the global

and local scale of the visual information plays a role in the generation of the spatial representations.

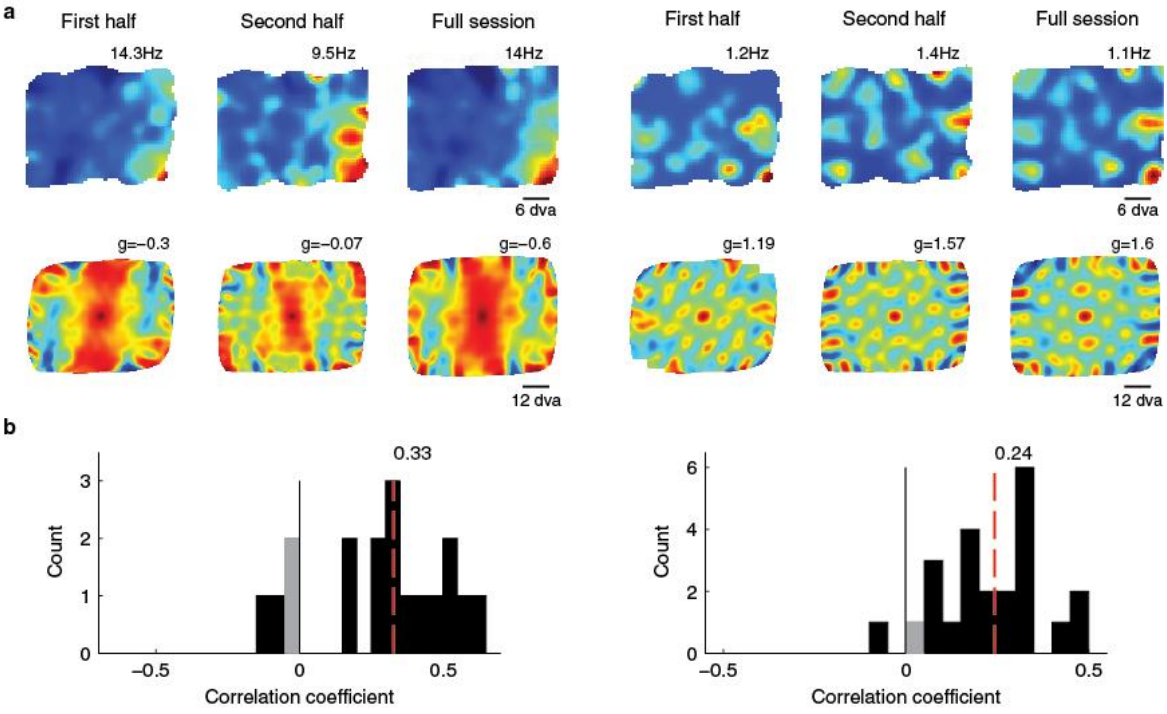

Figure 2.4 | Stability of firing rate maps of grid cells and border cells. a. Stability of spatial representation can be seen in the firing rate and autocorrelation plots using separate partitions of the data for an example cell with a significant border score, left (within-session correlation ρ = 0.54), and grid cell, right (within-session correlation ρ = 0.19). **b.** For the populations of units, firing rate maps were significantly correlated across the session. Correlation coefficients are shown in the histograms for cells in the EC with significant border scores (left) and significant gridness scores (right). The median correlation coefficients are represented by dashed red lines. Bars corresponding to cells with significant correlation coefficients ($p < 0.05$) are black. The population of cells with significant border scores had significant positive correlations as a population ($p < 0.01$, $N = 18$, Wilcoxon signed-rank test) and for 14 of 18 cells individually ($p < 0.05$). The population of grid cells also had significant positive correlations ($p < 1\text{x}10^{-5}$, $N = 23$, Wilcoxon signed-rank test) and for 21 of 23 grid cells individually ($p < 0.05$).

The proportion of grid cells identified in the hippocampus (4/119, 3.4%) was not significantly different from chance (p = 0.41, $\chi^2(0.67,1)$) and was significantly less than the number of EC grid cells (p = 0.009, $\chi^2(6.82,1)$). An important caveat is that the hippocampal recordings were all taken from the anterior hippocampus (Jutras et al., 2009), which is presumably comparable to the temporal hippocampus in rats which contains cells with larger place fields than in more septal regions. Accordingly, it is difficult to compare the scale of the spatial representations between the EC and HPC with the present data. I also found a significant population of neurons in the EC, but not the HPC, that fired in relation to stimulus borders (EC: p = 0.0058, $\chi^2(7.61,1)$, 18/193 (9.3%); HPC: p = 0.1995, $\chi^2(1.65,1)$, 9/119 (7.6%); Figure 2.1c,e). Border cells fired in relation to the stimulus bounds of both stimulus sizes tested (2 of 7 cells with the large stimuli and 16 of 186 cells with the smaller stimuli were classified as border cells). The presence of cells that represent spatial locations relative to the stimulus bounds independent of stimulus content, suggests that representations of objects within an environment may be anchored to this consistent framework, with the stimulus bounds serving as landmarks. However, it is possible that these neurons simply have view fields near the border of the image presentation region. This would need to be examined in future studies with shifted image frames (see Chapter 6).

In the rat and bat EC, grid cells increase in field spacing in the dorsomedial to ventrolateral direction, with distance from the border of the MEC with the postrhinal cortex (Yartsev et al., 2011; Hafting et al., 2005; Sargolini et al., 2006; Brun et al., 2008). This gradient mirrors the increase in the size of hippocampal place fields along the dorsoventral axis (Jung et al., 1994; Maurer et al., 2005; Kjelstrup et al., 2008), to which the MEC provides input in a topographical manner (Witter et al., 2000; Canto et al., 2008). In the present study, firing field spacing was significantly correlated with distance from the rhinal

sulcus for each monkey and for both monkeys taken together (MP: ρ=0.671, p = 0.024; TT: ρ=0.665, p = 0.026; both monkeys: ρ=0.567, p = 0.006) (Figure 2.1f and Figure 2.5).

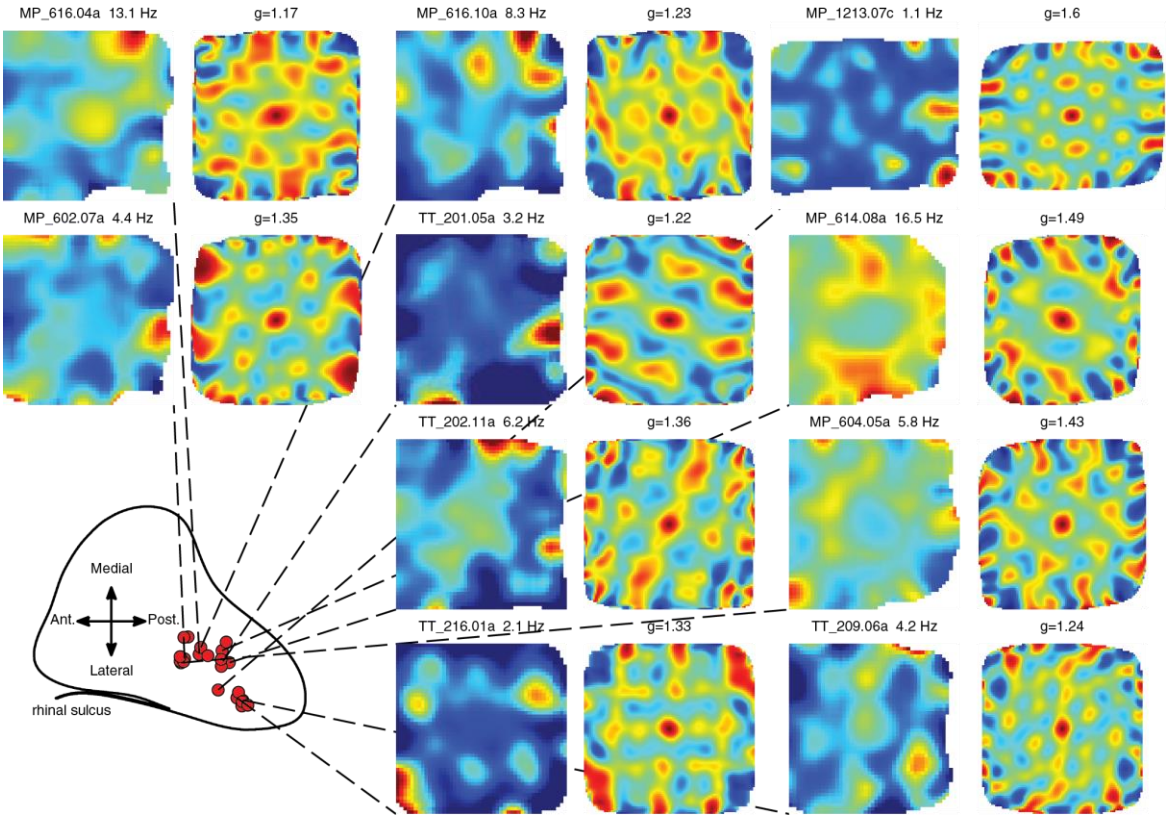

Figure 2.5 | Grid cell spatial firing rate maps and autocorrelograms. Shown are the rate map, autocorrelogram, and approximate recording location placed on a prototype map of the EC (Insausti and Amaral, 2008) for a selection of cells with significant gridness scores. Red circles indicate the recording locations of all grid cells.

Along with spatial representations, I also examined neuronal responses in the EC that might underlie recognition memory, as was previously identified in the hippocampus (Jutras and Buffalo, 2010). Consistent with the increase in input from perirhinal cortex to anterior EC, I found that neurons in anterior EC demonstrated stronger visual and memory responses than did neurons in posterior EC. Specifically, a larger proportion of neurons responsive to visual stimuli was found at more anterior locations (p = 0.0062, $\chi^2(7.5,1)$) and among these visually responsive neurons, a larger proportion demonstrated a reduction in firing rate for repeated stimuli, i.e., 'repetition suppression', at more anterior locations (p = 6.67x10-9, $\chi^2(33.63,1)$) (Figure 2.6a). This suppression response will be referred to as a 'memory response' and the neurons that have this response, though not necessarily exclusively, will be referred to as 'memory cells'. Furthermore, among the neurons displaying significant repetition suppression, the relative decrease in firing rate for repeat presentations was greater at more anterior locations (Figure 2.6b). Interestingly, the recognition memory and spatial representations were somewhat independent of each other; at more anterior recording locations, grid cells were more likely to also exhibit a memory response, with a firing rate reduction magnitude in line with the rest of the population of cells (p = 0.0034, $\chi^2(8.55,1)$). However, there was a gradual decline in the percentage of grid cells at more anterior locations and no grid cells were found in any of 3 separate penetrations in front of the posterior 50% of the EC, suggesting that there may be a functional border between posterior and anterior EC. Because most of my recordings were in the posterior EC, an important target of future studies will be to further characterize responses throughout the anterior EC.

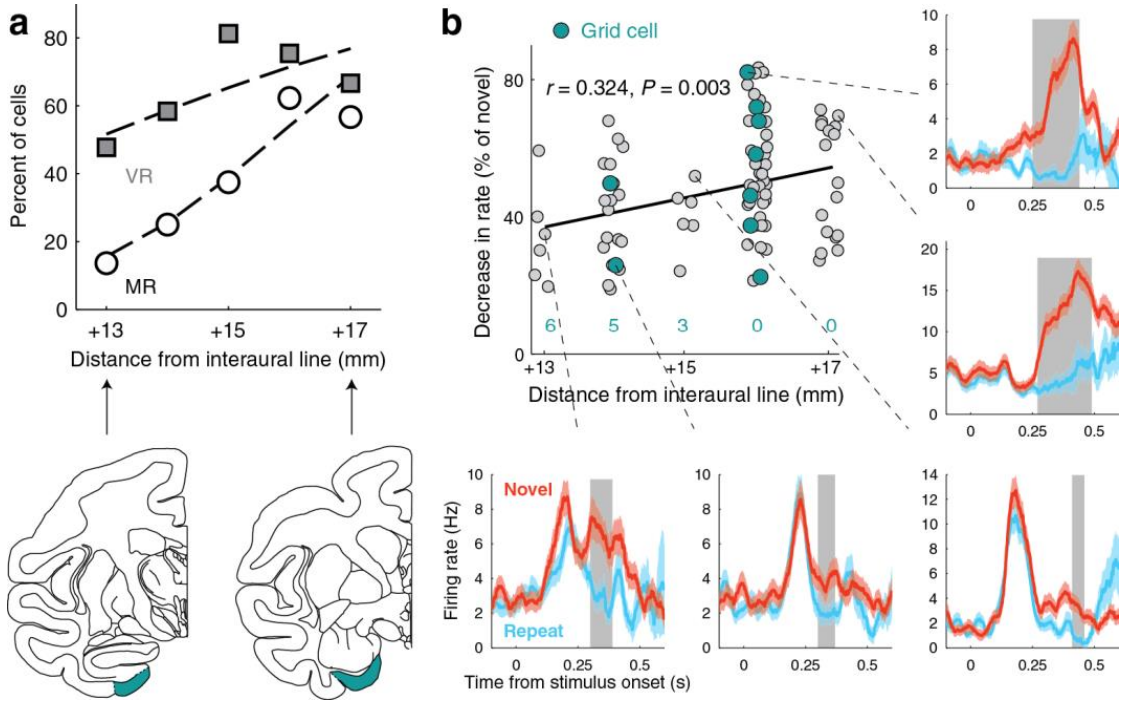

Figure 2.6 | Recognition memory responses and conjunctive grid-memory cells. a. At more anterior locations, cells were more likely to be visually responsive (VR, $p < 0.01$) and, among those, more likely to show a differential response for novel compared to repeated images (MR, $p < 0.001$), which might underlie recognition memory performance. The EC is shown in teal in the coronal slices. **b.** The strength of the memory response (% decrease in rate for repeated stimuli) increased in more anterior recording locations ($N = 85$ cells with a significant recognition memory response). Grid cells (teal) were more likely to show a recognition memory response at more anterior locations (the number of grid cells without a significant memory response at each location is shown in teal). Neuronal responses to novel and repeat presentations are shown for some representative neurons (mean ± SEM). Gray shading indicates a time region of significant decrease in firing rate for repeat presentations ($p < 0.025$) (Maris and Oostenveld, 2007).

Current-source density estimates were used to classify layers of the entorhinal cortex (Pettersen et al., 2006). Grid cells were found in both superficial and deep layers (14/163 in superficial layers and 5/30 in deep layers), suggesting that grid cells play a role in processing both input to and output from the hippocampus. Because many grid cells in layers deeper than layer II are modulated by head direction in rodents, it is possible that recording with the monkey's head positioned in variable directions would increase these percentages. In addition, the physical restriction of using dorsal to ventral penetrations precludes higher sampling of the thin layer II that possesses the largest percentage of grid cells in rodents.

Because theta-band modulation is critical to certain models that describe the generation of grid cells (Burgess et al., 2007), I next examined theta-band oscillatory activity in individual EC grid cells and in the simultaneously recorded local field potential (LFP) on the same electrode. I found that the EC exhibits intermittent bouts of theta oscillations similar to the theta bouts previously described in the primate hippocampus (Figure 2.7a,b) (Stewart and Fox, 1991; Ekstrom et al., 2005). These bouts, detected during blocks of image presentations, had a mean duration of 1.09 ± 0.86 s and a mean inter-bout interval of 0.95 ± 0.94 s (mean ± SD). I also found that in all of the data during these blocks, not restricted to theta bouts, the grid cells were phase-locked to near the trough of the LFP theta (Figure 2.7c) and the spike trains of 13 of 23 grid cells (57%) were theta-modulated (Figure 2.7c), consistent with findings in rodents (Mizuseki et al., 2009; Langston et al., 2010). The phase lag corresponding to the 120 degree 'lag' of the phase-locking peak relative to the peak of the 3-12 Hz theta oscillation would be on average 44 msec (taking a sinusoidal oscillation have a frequency of 7.5 Hz). Thus the theta oscillation leads the spiking by approximately 44 msec. Theta-modulation and phase-locking were not limited to grid cells but were seen in the population of EC and HPC neurons as a whole (Figure 2.8).

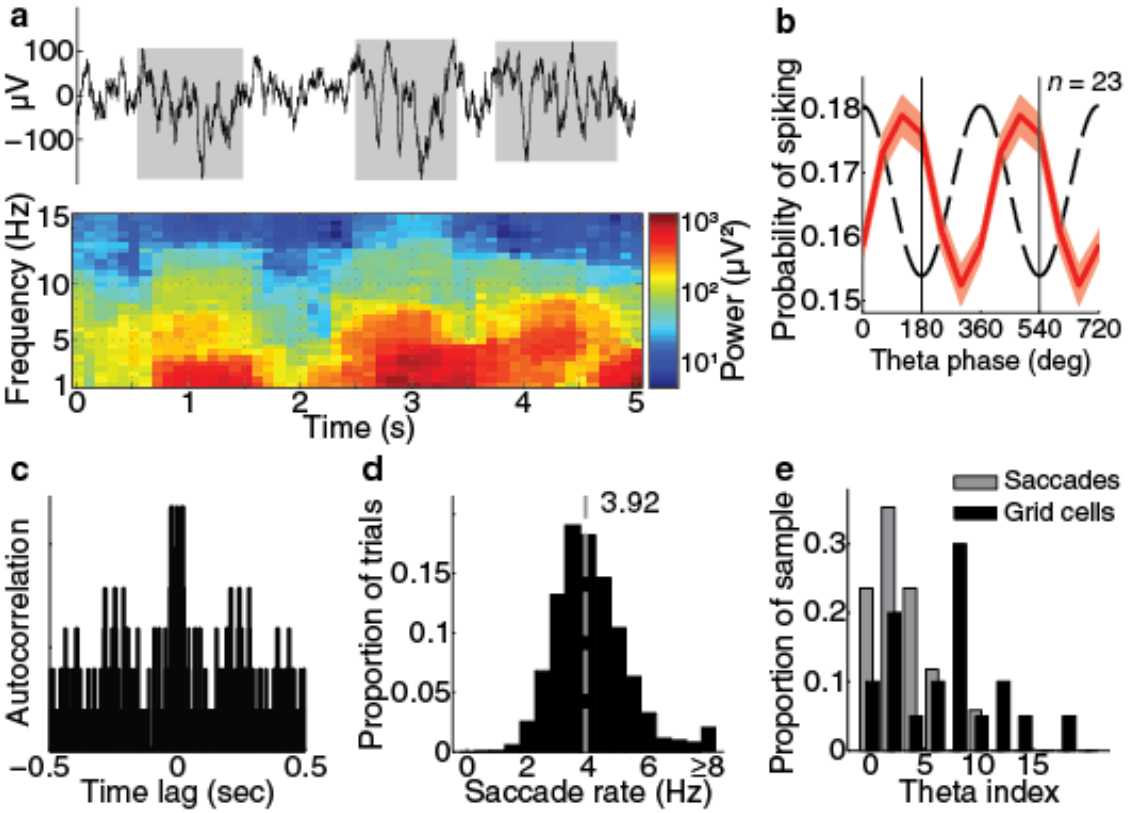

Figure 2.7 | Theta bouts and theta modulation of grid cells. a. Top: 5 second raw LFP trace with theta (3-12 Hz) bouts indicated in gray. Bottom: spectrogram showing the power (dB) of the top LFP trace. **b.** Grid cells were phase-locked to LFP theta (60° bins, red curve: mean ± SEM, dashed curve: prototype theta oscillation, two cycles are shown). **c.** Autocorrelation showing theta modulation of the spike train of a grid cell (theta index = 11.2 at 4.2 Hz). **d.** Histogram of the saccade rate during image viewings in 19 sessions (4.16 ± 1.49 Hz, mean ± SD, dashed gray line = median, 3.92). **e.** Saccade times (N = 17) resulted in lower theta indices than the grid cell spike trains (N = 20) ($p < 0.01$, N = 15, Wilcoxon rank-sum test).

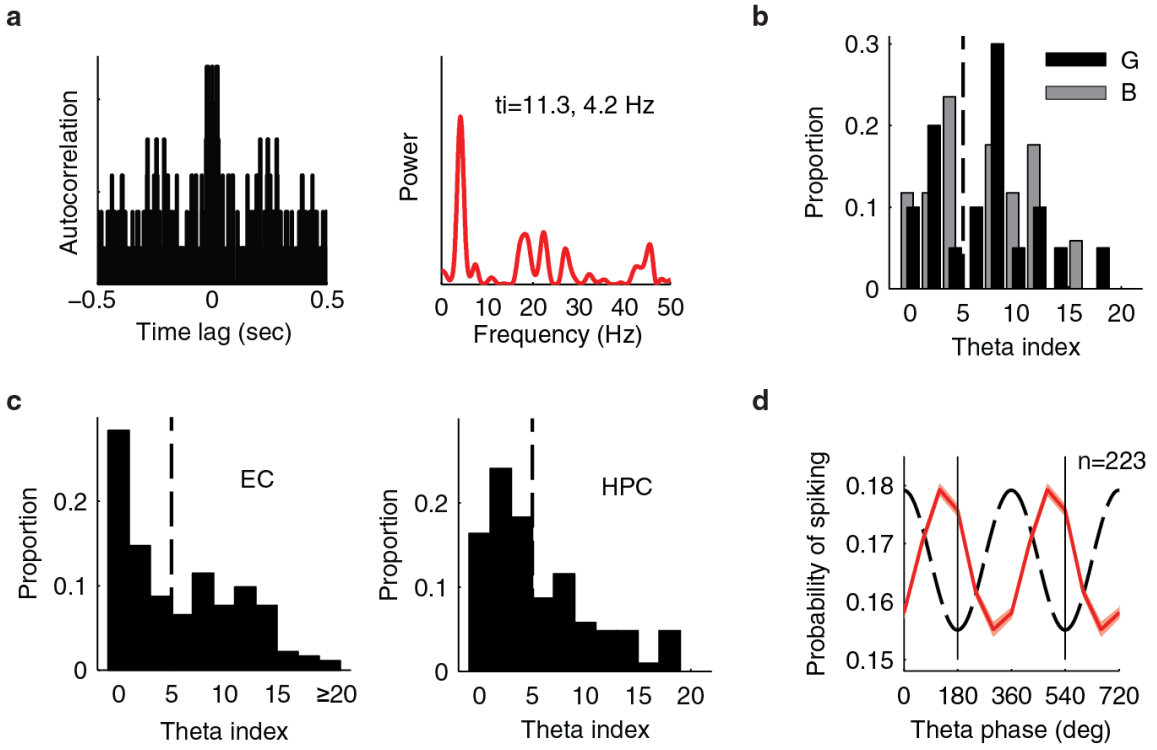

Figure 2.8 | Theta-band modulation of spiking and theta phase-locking to the LFP. a. Autocorrelogram and power spectrum of the autocorrelation for the example grid cell shown in Figure 2.7c. The theta index computed from the power spectrum is 11.3 at a peak frequency of 4.2 Hz. **b.** Histogram of theta indices for EC grid cells (G, N = 20/23 cells with a calculable theta index) and cells with significant border scores (B, N = 17/18 cells with a calculable theta index). Both groups showed theta-modulation. **c.** Histograms of theta indices for all entorhinal cortex (N = 183/223 cells with a calculable theta index) and hippocampus (N = 104/119 cells with a calculable theta index) neurons. Neurons were considered theta-modulated if the theta index was above 5 (to the right of the dashed line). **d.** The population of EC neurons as a whole shows phase-locking near the trough of theta. Shown is the probability of spiking (mean ± SEM) with respect to the theta-band LFP recorded at an electrode 150 or 300 microns away for all EC single units (cf. Figure 2.7b).

This modulation existed in the presence of the intermittent theta oscillations in the LFP, similar to those described in bats but with shorter inter-bout interval (Yartsev et al., 2011). Saccades were made at an average rate of 3.97 Hz (252 inter-saccade interval), but the precise timing of saccades was not theta modulated, so the theta modulation of grid cells was not due to rhythmicity in eye movements (Figure 2.7e). Firing rate maps for bout periods were correlated with non-bout periods ($p < 0.01$, Wilcoxon signed-rank test) and I did not find a significant difference in the grid pattern between firing during bouts and non-bouts

(Figure 2.9). Future experiments with disruption of theta would aid in understanding the relationship between primate theta and spatial firing patterns (Brandon et al., 2011; Koenig et al., 2011). Importantly, the present data demonstrate theta-band modulation among EC grid cells, even in a species that demonstrates non-continuous bouts of theta-band oscillations. This information is critical for informing computational models and increasing our understanding of the generation of these spatial representations (Burgess and O'Keefe, 2011; Burgess et al., 2007).

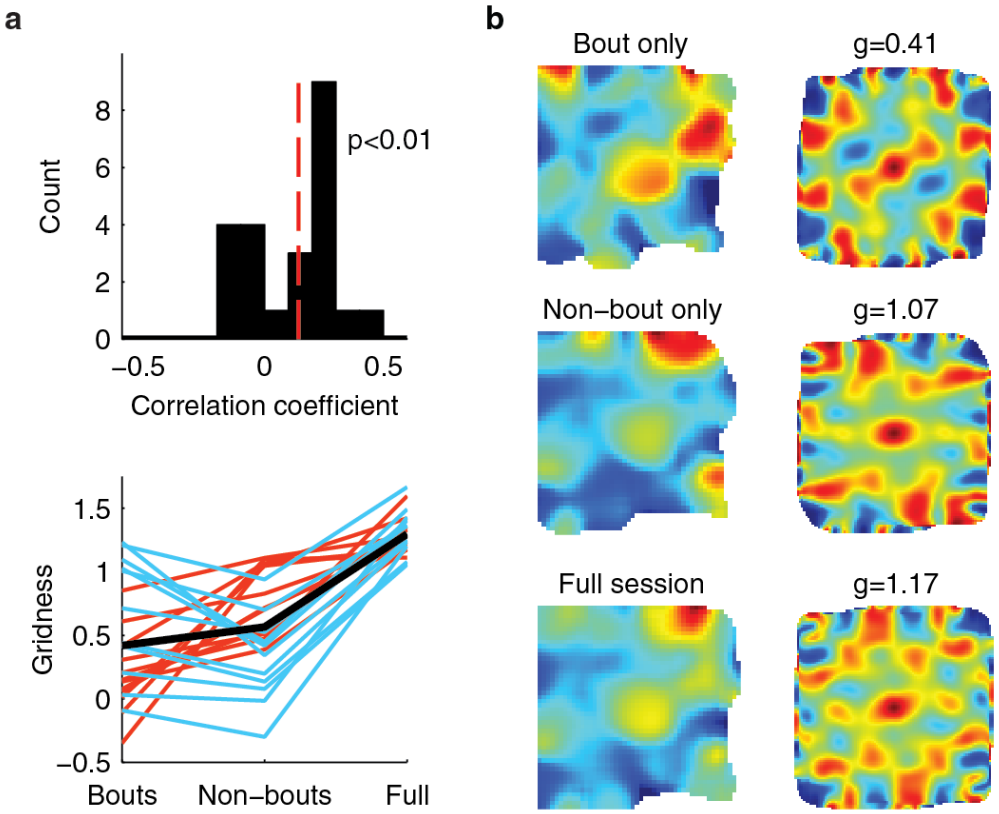

Figure 2.9 | Evidence for grid-like representations in both the presence and absence of theta bouts. a. Top: Histogram of bout compared to non-bout rate map correlations (Pearson's r). Rate maps were significantly correlated between bout and non-bout periods ($p < 0.01$, $N = 23$, Wilcoxon signed-rank test; the red dashed line indicates the median, 0.14). Bottom: Gridness was not significantly different between bouts and non-bouts ($p = 0.18$, Wilcoxon rank-sum test). Gridness was higher during bouts compared to non-bouts for 11 of 23 grid cells (blue lines), and lower for 12 of 23 (red lines); the black line represents the average gridness scores. **b.** The rate map (left) and autocorrelogram (right) for one grid cell are shown during theta bouts (top), during periods without theta bouts (middle), and during the full session (bottom).

Discussion

Taken together, these data provide evidence for grid cells in the primate entorhinal cortex. These spatial responses are similar in many respects to grid cells that have been described previously in the rat and bat during locomotion, but were identified with a distinct method of sampling the environment, i.e., visual exploration through eye movements. These results suggest that spatial representations in primates can arise during visual exploration at a distance, without requiring an actual visit to that place. Accordingly, these data suggest that theories of spatial representation in the context of navigation, such as theories related to the neuronal representation of path integration (McNaughton et al., 2006), could be applied to visual exploration.

Notably, although grid-cell spiking was theta-modulated, I found significant evidence for grid cells in the absence of continuous theta-band oscillations in the LFP. These data suggest that current models of grid cells based on interactions of continuous oscillations are species- or paradigm-specific or that they may need to be adapted to account for both intermittent theta and exploration through saccadic movements. One possibility is that saccades produce a theta-band phase shift in the LFP. This would modulate the theta-band frequency in a way that might be comparable to the modulation in frequency that occurs through movement velocity in rodents. It is also possible that an optimal model might include aspects of current oscillatory interaction and network attractor models (McNaughton et al., 2006). These results provide a potential challenge to the view that grid cells support path integration by combining self-motion and environment cues (Hafting et al., 2005). Because these experiments were performed with the monkey's head and the visual stimulus in a given, fixed position, I was not able to identify whether these grid cells represent allocentric or egocentric spatial locations. It is possible that the spatial representations

identified here reflect an integration of environmental context and the magnitude of eye movements, but this will need to be carefully examined in future experiments (see Chapter 6).

Methods

All experiments were in compliance with the Public Health Service (PHS) Policy on Humane Care and Use of Laboratory Animals, the Eighth Edition of the Guide for the Care and Use of Laboratory Animals, and the Animal Welfare Act. All use of animals and all procedures that used animals were reviewed and approved by the Emory University Institutional Animal Care and Use Committee.

In each VPLT session, 200 novel images were each presented twice on a computer monitor in a randomly interleaved fashion within 11x11 degrees in the center of the monitor. Monkeys were head-fixed and sitting in a chair with the center of the monitor aligned to their neutral eye position. An image was removed after the monkey looked outside the image bounds or after 5 seconds. In a second version of the task that was used to record from 7 EC units, images covered the entire viewable region of the monitor (33.3 x 25 degrees). In this large image version, each of 36 novel scenes was shown twice and a total of 10 seconds of visual exploration was required for each presentation. The monkey's gaze location was recorded with an infrared eye-tracking system (ISCAN). Rate maps were computed with a Gaussian smoothing procedure (Langston et al., 2010). Gridness scores and border scores were calculated using standard equations and significance was evaluated with a standard shuffling procedure (Langston et al., 2010; Solstad et al., 2008). Theta-band bouts in the LFP were detected by statistically analyzing the power spectrum over time (Ekstrom et al., 2005). Theta-band modulation of grid cells was analyzed with a standard autocorrelogram power spectrum metric, the theta index (Langston et al., 2010).

Behavioral task and parameters

I examined neuronal activity in the entorhinal cortex (EC) and hippocampus recorded from three male monkeys performing the Visual Preferential Looking Task (VPLT), using experimental control software (CORTEX; http://dally.nimh.nih.gov/) (Wilson and Goldman-Rakic, 1994; Jutras and Buffalo, 2010). Performance on this task represents recognition memory and is sensitive to the integrity of the hippocampus and adjacent cortical regions (Zola et al., 2000). For each recording session the monkeys (Macaca mulatta) performed the VPLT, in which 200 novel, complex visual images obtained from a database of over 25,000 images constituted the stimuli of one session. In this task, each image was viewed twice with up to 10 intervening stimuli between presentations. Between blocks of images, a bar-release task was used to implicitly reward the monkeys for viewing images, but not for the viewing itself. A food reward comprising a blended mixture of bananas, Lab Diet biscuits, and applesauce was delivered via a customized peristaltic pump after each successful trial (Appendix D). On each trial, after a 1-second fixation period, an 11 x 11 degree image appeared on the screen and the monkey was allowed to explore the image until the tracked eye position moved outside of a 12 x 12 degree region, or a maximum of 5 seconds (7 seconds in TT, EC recordings). For the experiments with the 33.3 x 25 degree images covering the entire viewable region of the monitor, 36 novel scenes were shown twice with 10 seconds of viewing required for each presentation. The gaze location was recorded with an infrared eye-tracking system (ISCAN, Inc.). Stimuli were presented on a CRT monitor with a 19 inch diagonal at a 120 Hz refresh rate. The monkeys were head-fixed and the distance of the centre of the monitor to the eyes was maintained at 60 centimeters. Before each recording, eye position was calibrated using the difference of the pupil centroid and corneal reflection centroid of the right eye using a similar bar-release task. When

necessary, eye position was re-calibrated offline (Appendix E).

Electrophysiological recordings

I recorded spikes (250-8000 Hz) and local field potentials (LFPs, 0.7-170 Hz) from the EC with a laminar electrode array mounted on a tungsten microelectrode (AXIAL array: 12-site, 30 μm diameter, 150 μm spacing, FHC, Inc., Appendix A). Recordings were performed using hardware and software from Plexon, Inc., and all subsequent analyses were performed using MATLAB (The MathWorks, Natick, MA). Spikes were recorded from the hippocampus with 4 independently moveable tungsten microelectrodes. All recordings were performed in the left hemisphere. Recording sites were planned with the aid of MRI. Custom 3-D-printed positioning adapters were created to improve accessibility of the EC when required (Appendix B). Electrodes inside a stainless steel guide tube were slowly lowered through a craniotomy at the beginning of each recording session. Electrodes were then advanced out of the guide tube to the recording site while the animals performed unrelated tasks. Electrodes in the hippocampus were advanced until single units could be isolated. The laminar array used to record from the EC was advanced very slowly with online MRI-based position monitoring (Appendix C) until noise on the tungsten tip was observed due to reaching the ventral surface (the array was then retracted until no such signal was present). Recordings were initiated after stable spiking could be verified (usually about 30 minutes). Spikes were sorted offline into distinct clusters using principle components analysis (Offline Sorter, Plexon, Inc.). Sorted clusters were classified as single units if the root-mean-square error (RMSE) of the waveforms from the mean waveform was below 0.3 after normalizing to the mean waveform of the cluster. This secondary criterion helped to restrict waveform groups to signals from single neurons, but may have included clusters with waveforms recorded from multiple neurons in some cases. In addition, units with fewer than

150 spikes and less than 500 seconds of total sampling were excluded from the analyses to reduce sampling error. Three monkeys were recorded from: 223 single units from the EC of 2 monkeys (MP and TT) and 119 single units from the hippocampus of 2 monkeys (MP and IW). For the EC recordings, 193 single units were recorded from the posterior region of the EC (up to IA +16) and the other 30 units were recorded from more anterior regions.

On average, the EC units exhibited a repetition suppression effect as reported previously (Suzuki et al., 1997). As a population, the EC units exhibited a decreased firing rate for the repeated stimulus from about 250 to 500 msec after stimulus onset. To analyze the firing rates for individual units, spike counts from 250 to 500 msec after stimulus onset were compared with a Student's t-test to spike counts 500 to 250 msec before stimulus onset. Variable trial lengths were allowed and only trials that lasted at least 310 msec were included in the analysis. Units were classified as visually responsive if either the encoding (novel stimulus presentation) or recognition (repeated stimulus presentation) trials had a significant difference in rate compared to baseline. Of the visually responsive units, units with memory responses were identified using a Student's t-test to compare the same time windows after stimulus onset with paired novel and repeat trials. The regions of significant differences between novel and repeat viewings for individual units in Figure 2 were computed using a cluster-based non-parametric permutation test ($P_{\text{two-sided}} < 0.05$, 30,000 randomizations per unit, $p < 0.1$ cluster threshold using a dependent samples *t*-test for each randomization) (Maris and Oostenveld, 2007). Logistic regression was used to examine the relationship between anterior-posterior location and proportion of visually responsive or differentially responsive cells. Significance of the anatomical location as a predictor was calculated using a chi-squared test with 1 degree of freedom on the increase in deviance of the fit without the predictor (likelihood ratio test).

Layer classification

Location within the EC was classified with the aid of current source density (CSD) analysis, using simultaneously recorded local field potentials (LFPs) (Pettersen et al., 2006). See Chapter 3 for more details on layer classification.

Rate maps and autocorrelations

Rate maps were computed with a Gaussian smoothing procedure (Table 2.1) (Langston et al., 2010). Data from the image presentation periods were concatenated across trials. Spikes and eye position sampled at 1 kHz were binned into square bins over the viewing region. The resulting values were smoothed by convolving with a 2-D Gaussian kernel approximation out to ± 2 standard deviations around the centre bin and divided to estimate the firing rate over space. To reduce sampling error, a minimum looking time of 100 msec per 1 deg^2 area was required. Pixels below the minimum looking time requirement were removed from rate maps if they were part of a contiguous 8-connected neighborhood (islands of a single bin were not removed). Spatial autocorrelations were computed by shifting a copy of the discretized rate map with respect to itself as in the autocorrelation function, but with the values at each x and y translation computed using the Pearson product-moment correlation coefficient formula (Langston et al., 2010). A set number of valid (above the minimum looking time) pixels were required to compute an autocorrelation value for a given translation. Stability of rate maps (Figure 2.4) was analyzed by removing the initial 120 seconds of the session (25% of the session on average), dividing the remaining data in half, computing the rate map for each half with smoothing performed after dividing binned spikes by binned time, and taking the Spearman's rank correlation coefficient between the corresponding pixels in the two rate maps.

Grid cell classification

The two gridness calculation approaches (with or without ellipse correction) were applied to the original data and 100 time-shifted versions the data. The spike train was shifted in 100 linearly-spaced increments from 20 seconds into the session to the end of the session minus 20 seconds and the resulting rate maps, spatial autocorrelations, and gridness scores were calculated. Units with a gridness score above the 95th percentile of the surrogate data for each unit were considered grid cells. Five percent of cells would be expected to have a significant gridness score by chance (i.e. 9-10 of 193 cells). A population of neurons with significant gridness scores was determined to be significant by performing Pearson's chi-squared goodness of fit test. The 95% confidence intervals displayed in Figure 2.1c were calculated from the chi-squared distribution by taking the range over which the null hypothesis would not be rejected.

To validate the time-shifting method, I designed an alternative test that uses a model of spiking to take into account other covariates. I modeled firing rate for each neuron using the average firing rate during times after saccade onset and stimulus onset. Simulated spikes were generated based on an inhomogeneous Poisson process with 1 msec time bins and having average firing rate as a function of time, $\lambda(t)$:

$$\lambda(t) = \sum_{i}^{N_i} \lambda_p(t - t_i)\left(u(t - t_i) - u\left(t - (t_i + l_i)\right)\right) \sum_{k}^{N_k} \lambda_s(t - t_k)\left(u(t - t_k) - u\left(t - (t_k + l_k)\right)\right)$$

For the i^{th} image presentation of N_i presentations of length l_i beginning at time t_i and N_k saccades of length l_k starting at time t_k with normalized mean rate $\lambda_s(t)$ where $u(t)$ is the Heaviside step function and $\lambda_p(t)$ is the mean rate with respect to stimulus onset. The saccade rate function was normalized to its maximum to modulate the rate based on stimulus onset time. One hundred simulations were run for each grid cell and the gridness score was

calculated for each resulting rate map. Neurons with gridness scores above the 95th percentile were classified as grid cells. With this test, 19 of 23 grid cells classified with the time-shifting test were still classified as grid cells and 1 new grid cell was identified. The number of grid cells with this test, 20 of 193 (10.4%), was significantly above what would be expected by chance with a *P*-value of 0.0006 using a chi-squared test of independence.

Border scores

Cells with a border score above the 95th percentile for 100 time-shifted permutations (the same permutations used for gridness scores) were classified as significantly preferring to fire along borders. The border score was the same as that used in Solstad et al. 2008, however where Solstad et al. used a rate map threshold of 30% of the maximum rate and a border score cutoff of 0.5 I used a rate map threshold equal to the mean firing rate over all bins and a permutation distribution to define significant border scores (Solstad et al., 2008). Significant border scores ranged from 0.53 to 0.69. The border score, b, was calculated by comparing the maximum coverage of a given stimulus edge by a single firing field, c_M, to the firing rate-weighted average distance to the nearest edge, d_m:

$$b = \frac{c_M - d_m}{c_M + d_m}$$

Firing field size and spacing

The distance between firing field centres was set to the best outer radius determined through the gridness score calculation procedure (Langston et al., 2010). This helped reduce error from peak detection, though some peak detection error remained through determining the inner radius. Correlations between anatomical location and field spacing were calculated using the Spearman's rho rank correlation coefficient. Only grid cells recorded with the

smaller images were used in the correlation (22 of 23 grid cells, 11 per monkey).

Grid cell locations

The posterior-anterior anatomical location of the EC was estimated by taking fourteen 1 mm slices from an MRI scan to constitute the range of the EC. The extent of the EC was identified by comparing anatomical features on the MRI scans to an atlas (Saleem and Logothetis, 2007). The fundus of the rhinal sulcus was identified in MRI scans to estimate the medial distance of the recording locations. Locations of all grid cells were estimated using MRI scans and known electrode positions (Figure 2.10). Grid cells were identified in all recorded layers of the EC.

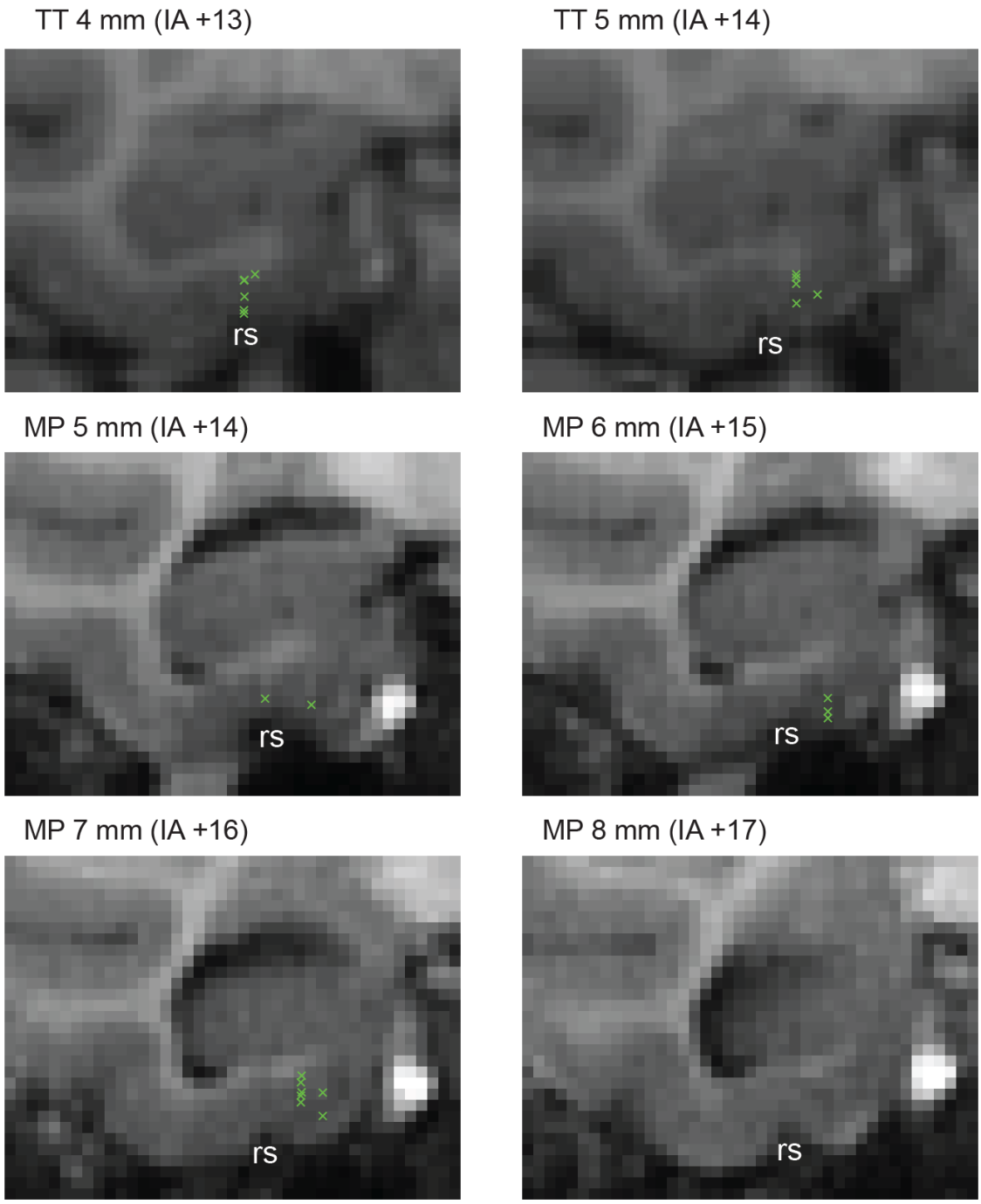

Figure 2.10 | Locations of entorhinal grid cells. Green markers label the locations of all 23 grid cells found in two monkeys (MP and TT). The monkey name, location anterior to the posterior border of the entorhinal cortex, and interaural location (Saleem and Logothetis, 2007) are given above each panel. rs: rhinal sulcus. 7 mm corresponded roughly to the midway point between the anterior and posterior borders of the EC. No grid cells were found anterior to this location.

Theta-band analyses

For each LFP recording, Morlet wavelets were used to calculate power over time for 30 $\log_2$-spaced frequencies from 2 to 16 Hz. For each frequency of interest, a chi-squared distribution with 2 degrees of freedom was fit to have a mean equal to the mean power and contiguous time points with power above the 95th percentile for at least 3 cycles were defined as bouts. Theta bouts were defined as any contiguous time points of bouts from 3-12 Hz (3.08-12.01 after $\log_2$-spacing) (Ekstrom et al., 2005). The percentage of time in a theta bout was higher during pre-stimulus fixation periods (0.57 ± 0.07%, mean ± SD) compared to image viewing (0.43 ± 0.09%, mean ± SD) ($p < 1x10^{-5}$, Wilcoxon rank-sum test), suggesting that bouts may have been modulated by saccades.

Theta modulation of individual neurons was quantified by the theta index of the power spectrum of the spike train autocorrelation (Yartsev et al., 2011; Langston et al., 2010). Individual blocks of images were truncated to 150 seconds. The autocorrelation was computed using a bin size of 2 ms and truncated to ± 0.5 seconds. The signal was zero-padded to 2^{16} samples and tapered with a Hann window before computing the FFT and the resulting power spectrum. The theta index was calculated as the ratio between the mean power from ± 1 Hz of the tallest local maximum (if any local maxima existed) between 3 and 12 Hz and the mean power from 0 to 125 Hz. If no local maxima existed, the theta index could not be calculated.

Theta phase-locking was examined by comparing spike times to the instantaneous phase of the theta-band LFP (the phase of the analytic signal taken after filtering from 3-12 Hz with a 4th-order Butterworth filter). For this analysis, the LFPs were recorded on an adjacent electrode 150 microns away (or 300 microns away if the nearest neighbor electrode was not in use). Sixty-degree bins (corresponding to 22 msec of a 7.5 Hz sinusoidal

oscillation) were used to compute the probability of spiking histograms (Yartsev et al., 2011; Mizuseki et al., 2009).

Saccade analyses

Saccades were detected by thresholding the eye movement speed at 25 degrees per second. To reduce detection of saccades due to noise in the recorded eye position, thresholding was performed after filtering the gaze location with a 30th-order low-pass (30 Hz cutoff) linear phase digital finite impulse response filter. For the analysis of saccade rate (Figure 2.7d), only image viewing trials at least 500 msec long with at least 2 detected saccades were included.

Table 2.1 | Rate map and autocorrelation parameters

	Image size	
Parameter	**small**	**large**
bin width (deg)	*0.25*	*0.5*
kernel dimensions (pixels)	*13x13*	*13x13*
Gaussian standard deviation (deg)	*0.75*	*1.5*
min. looking time (msec/deg^2)	*100*	*100*
min. overlap for autocorr. (pixels)	*10*	*50*

Acknowledgments

I thank S. Potter, C. Erickson, J. Manns, K. Dunne and M. Meister for comments on the work; K. Staikov, M. Tompkins, and D. Solyst for assistance with monkey care and training, and experimental preparation. I also thank the Potter lab and Buffalo lab members for useful discussions.

CHAPTER 3

EYE MOVEMENTS, IMAGE FEATURES, AND NEURAL RESPONSES[3]

The findings presented in Chapter 2 pose interesting questions regarding the mechanisms that underlie spatial representation in the EC as well as questions regarding the influences of spatial features of the images and eye movements themselves. In this chapter, I first explore the responses we might expect to observe based on theory. The influence of the presented images and the visual exploration patterns of those images will also be examined.

In Chapter 2, I demonstrated the existence of grid cells in the primate EC that have spatially periodic firing rate in response to locations of fixation during the viewing of complex images. An open question is whether entorhinal neurons might also represent the direction eye movement. In this chapter I describe the properties of a group of "saccade direction cells" in the EC. The responses of these neurons help to explain how information about eye position is used by the entorhinal cortex. The distributions of this new cell type and the cell types described in Chapter 2 are compared. Finally, I examine the relationship between firing rates and saccadic eye movements. The results of these analyses support that (1) the firing patterns observed for the various cell types described are independent of viewing patterns and stimulus features, (2) saccade direction is encoded by the EC, (3) spatial response types are largely independently encoded, but responses related to memory for images are exhibited by a large percentage of all spatially-responsive cell types, and (4) the timing of firing rate fluctuations of the different cell types are coordinated in relation to

[3] Portions of this chapter were adapted from: Killian, N.J., Potter, S.M., Buffalo, E.A. (2013). Encoding of saccade direction in the entorhinal cortex. Unpublished manuscript.

saccade times.

3.1 Theoretical rate map results based on eye trajectories and saliency

In this section I compare the firing rate analysis methods used in Chapter 2 to previously published methods to ensure that accurate comparisons can be made between my results and those that currently exist from studies of responses to egocentric position in the rodent EC. Additionally, the expected results based on these methods are examined with a simulated grid cell, by computing the gridness of viewing patterns, and by computing the spatial distribution of saliency in the sets of images.

The methods that I designed and used for analyzing spatial representation in Chapter 2 were based largely on rodent spatial representation studies (Hafting et al., 2005; Langston et al., 2010; Solstad et al., 2008; Sargolini et al., 2006). Some novel computations were introduced to speed analysis: faster histogram binning and smoothing and faster gridness score calculation by collapsing the gridness score annulus to a vector of single pixels after averaging with 3-degree wedges. To verify that the methods achieved the same results as in previously published studies, I evaluated the results of the methods I used to detect visual grid cells with rodent grid cell data. The methods do indeed produce results that agree with the previously published rodent results as demonstrated in Figure 3.1.

Next, I examined the theoretical results that would occur by observation of a 'perfect' grid cell, a cell whose firing rate follows a rate map that is a superposition of 2-D Gaussian probability distributions assigned to the nodes of a grid composed of equilateral triangles. Each Gaussian function represented an individual firing field. The viewing pattern with a resolution of 1 msec from one session was then used to pseudo-randomly generate spikes in MATLAB according to the probability at each viewing position (i.e. as a look-up table). The result is surprisingly less grid-like than might be expected and demonstrates that even in a

perfect situation, many samples are required to approach the theoretical distribution, Figure 3.2. However, a clear grid pattern can still be seen with only half a session of eye data (less than 5 minutes of total viewing in the 11x11 degree region). This implies that I collected enough data to find cells with grid-like firing distributions, but that I may have failed to detect cells with noisier or less stable firing distributions.

The viewing patterns themselves, were they in a grid-like pattern, could clearly produce erroneous detection of grid cells if neurons simply fired at a uniform rate. Thus I examined the gridness of the viewing patterns and found that they had gridness scores near 0 for the 23 grid cells described in Chapter 2 (Figure 3.3). Because firing rate tended to be higher earlier in image viewing (see Chapters 2 and 4), I examined the gridness associated with just the first fixations within images in addition to the gridness for all viewing trajectories combined. The gridness was near 0 in both cases. This indicates that the pattern of gaze locations did not independently produce grid-like rate maps.

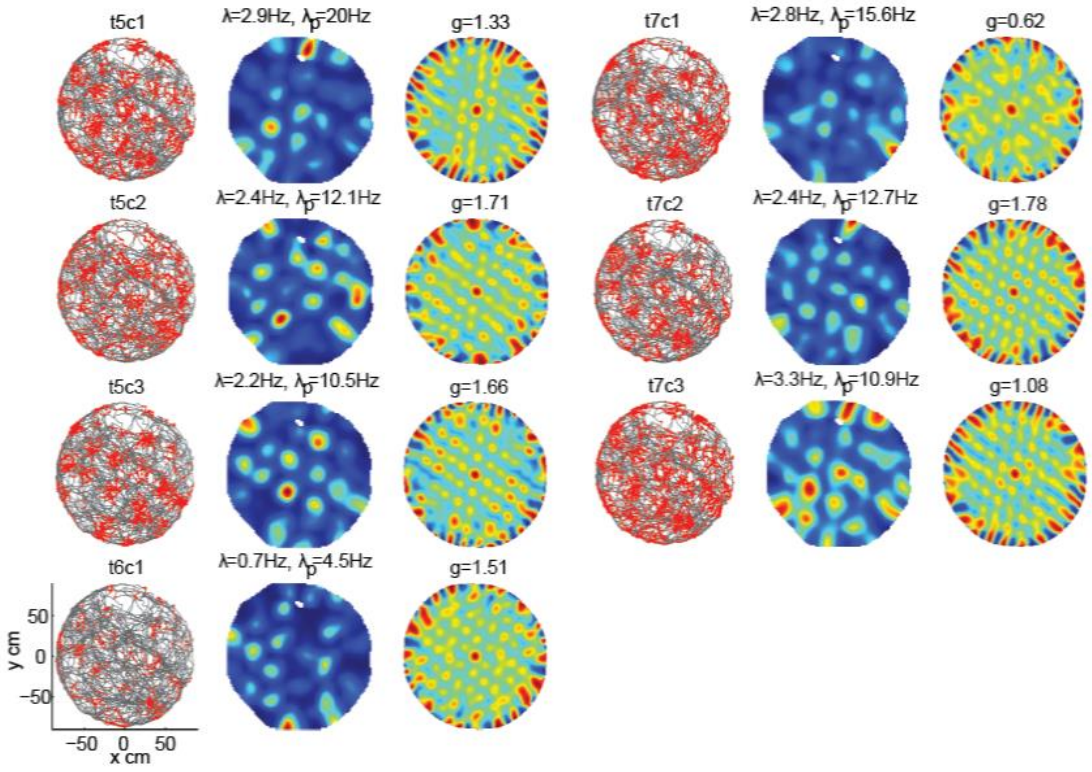

Figure 3.1 | Novel analysis procedures applied to data from Hafting et al., 2005. I applied my novel analysis procedure to data freely available online from Hafting et al., 2005 (http://www.ntnu.no/cbm/moser/gridcell). By comparison to figure 2c of Hafting et al., 2005, we see that my methods (shown here) produce results that are in agreement in terms of rate map and autocorrelation values. The rate map creation procedure produces edges that are somewhat less smooth because a rectangular filter is used to smooth both binned time and spikes, but the edges could be made smoother by requiring a more strict total occupancy time per bin requirement. The gridness analysis of the autocorrelations is novel compared to Hafting et al. where no gridness analysis was performed. This shows that most of these cells have very high gridness scores, except cell t7c1, which has a relatively low gridness score.

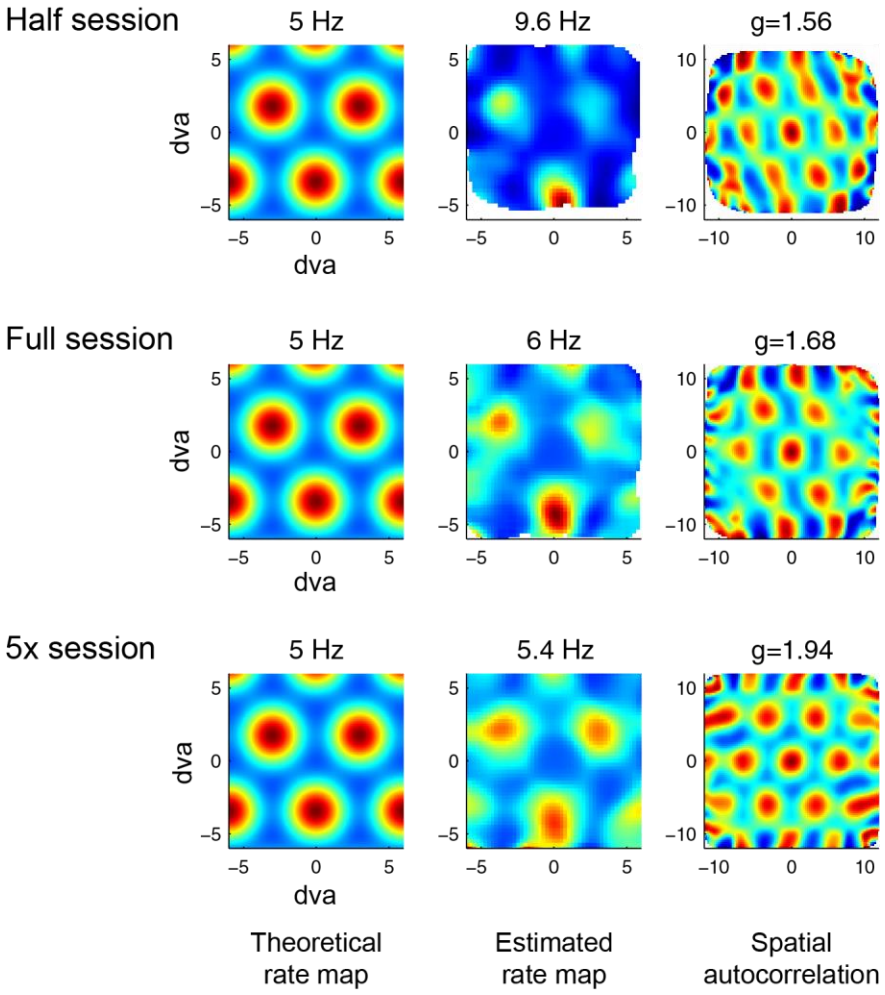

Figure 3.2 | Theoretical rate maps that would be obtained from a 'perfect' grid cell. The plots in the left column represent the idealized sum-of-Gaussians firing rate map of a 'perfect' grid cell. The middle column represents the rate maps obtained through pseudo-random number generation with actual eye data and using the position in the theoretical rate map as the instantaneous firing rate. The right column is the autocorrelation of these rate map instantiations. The peak firing rate of the map is given at the top of the rate maps and the gridness score of the autocorrelation is given at the top of the autocorrelation plots. The first row shows the procedure performed on eye position data from half of one session. The middle row gives results from using the full session and the bottom row is the result obtained after replicating the same session 5 times. As expected, it is clear that the estimation of the rate map improves as the sample size increases.

The features of the stimulus content may have played a role in generating the responses seen. In the simplest case, if a neuron prefers to fire when viewing objects that were consistently arranged in the same grid-like pattern across images, then a grid cell might be identified. However, to examine such a scenario it would be necessary to catalogue specific objects in entire stimulus sets, which is not trivial because the sets were randomly assembled from images posted on Flickr.com. A simpler analysis was made using saliency of image content. Here, saliency refers to overall spatial contrast at a pixel of an image, taking into account intensity, color, and orientation contrast on multiple spatial scales (Itti et al., 1998). If in general some neurons in the EC prefer salient image content, their firing may reflect a saliency map. To test this idea, a saliency map was calculated for each image presented (Itti et al., 1998). On average, no clear pattern of spatial periodicity in saliency was seen (Figure 3.4). The spatial maps were built up over an entire session with up to 200 novel images and were stable when taking separate halves of the session with distinct images (Figure 2.4). Thus the analysis of saliency suggests that saliency was not an important factor in forming the spatial representations of individual neurons. It's important to note that there was a bias toward more salient content near the image centers, which is likely a result of how photographs are typically framed with the salient subject matter near the center (Tseng et al., 2009).

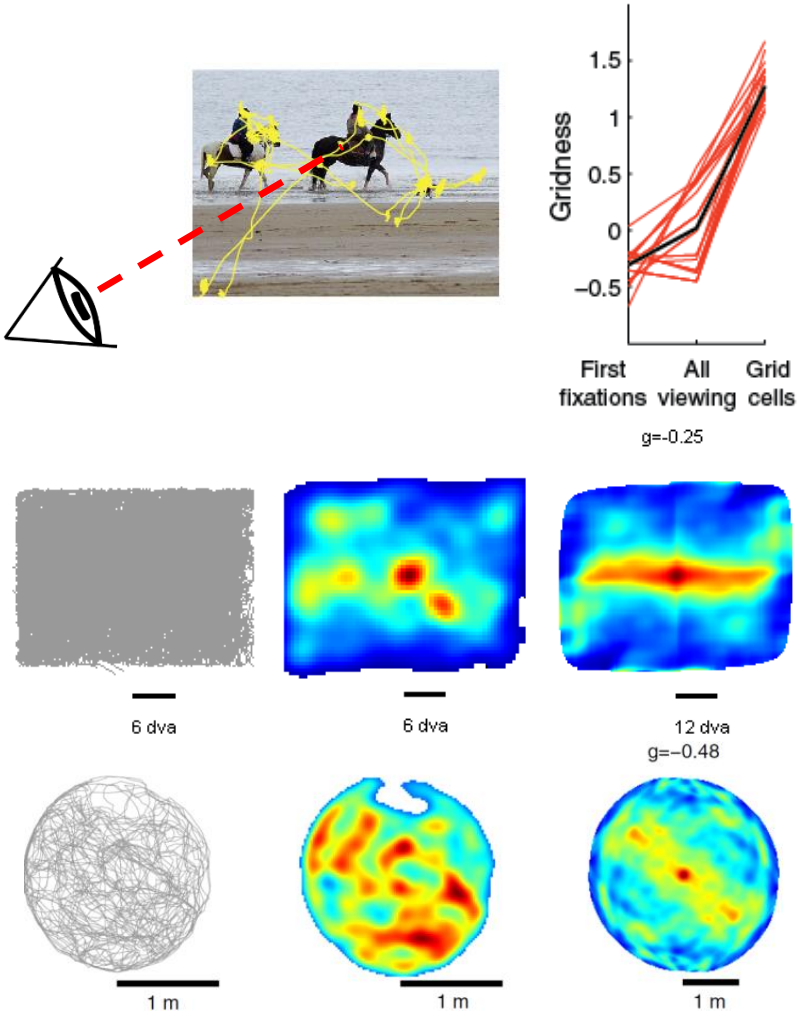

Figure 3.3 | Gridness of eye movements. Top row: The gridness of eye movements was near 0 for initial fixations within images and all viewing patterns collapsed across the session. The red lines represent values for each of the 23 grid cells and the associated eye data. The black line represents the average over all grid cells. The 'all viewing' case was used for calculation of grid cell rate maps. This was also described in Figure 2.3. **Middle row:** The lack of gridness can be seen in the 'rate map' and autocorrelation of the viewing trajectory for this example session. The plots follow the convention used in Chapter 2. **Bottom row:** the same plots for one session of rodent data (Hafting et al., 2005).

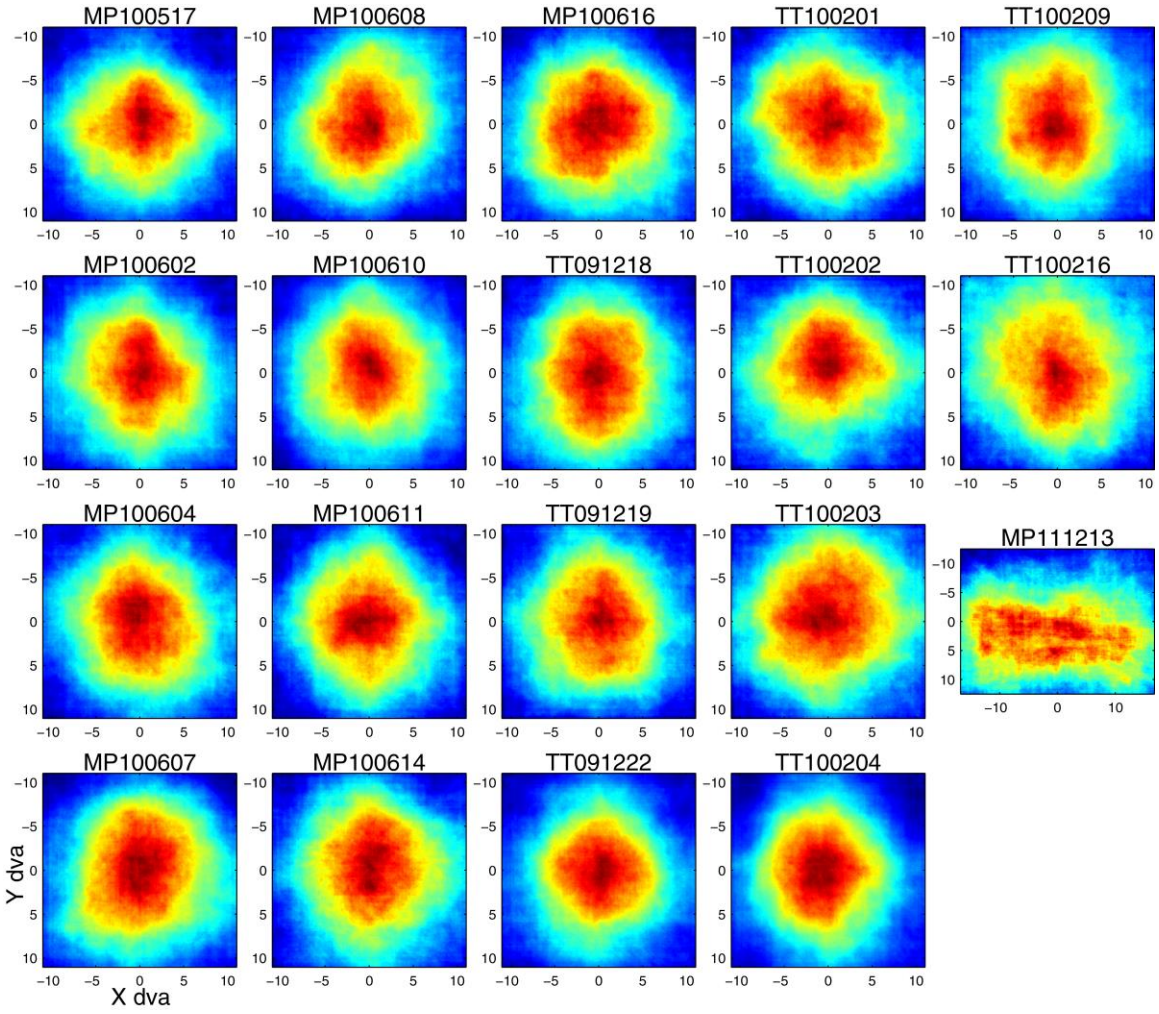

Figure 3.4 | Average saliency map for each session. The saliency map averaged over all images is plotted for each session (Itti et al., 1998). Units are in degrees of visual angle (dva). Saliency is on average higher near the center, likely because of the way that photographic subjects are typically framed (Tseng et al., 2009).[4] Note that the session MP111213 was performed with larger rectangular photographs that tended to have salient content placed closer to the bottom of the frame. Saliency is on average not spatially periodic.

[4] Support for saliency analysis was provided by Seth Koenig.

3.2 Relationship between saccade direction and spiking

While no features of the stimuli or eye movements that went into the rate map calculations clearly influenced the resulting maps, I hypothesized that individual saccadic eye movements would be represented in a simple way in the EC in order to facilitate mapping of visual space. Support for this idea comes from the findings of head-direction cell projections to the EC, head-direction cells within the rodent EC itself, and head-direction modulated grid cells (Sargolini et al., 2006). Head-direction cells have been defined as cells with a firing rate vs. movement direction distribution that has a single mode –a preference for a particular heading when the rodent is moving within the environment (Taube et al., 1990). Such cells may also be conjunctive with other cell types such as grid cells, particularly those in layer III of the rodent EC (Sargolini et al., 2006). Considering the trajectory of the gaze location, the analogous feature in visual exploration may be saccade direction. To examine the relationship between spiking and individual saccades, I applied circular statistics to data near saccade events. Spike counts were taken from 100 msec periods before and after saccades during each image viewing period. Figure 3.5A shows example traces for eye location (x, y), velocity (v), and velocity threshold (dashed line) to illustrate the time periods that were taken for this analysis. Any saccades with flanking periods shorter or longer than 100 msec were removed from the analysis. To reduce bias in the analysis from any saccade bias of the monkey, spike counts in 6-degree bins were normalized by the number of saccades in the same bins, yielding firing rate as a function of binned saccade directions (Figure 3.5B). The Rayleigh test was performed on the binned firing rate data to test for non-uniformity in the firing rate – saccade direction relationship.

Out of 193 units in the posterior EC, there were 42 units that passed the Rayleigh test for non-uniformity ($p < 0.05$): 34 in the pre-saccade period, 5 in the post-saccade

period, and 3 in both pre- and post- periods. The pre-saccade period group represented a significant population of units (p < 1x10-15, $\chi 2(64.7,1)$) that for ease of discourse I will refer to as 'saccade direction cells'. Three saccade direction cells are depicted in Figure 3.6. The blue angular histogram is the pre-saccade firing rate histogram, and the gray angular histogram represents post-saccade firing rate.

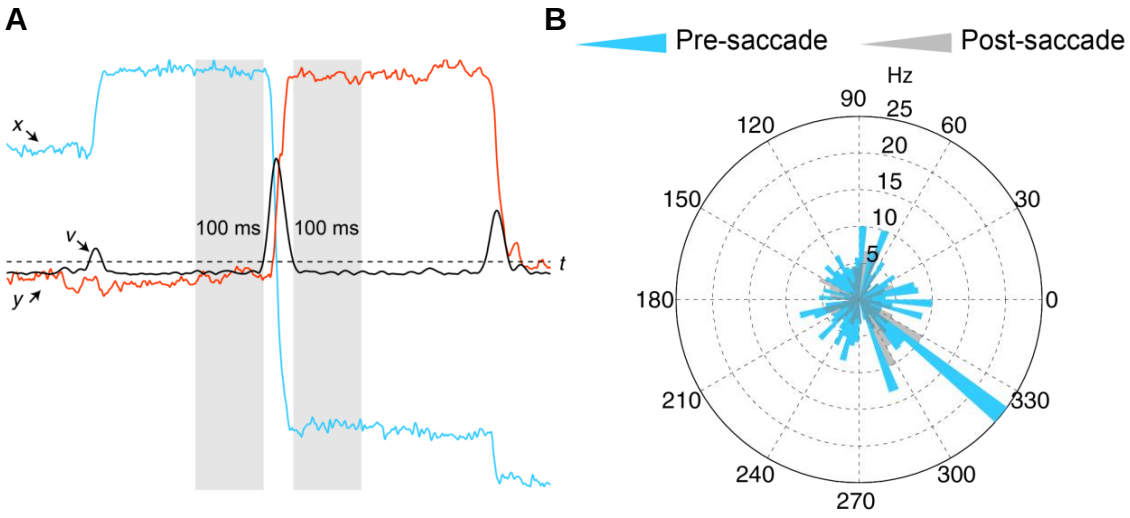

Figure 3.5 | Saccade-direction analysis. A. For each unit, the firing rate 100 ms before eye velocity crossed the saccade detection threshold (the dashed line) and the firing rate 100 ms after the eye velocity went below threshold were compared to the angle of saccade with respect to the center of the viewing region (approximately the neutral eye position). This comparison was made using all saccades in a session and only saccades with at least 100 msec of fixation before and after the saccade were used. **B.** Rose plot representing firing rate pre- (blue) and post- (gray) saccade for one cell with a significantly non-uniform firing rate distribution in the pre-saccade periods (Rayleigh test, p < 0.05; 6-degree bins).

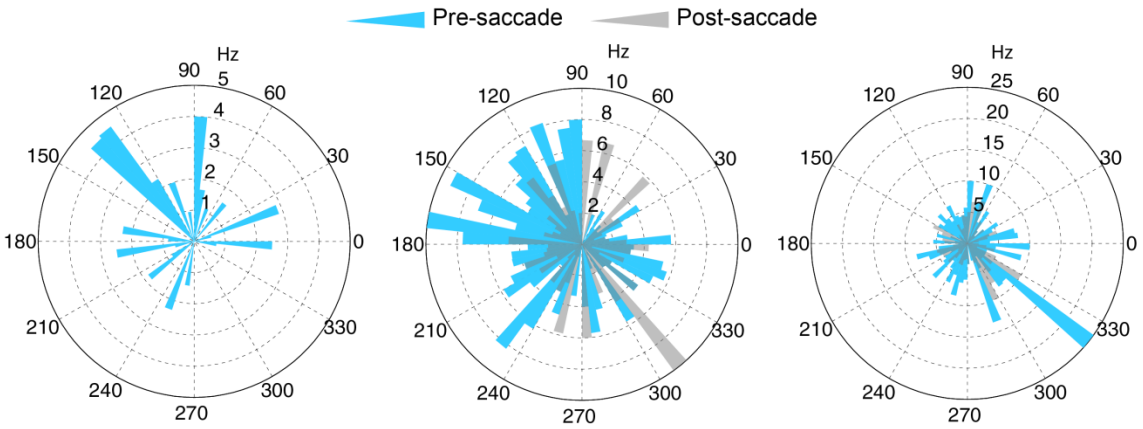

Figure 3.6 | Example saccade direction cells. Three representative saccade direction cells are shown, each with a different preferred saccade direction. Pre-saccade firing rates are represented in blue and post-saccade rates are in gray (6 degree bins). Note that no spikes occurred during post-saccade periods for the cell represented on the left.

To assess the strength of the relationship between spiking and saccade angle, I calculated the circular-linear correlation coefficient (Figure 3.7). This quantifies how sinusoidal the relationship between spiking and saccade angle was (i.e. a value of 1 is obtained for $r = \cos(\theta + \varphi)$, where r is the firing rate or spike count, θ is the saccade direction, and φ is an arbitrary phase shift) (Fisher, 1995). Unlike the Rayleigh test, it was possible to perform the correlation coefficient calculation on the raw, unbinned spike counts and saccade directions. Figure 3.7 shows the circular-linear correlation coefficient for the 42 units with a significant pre- and/or post-saccade Rayleigh statistic. Only 2 of the 42 units (blue lines) had higher correlations for the post-saccade compared to the pre-saccade period.

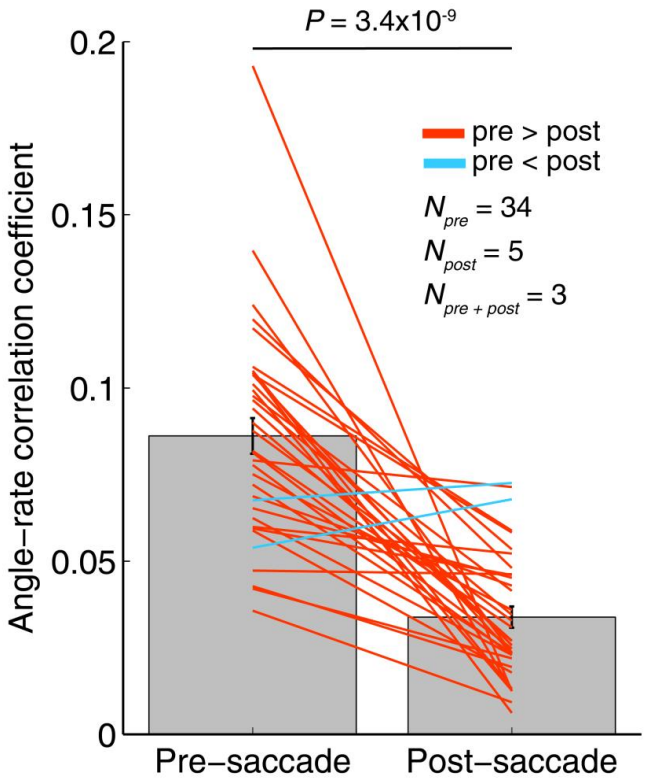

Figure 3.7 | Saccade angle – firing rate correlation coefficient. The circular-linear correlation coefficient was calculated between saccade angle and firing rate pre- and post- saccade for the 42 units that passed the Rayleigh test for non-uniformity. Out of 193 units, there were 34 units that passed the Rayleigh test in the pre-saccade period, 5 in the post-saccade period, and 3 in both periods. The correlation coefficients for these 36 units are plotted. The correlation coefficient is higher in the pre-saccade periods overall ($p = 3.4\text{x}10^{-9}$, Wilcoxon rank-sum test) and for 34 units individually (red lines). Two of the three units with significant pre- and post-saccade relationships had a higher correlation during the post-saccade period (blue lines). The gray bars represent the mean and the error bars represent the mean ± SEM for each condition.

3.3 Distribution of spatial responses

I examined 3 types of spatial responses in EC neurons using statistical measures for border cells and grid cells in Chapter 2 (see Chapter 2: Methods for descriptions of how the border scores and gridness scores were calculated) and saccade direction as described in this chapter. Overall, 34% of units were found to have only one of these 3 response types, while an additional 5% were either conjunctive grid- or border-saccade direction cells. The saccade direction cells, those cells that had a significant non-uniform relationship between firing and

the upcoming saccade direction (and not the previous saccade direction) made up 18% of the population of neurons recorded in the EC. Grid cells and border cells made up 12% and 9% of EC neurons respectively (Figure 3.8A). Interestingly, I saw little overlap in the spatial response types examined (Figure 3.8A), with 28% of border cells and 17% of grid cells having conjunctive saccade direction responses. However, I did see significant overlap in the spatial response types and those cells with memory responses (Figure 2.6, Figure 3.8B). 53% (18/34) of saccade-direction cells, 39% (9/23) of grid cells, and 39% of border cells (7/18) had significant memory responses. In total, I was able to classify more than half of the recorded units in the posterior EC (105 of 193) as belonging to at least one of these four main groups, which is well above the chance classification quantity of 20% (4 tests performed at a critical level of 0.05).

Using laminar analyses described in Chapter 4, I examined the layer specificity of the different response types. There were some laminar differences in terms of cell count proportions, but overall most cell types could be identified in all layers. Table 3.1 presents a breakdown of classified cell types by EC layer. See Chapter 4 for details on how layers were classified.

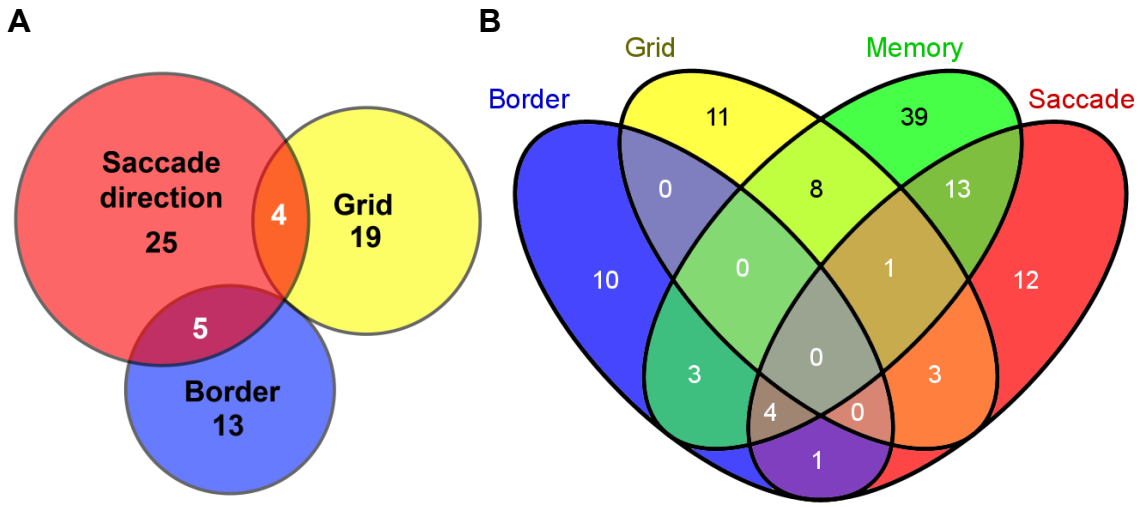

Figure 3.8 | Counts of different cell types identified in the posterior EC. A. 66 of 193 cells (34%) recorded in the posterior EC from two monkeys had at least one spatial response type; these are represented in the Venn diagram. Saccade direction cells that had a significant relationship with the direction of upcoming saccade made up 18% of the neurons. Border cells, cells with a significant preference for firing near borders of images, made up 9% of the neurons. Grid cells, cells that tiled visual space with a hexagonal grid pattern made up 12% of the neurons. 28% of border cells and 17% of grid cells had conjunctive saccade direction responses. **B.** Venn diagram representation that includes cells with significant memory responses. Notably, 44% of spatially-responsive cells (53% saccade, 39% grid, and 39% border) also had a significant memory response. In total, 54% (105/193) of cells recorded in the posterior EC are represented here.

Table 3.1 | Distribution of cell types by EC layer

Layer	Saccade direction (*N* = 34)	Grid (*N* = 23)	Border (*N* = 18)	Memory (*N* = 68)
II	14/75 = 18.7%	10/75 = 13.3%	3/75 = 4%	27/75 = 36%
III	15/88 = 17%	8/88 = 9.1%	12/88 = 13.6%	34/88 = 38.6%
V/VI	5/30 = 16.7%	5/30 = 16.7%	3/30 = 10%	7/30 = 23%

3.4 Timing of firing rate changes with respect to saccades

The percentage of spikes in fixation periods was very consistent across all recorded units, regardless of response type. For all entorhinal cells, 89.83 ± 0.02% (mean ± SEM) of spikes occurred during fixation periods, and similarly 89.84 ± 0.03% taking only spatially-responsive cells (grid cells, border cells, or saccade direction cells). So, for all EC units, only 10.17% of the spikes occurred during saccades (Figure 3.9). In fact there tended to be fewer spikes after saccades, particularly in the cells with memory responses. For the memory response cells (see definition in Chapter 2) this is because of the timing of repetition suppression; the suppression in firing rate typically occurs after the first saccade is made. This potential bias had little noticeable effect on the saccade direction cells; when randomly downsampling to obtain the same number of spikes before and after saccades, the same number of saccade direction cells was obtained.

The firing rates varied with respect to the timing of saccades (Figure 3.9). The spatially-responsive cell types all appear to have increased firing before or very early during the time periods that they are purported to be encoding: saccade-direction cells have a peak in firing rate 50 msec before saccades begin (albeit a relatively weak peak), border cells have peak firing at the beginning of fixation periods, and grid cells have their peak firing 30 msec after fixations begin. Memory response cells have generally decreased firing after saccades. This effect is partially influenced by the close alignment of the time of the first saccade and repetition suppression.

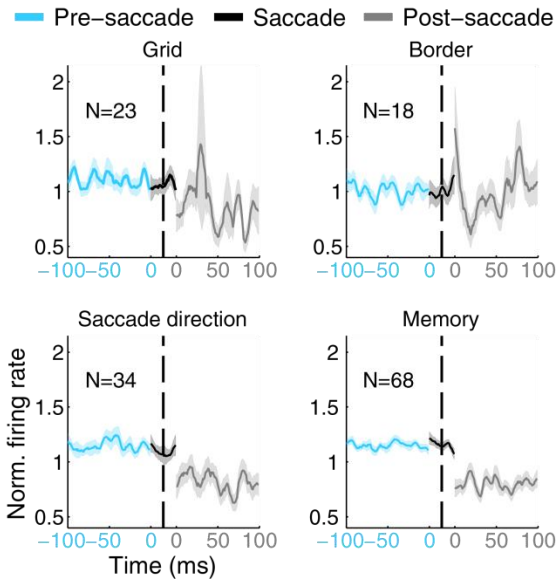

Figure 3.9 | Relationship of firing rate to saccade times. The rates with respect to saccade times for 100 msec pre- and post- saccade are plotted. 30 msec of the rates during saccades are also plotted and aligned to the peak of the saccade. The rates were normalized to the mean over this 230 msec sample for each cell. Axis limits are the same for all plots.

Discussion

In this chapter I first compared the findings described in Chapter 2 to theoretical results from the rate map calculation procedure. Next it was shown that eye movement patterns and salient image features could not have led to grid-like response patterns in any obvious fashion. While no pattern of saliency appeared to have influenced spiking of grid cells, it is possible that cells preferring to fire near image centers or borders were influenced by saliency, which tended to be higher near image centers. This could be examined in future experiments by carefully controlling for the distribution of salient image content so that there is no bias toward less salient content at image borders.

I next identified a new class of neuron in the EC, cells that respond to the direction of upcoming saccades. The presence of saccade direction cells in all layers of the EC may support the use of future saccade direction as a fundamental ingredient in the formation of

other spatial representation types, e.g. visual grid and border cells. The myriad recurrent connections within and between layers of the EC may support the building up of spatial representation types from such ingredients within the EC itself (Canto et al., 2008). As with the grid and border cells, it's not immediately clear how these representations might arise or be used in the primate EC. This is largely because our knowledge of the EC and surrounding regions is still relatively limited (Canto et al., 2008). However, one hypothesis is that saccade direction cells in primates perform analogous functions to head direction cells in rodents. The clearest parallel between head-direction and saccade-direction cell types is in terms of the trajectories that make up the rate maps themselves, where head direction and saccade direction take on identical meanings, with the eye trajectories being less smooth due to saccades. Head direction cells are found in layers III-VI of the rodent MEC and have increased firing rate when the rat is moving/looking in a particular direction. The field of view of rats is approximately 270° (derived from a 60° optic axis orientation with respect to the body axis and 150° angle subtended by the retina) (De Araujo et al., 2001). Despite this large field of view, head direction cells tend to have a firing distribution with a narrow width –the angular standard deviation is on average about 55° (Sargolini et al., 2006); there is incoming sensory input from nearly a full circle arc around the rat, but head-direction cells are sensitive to a limited range of visual information. This may be analogous to the roughly full circle view of the periphery during fixation with central foveal acuity of about 20-30° in primates (Rolls and Cowey, 1970). If you project this field of view onto a flat visual scene, then the ability of saccade-direction cells to be sensitive to movement toward a limited arc within that field of view becomes similar to the description of head-direction cells.

Rats likely cannot view a visual scene in the same way as primates because of the wide field of view, but is it requisite that they move through the environment to obtain novel

information? Eye-tracking experiments with rats have shown that they make spontaneous horizontal saccades showing similar quantitative properties (i.e. duration and velocity relationships) to saccades observed in primates (Chelazzi et al., 1989, 1990; Zoccolan et al., 2010). Further studies are needed to fully understand how rodents visually sample their environment as they move through it; knowing what regions of visual space are sampled by rodents during foraging behavior used for place cell and grid cell recordings may hold the key to understanding how the same brain circuits could produce maps of fundamentally different sets of sensory input.

Here I demonstrated that the response properties of neurons in the primate EC to visual space are not easily derived from stimulus features and eye trajectories alone. However, neurons that provide a directional signal could form the basis of more complex spatial representations. For example, access to fixation location information in advance of actually reaching the location could help prepare grid cells to fire in alignment with grid firing fields. I did find that grid cells and border cells have their peak firing after fixations begin, while saccade-direction cells have a peak firing rate soon before saccades begin. Memory response cells have generally decreased firing after saccades. Taken together, the timing of these firing rate levels seems to fit with our idea of what these different cell types may be doing: saccade direction cells fire soon before a saccade occurs and this could serve to prepare grid cells and border cells to fire soon after the gaze reaches a firing field (through synaptic connections that have yet to be described). In conjunction with neurons that encode information about specific items (Suzuki et al., 1997), these neuronal signals may then be temporally matched in a way could then provide a means to associate items with the places where they were seen. Such item-place associations could be encoded by individual neurons receiving coordinated synaptic input from semantic neurons (e.g. memory cells) and spatial neurons (e.g. grid cells)

or simply implicitly by the population of neurons possessing both types of responses.

The description that I have presented thus far supposes that the signals from saccade direction cells represent an efferent copy of eye movement plans. Interestingly, in contrast to the 39% grid and 39% border cells that had conjunctive memory responses, over half of the saccade direction cells (53%) also exhibited memory responses. This presents a potential mechanism by which saccade direction cells may actually be involved in controlling eye movements. Supposing a mechanism by which eye movements are planned by weighting the activity of saccade direction cells, inhibition of activity in cells corresponding to a particular direction would result in inhibition of saccades to that direction. Importantly, this scheme could also explain inhibition of return, the finding that saccades to recently fixated items are inhibited (Wang and Klein, 2010).

CHAPTER 4

LAMINAR ANALYSIS OF ENTORHINAL ACTIVITY[5]

The entorhinal cortex (EC) is positioned such that sensory information from the neocortex is processed by the superficial layers of the EC before reaching the hippocampus, a structure that plays an important role in memory processes (Eichenbaum et al., 2007). The hippocampus in turn processes this input and sends most of its output to the deep layers of the EC, which then return signals to the neocortex. This loop suggests that the superficial and deep layers may be performing unique roles in memory formation and recognition processes. Despite the unidirectionality of this description, there are significant connections within the EC itself that may also play an important part in memory functions (Iijima et al., 1996; Canto et al., 2008). In this chapter, I demonstrate, for the first time in awake, behaving primates, that there are laminar differences in EC neuronal activity related to memory formation and recognition. Furthermore, these data demonstrate that deep and superficial layers are functionally connected through both 'gamma' -band (30-140 Hz) field potential activity and the timing of spikes in multiple distinct ways in the context of a recognition memory task.

Introduction

Interest in the EC has increased recently due to the discovery of intriguing neuronal activity patterns in the EC related to spatial variables as described in Chapters 1-3 (Hafting et al., 2005; Killian et al., 2012; Yartsev et al., 2011; Solstad et al., 2008; Krupic et al., 2012;

[5] Adapted from: Killian, N.J., Buffalo, E.A. (2013). Functional circuitry for memory in the entorhinal cortex. Unpublished manuscript.

Sargolini et al., 2006) and the association of the EC with many neurological diseases (Braak and Braak, 1992; Gomez-Isla et al., 1996; Du et al., 1995; Arnold et al., 1991). Much research in rodent models has focused on the spatial representation of neurons in the medial entorhinal cortex (MEC) (Moser et al., 2008). More recently, the representation of objects by neurons in the lateral entorhinal cortex (LEC) has been examined (Deshmukh and Knierim, 2011). The responses of primate EC neurons to the viewing of images have been studied in some detail, and like other temporal lobe cortices (perirhinal, parahippocampal, and area TE), there is a strong suppression in firing rate during repeated viewing of images (Suzuki et al., 1997; Xiang and Brown, 1998; Brozinsky et al., 2005; Killian et al., 2012). Repetition suppression is in general thought to be related to recognition memory. Lesion experiments have primarily attributed recognition of items to the adjacent perirhinal cortex (Zola-Morgan et al., 1989; Buffalo, 2000). Lesions of the entorhinal cortex in monkeys, which removed most of the connections between the hippocampus and the perirhinal cortex, produced temporary impairments on a delayed nonmatching-to-sample (DNMS) task (Leonard et al., 1995). This finding demonstrated that the EC is important for recognition memory. Others have found that lesions of the EC in monkeys failed to elicit impaired performance on a DNMS task and instead produced profound impairments in visuospatial relational learning and memory (Buckmaster et al., 2004). Another lesion study revealed that spatial memory in rodents depends in part on the dorsolateral EC (Steffenach et al., 2005). The role of the EC in recognition memory performance may be subtle or simply undetected because of redundancy in other MTL areas or through compensatory mechanisms after lesioning (Leonard et al., 1995; Meunier et al., 1993; Eichenbaum et al., 2007). Despite the somewhat ambiguous results from lesion experiments, the activity of EC neurons is indeed related to visual exploration of complex images in an experimental design that is sensitive to

recognition memory, as described in Chapters 2 and 3 (Killian et al., 2012). Taken together, the results of these experiments suggest that a major role of the EC in learning and memory is to assist in placing items in visuospatial contexts.

Because of its anatomical connectivity, the EC is well-positioned to play a critical role in hippocampal-cortical interaction. Superficial layers (I-III) of the EC receive processed multisensory information from multimodal association cortices and provide the main cortical input to the hippocampus, with layer II projecting to the dentate gyrus (DG) and CA3 and layer III projecting to CA1. These connections are made primarily via a pathway through the subiculum known as the 'perforant path'. The dentate gyrus projects to CA3, which in turn sends Schaffer collateral axons to CA1, these three synapses, starting with layer II, form what is known as the 'trisynaptic circuit'. The layer II – DG connections as well as the CA3-CA1 connections are particularly well-known for, respectively, being the original and conventional locations for studies of long-term potentiation and long-term depression, phenomena which may be important biophysical correlates of memory (Bliss and Lomo, 1973; Malenka and Bear, 2004). The deep layers of the EC (V/VI) receive signals from CA1 and the subiculum and provide feedback to other cortical areas (Witter et al., 2000). Owing to this arrangement, it is reasonable to suppose that the EC may show layer-specific differences in activity related to memory formation and recognition.

The most prominent connections between the EC and hippocampus are from superficial layers of the EC to the hippocampus and from the hippocampus back to the deep layers of the EC. Despite the unidirectionality of this conventional description, there are significant synaptic connections within the EC that may play important roles in memory functions (Iijima et al., 1996; Canto et al., 2008). These connections may be useful in gating information to the hippocampus by comparing information from current and past

experiences, but they also have the potential to create new associations between sensory inputs and stored memories. Here I show that there are laminar differences in EC activity related to memory encoding and recognition functions and furthermore, to the strength of memory encoding. In addition to differences observed within individual laminae, I found patterns of connectivity between superficial ('input') and deep ('output') layers that suggest communication between layers occurs through the use of specific frequency bands related to different functions. The results demonstrate that synchronization and communication within the EC may be useful for recognition memory.

Accumulating evidence suggests that oscillatory neuronal activity plays an important role in memory formation. In particular, synchronization of gamma-band activity (ranging from 30 to 140 Hz) in the medial temporal lobe during visual stimulus (images or written words) encoding has been associated with recognition memory performance (Jutras et al., 2009; Fell et al., 2001). Here, I examined neuronal activity in the EC of rhesus macaques during the encoding and recognition of visual stimuli. I recorded both neuronal action potentials ('spikes') and local field potentials (LFPs) from the EC with a 12-contact electrode array in monkeys performing the Visual Preferential Looking Task (VPLT) (See Chapter 2: Methods) (Wilson and Goldman-Rakic, 1994; Jutras and Buffalo, 2010) (Figure 4.1A). Performance on the VPLT is presumed to be dependent on recognition memory because of findings from the use of a task called visual paired comparison (VPC). Performance on the VPC task is correlated with recognition memory and is sensitive to the integrity of the hippocampus and adjacent cortical regions (Manns et al., 2000; Zola et al., 2000; Buffalo, 1999). In the present work, complex visual stimuli were presented twice and the strength of memory formation for a given image was quantified by the preference for viewing the image when it was novel. Stronger memories were associated with looking away relatively sooner

when the image was repeated. Thus the strength of memory was calculated by taking the relative preference for viewing an image when it was novel yielding a value between 0 (weakest) and 1 (strongest):

$$strength = t_{novel}/(t_{novel} + t_{repeat})$$

The monkeys explored the static images with a dynamic sequence of fixations. Their eyes moved around an image, extracting information about features of interest to them. By using a measure of memory based on relative looking times one can control for the overall interest in each image. Monkeys have been shown to be more interested in specific images and image categories (Humphrey, 1972; Wilson and Goldman-Rakic, 1994). In Wilson and Goldman-Rakic 1994, rhesus monkeys generally preferred to view faces over complex pictures and both faces and pictures over monochromatic color fields. However, the novelty preference (strength of memory) for faces, pictures, and color fields appeared to lie along roughly the same curve dependent on the novel and repeat looking times (independent analysis of the data presented in Table 1 of Wilson and Goldman-Rakic 1994). Thus an image of another monkey may be particularly interesting and elicit prolonged viewing, but the relative preference for the image when it was novel is expected to correlate with declarative memory for the image as in Manns et al., 2000, independently of the image content.

Results

I classified layers of the EC by alignment to current-source density (CSD) template profiles corresponding to known locations within the EC. The locations of these template profiles were determined through electrical microlesions followed by histological analysis (see Methods; Figure 4.1, Figure 4.6-Figure 4.9). A prominent phase-reversal in the LFP that was particularly apparent at low-frequencies (1-20 Hz, Figure 4.9) was seen near layer II (Figure

4.6-Figure 4.9). I aligned to the onset of visual saccades to observe this phase reversal and it appears to be very similar to the phase reversal seen across layer II in the rodent EC, where it is one of the primary identifying laminar features (Alonso and García-Austt, 1987; Chrobak and Buzsáki, 1998a). In my data, and in rodents, the deep layer LFPs are roughly in phase with layer III, making separation of layer V and layer III based on the CSD difficult. Thus I used the CSD to find the layer II phase reversal for each session and then, based on the layer widths at my recording locations, I assigned the 5 channels (spanning 600 μm) deeper to the layer II phase reversal to layer III. All channels deeper to the designated layer III channels were assigned to layers V/VI.

I recorded the activity of a total of 222 single neurons from the EC of monkeys performing the VPLT. Many neurons in the EC were visually responsive (155/222 = 70%), firing spikes at an increased (124/155 = 80%) or decreased (31/155 = 20%) rate, relative to pre-stimulus baseline firing, as images were viewed (see Chapter 2). Over all neurons recorded, there was a distinct suppression in firing for repeat image viewings compared to novel viewings (a familiarity effect), a phenomenon seen in many regions of the temporal lobe (Figure 4.1D) (Pedreira et al., 2010; McMahon and Olson, 2007; Suzuki et al., 1997; Miller et al., 1993; Xiang and Brown, 1998). The latency to the onset of suppression for the population of EC units was 222 msec (the start time of the significant cluster found with a nonparametric permutation test), consistent with previous reports (Xiang and Brown, 1998; Suzuki et al., 1997). In the population, the suppression was transient, lasting for 238 msec, ending at 460 msec into viewing. With respect to baseline, the population firing rate increased by 51 ± 5% during novel image viewing and increased by 18 ± 4% during repeat image viewing (mean ± SEM). The corresponding suppression relative to the rate during novel image viewing was 11 ± 4%. This suppression appears to be primarily in the superficial

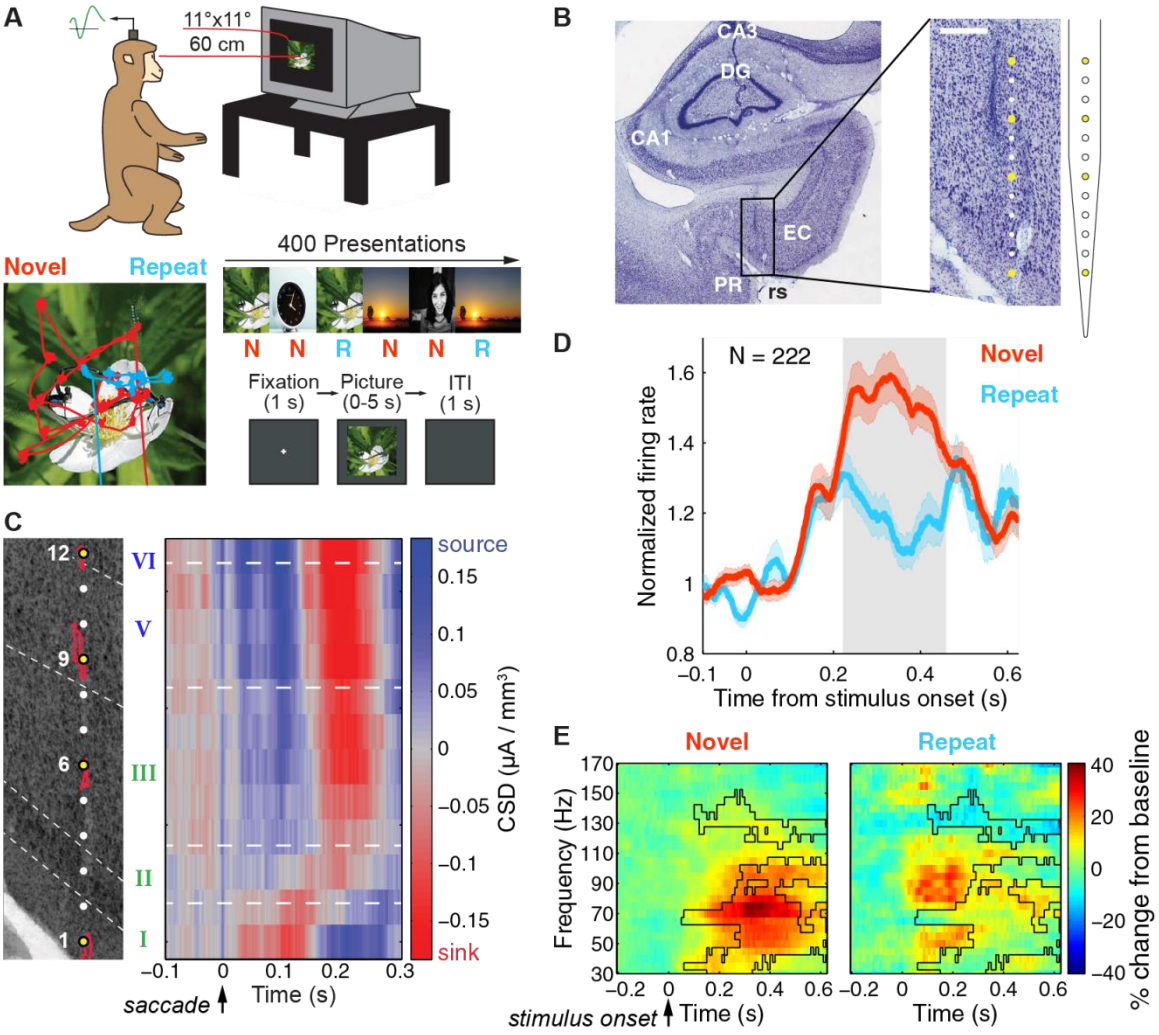

Figure 4.1 | Laminar recordings from the EC during free-viewing of photographs. A. Spikes and LFPs were recorded from the EC while Monkeys viewed 11x11 degree images on a computer monitor until looking away (up to 5 seconds per image). 200 images were presented twice during each session, when novel (N, red) and repeated (R, blue). **B.** Nissl-stained brain section showing the caudal EC and a region where DC current microlesions were made (indicated by yellow dots). **C.** At the end of experiments in one monkey, current was applied to electrode sites 1, 6, 9 and 12 to create microlesions. Lesion locations (red outlines) were determined by processing multiple Nissl- and MAP2-stained sections. The CSD averaged over the first 300 msec after saccade onset was then used to create a template CSD profile to estimate all recording locations. **D.** Taking neurons recorded from all layers and both monkeys together, a significant suppression of firing rate was seen from 222–460 msec after presentation of the repeated stimulus onset (N = 222; gray shading: $p < 0.025$, cluster-based permutation test). **E.** Gamma-band power (30-150 Hz) was increased during novel image viewing but not during repeated viewing (N = 210, black outlines represent significant differences between novel and repeat image viewings, $p < 0.025$, cluster-based permutation test).

layer neurons (87/185 = 47%), although a small suppression effect was also observed in deep layer neurons (10/37 = 27%), particularly around 400 msec into viewing at more anterior locations within the EC (Figure 2.7, Table 3.1, Figure 4.5).

Oscillations in the LFPs at gamma-band frequencies exhibited dynamics that, like the firing rate changes, differentiated novel and repeat image presentations at approximately the same times during image viewing. Previous studies have found that synchronization in hippocampal and entorhinal LFPs at frequencies above 30 Hz occurs in 3 frequency bands, which are often reported as approximately 30-60 Hz for 'low-gamma', 60-140 Hz for 'high-gamma', and 140+ Hz for ripple oscillations (Colgin et al., 2009; Buzsáki and Wang, 2012; Chrobak et al., 2000). Considering all LFPs recorded from the EC of two monkeys, gamma-band power (30-150 Hz) was increased relative to baseline (425 msec preceding the stimulus onset) during both image presentations at approximately 200-600 msec after stimulus onset (Figure 4.1E). Additionally, gamma-band power was greater during viewing of novel images compared to repeat images. In Figure 4.1E, the regions of significant differences in power between novel and repeat viewings were determined with a cluster-based nonparametric permutation test and are outlined in black ($p < 0.025$ for each of the two clusters).

I next examined gamma-band synchronization with respect to different layers of the EC (Figure 4.2). Strikingly, as shown in Figure 4.2A, deep layers did not display significant modulation of gamma-band synchronization by novelty; the suppression in gamma-band synchronization during repeat image viewing was restricted to superficial layers. See Table 4.1 for the mean ± SEM of the gamma-band power of the data presented in Figure 4.2, averaged over 30-170 Hz and 0.005 to 0.625 msec.

To examine whether gamma-band synchronization during novel image viewing reflected the strength of subsequent memory, I tested the difference in power during novel

Table 4.1 | Mean ± SEM gamma-band power (% change from baseline)

Layer	Novel	Repeat	Repeat - Novel
I/II	11.64 ± 3.20	3.44 ± 1.94	-8.2 ± 3.59
III	8.33 ± 2.45	5.42 ± 2.06	-2.9 ± 2.42
V/VI	-1.93 ± 2.79	0.23 ± 2.23	2.16 ± 2.64

Layer	Strong	Weak	Weak - Strong
I/II	4.98 ± 1.39	6.32 ± 2.34	1.34 ± 1.52
III	4.45 ± 1.89	9.86 ± 2.54	5.41 ± 1.39
V/VI	-5.59 ± 1.62	2.66 ± 1.76	8.25 ± 1.41

viewings associated with the 30 strongest and 30 weakest recognition memory performance trials (Figure 4.2B). As expected, unlike the clear difference seen from about 200-600 msec in the novel vs. repeat viewing time-frequency patterns in the superficial layers, both strong and weak encoding trials generally resembled the time-frequency profile during novel viewing in all layers. Interestingly, the strong encoding trials were associated with significantly lower gamma-band power in layer III and the deep layers. However, layers I/II, which were strongly modulated by novel vs. repeat viewing, did not exhibit a modulation in gamma-band power associated with the strength of encoding. See Table 4.1 for average percent change from baseline for different layers. The range of frequencies over which the strength of encoding effect was observed was very broad (about 40-170 Hz) and no clear band-limiting into distinct gamma frequencies (i.e. low or high gamma) was observed. Interestingly, the deep layer LFPs, which were not strongly modulated by novelty, showed a strong modulation by encoding strength (on average 8.25% greater percent change from baseline during weak encoding; see Table 4.1 and black outlines in Figure 4.2B). This effect was more prolonged in deep layers compared to layer III, being present over the entire time range examined (5-625 msec) at 120 Hz. Notably, power at these high frequencies (105-170 Hz) was on average decreased during nearly the entire length of the strong encoding trials.

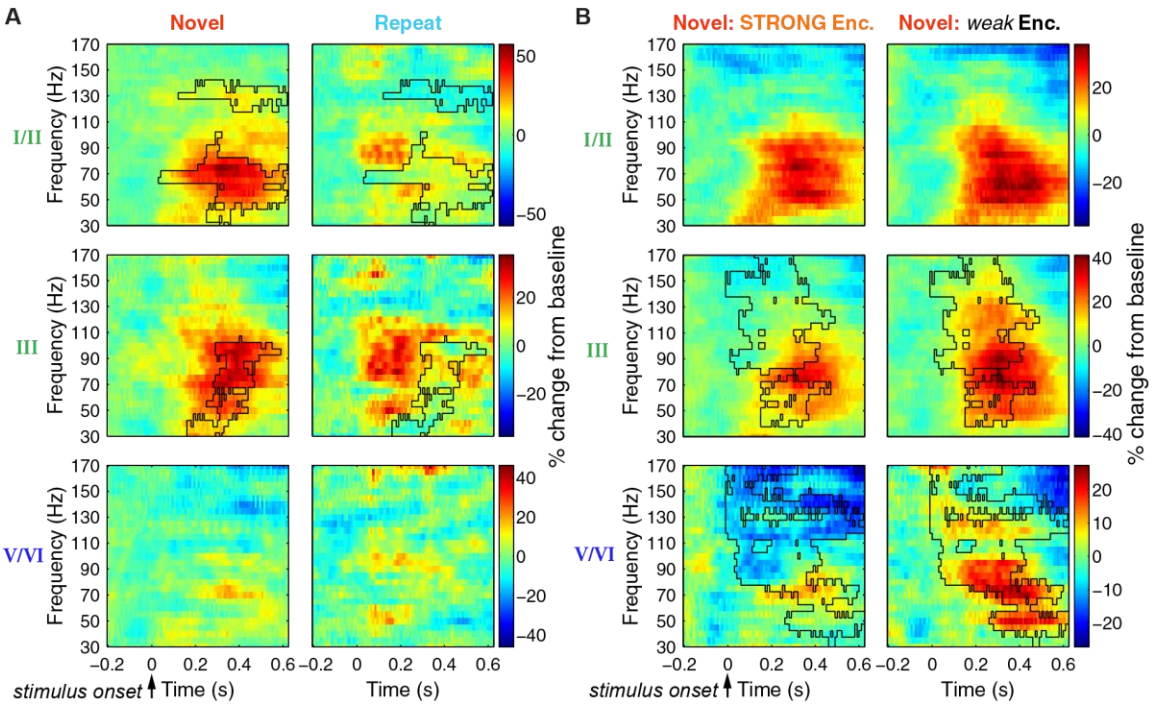

Figure 4.2 | Laminar differences in LFP power during image viewing. A. LFP power at frequencies from 30 to 170 Hz (5 Hz steps) was estimated with 3 Slepian tapers in 250 msec windows stepped at 10 msec and was averaged across trials for each LFP. The power was then normalized to baseline (-425 to -5 ms) for each LFP at each frequency. The novel and repeat viewing conditions were compared with a cluster-based permutation test (Maris and Oostenveld, 2007). Time-frequency regions with significantly greater power for the novel viewing period are outlined in black ($p < 0.025$ for each cluster). Both layer I/II ($N = 88$) and layer III ($N = 80$) showed an increase in power from 30-140 Hz and 100-600 msec during novel viewing and during the first 300 msec of repeat viewings. Deep layers ($N = 42$) showed relatively little modulation by stimulus novelty. Superficial layers (I/II and III) showed a significant decrease in gamma-band power at about 200-500 msec during viewing of repeated stimuli. **B.** Gamma-band power during the novel image viewings separated by strength of subsequent image recognition: top 30 strong trials vs. bottom 30 weak trials. Weak memory formation was associated with a significant increase in gamma-band power in layer III and layers V/VI. Additionally, deep layers showed a significant decrease in power at 90+ Hz relative to baseline during strong encoding. (I/II, $N = 64$; III, $N = 56$; V/VI, $N = 35$; $p < 0.025$ for each cluster).

The LFP power values displayed in Figure 4.2 were averaged from 30-170 Hz and conditions were compared across time in order to better visualize the differences between conditions (Figure 4.3). As shown in Figure 4.3, the layers and conditions with significant differences are the same as in Figure 4.2: superficial layers are modulated by novelty and gamma-band synchronization in layer III and layers V/VI is modulated by the strength of encoding.

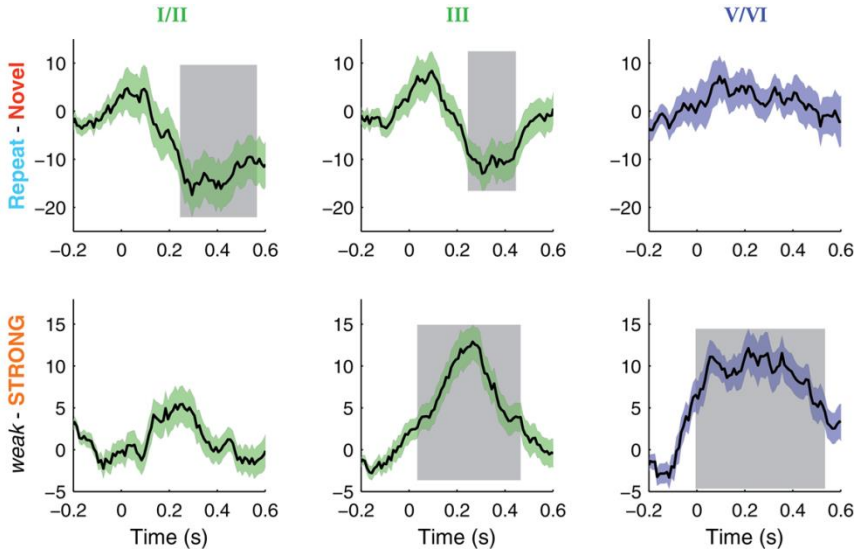

Figure 4.3 | Gamma-band LFP power separated by conditions and layers. The top row shows the difference in gamma-band power between repeat and novel presentations for layers I/II, III, and V/VI, averaged over 30-170 Hz. The bottom row shows the difference in gamma-band power between weak and strong encoding conditions, averaged over 30-170 Hz. The curves represent the mean ± SEM and the gray bars represent regions of a significant differences between the two conditions (same test procedure as in Figure 4.1D).

Previous work has shown that distinct gamma bands operate independently in the hippocampal formation and act to couple neuron populations in different regions. As described in Colgin et al., 2009, 'low-gamma' (30-60 Hz) oscillations are coherent between CA3 and CA1 regions of the rodent hippocampus, and 'high-gamma' (60-140 Hz) oscillations are coherent between EC layer III and CA1 (Colgin et al., 2009). Colgin et al. did not examine memory, but posed the intriguing hypothesis that the two gamma frequency ranges might be associated with distinct functions, i.e. that the accessing of stored memories might occur through the low-gamma coupling and that high-gamma may be used for encoding of information. The LFP power analyses presented here associated individual laminae of the EC with different memory functions, but did not relate individual gamma bands to particular functions. Such effects would be lost through averaging if multiple synchronization bands are present in the EC simultaneously or with short time delays.

Presuming that different gamma bands are used as 'carrier' frequencies for communication between different anatomical regions for distinct functions, an analysis of connectivity may reveal the directionality and functional relevance of different gamma bands, even when averaging over time. To investigate interlaminar connectivity in the EC, I applied Granger causality (GC) analysis to the LFPs (Figure 4.4; see Methods for derivations and parameters) (Gregoriou et al., 2009; Granger, 1969).

As used here, GC describes the amount of power transferred from one signal to another at a given frequency; GC is a measure of the predictability of one recorded LFP signal by a second simultaneously recorded LFP signal. Like many other directed connectivity measures, GC does not infer true causality as there may be any number of factors acting as intermediate nodes or controlling two disconnected signals with a time delay. I examined the transfer of power between layers of the EC, specifically between superficial layers (I-III) and deep layers (V/VI). GC was higher for deep to superficial layers across all frequencies examined, 1-170 Hz (Figure 4.4A). This is consistent with the relatively large number of deep to superficial connections compared to superficial to deep connections observed in anatomical studies (Van Haeften et al., 2003; Canto et al., 2008)

I examined GC between layers relative to this background level of connectivity by dividing by the GC values in the prestimulus baseline period (-425 to -5 msec). After this normalization, during image viewing (5 to 625 ms) there was an increase in high-gamma GC (61-86 Hz) going from superficial to deep layers (Figure 4.4B). Deep layers exhibit greater 1-40 Hz GC and greater 140+ Hz power transfer to superficial layers during image viewing.

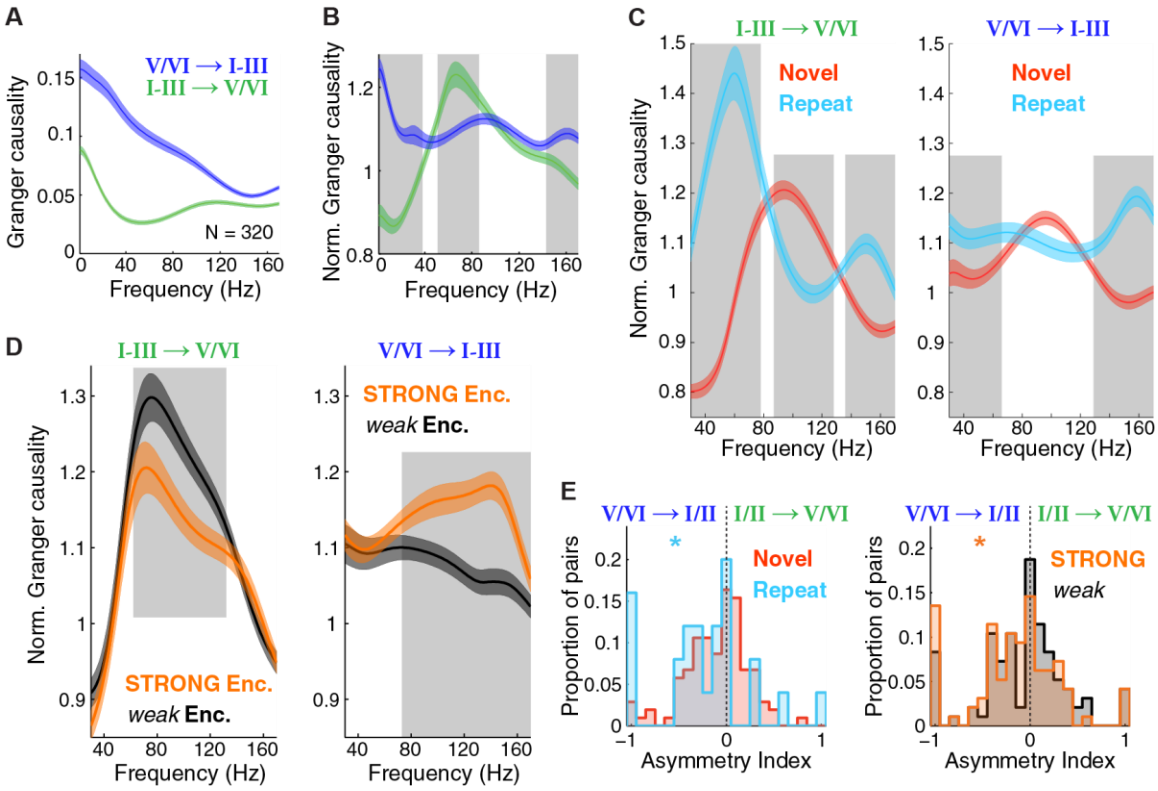

Figure 4.4 | Inter-laminar connectivity associated with strength of memory formation. A. There was significantly greater raw, unnormalized Granger causality from deep to superficial layers (purple) at 1-170 Hz compared to the superficial to deep direction (green). Curves represent the mean ± SEM. **B.** When normalizing to baseline, during image viewings there was increased gamma-band power transfer from superficial to deep layers (61-86 Hz) and increased low frequency (1-38 Hz) and high frequency (143-170 Hz) power transfer from deep to superficial layers. The color convention is the same as in 'A'. Gray shading represents a significant difference between the two directions (1 Hz resolution; cluster-based permutation test, $p < 0.025$). **C.** Three distinct gamma bands were seen when separating by viewing condition. Novel image viewing was associated with greater power transfer from superficial to deep layers at 90-130 Hz, whereas repeat image viewing was associated with a strong increase in power transfer at 30-80 Hz (low gamma). A relative increase in low gamma and 130+ Hz power transfer from deep to superficial layers was seen during repeat image viewings compared to novel viewings. **D.** Stronger memories were formed when there was relatively less power transfer in the gamma range from superficial to deep layers (orange vs. black curves on the left). Stronger memories were formed when there was relatively more power transfer in the gamma range from deep to superficial layers (orange vs. black curves on the right). **E.** The asymmetry index revealed a significant deep (V/VI) to superficial (I/II) directional bias in the spike train CCGs. This bias was seen in both repeat viewing (left histograms) and strong encoding conditions (right histograms). The * denotes $p < 0.05$, sign test.

These results demonstrate that there is indeed directed connectivity between the hippocampal formation input and output layers that is distinguished by different frequency bands for different directions of connectivity.

For the gamma-band (30-140 Hz), GC separated by novel and repeat image presentations further differentiated gamma-band LFP power into sub-bands (Figure 4.4C). Increased GC at 70-130 Hz (high-gamma band) between both layer groups was found during novel image viewings. GC at 30-70 Hz (low-gamma band) directed from superficial to deep layers was observed in repeat image viewings. Additionally, high-frequency power (140+ Hz) was directed between both layer groups during repeat image viewings. Interestingly, the low- and high- gamma bands were associated with, respectively, repeat viewings (image recognition) and novel viewings (image encoding). Thus the data are consistent with the hypothesis put forth in Colgin et al., 2009. Furthermore, both low- and high-gamma directed influences are relatively larger on the sensory side, meaning from superficial layers (to the hippocampus) to deep layers, whereas the most prominent power transfer on the putative 'recall' or 'reconstruction' route from deep to superficial layers (Chrobak et al., 2000) is at frequencies above 140 Hz. These high frequencies typically do not occur as part of a continuous rhythm in the MTL, but are instead often associated with ripple oscillations that occur in brief bursts. Ripples are thought to be key ingredients in memory trace replay and consolidation (Skaggs et al., 2007; Girardeau et al., 2009; Davidson et al., 2009). Furthermore, deep layers are known to exhibit ripple-frequency (140-200 Hz) activity during sharp waves (a type of large, slow LFP fluctuations) that occur concurrently in the hippocampus (Chrobak and Buzsáki, 1994, 1996). Previous studies found little activation of layer II neurons during sharp waves, but some activation of layer III neurons (Chrobak and Buzsáki, 1994, 1996). Consistent with this finding, the 140-170 Hz

GC was primarily directed from deep layers to layer III and not to layer II. It is important to note that I was not able to consistently detect unequivocal sharp-wave ripple complexes using standard methods (Skaggs et al., 2007). This is likely the result of using an analog low-pass filter with a cutoff of 170 Hz before digitization at 1 kHz, which limited the ability to distinguish clear ripple-frequency oscillations from the surrounding signal.

Taking the best and worst encoding trials (novel viewings) I found that, similar to the excessive high-gamma power associated with weak memory formation in Figure 4.2B, excessive high-gamma (70-130 Hz) power transfer from superficial to deep layers was associated with weaker memory formation (Figure 4.4D, left). This finding stands in contrast to the observed benefit of power transfer at high-gamma frequencies and above (75-170 Hz) from deep to superficial layers during encoding (Figure 4.4D, right). Even though excessive gamma-band synchronization within the deep layers can be detrimental, the greater the gamma-band influence that deep layers have on superficial layers during encoding, the better a stimulus may be remembered. The axons from deep to superficial layers are thought to be excitatory and are equally likely to form synapses with excitatory and inhibitory neurons (Van Haeften et al., 2003). It has been demonstrated that activation of deep to superficial connections often results in strong inhibition of superficial layer neurons (Bartesaghi et al., 1989; Finch et al., 1986, 1988; Jones, 1993; Jones and Heinemann, 1988). This inhibition has been proposed as a negative feedback mechanism that could provide an error signal for the hippocampus via projections from neurons in the superficial layers of the EC (Bartesaghi et al., 1989; Chrobak et al., 2000). The heightened gamma-band power transfer from deep to superficial layers during repeat stimulus viewing and strong encoding (Figure 4.4C,D) may ultimately result in the neuronal suppression effects observed in the superficial layers: repetition suppression of firing rate and gamma-band

power, and relatively decreased gamma-band power during strong encoding (Figure 4.1, Figure 4.2).

Because the LFPs are thought to primarily reflect summated local synaptic activity, I expected that the LFPs may influence spiking and that the connectivity described with GC should be similar when considering only spike times. To examine the directionality of interlaminar correlations in spiking activity, I calculated cross-correlations for spike train pairs recorded from the three layer groups: I/II, III, and V/VI. The cross-correlograms (CCGs) were z-scored and the asymmetry index (AI) was calculated within ±20 msec to quantify the directional bias in the CCGs (Figure 4.4E, see also Methods) (Takeuchi et al., 2011). I found no significant directional bias in the CCGs for neuron pairs between layers I/II and layer III or between layer III and layers V/VI. However, similar to the increase in deep to superficial GC for repeat viewings compared to novel viewings, there was a significant directional bias in the CCGs from layers V/VI to layers I/II during repeat image viewings ($p < 0.05$, sign test). This suggests that deep layer neurons may relay a recall signal to layer II neurons, which fits with current theories of hippocampal circuitry (Chrobak et al., 2000). Additionally, similar to the increased GC from layers V/VI to layers I-III in the LFPs during strong encoding trials, there was a significant directional bias in the CCGs from layers V/VI to layers I/II associated with strong encoding ($p < 0.05$, sign test). No other combinations of laminae and conditions had significant directional biases.

Discussion

The experiments described here represent the first laminar analysis of the primate EC through recordings in awake, behaving monkeys. Note that laminar analyses of EC activity from a human epilepsy patient during word-based tasks has been performed previously, but attributing specific activity patterns or functions to individual layers or combinations of

layers has not been attempted (Knake et al., 2007; Chan et al., 2011). The present results suggest that there are distinct patterns of laminar activity and connectivity within the entorhinal cortex that are associated with stimulus familiarity (novel vs. repeat images) as well as the strength of subsequent recognition during novel image viewings.

It has been hypothesized that the superficial layers of the entorhinal cortex act as a gateway for information to the hippocampus and that the gate is normally only partially open, forming a 'wall of inhibition' (De Curtis and Paré, 2004). This may allow for efficient and selective transfer of novel information from the neocortex to the hippocampus. My findings support this idea through the observations of suppressed firing and decreased synchronization during repeat image viewings. This hypothesis was further supported through the observation of two activity patterns associated with weak memory formation: (1) excessive gamma-band synchronization within layer III, and (2) excessive transfer of high-gamma signal power from superficial to deep layers. The first finding is consistent with a previous study of the human rhinal cortex demonstrating increased gamma-band power during stimulus encoding relative to baseline that, when excessive, was associated with weak memory formation (Fell et al., 2001). The present results extend this finding through examination of a wider frequency range, separation by laminae, separation by novel and repeat image viewings, and by examination of directed connectivity between EC layers.

Neuronal activity that is separable and repeatable is necessary to, respectively, form and recall memories of multiple distinct sensory experiences. Most visually-responsive neurons in the EC were excited in response to image presentation, which is in contrast to neurons in the hippocampus that were mostly inhibited by image presentation (Jutras and Buffalo, 2010). This difference might reflect encoding of more general aspects of stimuli by EC neurons such as location in space, whereas hippocampal neurons may represent specific

aspects of an experience or environment. In particular, the neurons in the DG and CA3 regions (where most of the neurons were recorded in Jutras et al., 2010) are thought to provide for the ability to encode separate experiences, termed 'pattern separation'; this necessitates (1) that different experiences have functionally distinct cell assemblies and (2) that neurons in some way fire selectively and separably for stimuli that are to be encoded. There are many ways for a neuron population to achieve these goals, but low firing rate and generally asynchronous activity may be a reflection of specificity in individual neurons. Despite the clear increase in firing rate and gamma-band synchronization in the EC during image viewing, it appears that a balance of synchronization and separability of activity in the EC are important components of memory formation and recognition; excessive synchronization may be detrimental to the encoding of specific aspects of stimuli.

Synchronization in distinct gamma bands as a mechanism to route different memory processes was first proposed by Colgin et al., 2009. The present GC connectivity analyses revealed distinct frequencies associated with novel image encoding and repeat image recognition, lending strong support for this hypothesis. Interlaminar communication in a high-gamma band (70-130 Hz) was found during novel stimulus encoding, and communication in a low-gamma band (30-70 Hz) was associated with repeat image recognition. During repeat image viewing I also found enhanced communication at frequencies typically associated with ripple oscillations. This high-frequency activity was particularly prominent from deep to superficial layers (Figure 4.4B and Figure 4.4C). Multiple gamma sub-bands have been found to occur in several different neuronal regions but the functional importance of specific gamma-band frequencies is still largely conjectural (Jackson et al., 2011; Colgin et al., 2009; Belluscio et al., 2012; Buzsáki and Wang, 2012; Kay, 2003). It is clear from these results that to improve our understanding of the neural

circuitry of memory we must continue to enhance the resolution and scale of our recording techniques. Future studies utilizing high channel-count simultaneous recordings from the EC, hippocampus, and associated structures will be important to more completely identify the functional circuitry of memory formation associated with these different synchronization patterns.

The raw GC results, as well as the spike train cross-correlations, demonstrate the importance of the directed influence of deep layer neurons on superficial layers. Only after normalization was the influence of superficial layers on deep layers apparent. Based on current anatomical evidence, it's not clear how the superficial to deep signals are being transmitted, but there are many possibilities. Superficial layer influences on deep layer neurons might occur through axon collaterals that synapse on deep layer neuron apical dendrites within the superficial layers themselves (Tahvildari and Alonso, 2005; Canto et al., 2008). This may induce spiking in deep layer neurons and subsequent recurrent activity within the deep layers that is recorded in the LFP. However, I did not find a significant directional bias in the CCGs from spike times in layer II toward spike times in layers V/VI, which might have been expected if direct synaptic connections were involved. A portion of the LFP signals in the deep layers may reflect activity from direct connections of layer III to CA1 pyramidal cells that then synapse on deep layer neurons. It is also possible that outside structures participate in orchestrating oscillations in the hippocampal formation such that oscillatory activity appears in different regions with a time delay. For example, theta oscillations paced by the medial septum could be cross-frequency coupled with gamma oscillations in laminae in a way that gives the appearance of causal influence between laminae.

The source for repetition suppression in both firing rate and gamma-band power is

not known, but the prominent deep to superficial connectivity in comparison to the weak superficial to deep connectivity (Figure 4.4A) provides an attractive candidate. Many prevailing theories regarding episodic memory have suggested that the hippocampus is an important processing stage in memory formation and recall (Buzsáki, 1989; Eichenbaum et al., 2012). Thus to access a newly-formed memory it may be important to access the hippocampus, which is thought to be read out through the deep layers of the EC (Chrobak et al., 2000). Accordingly, if repetition suppression reflects declarative memory, then we would expect deep layers to carry the recognition signal. As mentioned above, deep layers form excitatory synapses with superficial layers that typically result in inhibition of neurons in superficial layers (Chrobak et al., 2000). The decreased LFP power and decreased firing rate in superficial layers during repeat image viewing may be due to deep layer activation and/or recurrent inhibitory connections within layers I-III. Some of the suppression may also be due to a simple reduction in the power of input to the superficial layers of the EC; as described previously, repetition suppression is seen in many cortical areas associated with vision that have connections with the EC (Xiang and Brown, 1998; Suzuki et al., 1997; Miller et al., 1993). In particular, the perirhinal cortex is highly connected with the EC (Suzuki and Amaral, 1994). However, this description may be problematic because studies have found very little propagation of activity from perirhinal to entorhinal cortex (De Curtis and Paré, 2004); it is not clear why firing rates in the EC would simply reflect firing rates in structures that project to the EC such as the perirhinal cortex. It would be necessary to record from many of these areas simultaneously to fully understand the signal flow, determine the sources of the repetition suppression signals, and disentangle different processes associated with decreased activity during repeated presentation of stimuli (i.e. habituation, priming, and signals representing declarative memory).

The exact nature of the information carried from deep to superficial layers is unknown, but a reasonable hypothesis is that it represents information originating from the hippocampus and that the superficial layers use this information to efficiently gate the sensory input to the hippocampus by way of comparison to previously encoded information (Chrobak et al., 2000; de Curtis and Paré, 2004). When the deep and superficial layers do not successfully work together to gate information to the hippocampus, poor memories may be formed (Figure 4.4D, right and Figure 4.4E, right). Note that synchronization in the EC can be beneficial in providing a novelty signal; I observed an increase in synchronization in superficial layers during encoding and a decrease associated with recognition. However, excessive synchronization was detrimental to encoding processes within layer III and layers V/VI and in the directed influence from superficial to deep layers.

Activity within and between superficial and deep layers appears to have a functional range that can in turn produce a range of memory strengths in normal monkeys, but it may go awry under pathological conditions. One such instance may be failure of inhibition in superficial layers linked to seizure propagation in epilepsy (Du et al., 1995; de Curtis and Paré, 2004; Empson and Heinemann, 1995; Pare et al., 1992). Fully understanding the range of possible detrimental and beneficial activity in the EC may eventually aid in designing treatments for diseases that affect the EC, e.g. through emulating the 'strong' activity patterns with electrical microstimulation. Recent experiments in humans (Suthana et al., 2012) have demonstrated the potential for memory enhancement via electrical microstimulation of the EC. We have planned experiments to study electrical memory enhancement through stimulation in monkeys that will make use of the findings in humans and the information gained from the experiments in this thesis (see Chapter 6 and Appendix F). Devices that allow long-term high resolution study of the EC in culture may significantly

aid in the development of such treatments (see Chapters 5 and 6).

Methods

Please refer to Chapter 2: Methods for details on subjects, surgical procedures, the behavioral task, and recording methodology.

Unit recordings

Single units were recorded as in Chapter 2. In this Chapter, I examined repetition in more detail than in Chapter 2. Here it is noted that repetition suppression tended to be greater in superficial layers and at more anterior locations, as shown in Figure 4.5.

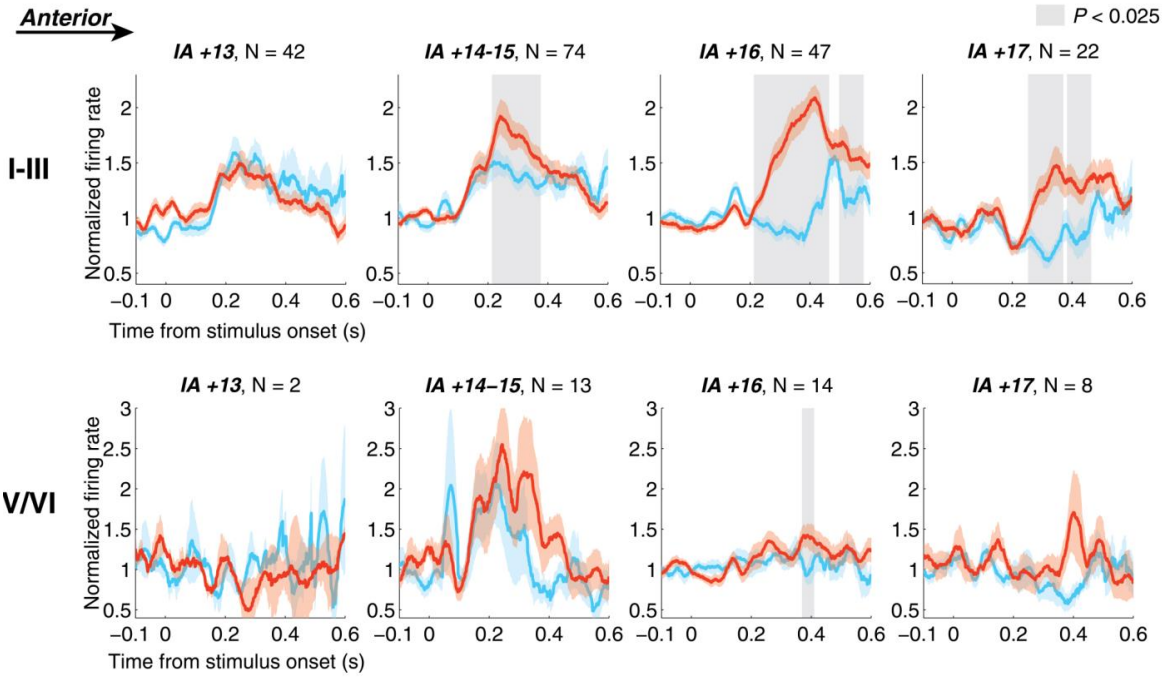

Figure 4.5 | Firing rate signals in the EC. Units in superficial layers of the EC (I-III, N = 135) exhibit stronger responses to image viewing compared to units in deep layers (V/VI, N = 82). Superficial units also exhibit a strong repetition-suppression effect (novel rate significantly greater than repeat rate), while units in deep layers do not show this effect as a population. The units are pooled across recordings from two monkeys and plotted as a function of interaural (IA) anatomical location (larger IA values are more anterior). The gray regions represent a temporal cluster of a significant difference in firing rate between novel and image viewings (p < 0.025 per tail, non-parametric permutation test on maximum cluster sums after dependent samples t-tests using a sample threshold of α < 0.05 per tail from -0.1 to 0.6 seconds from stimulus onset, 10,000 permutations; (Maris and Oostenveld, 2007)). Curves show the mean ± SEM across units, red is for novel and blue is for repeat viewings.

Electrical lesioning and histology

At the end of experiments in one monkey, the tissue near 4 electrode sites was lesioned with DC current, using the stainless steel guide tube as the reference site. Before lesioning, impedance was measured to verify the health of individual electrode sites. Impedances ranged from 0.5 to 1 MΩ at 1 kHz. Using a NeuroNexus Instrumentation Pod system, 6 μA was sequentially applied for 10 seconds to channels 1, 6, and 12. To assist in later alignment, 7 μA was also applied for 12 seconds to channel 9, resulting in a larger lesion size. Injected charge was kept relatively low in order to restrict lesion size so that individual layers could more readily be localized (Parikh et al., 2009; Yazdan-Shahmorad et al., 2011). After applying the lesioning current, the probe was removed and the animal was euthanized according to methods approved by the AVMA panel on euthanasia. The animal was given an overdose of sodium pentobarbital (100 mg/kg, i.v.), and then transcardially perfused with oxygenated Ringer's solution followed by 2 liters of fixative (4% paraformaldehyde, 0.1% glutaraldehyde in phosphate buffer (PB; 0.1 M, pH 7.2)). The brain was then removed from the skull and cut into blocks that were then immersed in a 30% sucrose solution for three days before being sectioned in serial 50 μm-thick sections with a freezing microtome. Alternate sections were stained with cresyl violet (for Nissl substance) and microtubule-associated protein 2 (MAP2) antibodies to verify electrode locations. The Nissl-stained sections highlighted cellular damage and gliosis with darker staining (Figure 4.6A). MAP2 is expressed primarily in neurons, which results in lighter staining where there are fewer neurons. Thus MAP2-staining highlights neuron death due to lesioning, but the absence of neurons due to mechanical disruption of tissue by the penetration itself is also readily visible with this stain (Figure 4.6B).

To localize the lesion locations, I took the intersection of the darkest regions of the

Nissl-stained sections and the brightest regions of the MAP2-stained sections (Figure 4.7). The intersection removed spurious regions in both types of staining and highlighted regions of the greatest amount of cellular damage associated with the lesions. The processing resulted in four regions that were readily matched with the locations of the four lesion sites.

Estimation of recording location and layer classification

The posterior-anterior anatomical location of the EC was estimated by taking fourteen 1 mm slices from an MRI scan to constitute the range of the EC. The extent of the EC was identified by comparing anatomical features on the MRI scans to an atlas (Saleem and Logothetis, 2007). The fundus of the rhinal sulcus was identified in MRI scans to estimate the medial distance of the recording locations.

Location within the EC was classified with the aid of current source density (CSD) analysis, using simultaneously recorded local field potentials (LFPs). The CSD assists in determining the locations of current sinks and sources when assuming that the current sources in laminae are homogenous in the transverse directions (parallel to cortical laminae and perpendicular to the penetration). The standard CSD method assumes that the sources lie in infinite sheets. I used the inverse CSD (iCSD) method that uses the assumption that the sources are circular discs of a specified finite diameter, here 500 μm was chosen (Pettersen et al., 2006). If the layers can be assumed to be consistent within the specified source diameter, then this method reduces error that would arise from using the standard method with penetrations that are somewhat oblique to the cortical laminae. If any electrode site was damaged and could not be used, the LFP was taken to be the average of the two adjacent sites, or equal to an adjacent site if an edge channel was to be estimated. LFPs were aligned to the onset of visual saccades because at saccade onset a clear low-amplitude, positive increase in the field potential occurred across all channels, aligning the phase of the LFPs.

This phase alignment ensured that an average could be taken across hundreds of saccades in a session to obtain an estimate of the mean CSD with high confidence. Layer definitions were then based on the CSD obtained during the following 300 msec, which encompassed the

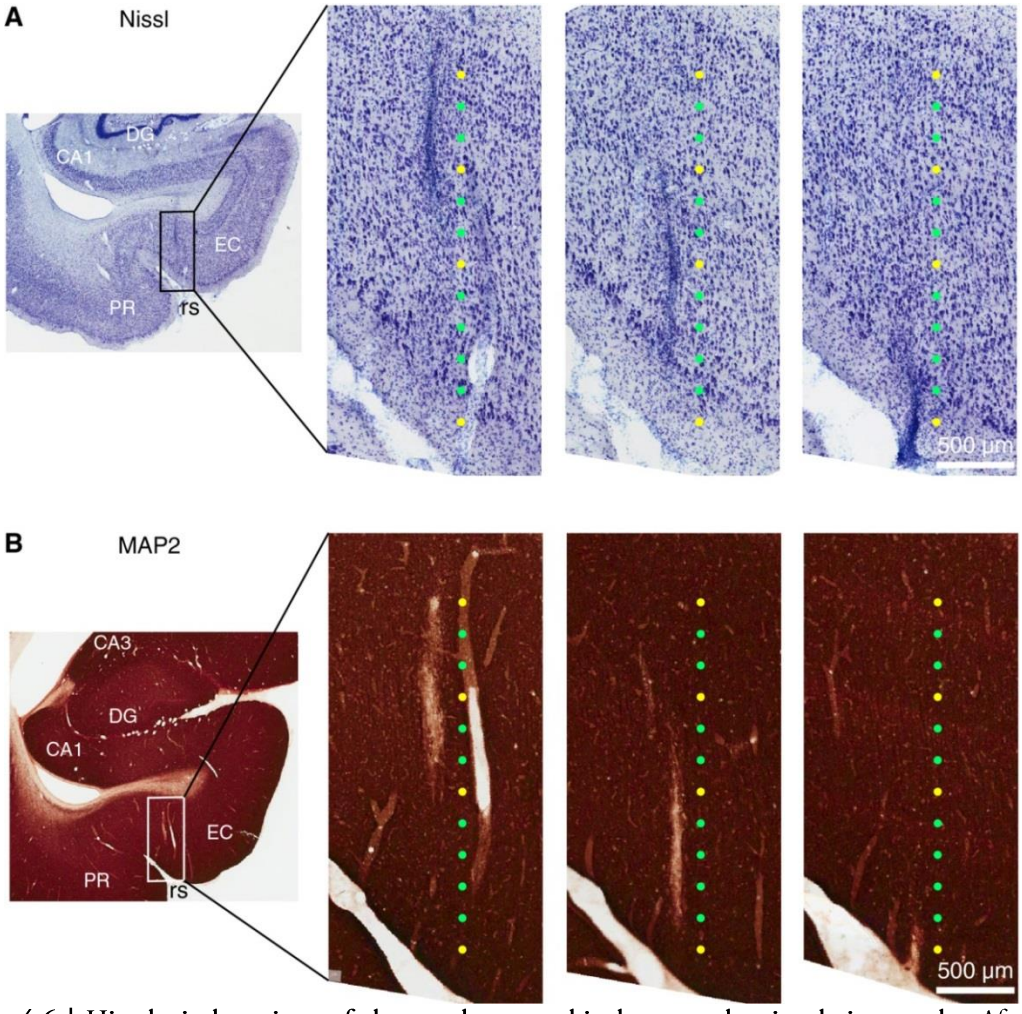

Figure 4.6 | Histological sections of the monkey entorhinal cortex showing lesion marks. After field potential recordings, the EC was lesioned with constant current at 4 locations (yellow dots). The animal was sacrificed and the brain was fixed and cut into 50 µm thick sections. Alternate sections were Nissl- and MAP2-stained. Because slicing was performed at an angle to the penetrations, multiple sections were needed to locate the track. Moving to the right, sections are progressively more posterior. **A.** Nissl-stained sections show the lesion marks in the EC (darker staining due to tissue damage and gliosis). Electrode locations were estimated based on the lesion locations after accounting for the slope of the penetration with respect to the sectioning plane (1.7% compression). The electrode locations are offset to the right of the track for clarity. Green dots denote non-lesioned electrode sites and yellow dots denote the 4 lesioned sites. See Figure 4.7 for details of alignment procedure. **B.** MAP2-stained sections that are each 1 section posterior to sections in 'A', showing neuronal loss at the lesion locations (light staining). Note that there is a gap due to a blood vessel in the left section to the right of the lesion track. The electrode locations and colors are plotted in the same manner as in 'A'. (DG: dentate gyrus; PR: perirhinal cortex; EC: entorhinal cortex; rs: rhinal sulcus).

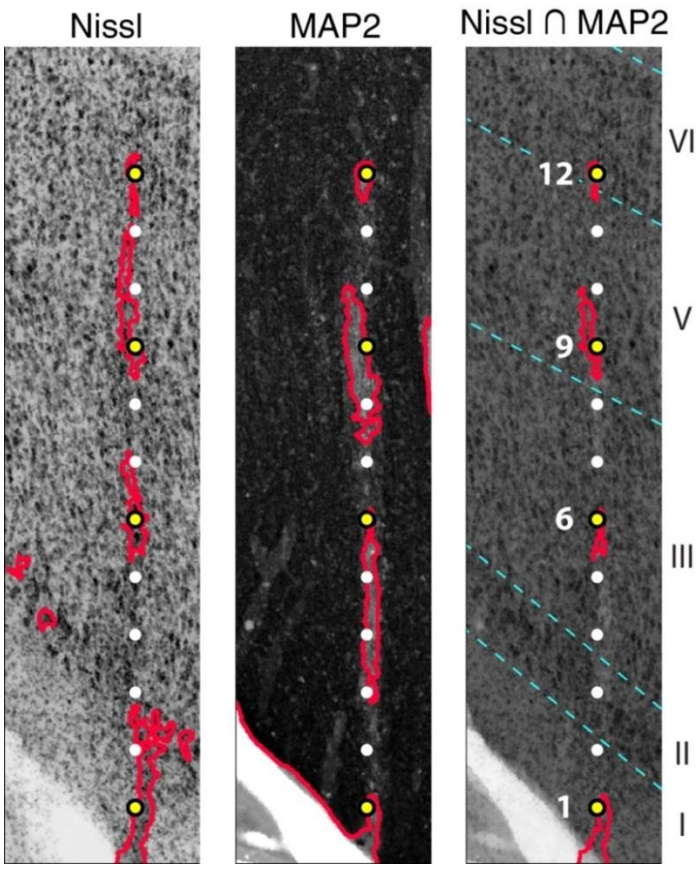

Figure 4.7 | Composite histological sections of the monkey entorhinal cortex with lesion marks used to estimate recording location. The 3 Nissl-stained sections shown in Figure 4.6 were aligned according to the rhinal sulcus and layer II. The intensity was thresholded to find the darkest regions (areas associated with damage and gliosis) in the image (outlined in red). The 4 lesioned sites are depicted in yellow and other electrode sites are in white. The average intensity of these sections is plotted in grayscale. The MAP2 sections were processed in the same manner as the Nissl sections but thresholded to find the brightest regions (neuronal loss). The intersection of the darkest Nissl regions and the brightest MAP2 regions was taken to further localize the lesion marks. Spurious regions are eliminated by this histological analysis method, these regions are primarily: the darkly stained cells in layer II of the Nissl sections, the bright areas in the rhinal sulcus of the MAP2 sections, the bright region on the MAP2 sections due to mechanical damage, and the bright region on the far right of one of the MAP2 sections corresponding to a blood vessel. The best fit to the intersection regions (the regions outlined in red) was taken to be the location of the lesioned sites. Note that site 9 was intentionally lesioned with more current and for a longer duration than sites 1, 6, and 12 to further assist in alignment. Site 1 was in layer I, site 6 was near the middle of layer III, site 9 was in the superficial part of layer V and site 12 was at the most superficial part of layer VI. The roman numerals and dashed cyan lines delineate the laminae. 30 μm diameter electrode sites spaced at 147.5 μm (the spacing after compression to align with sectioning angle) are plotted to scale.

saccades and the following fixation periods (Figure 4.8). The CSD pattern obtained after stimulus onset was similar, but more variable due to the variable timing of saccades inherent to the free-viewing task. The CSD from the session where the lesions were applied was used

to estimate the CSD associated with each layer of the caudal EC (layers I, II, III, V, and VI).

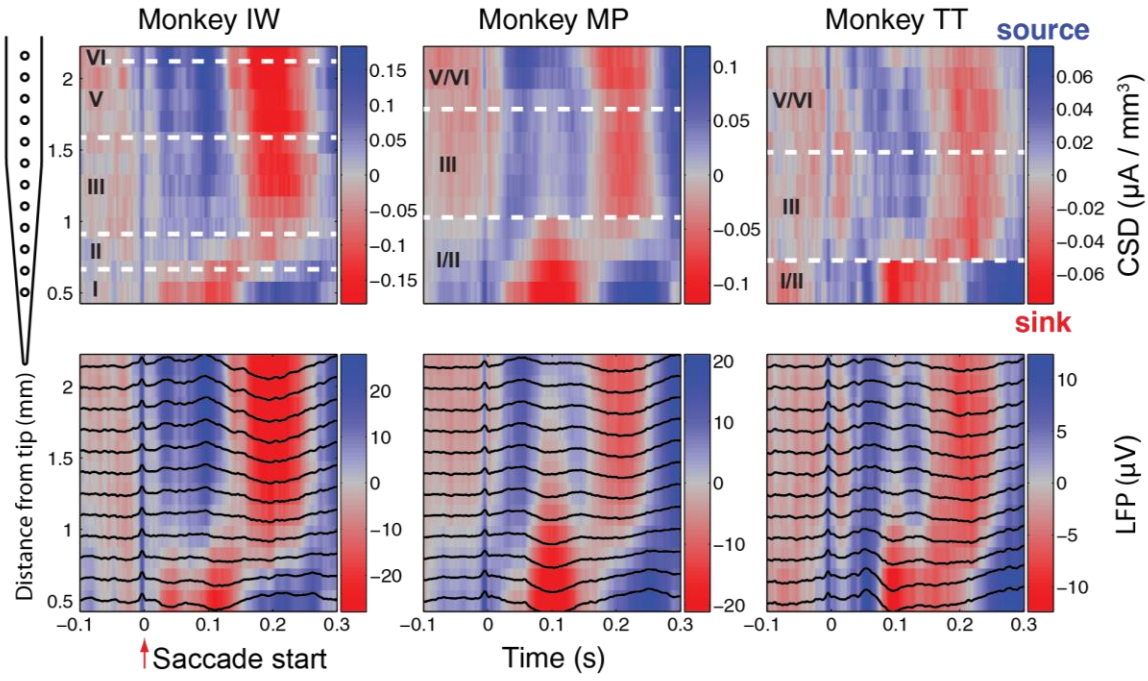

Figure 4.8 | Current-source density (CSD) and local field potentials (LFPs) in the EC for 1 recording session in each of 3 monkeys. Shown at the top are CSD maps aligned to saccade onset during image viewings. At the bottom are LFPs plotted in the same manner as the CSD, black lines are individual average LFPs for one of the 12 channels. The amplitude has been normalized to the maximum over all LFPs. On the CSD plots, dashed white lines delineate laminae. The laminae for monkey IW were determined directly from the histological analysis. The layers for monkey MP and TT were determined algorithmically using the information obtained from monkey IW. The color scales for each map have been chosen to be symmetric with a range of ± the maximum deflection. Note the CSD phase reversal near layer II.

From these data, it was clear that an LFP phase reversal, most obvious at low frequencies (Figure 4.9), occurred across layer II, just as is seen in the rodent EC (Alonso and García-Austt, 1987; Chrobak and Buzsáki, 1998a). Layers III, V, and VI were then largely all in-phase throughout the fixation periods. Only one channel was placed in layer VI, but the LFP recorded on this channel was also in-phase with the LFPs recorded in layer V. In other sessions no clear difference in phase was seen after the shift in phase between layers II and III,

Principal components analysis (PCA) and k-means clustering were performed on the

CSD values in the first 300 msec after saccade onset in order to classify the layers of the channels in the sessions without associated histology. Three clusters were initially defined that identified the patterns associated with the phase reversal just described, clustering CSD curves related to the patterns of layer I, layer II, and layers III-VI. One layer group was taken as all channels up to the last channel in the layer II group, i.e. the clusters corresponding to layers I and II.

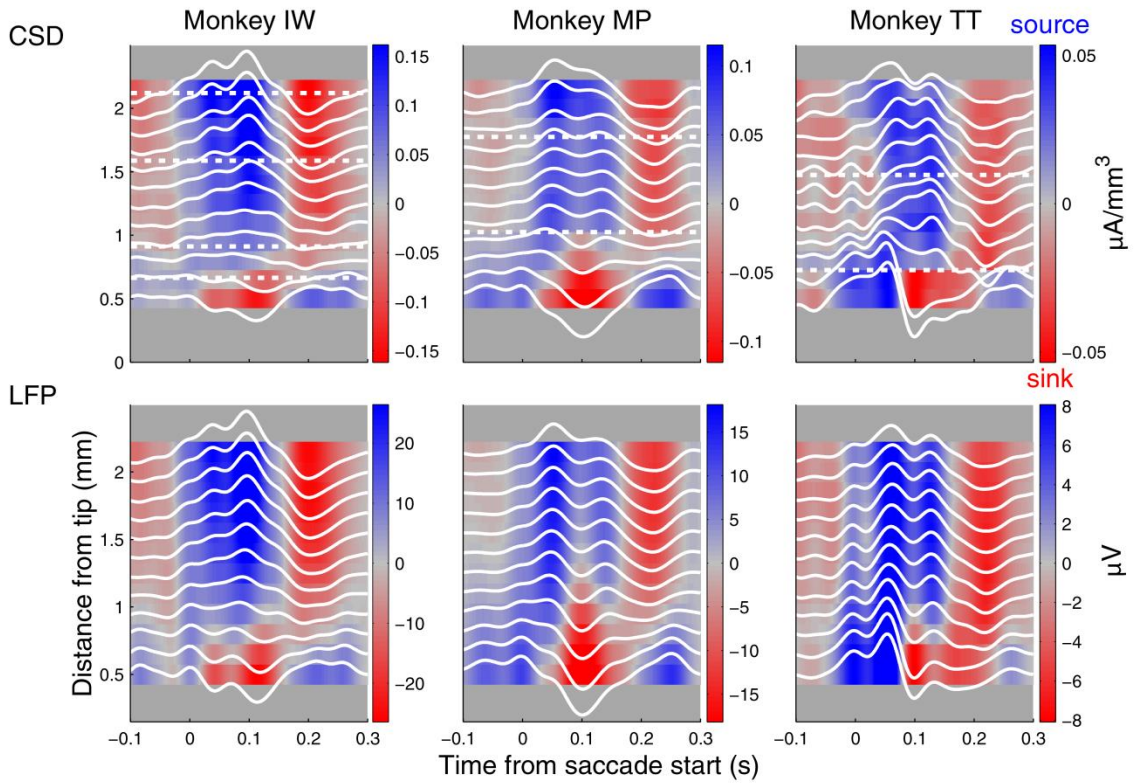

Figure 4.9 | Theta oscillation phase reversal near layer II. CSD and LFPs as in the previous figure, but filtered from 1-20 Hz. Low frequencies reverse in phase near layer II.

Because I estimated the width of layer III where recording penetrations were made to be from about 600-800 microns, I took the next five channels (spanning 600 microns) to be in Layer III. Any channels above these were taken to be in layers V-VI. For subsequent analyses, layers I-III were grouped as superficial layers and layers V-VI were grouped as deep layers.

Time-frequency LFP power analysis

Spectral analyses were performed with the aid of the Fieldtrip toolbox in MATLAB (Oostenveld et al., 2011). I examined activity using time-frequency representations based on windowed Fourier transforms, employing the multitaper method with Slepian tapers to achieve optimal spectral concentration (Thomson, 1982). To reduce the presence of responses related to reward blocks, the first and last trials of each image viewing block were removed. Additionally, the LFPs recorded on the tip electrodes were not included in these analyses because the tip was often in the meninges outside of the EC. Comparisons between conditions and layer groups were made using a nonparametric cluster-based permutation test with (Maris and Oostenveld, 2007). For comparisons between encoding and recognition viewing periods, and between high and low recognition trials, a dependent-samples t-test was used as the ingredient for forming clusters, an independent samples t-test was used for comparing different layer groups. All 4-connected pixel neighborhoods with a t-score corresponding to a p-value below 0.05 were considered part of a cluster and the largest positive and negative cluster sums were taken for each of 10,000 random permutations of the condition or layer labels to form a two-tailed permutation distribution. The clustering was then performed on the actual data and any clusters exceeding the 97.5th percentile of either tail of the permutation distribution were considered significant clusters. In Figure 4.1 and Figure 4.2, significant clusters were outlined in black after increasing the resolution of the cluster boundaries by a factor of 10 to improve plotting accuracy.

Granger causality analysis

Granger causality (GC) analysis was used to quantify directional influences between superficial (II/III) and deep (V/VI) layers of the EC. The methods employed have been used previously to examine directed influences between LFPs recorded in the neocortex. The

methods were used to examine connectivity in the somatosensory and motor cortices of rhesus monkeys performing a GO/NO-GO visuomotor task with a bar release to signal stimulus change (Brovelli et al., 2004) and between LFPs in FEF and V4 of rhesus macaques performing a visuomotor attention task with a bar release to signal color change in an attended-to region of visual space (Gregoriou et al., 2009). In the latter study, by examining latencies of Granger causality changes in different conditions, the authors were able to determine that gamma-band synchronization (near 40 Hz) between FEF and V4 may have been initiated by FEF. In both studies the analyses were restricted to particular frequency ranges of interest (beta and gamma). The reasons for this were not explicitly stated but it may have been because the communication between the areas being studied was restricted to those frequency ranges or perhaps that individual cortical layers were not identified and a segregation in frequency bands was not seen; many studies have reported that oscillatory activity can be localized to specific layers of the cortex (Sun and Dan, 2009; Buffalo et al., 2011; Ainsworth et al., 2011). The EC exhibits interesting activity across a wide range of frequencies and different frequency bands appear to be associated with particular directions of influence and task conditions within the EC, as reported in this chapter. The GC values were visibly similar in all monkeys tested and were thus combined in the main text. For discussion of the GC effects (as in Figure 4.4) in different monkeys, see Methods: Granger causality analysis.

Granger causality gives that one stochastic process X(t) 'causes' a second stochastic process, Y(t) if autoregressive predictions of Y(t) are significantly improved by including past values of X(t) (Granger, 1969). Autoregressive models were fit to pairs of LFPs using sliding 150 msec time windows. The model was transformed to the frequency domain to obtain Granger values as a function of time (the center of the sliding window) and frequency. The

Granger causality values give an estimate of power at a particular frequency that one signal contributes to another signal. The Granger causality measure was used to compare different conditions for the same pairs of signals: encoding vs. recognition and strong vs. weak encoding.

From (Brovelli et al., 2004), the bivariate autoregressive model for a pair of LFPs (i.e. superficial and deep layers) as a function of time t, X_t, is:

$$\sum_{k=0}^{m} A_k \, X_{t-k} = E_t$$

where m is the model order (1 msec time lags), the A_k are the 2x2 coefficient matrices, and E_t are the residual errors with covariance matrix Σ.

In order to remove the first-order nonstationarity and consider the time series to be zero-mean stochastic processes, which is required to perform the autoregressive modeling, the mean was subtracted from each LFP on each trial followed by dividing by the standard deviation (Zhang et al., 2008; Ding et al., 2000). The short overlapping time windows allowed the stochastic processes to be considered locally stationary. The AR model parameters were estimated using the Burg algorithm for vectors (Nuttall-Strand method) after determining the optimal model order (sample lags) for each signal and each time window considering all trials using the combined information criterion (De Waele and Broersen, 2003; Broersen, 2000; Gregoriou et al., 2009). The covariance matrix and the partial correlations matrices were estimated for each trial separately and then averaged across trials. The 'Automatic Spectral Analysis' computational toolbox by Stijn de Waele obtained from the MATLAB File Exchange was used to perform the modeling.

After determining the model coefficients A_k and the covariance matrix Σ, the spectral matrix $S(f)$ as a function of frequency, f, is

$$S(f) = H(f)\Sigma H^{*}(f)$$

$$H(f) = \left(\sum_{k=0}^{m} A_k \, e^{-2\pi i k f}\right)^{-1}$$

with transfer function $H(f)$ and where * represents matrix transposition and complex conjugation. The 2x2 spectral matrix $S(f)$ contains the individual power spectra and cross spectra, with the power spectra on the main diagonal.

The total power in one signal can be decomposed into a sum of two terms, which can be interpreted as an intrinsic power component and a component that can be predicted by another signal, the 'causal' power (total = intrinsic + causal) (Geweke, 1982). The Granger causality spectrum is then defined to reflect the relative amount of causal power to total power. Considering a superficial layer LFP '*S*' and a deep layer LFP '*D*', the Granger causality spectrum for a given direction is defined as the logarithm of the ratio of total power to intrinsic power, which is equal to the negative logarithm of 1 minus the ratio of causal power to total power, as given here (Geweke, 1982; Brovelli et al., 2004):

$$I_{D\to S} = -\ln\left(1 - \frac{\left(\Sigma_{DD} - \frac{\Sigma_{SD}^2}{\Sigma_{SS}}\right)|H_{SD}|^2}{S_{SS}(f)}\right)$$

$$I_{S\to D} = -\ln\left(1 - \frac{\left(\Sigma_{SS} - \frac{\Sigma_{SD}^2}{\Sigma_{DD}}\right)|H_{DS}|^2}{S_{DD}(f)}\right)$$

where Σ_{SS}, Σ_{DD}, and Σ_{SD} are the elements of the covariance matrix Σ .

To find time or frequency regions of significant differences in Granger causality between conditions, a cluster-based nonparametric permutation test was used (Maris and

Oostenveld, 2007; Oostenveld et al., 2011).

The GC results as plotted in Figure 4.4 are shown in Figure 4.10 to Figure 4.12, separated by each monkey, MP and TT. The patterns in each monkey are qualitatively consistent with the combined population results.

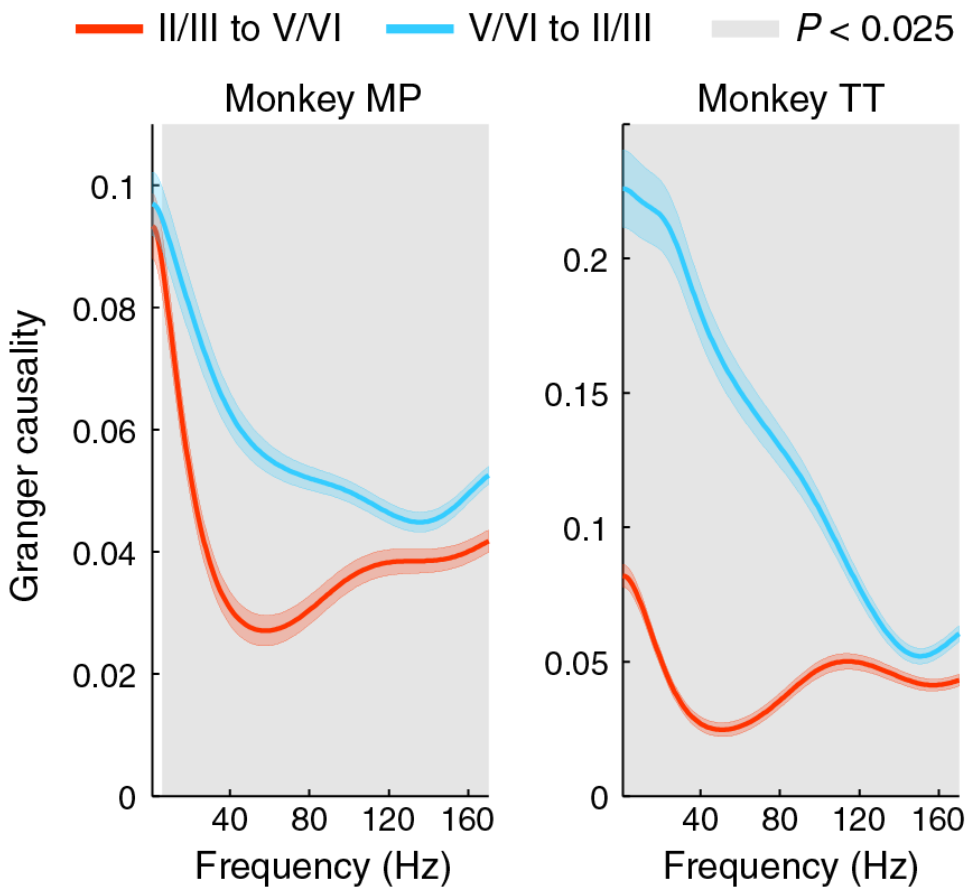

Figure 4.10 | Raw Granger causality values between superficial and deep layers of the EC during image viewing, from 1 to 170 Hz. These plots represent the LFP pairs included in Figure 4.4A for monkeys MP and TT. Deep layers were significantly more influential on superficial layers across nearly all frequencies, Deep to superficial Granger causality was greater for monkey MP from 7-170 Hz (N = 171) and for monkey TT from 1-170 Hz (N = 149). Power transfer from deep to superficial layers is represented by the blue curves (mean ± SEM). Power transferred from superficial to deep layers is represented by the red curves (mean ± SEM). Gray shading represents a significant difference between the two directions (1 Hz resolution; cluster-based permutation test, $p < 0.025$).

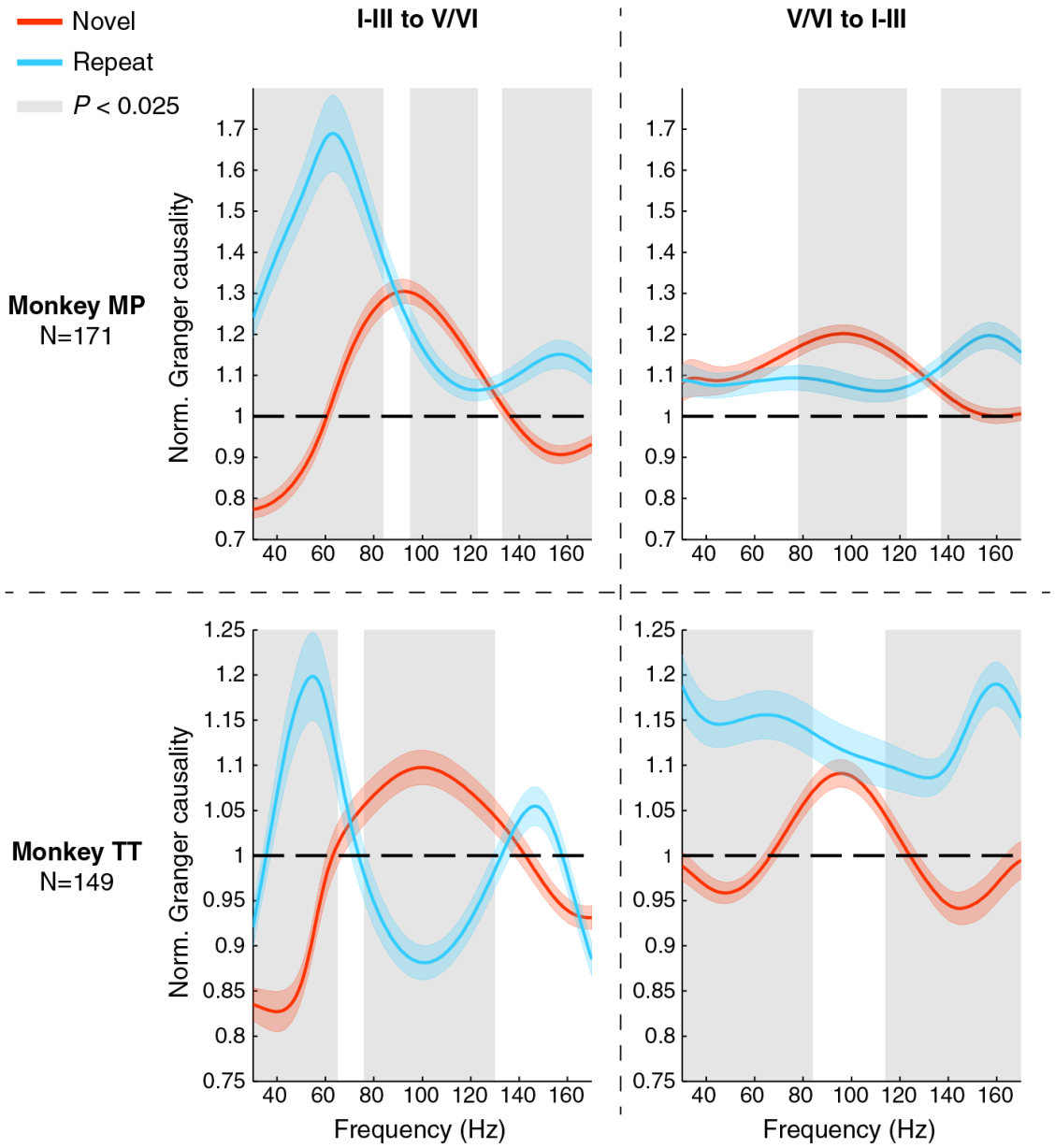

Figure 4.11 | Granger causality separated by monkey for novel and repeat image viewings. The GC values normalized to baseline are shown for the two monkeys used in the analyses described in Figure 4.4C. The curves are qualitatively quite similar for both monkeys and the pairs were thus pooled together. The curves represent mean ± SEM and each region of grey shading represents a cluster of significantly different frequencies of GC for the novel and repeat viewings ($p < 0.025$).

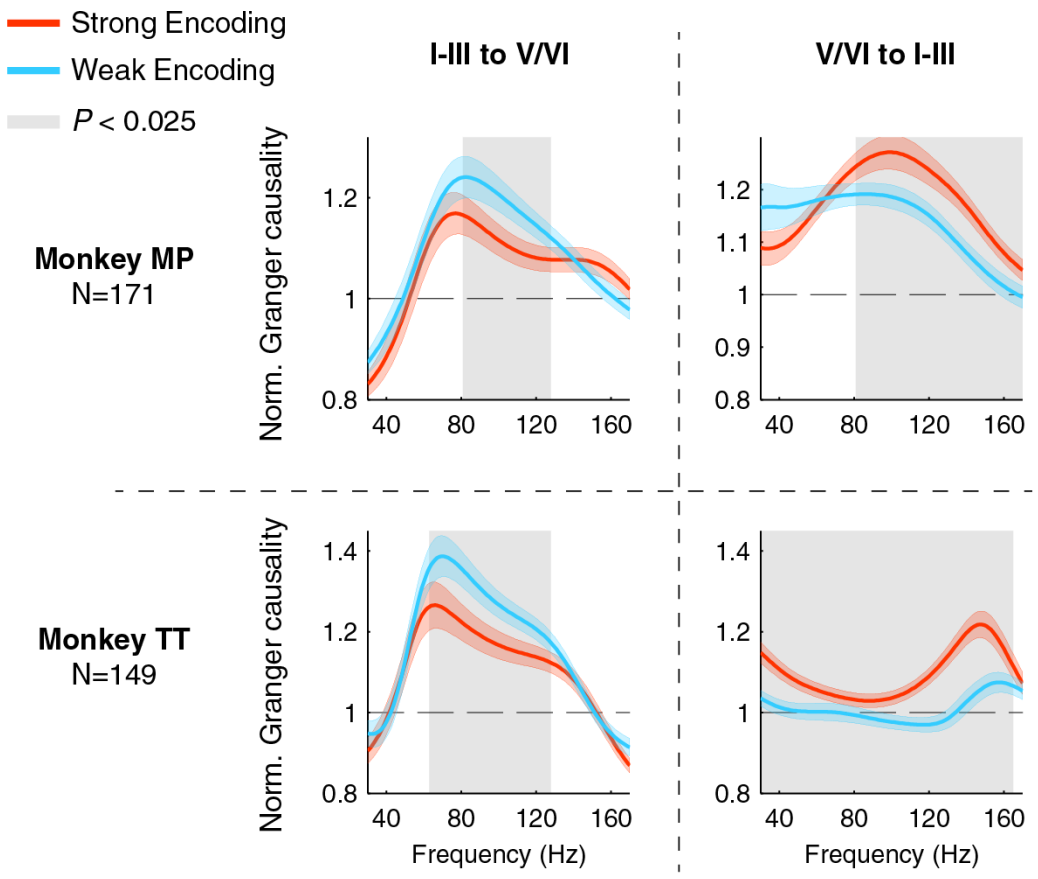

Figure 4.12 | Granger causality separated by monkey for strong and weak encoding trials. The GC values normalized to baseline are shown for the two monkeys used in the analyses described in Figure 4.4D. The curves are qualitatively quite similar for both monkeys and the pairs were thus pooled together. The curves represent mean ± SEM and each region of grey shading represents a cluster of significantly different frequencies of GC for the novel and repeat viewings ($p < 0.025$).

Spike train cross-correlation analysis

The cross-correlations between binary spike trains were computed for pairs having at least 30 trials in the relevant task condition that lasted at least 750 msec. These restrictions were chosen for consistency with the LFP analyses. The correlations were calculated at a resolution of 2 msec and averaged across trials. Cross-correlograms (CCGs) were truncated to ±30 msec and converted to z-scores. The z-scores were calculated using the expected number of inter-spike intervals assuming independent Poisson processes having mean rates equal to the mean rates over all of the trials included in the analyses, λ_1 and λ_2. The joint

number of expected intervals per second is then the product: $\lambda_1\lambda_2$. The expected number of intervals per bin is this product divided by the number of bins per second and the standard deviation is the square root of this number (De Oliveira et al., 1997; Takeuchi et al., 2011).

Separating the sum of values corresponding to the right, R, and left, L, sides of the CCG, directional connectivity can be examined. Directional bias was quantified by calculating the asymmetry index (AI) using the R and L values for each pair (Takeuchi et al., 2011):

$$AI = (R - L)/(R + L)$$

Acknowledgments

I greatly appreciate: Megan Jutras, Laura Kakalios, Drew Solyst, and Kiril Staikov for assistance with experiments; and Susan Jenkins and Yoland Smith for dissecting the brain and creating the histological sections.

CHAPTER 5

A NOVEL METHOD FOR *IN VITRO* PERFUSION, IMAGING, AND ELECTRICAL INTERFACING OF BRAIN TISSUE[6]

Distributed microelectrode array (MEA) recordings from consistent, viable, thick (≥ 500 μm) tissue preparations over time periods from days to weeks are useful for studying a wide range of problems in neurobiology that require *in vivo*-like organotypic morphology. Existing tools for electrically interfacing with organotypic slices do not address necrosis that inevitably occurs within thick slices with limited diffusion of nutrients and gas, and limited removal of waste. We developed a simple tool that enhances cell viability via long-term *interstitial* perfusion, and enables recordings from thicker sections of explanted tissue on a perforated multi-electrode array. The novel device allows for perfusion, imaging, and extracellular multi-electrode interfacing with brain slices, 3-D cell cultures, and potentially other tissue culture models. The device is economical, easy to assemble, and integrable with standard electrophysiology tools. I found that convective perfusion through the culture thickness provided a functional benefit to the preparations as firing rates were generally higher in perfused cultures compared to unperfused cultures. This work is a step towards the development of integrated tools for days-long experiments with more consistent, healthier, thicker, and more active tissue cultures with built-in distributed electrophysiological recording and stimulation functionality. The results may be useful for the study of normal processes, pathological conditions, and drug screening strategies currently hindered by the

---

[6] Adapted from: Killian, N.J., Vernekar, V.N., Potter, S.M., Vukasinovic, J. (2013). A device for long-term perfusion, imaging, and electrical interfacing of brain tissue *in vitro*. Under review.

limitations of acute (a few hours long) brain slice preparations.

Introduction

There are presently no tools that combine long-term (days-long) metabolic support of thick brain tissue preparations via intra-culture perfusion with integrated microelectrode arrays for distributed recording of physiological activity, all in a single system. Here I describe the design, fabrication, and validating experimental results of a device that meets this need. The tool supports interfacing with thick brain tissue sections and provides for long-term electrical stimulation and recording, which will be valuable for studying a wide range of neurobiology phenomena that cannot be understood through acute experimentation lasting only a few hours. For example, the long-term development of spatiotemporal activity patterns that underlie epilepsy could be studied with respect to the structure of the hippocampus *in vitro* (Ferrea et al., 2012) – currently limited to acute slice experiments. Hypotheses regarding the structure-function relationships of cortical laminae and local field potentials (Bakker et al., 2009) could be tested with greater accuracy by retaining more neurons, neuronal connections, and cellular laminae from the *in vivo* brain – currently limited by the use of thin tissue sections that quickly lose important laminar structures without perfusion. Another important avenue of research would be re-examining knowledge gained from two-dimensional (2-D) dissociated cultures (Jones et al., 2011) and three-dimensional (3-D) cell cultures (Cullen et al., 2011) to determine the general functions of unrestricted neuron growth. Such studies would illuminate mechanisms that underlie normal or pathological neuronal conditions, thus deepening our understanding and providing avenues for the creation of novel medical treatments.

Present day tools typically resolve only one of the needed requirements for long-term physiological activity recordings from thick preparations, either distributed recordings or

perfusion (Huang et al., 2012). Systems which focused on perfusion of thick tissue sections (Vukasinovic et al., 2009; Choi et al., 2007) were confined to one or a small number of electrodes. While a few electrode sites could serve as a read-out or index of the global state of activity, the reality is typically much more complex; neuronal activity moves in varied and unexpected ways both in the intact brain and in neuronal cultures (Lubenov and Siapas, 2009; Thiagarajan et al., 2010). Indeed, researchers continue to increase the number and density of electrode sites to examine neuronal properties with greater spatial and temporal resolution (Frey et al., 2009; Franke et al., 2012). The utility of multi-channel interfaces is, of course, not limited simply to electrical recording; closed-loop interfaces with stimulation have made use of large numbers of electrodes to produce separable stimulus sets (Bakkum et al., 2008). In essence, the performance of neural implants increases with the number of interface sites. The study of brain-machine interfaces *in vitro* with clinical applications is emerging and devices such as the one described here may help make this a viable enterprise by increasing electrical interface resolution and enhancing the *in vivo* relevance of the cultured tissue. The other class of systems which have focused on multi-electrode array recordings of biological activity from 3-D cell cultures and tissue slices (Stoppini et al., 1997; Musick et al., 2009; Rajaraman et al., 2011; Gholmieh et al., 2006) lacked forced interstitial perfusion for long-term tissue sustenance and thickness maintenance. Integration of intra-culture perfusion and distributed recording sites into a single tool remains a complex task. Accordingly, recordings from thick tissue sections have remained limited to manual insertion of electrodes into the tissues (Rambani et al., 2009; Irons et al., 2008; Passeraub et al., 2003; Blake et al., 2010).

In the absence of tools for maintaining viability of thick tissue preparations, researchers have resorted to thin (<400 μm) tissue sections to record physiological activity

using electrode arrays (Thiébaud et al., 1997; Berdichevsky et al., 2009). An example of such a tool is the perforated microelectrode array (pMEA) available from Multi Channel Systems, GmbH (MCS). In the past, pMEAs were successfully implemented to provide perfusion and electrical interfacing for thin slice cultures (Boppart et al., 1992; Stett et al., 2005; Egert et al., 2006). In such an arrangement, pMEA perforations either served to improve diffusion mass transport intra-culture by providing gas-equilibrated medium above and below the cultures, or as suction ports to withdraw the medium that was above the culture. Here we adapted pMEAs for surface recording, stimulation, and perfusion of thick tissue cultures, with perforations serving as inlet ports for forced intra-culture perfusion of thick tissue sections. To permit this, we created a closed-perfusion system using polydimethylsiloxane (PDMS) components which sandwiched the pMEA array, forcing flow of fresh medium through the tissue and withdrawing perfusate[7]. I cultured 0.5-1 mm thick brain slices for up to 5 days *in vitro* (DIV) and 3-D dissociated cell cultures in Matrigel® for up to 6 DIV using these tools[8]. Spontaneous and evoked neuronal action potentials were recorded and activity was elicited via electrical or chemical stimulation. Furthermore, cultures were imaged on the devices to assess culture viability and thickness. I demonstrated that the system can successfully culture, metabolically sustain, and provide for *in situ* electrical and optical interfacing with thick sections of brain tissue. The novel perfusion system was easily assembled and provided for straightforward integration with the widely used MEA1060 *in vitro* electrophysiology system from Multi Channel Systems. This lays out a cornerstone for long term electrophysiological recordings from thicker sections of brain tissue, which comprise a greater number of cell layers, and a greater number of live and functionally active

---

[7] PDMS components designed by JV with input on design constraints from NJK and fabricated by JV.
[8] Culturing assistance was provided by VNV.

cells for more predictive and consistent results in both short-term and for the first time, long-term experimentation.

Methods

Design and adaptation of perfusion chamber for multielectrode array interfacing

A method of non-invasive forced convection interstitial perfusion for long-term maintenance of thick tissue preparations was previously invented [US Patent 7,855,070 Jelena Vukasinovic and Ari Glezer 2010]. This method is unique in that it forces equilibrated medium to pass through the mass of cells and throughout the culture thickness (Figure 5.1A). This approach contrasts with previously applied perfusion methods for integrated MEA devices wherein fluid passes along one or more sides of the tissue but it is not forced through it (Thiébaud et al., 1997; Scott et al., 2013). Consequently, due to significantly lower resistance to fluid flow in a channel below the tissue (Figure 5.1B) or a medium pool which surrounds the tissue, flow is not forced to pass through the full culture thickness. As shown in Figure 5.1B, in a typical perfusion arrangement, a tissue slice wicks the medium from the channel below by capillarity and intra-culture mass transport remains diffusion limited for thicker tissue sections. In the new device, flow is forced to pass through the full culture thickness by controlling the flow geometry and ensuring adequate culture adhesion. This eliminates paths of low resistance to fluid flow around the culture, and all forced fluid passes through the culture at flow rates that are not deleterious to the cells (Rambani et al., 2009).

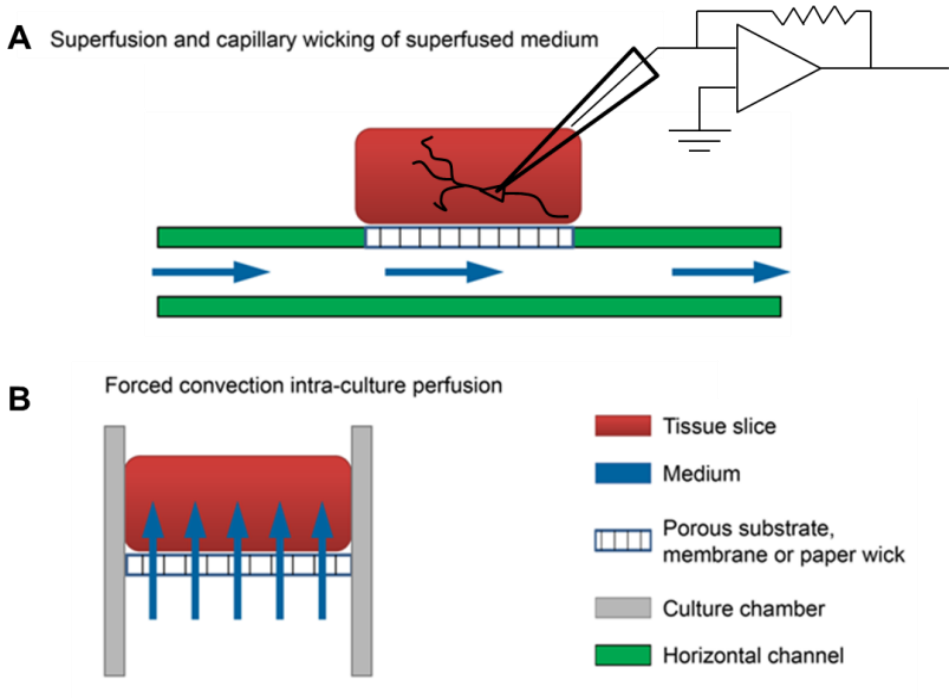

Figure 5.1 | Comparison of brain slice perfusion methods. A. Superfusion and capillary wicking of superfused medium by the tissue slice. The flow of equilibrated medium is not forced to pass through the mass of cells and through the full culture thickness. The resistance to fluid flow through the culture thickness is much higher than the resistance to fluid flow in a channel below the tissue. Flow passes through the channel and the tissue slice wicks the medium by capillarity. Neuronal recordings in this arrangement are performed by inserting a moveable electrode such as the patch electrode shown in the black outline. **B.** Forced convection intra-culture perfusion. The flow of equilibrated medium is forced to pass through the mass of cells and through the full culture thickness.

The device design builds on this previously validated perfusion tool (Rambani et al., 2009; Vukasinovic et al., 2009). The tool enabled long-term maintenance of thick 3-D preparations with enhanced viability by delivering gas-equilibrated medium through the mass of cells with concomitant withdrawal of waste products. I will describe this perfusion tool briefly and then elaborate on its adaptation to accommodate multi-electrode array interfacing in this current work.

Using a custom PDMS perfusion chamber with built-in gold mesh for seating the cultures, the previous tool provided for a slow rate of forced interstitial perfusion through 700 μm thick organotypic brain slices cultures (Rambani et al., 2009). This resulted in

higher viability of cells in virtually all cell layers when compared to unperfused slice controls in which the mass transport was limited solely to diffusion of gas and nutrients. The medium was injected into the perfused cultures via a gold mesh to which the slice cultures were adhered so that there were no paths of lower resistance around the culture. This forced the medium to pass intra-culture. The medium was withdrawn from circularly cut brain slices via microchannels built into the cylindrical wall of the perfused culture chamber. For enhancing gas transport, an aseptic, gas-permeable, and liquid-impermeable membrane was placed around the top face of the chamber. Electrical recordings with the previous tool were realized by manually inserting penetrating electrodes into the brain slices, a technique which is serial, difficult, and limited to a few isolated recordings. Present work focuses on an adaptation and improvement of the above described perfusion chamber to provide for integrated distributed recording and stimulation functionality.

To resolve and study functional slice activity both spatially and temporally demands distributed, multi-site recordings. Today, such recordings are realized by multi-electrode arrays with the added advantages of lower infection risk, improved recording consistency, and unparalleled ease of electrical interfacing with cultures, when compared to manual electrode insertion. This led to a new design, a perfused recording chamber with an integrated perforated microelectrode array to enable more consistent long-term electrophysiological recordings from thicker and healthier tissue models (Figure 5.2). Perfusion methodology was not changed from Rambani et al., 2009, except that the pMEA perforations assumed the function of the perfusion openings of the gold mesh. In a sandwich-like design we integrated pMEAs into unidirectional perfusion chambers. The perforations served as perfusion holes. Removable aseptic, breathable lids were placed on top of the culturing chamber to seal the device, maintain humidity, and prevent evaporation

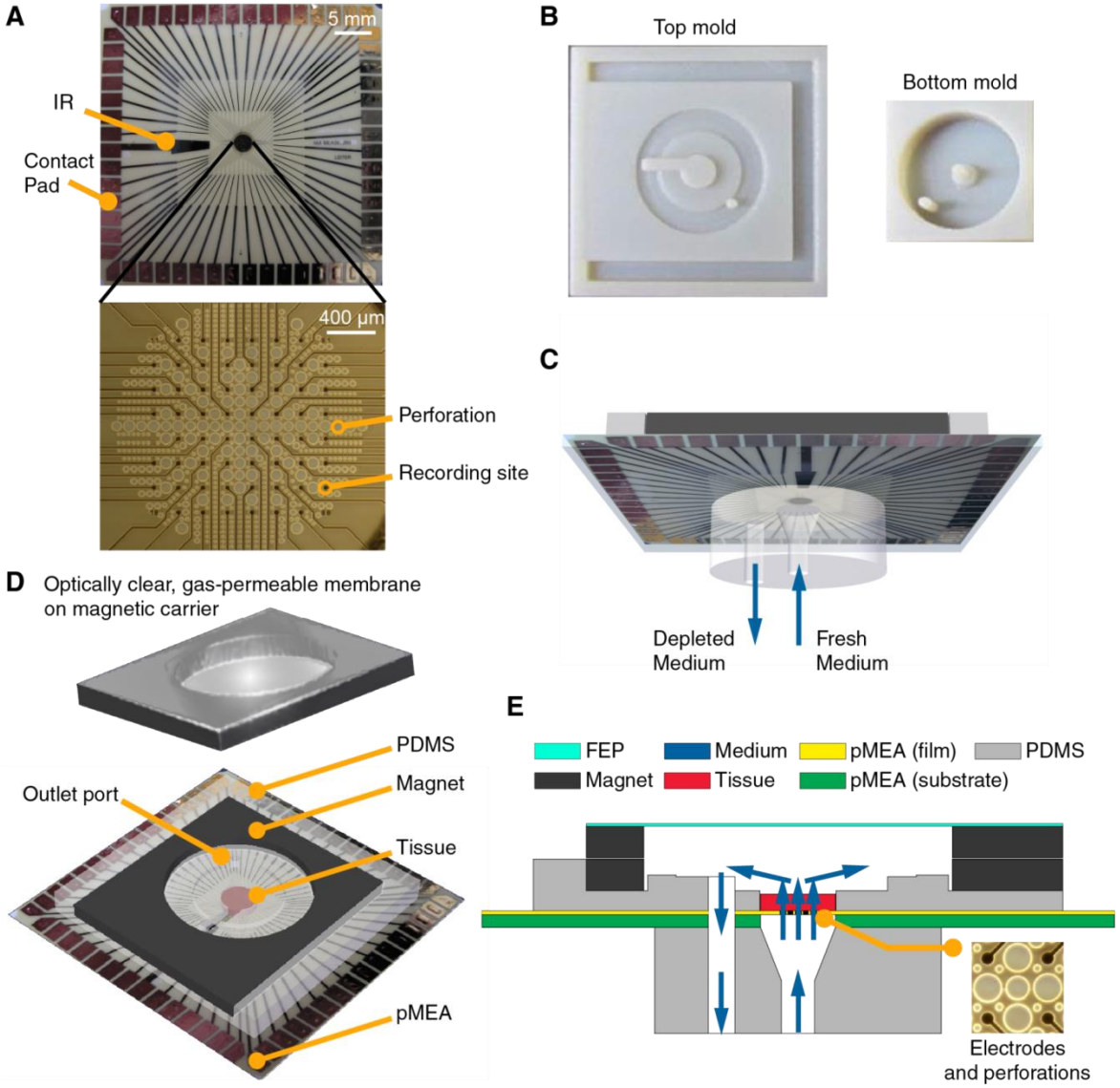

Figure 5.2 | PDMS-pMEA sandwich design. A. pMEA as supplied by the manufacturer. The pMEAs have recording sites and perforations which were used to deliver fresh medium to the tissue culture seated and adhered to the pMEA. The pMEAs have 60 electrodes (59 recording, 1 internal reference (IR)) which were used to record and stimulate electrical activity from the cultures. **B.** Plastic molds for the top and bottom pieces of the PDMS-pMEA sandwich. **C.** The bottom PDMS piece of the PDMS-pMEA sandwich comprising an inlet port to force fresh medium through the tissue and an outlet port to withdraw depleted medium. **D.** The top PDMS piece of the PDMS-pMEA sandwich comprising perfused culture chamber, a co-axial outer chamber for perfusate withdrawal, and the magnet for attaching the lid. The tissue was seated in the culture chamber directly over the electrode array. **E.** Vertical cross-section view of the device showing key design components. Medium, depicted by blue arrows, was delivered through the inlet port. It passed through the pMEA perforations and through the tissue, before it was withdrawn through the outlet port.

losses that would otherwise cause osmotic shocks to the cultures. Leak tests, evaporation tests, and other material tests for cytocompatibilty and adhesiveness were conducted before finalizing the materials and design. The chamber provided a supply of fresh media to the tissue and withdrawal of effluent (depleted medium) in a sterile manner without leakage and evaporative losses.

Design, fabrication, and fluidic interfacing of PDMS-pMEA sandwich components

Many successful neuronal culturing and interfacing devices have been developed and validated using PDMS (Vukasinovic et al., 2009; Rambani et al., 2009; Choi et al., 2007). PDMS is an excellent material choice for these applications because of biocompatibility, water-tight and water sealing properties, convenience of use, and accuracy in replica-molding features down to microscopic level, all at a low cost. Here, we replica molded PDMS components, a top and a bottom piece, which sandwiched the pMEA to enable perfusion of thick preparations cultured on the pMEA. These PDMS components were made by pouring and curing Dow Corning Sylgard® 184 resin at a 1:10 ratio of catalyst to pre-polymer in custom-made molds fabricated using standard additive manufacturing methods (Figure 5.2B). A 4.5 mm diameter cell culture chamber was formed in the top PDMS piece. It served to laterally confine a circular slice of explanted tissue or a 3-D cell culture. A section of the cylindrical wall of the culture chamber opened to a channel that contained the medium above the internal reference (IR) ground electrode (Figure 5.2A). The inner cell culture chamber was built into an outer co-axial chamber that was seated over the withdrawal port built into the pMEA. The flow through the culture residing in the inner culture chamber was unidirectional, bottom-to-top (Figure 5.2C, E). The top component of the PDMS sandwich was sealed to the pMEA using a 200 μm thick double-sided silicone tape

(Scapa 702) that enables water-tight sealing and a high-strength bonding of silicone substrates to other silicone substrates and other difficult to bond surfaces. The precise tape layout conformed to that of the bottom side of the top PDMS component. It was cut using a computer-controlled automated cutter. The bottom piece of the PDMS sandwich was replica molded to contain two vertical circular channels, a center channel and a side channel (Figure 5.2C). The center channel was made to interface with the perforations on the pMEA and served as an inlet port. The side channel was made to interface with the outer co-axial chamber, surrounding the culture chamber; thus creating an outlet port for withdrawal of perfusate. The top side of the vertical center channel was made wider to have a diameter equal to that of the inner culture chamber, thus allowing laminar flow of nutrients to uniformly permeate all perforations on the pMEA. The bottom side of both the vertical center channel and the vertical side channel permitted for straightforward insertion and leakproof interfacing with barbed tube fittings (Figure 5.3B). The bottom piece of the PDMS- pMEA sandwich (Figure 5.2C) was sealed and bonded to the underside of the pMEA using the double-sided silicone tape, cut using a layout which conformed to that of the top side of the bottom PDMS component. To prevent leaks and increase wet strength, a thin layer of PDMS was added and cured around the barbed connectors and at the corners formed where the top and bottom PDMS parts met the pMEA.

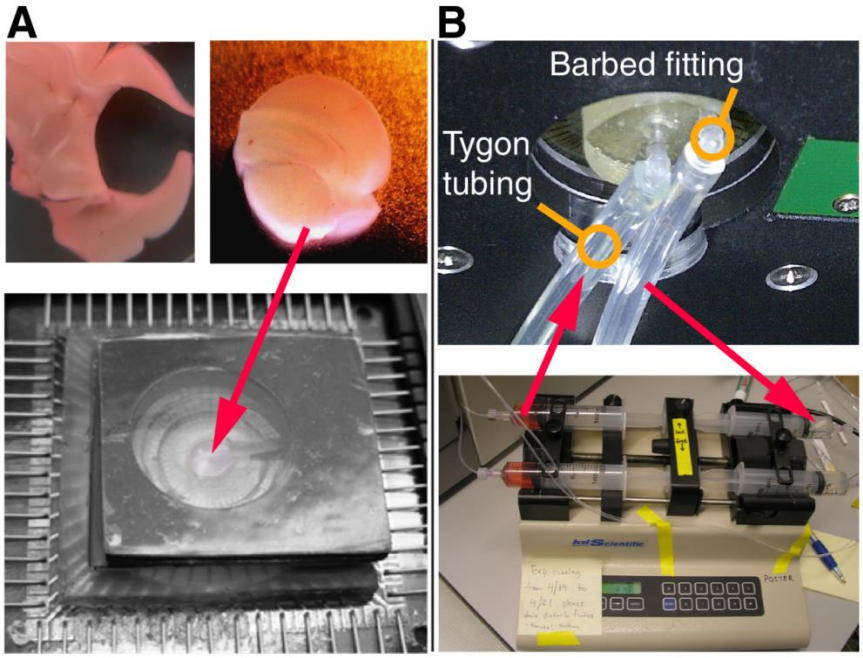

Figure 5.3 | Perfused pMEA interfacing with brain slice culture. A. 4.5 mm diameter rat brain sections were cut from 500-1000 μm thick slices with a biopsy punch tool and gently placed in the perfusion chamber (red arrow). Brain tissue was adhered to the perfusion chamber with the device seated into the pre-amplifier. Magnetic lids with FEP membranes were used to seal the chamber and permit gas exchange. **B.** Bottom view of the perfusion device seated in the pre-amplifier showing inlet and outlet tubing attached to the bottom piece of the PDMS-pMEA sandwich using barbed elbow fittings. A syringe pump provided mass-equilibrated continuous infusion of fresh medium and withdrawal of depleted medium (red arrows).

The pMEAs have an arrangement of circular openings (perforations) surrounding recording sites over a circular recording region measuring approximately 2 mm in diameter (Figure 5.2A, bottom). These perforations served as flow entry ports into the culture. An outlet port, measuring approximately 1 mm in diameter was drilled through the polyimide pMEA array film and through the approximately 1-mm thick pMEA carrier substrate (glass or ceramic) near site '81' (the upper right corner of the 8 x 8 MEA grid). The outlet port location was chosen to minimize damage to the array. Leads that were unavoidably damaged by drilling, typically 3-5 channels in the upper right corner of the array, were connected to ground through the preamplifier. A custom MEA lead layout could be designed that would accommodate this port without sacrificing channels. The wall of the outer chamber was

raised above the culture chamber allowing withdrawal of perfusate from the culture chamber and providing for a total medium pool volume of 120 μL for a 500 μm thick culture and 112 μL for a 1000 μm thick culture. Due to surface tension, we were able to obtain an empirical medium pool volume of up to 200 μL.

Short sections of Tygon tubing, approximately 8 cm long, were attached to the inlet and outlet port formed in the bottom PDMS piece (Figure 5.3B). I used high-purity (biocompatible, USP class VI) Tygon-2475 tubing, with thick walls to limit evaporative loss of medium during perfusion. The flexibility of the tubes provided for ease of insertion and removal of fluidic connectors without disturbing the PDMS-pMEA sandwich. Next, to limit pressure surge on the cultures and prevent air entry during connector insertion and removal, we used zero-fluid-displacement connectors (RyMed Technologies, Inc.) (Figure 5.4A). In perfused cultures, the distal ends of the respective connectors were interfaced with stiff fluorinated ethylene propylene (FEP) tubes (Figure 5.3B). The FEP tubes were then interfaced with 30 mL polypropylene infusion and withdrawal syringes of a syringe pump using LuerTight fittings. The syringe pump (KD Scientific 260) carried opposing, infusion and withdrawal syringes on a single drive (Figure 5.3B). The pump enabled mass-equilibrated infusion of nutrients into the culture and withdrawal of perfusate from the culture with a flow rate of 28 μL per hour. In unperfused control cultures, Tygon tubes were plugged with Luer-lock end-caps following filling of the tubing with medium.

The PDMS pieces were designed to be thin, less than a few millimeters in thickness for the top piece, for ease of culture imaging on the array using an upright microscope and effective interfacing with the MEA1060 preamplifier from Multi Channel Systems. The bottom piece of the sandwich was designed to easily fit in the preamplifier stage with sufficient tolerance for straightforward alignment, secure positioning, and good electrical

contact between contact pads and preamplifier pins. To further ease positioning of the device, the central hole of the MEA1060 base was enlarged with a CNC mill (Figure 5.3B). Custom 3-D printed legs (FullCure720) provided clearance for the tubing to pass underneath (Figure 5.4A).

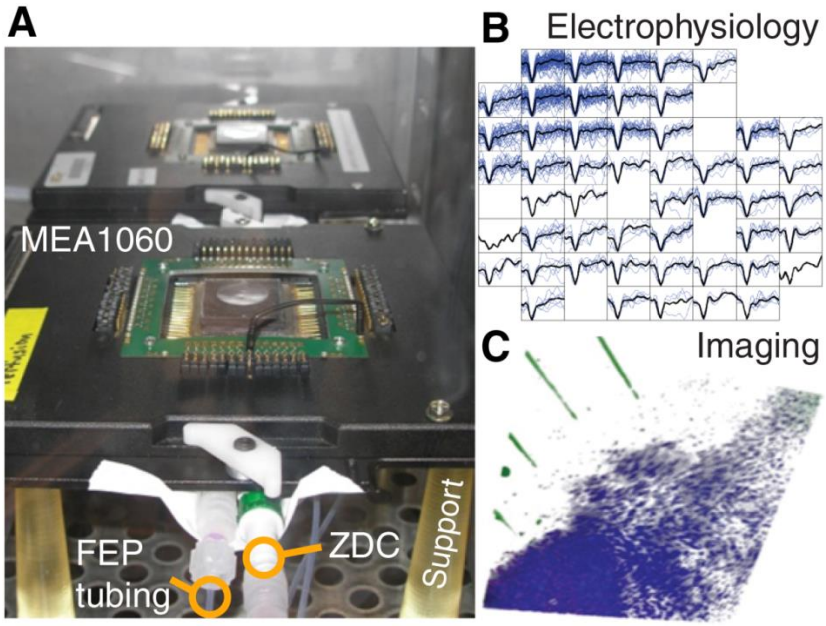

Figure 5.4 | Multi-channel electrophysiology and confocal imaging of perfused slice cultures. A. Two perfused pMEAs seated in 60-channel preamplifiers supported by custom 3-D-printed legs. The FEP tubing and a zero-displacement connector (ZDC) can be seen. **B.** Spike waveforms recorded from a slice at 1 DIV (blue: individual spikes, black: average waveform). For this slice, the activity was predominantly confined to the upper-left region of the array. **C.** Confocal 3-D rendering of a perfused brain slice seated in the perfusion chamber at 1 DIV. Blue: Hoechst dye, stained all cell nuclei; Red: propidium iodide, stained dead cell nuclei; Green: electrode traces.

Novel magnetic components for the attachment of breathable lids to perfused MEA recording chambers

A method was previously invented to use hydrophobic membranes to seal culture chambers in a way that permits gas exchange, prevents evaporative losses of medium, and reduces the risk of infection [US Patent 6,521,451 Potter 2001]. This is implemented by

attachment of a gas-permeable FEP membrane to a plastic ring, which is in turn attached to a glass ring serving as the culture well on Multi Channel Systems MEAs and other MEAs of a similar design (Potter and Demarse, 2001). To adapt this method to the thin PDMS-pMEA sandwich, I attached FEP film (DuPont) to a 2.5 mm thick sheet magnet (ferrite-bonded with synthetic rubber) that was cut to mate with another 1.5 mm thick sheet magnet (Figure 5.2D,E)[9]. The latter was built-into the top piece of the PDMS sandwich (Figure 5.2D). I found that a 100 μm thick FEP membrane prevented evaporative losses of medium, whereas 50 μm or thinner FEP film led to small but detectable evaporative losses in medium.

Magnetic interfaces provided for a tight seal that was leak-resistant with no detectable relative motion between magnetic components under typical culture transport conditions (e.g. placement into the preamplifier). Magnetic, FEP membrane-carrying lids could also be easily removed by hand, thus allowing ergonomic access to the cultures when required (e.g. for media exchanges in unperfused control cultures or addition and aspiration of test compounds). Because magnets provided for a tight seal even when the FEP membrane was between them, the lids could be flipped so that the FEP membrane is further (Figure 5.2E) or closer to the top of the culture. Although the lids were removed for all imaging studies described herein, culture imaging using an upright microscope can be done even in the presence of a lid, through the transparent FEP membrane material.

Tissue culturing and plating

Before each experiment, the devices were prepared by sterilization with 70% ethanol and ultraviolet-C exposure. External tubing and connectors were sterilized using a steam autoclave. The pMEA surfaces were prepared using glow discharge treatment (EMS-100

[9] The use of magnets was conceived by JV, design was optimized by NJK and magnetic lids were fabricated by NJK and JV.

glow discharge unit set at 25 mA for 60 seconds), followed by application of poly-D-lysine (0.1 mg/mL) and laminin (1 mg/mL) coatings to enable sustained adhesion of the tissue to the pMEA surface during the culturing period.

I obtained coronal sections of the brain (4.5 mm diameter, and either 500 or 1000 μm thick) from Sprague-Dawley rat pups (Charles River; ages P1-9) after euthanasia by isoflurane anesthesia and rapid decapitation. Slices were cut to include regions of the neocortex, hippocampus, and the thalamus. For consistency, sections were taken from what is approximately 3 mm posterior to bregma in the adult rat (Paxinos and Watson, 2007). The brain slices contained some of the same regions that were studied in previous chapters (i.e. the hippocampus) but not the entorhinal cortex. This was done because the primary goal of the work described in this chapter was to validate the device (rather than to study the EC) and the coronal section described was easily obtained and identified with the aid of the dissection microscope. Brains were sliced with the aid of a 500 μm spacing brain matrix or a McIlwain tissue chopper for the 1000 μm slices. A 4.5 mm diameter disc was cut out with a disposable skin biopsy punch tool (Acuderm, Inc.). These slices were placed in the culturing chamber on the perfusion MEA with a wide-opening transfer pipette (Figure 5.3A). Slice cultures were perfused with medium for up to 5 days *in vitro* using the perfusion system (Stoppini et al., 1991; Gähwiler et al., 2001) (medium composition: 41% MEM (no L-glutamine) + 31.4% deionized H_2O + 21% HBSS + 21% horse serum + 0.83% D-glucose + 0.83% antibiotic/antimycotic + 0.41% GlutaMAX; buffered with 0.2% $NaHCO_3$ + 4.96 mM tris base + 5.6 mM HEPES and sterile filtered; 294 mOsm/kg).

In addition to brain slices, we validated the tool with dissociated 3-D cell cultures. 3-D cell cultures were 500 or 1000 μm thick dissociated 2:1 neuron-glia co-cultures in 8 mg/mL Matrigel® (Cullen et al., 2007). With the exception of medium composition, we used

the same preparation procedures for 3-D cell cultures and tissue slices. Additional unperfused 3-D cell cultures were maintained in identical culturing chambers mounted on glass slides. For 3-D cell cultures the medium composition was based on Neurobasal® (Neurobasal + 2% B-27 + 1% G-5 + 0.5 mM L-glutamine + 1% antibiotic/antimycotic). The 3-D cell cultures were maintained for 6 days in each of two experimental runs. Cells were plated at a density of 2,500 cells per μL, about 40,000 cells in a 1000 μm thick culture and 20,000 cells in a 500 μm thick culture.

Medium was infused and withdrawn with a syringe pump using polypropylene syringes and stiff FEP tubes 0.5 mm ID, 1.6 mm OD (Figure 5.3B). Typically 2 cultures, each sitting in a preamplifier, were perfused simultaneously using a single pump (Figure 5.3B, Figure 5.4A). For all experiments the flow rate was set at 28 μL/hour. This rate provided for approximately 3.5 culture volume exchanges per hour for 500 μm thick cultures and approximately 1.8 culture volume exchanges per hour for 1000 μm thick cultures. The medium was equilibrated with the incubator environment (35 °C, 21% O_2, 5% CO_2, 65% RH) before being loaded into the syringes. The pump and syringes were placed outside of the incubator and there was sufficient length of tubing within the incubator to warm the media before reaching the culture.

Unperfused control cultures underwent the same preparation procedures as their respective perfused cultures. They were kept in the same incubator, and used the same medium. The medium on the surface of unperfused cultures (200 μL) was manually exchanged by pipette in a sterile manner with medium equilibrated with the incubator environment every 12 hours for the duration of the experiment.

Recording and stimulation

Recordings were made via substrate microelectrodes at the bottom surface of the

cultured tissue through the pMEAs with a modified MCS 60-channel preamplifier designed for upright microscopes (Figure 5.4). Spontaneous and evoked electrical activity were recorded using MEABench software (Wagenaar et al., 2005b). Stimuli designed to effectively elicit activity (Wagenaar et al., 2004) were delivered using the RACS system (Wagenaar and Potter, 2004) and the SALPA stimulus artifact recovery program was used to record as early as a few milliseconds after stimulus delivery (Wagenaar and Potter, 2002). To detect spikes for analyses of spontaneous firing rates, raw signals were filtered offline with a 200-8000 Hz 4^{th}-order Butterworth band-pass filter. Filtering was performed using zero-phase digital infinite impulse response filtering in MATLAB. For each recording channel, spikes were detected using a constant voltage threshold of ± 4.25 times the standard deviation of the raw signal sampled at 25 kHz and digitally filtered. Firing rates for perfused and unperfused cultures were compared over the culturing duration. To examine stimulus-locked responses, SALPA-filtered data was used and any negative-going spikes with a trough below -3 standard deviations were considered. Spikes occurring within 1 ms after a detected spike were discarded. The presence of noise was reduced by removing: unusually small or large waveforms (peak-trough amplitudes below 10 μV or above 150 μV), waveforms that were monophasic, waveforms with unusually sharp peaks (a slope at the peak of more than $7x10^5$ μV/s), and waveforms that occurred with a time delay of less than 1 ms on more than 15% of the channels with recorded spikes. Time-frequency analyses of stimulus-evoked signals were performed using the multitaper method and described with non-parametric statistics (Thomson, 1982; Maris and Oostenveld, 2007; Oostenveld et al., 2011).

To chemically stimulate activity, we applied medium containing 20 mM KCl. These experiments were performed with the cultures in place in the preamplifier by manually exchanging the medium at the surface of the cultures by pipette. The magnetic lids made this

procedure easy to perform. Nevertheless, to reduce the risk of infection, the infusion fluid can be exchanged with any desired fluid with the aid of the zero-displacement connectors. A 'Y' connector can also be inserted to provide an additional port for infusion of desired substances.

Staining, imaging, image processing, and outcome measures

On the final day of each experiment, confocal laser-scanning microscopy (CLSM; microscope model Zeiss LSM 510) was used to perform assays of culture health. Imaging was performed with an EC Plan Neofluor 10x/0.3 N.A. objective lens and 364 nm, 488 nm, and 543 nm excitation for Hoechst, Calcein AM or Fluo-5f AM, and Propidium Iodide fluorescence, respectively. Devices were placed directly on the microscope stage and z-stacks through the culture were obtained with the tissue *in situ* on the device. Images were processed and quantified using custom cell counting code in MATLAB and Zeiss ZEN software. Culture thickness may be indicative of culture health and maintenance of tissue structure (Gähwiler et al., 1997; Rambani et al., 2009). Thickness was estimated by taking the vertical range from the culture substrate (imaged with transmitted light) to the last slice in the stack where stained cells were visible. Staining and imaging of cells was done with separate protocols, described in the following subsections, for slices and 3-D cell cultures.

Because of imaging and staining limitations associated with the use of thick cultures, we could not stain and image through the entire culture thickness. Dyes were loaded on top of the cultures in order to reduce the risk of culture movement or damage to the cultures that might occur through exchanging tubing in order to load dye through the perfusion system. It is possible that dye loading through the perfusion system would have resulted in more uniform staining. Confocal imaging of stained cells was typically limited to about 400 μm thickness in 3-D cell cultures and 200 μm thickness in brain slices, measured from the top

surface of the cultures. The depth limitation of confocal imaging is due to the scattering of visible light, which produces a greater limitation for denser tissues (i.e. slices). However, we were able to image the electrode array (adhered to culture bottom) via transmitted light. The resultant imaging "gaps" between the electrode array and the imaged tissue sections were assumed to comprise live cells. This is because the cultures were adhered to the array, i.e. they did not detach or float during studies or imaging, as confirmed visually. Furthermore, we were able to measure the electrophysiological activity of the cells via the extracellular electrode array, which would not have been possible without close cell proximity to the electrodes such as that achieved by cellular adhesion. Also, cells that did not exhibit detectable fluorescence could often be delineated at the deepest points in the culture with bright field imaging. This suggests that typical passive diffusion-based staining, applied to both unperfused and perfused cultures for procedural consistency, may not be sufficient for staining thick tissue sections due to intra-culture mass transport limitations. In addition, traditional confocal microscopic imaging is severely inhibited beyond about 500 μm of sample thickness (depending on sample optical properties) primarily because of large amount of light scattering by the sample.

Staining and imaging of brain slice cultures

Live and dead cells in slice cultures were identified with the aid of Hoechst 33342 and propidium iodide (PI) dyes. Hoechst, which is membrane permeable, stained nuclei of both live and dead cells and fluoresced blue. In contrast, the cell-impermeant PI stained only nuclei of dead or dying cells that it gained access to via compromised cell membranes and fluoresced red. To quantify the number of live vs. dead cells (Figure 5.4C), we imaged through a sample of the volume using two-channel confocal microscopy; "red" channel for PI fluorescence, and a "blue" channel for Hoechst fluorescence. This provided for two

separate culture images at each z-location: an image showing dead cell nuclei (stained by PI), and an image showing nuclei of live and dead cells (stained by Hoechst). All images in a stack were thresholded by selecting pixels with intensities above the 70th percentile for each image and for each channel (red and blue). To aid in discriminating stained nuclei, the watershed transform was applied to distance transformed binary images. Cells were then identified as 4-connected pixel neighborhoods. Only cells with areas between 5 and 500 μm^2 were considered to reduce erroneous cell identification due to noise or accumulations of dye. I then estimated cell survival as the density of live cells with respect to the original slice volume: the number of live cells (cells with blue but not red staining) per μL. A volume fraction was used in order to put data from slices of 500 μm and 1000 μm thickness on the same relative scale.

Staining and imaging of 3-D dissociated cell cultures

At the conclusion of experiments, we estimated cell survival as an indicator of overall culture health. To do so, 3-D cell cultures were stained with an acetoxymethyl (AM) ester dye (either calcein AM or Fluo-5f AM), which stained live cells (Figure 5.5). Live cell fluorescence was measured using confocal microscopy in a z-stack. Each confocal micrograph in the stack corresponded to a specific z-location (depth) within the culture. The live cell volume in 3-D cell cultures was calculated from respective z-stacks by quantifying fluorescence. First, all images in a z-stack were thresholded and transformed to binary images by selecting pixels with intensities above the 80th percentile for each image. This allowed discrimination of live cells, stained by the fluorescent dye, from the background. Cell survival, was then estimated as the volume fraction, i.e. as the volume stained by the AM ester dye divided by the culture volume in the imaged field of view.

Results

Imaging and electrophysiology data were processed and analyzed to assess the effects of perfusion on culture thickness, cell survival, morphology, and functional activity. Shown in Figure 5.5A is a planar projection of the entire z-stack of a 3-D cell culture of neurons and astrocytes distributed in Matrigel extracellular matrix on a perfused pMEA at 6 DIV. In this figure, the culture was stained with a live cell (AM) dye, and color-coded cell depth indicates the z-distribution of live cell bodies and processes. Clearly, perfusion maintained 3-D cell culture thickness of 500 μm at plating throughout most of the culture even after 6 DIV. Another depth projection is shown in Figure 5.5B. Here, cell bodies and processes can be seen more clearly as a function of z-location within the culture. Figure 5.5C is a 3-D rendering of the confocal z-stack of live cells in the same culture; the culture is thick and live stained cells (green) are densely packed over the pMEA recording region (gray), albeit with a roughly 100 μm gap due to the difficulties in imaging deep into the cultures (see Methods).

The health of tissue slices was assessed using cell survival, defined as the number of live cells in a given volume (number of live cells per μL). Unperfused slices had 1.8x104 ± 8.1x103 live cells per μL and perfused slices had 1.2x104 ± 2.9x103 live cells per μL (mean ± SEM; Figure 5.5D). Considering that we could only effectively stain and image a portion of the slices, estimated cellular densities were consistent with known cellular densities of the rodent brain (Herculano-Houzel et al., 2006), suggesting that a significant fraction of cells survived up to the point of slice imaging. The quantified cell survival per μL of imaged volume was higher in unperfused than in perfused slices. However, this result should be understood with the following caveats (1) unperfused control slices were thinner than perfused slices, (2) owing to diffusive mass transport limits, the thinner (unperfused) slices likely stained more uniformly than thicker (perfused) slices, and (3) the thinner (unperfused)

slices were imaged more completely through the z-thickness without loss of light signal via scattering.

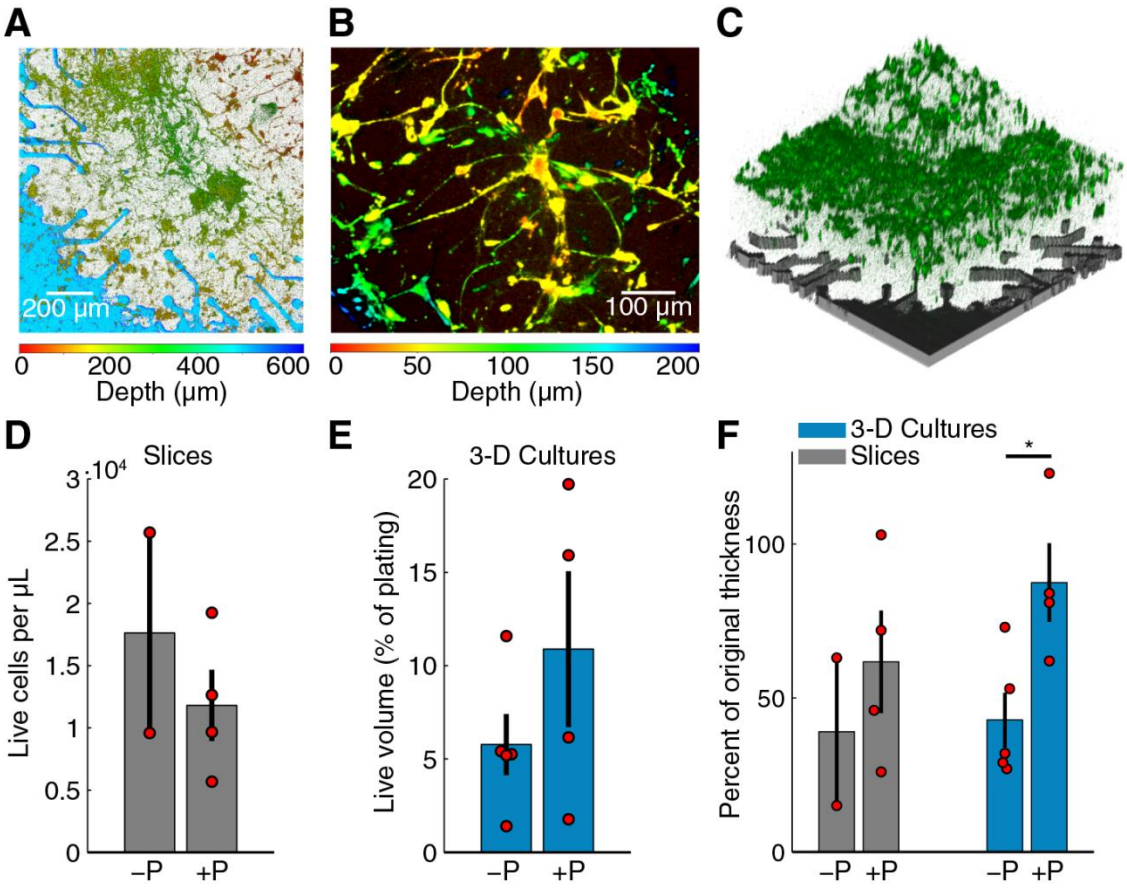

Figure 5.5 | Effects of perfusion on culture health. A. Confocal z-stack through the full 3-D cell culture thickness projected onto a single plane. The color bar below the figure indicates the z-location of live stained cells. The culture was 500 µm thick at plating and cell depth is shown at 6 DIV. Perfusion maintained good cellular viability and 3-D cell culture thickness. **B.** A depth-colored projection of a perfused 3-D cell culture showing cells that have grown in three dimensions. **C.** 3-D rendering of the confocal z-stack in 'A' taken through the full culture thickness. Live cells stained with an AM dye are shown in green. The location of the pMEA with corresponding perforations and recording sites is shown for reference in gray color. **D.** Live cell density in brain slice cultures (mean ± SEM). The gray bars represent the average density for perfused (+P) and unperfused (-P) slices, and red markers represent individual cultures. **E.** Live cell volume fraction for 3-D cell cultures as a percent of the original plating volume. **F.** Final culture thicknesses as a percentage of the thickness at plating for perfused (+P) and unperfused (-P) slices and 3-D cell cultures (mean ± SEM). Data for individual cultures are plotted as red dots. When perfused, both slices and 3-D cell cultures retained more of their thickness at the end of the experiment. The maximum thickness was taken, which could be greater than the intended thickness at plating due to unevenness at the top surface (see Methods).

In 3-D cell cultures, the fraction of the culture volume stained with live cell dye (Figure 5.5E) was used to estimate cell survival as an indicator of culture health. At 6 DIV, perfused 3-D cell cultures had 10.88 ± 4.17 % (mean ± SEM) of the volume (the original volume at plating) stained with live cell dye compared to 5.76 ± 1.64 % for unperfused 3-D cell cultures. The larger volume fraction of live cells in perfused than in unperfused 3-D cell cultures suggests that perfusion may have improved cell survival. Note that the staining of 3-D cell cultures was typically more uniform than the staining of slices, owing to lower cell densities in the former.

In addition to cellular survival, we examined the maintenance of tissue thickness between perfused cultures and their respective unperfused controls. Thickness maintenance was defined as the ratio between the final culture thickness (at the end of experiment) and the culture thickness at plating. I found that the thickness maintenance was greater in perfused cultures compared to their respective unperfused cultures, for both brain slices and 3-D cell cultures (Figure 5.5F). The thickness was on average greater in the perfused slice cultures by 58% compared to unperfused slices (thickness maintenance of 39 ± 24 % in unperfused vs. 61.8 ± 16.7 % in perfused slices; mean ± SEM). Thickness was on average greater by 104% for perfused compared to unperfused 3-D cell cultures (thickness maintenance of 42.8 ± 8.9 % in unperfused vs. 87.5 ± 12.8 % in perfused 3-D cell cultures; mean ± SEM). The thickness maintenance was significantly greater for perfused 3-D cell cultures ($p < 0.05$, Wilcoxon rank-sum test). Considering both slices and 3-D cell cultures together, perfusion corresponded to an average 79% greater culture thickness compared to unperfused controls, while maintaining 75% of the original thickness on average. Indeed, an Analysis of Variance revealed a significant main effect of greater culture thickness with perfusion ($F(1,11) = 5.2$, $p < 0.05$) and no significant effect of culture type (slice or 3-D cell

culture). This maintenance of culture thickness by way of interstitial culture perfusion is consistent with previous findings from interstitial perfusion of slice cultures (Rambani et al., 2009).

I was able to record spontaneous activity from the cultures via the substrate electrodes and to chemically evoke activity using medium with elevated K^+ concentration. Medium containing 20 mM KCl was applied to the surface of a perfused and unperfused 3-D cell culture at 6 DIV. The elevated KCl significantly increased the firing rate of both cultures as shown in Figure 5.6. Significance was assessed with a paired t-test applied after removing channels with mean rates below 0.2 Hz and log-transforming the values to satisfy the assumption of normality (Lilliefors test). Activity could also be elicited from the cultures using electrical stimulation. Figure 5.7 shows the responses recorded on an electrode 283 μm from an electrode stimulated every 1.2 seconds with the waveform shown at the top of panel A. Spike events occurred at about 10, 25, and 45 ms after stimulation. Spike waveforms were discernible from the background activity and likely originated from multiple neurons (Figure 5.7B). Stimulation also appeared to evoke high-frequency activity at sites near the stimulation electrode (Figure 5.7C). Across the entire culture, within 100 ms of stimulation, an increase in signal power around 350 Hz was seen compared to the 100 ms preceding stimulation (Figure 5.7C; $p < 0.025$, cluster-based permutation test) (Maris and Oostenveld, 2007). This is approximately the peak frequency of the stimulus-induced oscillation described in (Hales et al., 2012), suggesting that it may have arisen through a similar mechanism. The oscillation described in Hales et al., 2012 was restricted to the stimulated electrodes, whereas the result described here was observed over a population of recordings sites, suggesting that it may reflect propagating multi-unit activity (MUA). However, there remained a significant increase in high-frequency signal power even after removing the effect

of spikes by replacing ± 3 msec around spike times (detected at ± 3 standard deviations of the raw signal and resolved at 1 kHz) with the mean value during each snippet. This suggests that the high-frequency signal power may have been independent of action potential waveforms and was instead arising from synaptic potentials.

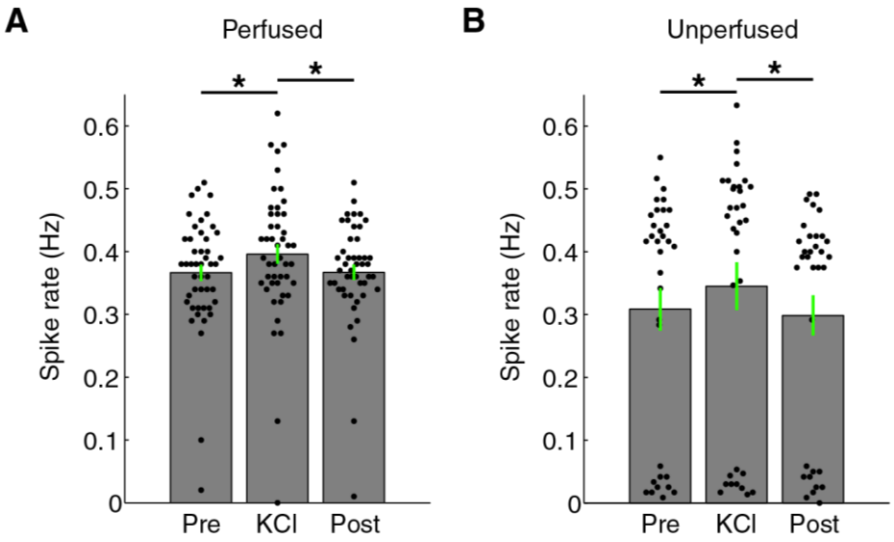

Figure 5.6 | Detectable changes in firing rate with addition of 20 mM KCl. A. Spikes were recorded via substrate electrodes from a perfused 3-D cell culture for a baseline period ('Pre'), with 20 mM KCl medium applied to the surface of the culture, and after a 5X washout of the KCl ('Post'). Each black dot represents the mean spike detection rate on a single electrode. The gray bars are the spike rates averaged over all channels ± SEM. The firing rate of the culture increased upon introduction of KCl solution (*, $p < 0.05$, paired t-test, N = 47 electrodes). **B.** Spike rates from an unperfused 3-D cell culture recorded under identical conditions as in 'A'. There were more channels with lower spiking rates in the unperfused culture, and in particular many more channels without active neurons (dots below 0.1 Hz), but the culture also increased its firing compared to baseline ('Pre') and after washout ('Post') conditions (*, $p < 0.05$, paired t-test, N = 33 electrodes). There was no significant difference in firing rates between the Pre and Post periods in either case. Fluid was added in in the same manner for the KCl and 'Post' periods in both the perfused and unperfused cultures.

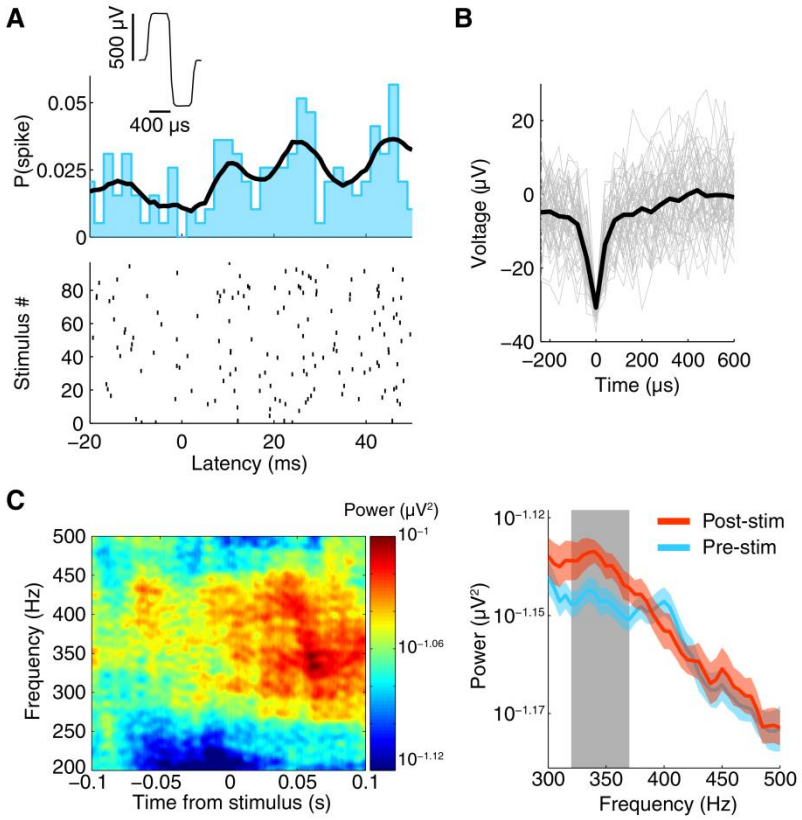

Figure 5.7 | Stimulus-evoked spiking in a perfused 3-D cell culture at 6-DIV. A. Spikes were evoked by electrical stimulation. A stimulus was repeated at 0.83 Hz on a single electrode and induced neuronal spiking at the electrode depicted here. The electrode was 283 µm away from the stimulated electrode. Spikes are shown as black ticks in the raster plot. Each row of the plot represents a different stimulus delivery trial. The spiking probability (probability of a observing a spike at a given time) from 20 ms before to 50 ms after stimulus delivery is shown above the rastergram (2 ms bin width was used, the black curve is the histogram smoothed with a Gaussian, σ = 5 ms). The stimulus waveform was biphasic with 400 µsec per phase at ± 500 mV levels (mean ± SEM is represented at the top). **B.** A random sample of 50 trough-aligned spike waveforms (gray) collected from the electrode in 'A' (average waveform is in black). **C.** In the same experiment, high-frequency activity between approximately 250 and 450 Hz was evoked by the stimuli. Left: At an electrode 200 µm from the stimulus site, signal power around 350 Hz increased in the first 100 ms following stimulation (80 ms sliding window, 7 tapers). This can be seen by warm colors in the time-frequency representation of the signal power (μV^2) on this electrode averaged over all stimulus deliveries. Right: Over all functional recording sites in the culture, there was a significant increase in signal power near 350 Hz in the first 100 ms after stimulus delivery compared to 100 ms before stimulus delivery (100 ms sliding window, 3 tapers; Red: mean ± SEM post-stimulus power; Blue: mean ± SEM pre-stimulus power; Gray: frequency region of significant difference between the two conditions, $p < 0.025$).

Spontaneous spiking activity was recorded at multiple time points throughout the experiments (Figure 5.8). The perfused slices and 3-D cell cultures tended to have higher firing rates than their unperfused counterparts. The firing rates of slices also tended to be

higher at earlier time points in culture, consistent with initially well-developed cells and cellular networks and gradual culture decay and cell death. A 2-way Analysis of Variance was performed on the firing rates averaged over all recordings for each culture (unperfused: 2 slices and 2 3-D cultures; perfused: 7 slices and 4 3-D cultures). Perfusion correlated with a significant increase in firing rates ($F(1,11) = 6.6$, $p < 0.05$), and slices had overall higher recorded firing rates than 3-D cell cultures ($F(1,11) = 8.86$, $p < 0.05$). There was no interaction of perfusion condition and culture type ($F(1,11) = 0.61$, $p = 0.45$), indicating that the greater firing rates observed in slices may have been due to differences between slices and 3-D cultures themselves, such as more extensively developed neurons and cell networks, as opposed to differences in how perfusion affects slices compared to 3-D cultures.

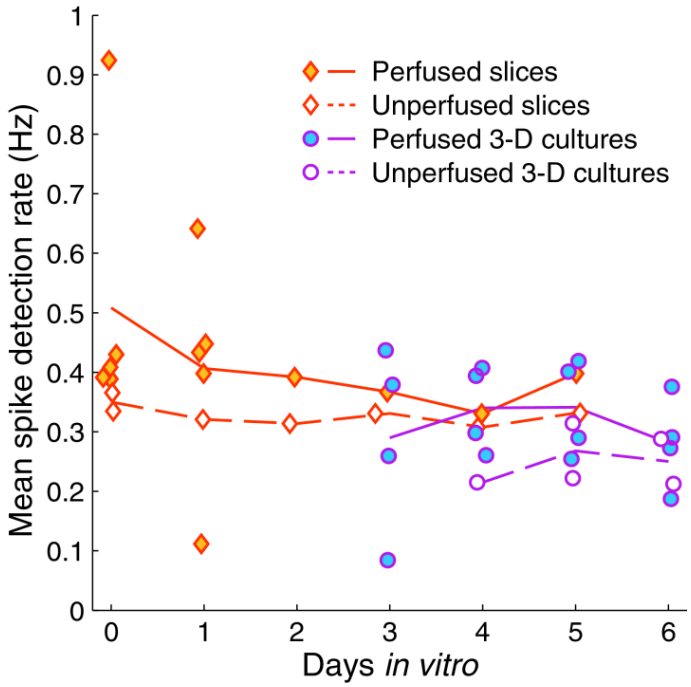

Figure 5.8 | Perfusion increased firing rates of both slices and 3-D cell cultures. The mean spike detection rate (Hz) per electrode tended to be higher for perfused cultures compared to unperfused cultures. Each marker represents the average rate over all electrodes recording from a single culture at a particular day in *vitro*. The lines represent the average rates. Perfused cultures had on average slightly higher spike detection rates at each time point. This effect of perfusion was statistically significant as

analyzed with 2-way ANOVA ($p < 0.05$; 9 slices, 6 3-D cultures, see Results for more details). Slices recorded at early times (in particular, 0 and 1 DIV) also tended to have higher firing rates than 3-D cell cultures for recordings taken between 3-6 DIV). This is consistent with more developed cell networks and higher cell density in slices than in 3-D cell cultures.

Discussion

The perfused pMEA interface provided several enabling qualities for electrophysiology research. It enabled longer sustenance of more consistent and functionally more active, thicker sections of explanted tissue, with concomitant automated culturing, distributed electrical recordings and stimulation, and *in situ* culture imaging.

To assess viability, the cultures were stained by loading the dye on the top of the cultures. As a consequence of the staining methodology, the staining of cultures may not have been equally uniform in thin (unperfused) vs. thick (perfused) cultures due to diffusive mass transport limitations in thin vs. thick cultures. For this reason, it is possible that not all cells had been counted in perfused cultures, due to both confocal imaging-depth limitations and diffusive limitations in intra-culture dye mass transport in thicker (perfused) than in thinner (unperfused) slice cultures. While the sample size was limited, the observed higher than expected mean cell survival in unperfused slices may have been a result of this effect. In contrast with slices, in perfused 3-D cell cultures, cell survival was higher than in respective unperfused 3-D cell culture controls. However, 3-D cell cultures typically provided less resistance to mass transport resulting in more uniform staining and further allowed for greater depth of imaging than did the tissue slices. Considering (1) higher live cell densities in perfused 3-D cell cultures than in unperfused 3-D cell cultures and (2) easier staining and imaging in 3-D cell cultures than in tissue slices of the corresponding thickness, cell survival in perfused slices may have indeed been underestimated relative to unperfused slice controls due to both less uniform staining and more difficult imaging of thicker (perfused) compared

to thinner (unperfused) cultures. Previous work by Rambani et al., 2009 corroborates that perfused slices were both thicker and healthier than unperfused slice controls. In that study, PI and Hoechst dyes were (1) perfused which allowed for more uniform slice staining, and (2) excited using two-photon 800 nm excitation for both dyes which provided a higher signal-to-noise ratio for deeper tissue imaging. Notably, both perfused and unperfused cultures in the PDMS-pMEA interface were expected to perform better than a culture in a dish or a culture in a typical MEA interface without perforations (and without the corresponding access to gas equilibrated medium through the perforations). Unperfused pMEA controls had two interfaces for mass transport, the bottom (through the pMEA perforations) and the top, whereas ordinary MEA setups provide only for gas-equilibrated nutrient-rich medium at the top of the culture when lateral culture surfaces are adhered to the well.

Perfusion correlated with relative maintenance of culture thickness, as compared to culture thinning observed in cultures without perfusion. Culture thinning is thought to be associated with degradative processes set off by cell death occurring in the culture interior that may be limited by diffusive mass transport (Gähwiler et al., 1997). Intra-culture perfusion by way of convectively enhanced mass transport attempts to mimic *in vivo* circulation (Levick, 1987), providing the nutrient availability, catabolite removal, and gas exchange necessary for the maintenance of healthy thick cultures *in vitro*. Perfusion was associated with higher thickness of slice cultures with respect to unperfused control cultures (62% vs. 39% of the thickness at plating, on average). The same was found for 3-D cell culture models of the brain tissue (thickness maintenance of 88% vs. 43% of the plating thickness, on average). While not statistically significant, 3-D cell cultures appeared to maintain thickness better than did the slices. This and previous work suggests that it may be

easier to maintain thickness in 3-D cell cultures because of their lower cell density, lower corresponding metabolic culture demand, and lower resistance to mass transport compared to slices of explanted tissue.

Improved thickness maintenance may be associated with the prevention of necrotic core formation, associated with culture thinning and collapse (Gähwiler et al., 1997). Intra-culture perfusion of gas-equilibrated medium may have prevented the formation of a necrotic core, resulting in thicker cultures. The flow rates were approximately 3.5 culture volume exchanges per hour for 500 μm thick cultures and approximately 1.8 culture volume exchanges per hour for 1000 μm thick cultures. The flow rates were below the 4.5 volume exchanges per hour at which damaging fluid channels formed in brain slices (Rambani et al., 2009). Perfusion with prohibitively high flow rates could contribute to culture peeling from the pMEA surface or cell migration from the surface of the array. Perfusion in the opposite direction, from top to bottom, might reduce the risk of cellular detachment, perhaps improving cell adhesion and the quality of recordings. In experiments not described here, I reversed flow direction; however, medium leaked out at the magnet interface because of the relatively higher resistance of the culture. Therefore, we decided to keep the design simple and use bottom up perfusion. The device design could be improved in other ways, for example, by way of a custom pMEA layout providing a larger array of perforations and a built-in outlet hole. While difficult to form on a thin film, another approach to improving recording and stimulation quality would be to use 3-D electrodes that penetrate the tissue construct (Rajaraman et al., 2011).

The benefit of perfusion on culture health was further supported by an increase in spiking activity of perfused cultures compared to unperfused cultures (Figure 5.8). Thus I postulate that greater perfusion meets metabolic requirements of thicker cultures. Greater

cell survival and sustained neural growth leads to a higher number of active neurons with improved network connectivity near recording sites. In turn, this permits successful electrophysiology recordings to take place over a period of days, as shown here, rather than being confined to experimentation lasting only a few hours.

In addition to spike detection, I also validated the ability of the tool to manipulate the activity of perfused cultures. As depicted in Figure 5.7, I was able to detect significant modulation of high-frequency activity induced with electrical stimulation. This suggests that the device may be amenable to studies of population activity such as multi-unit activity and field potentials. While field potentials have long been studied in isolated brain slices, they are typically recorded using only a small number of manually inserted electrodes. The PDMS-pMEA device enables such population activity studies to be performed on tissue slices or dissociated cultures in three dimensions with more electrode sites and over longer periods of time than traditional methods. Planar electrode arrays, like the pMEA, that are close to neurons but typically not close enough to record single units (i.e. subdural implants) have been useful for studying population activity and for use in brain-machine interfaces (Bosman et al., 2012; Leuthardt et al., 2004). Future experiments with the PDMS-pMEA device could capitalize on this analogy to accelerate development of neural implants that will ultimately make use of planar electrode arrays in humans.

For basic science research, the device may augment existing methods for studying population activity. Specifically, the device may allow resolution of: (a) cell activity in a subset of cells in a population, (b) plurality of subsets of cells in a population, and (c) cell activity in mixed cell populations. This can all be done in a physiologically closer 3-D cell culture tissue model *in vitro*, with a greater fidelity to *in vivo* cell morphology and cell network connectivity. Today, such studies are confined to a small number of electrodes

which typically resolve global cell activity or cell activity in a subset of cells at a few discrete locations in the thick culture. This effectively reduces the whole 3-D tissue model to an average cell result, negating the benefit of using physiologically-closer tissue models to study cell function in health and disease. The advantage of using physiologically-closer tissue models enabled by the PDMS-pMEA sandwich interstitial perfusion system, is that they allow, for the first time, to spatially and temporally resolve electrical recordings from subsets of cells in a population, where each subset may surround a specific recording site and where the number of recording sites is measured by multiples of ten, not one. In turn, this allows investigation of specific patterns of cell activity in a subset of cells, or plurality of subsets of the cell population. Collectively, the PDMS-pMEA sandwich interstitial perfusion system allows for a coupled improvement in tissue models and recording fidelity to *in vivo* conditions.

Brain models *in vitro* are a valuable tool for many questions in neuroscience. Studies *in vitro* generally provide for improved experimental control, higher number of replicates, and sometimes higher resolution in isolation and study of specific functions and responses than experiments done in whole animal models such as rodent or monkey models. Furthermore, microscopic imaging and chemical and electrical manipulation of the tissue is often less difficult to perform *in vitro*. Despite recent advancements of *in vitro* electrical interfacing, the metabolic sustenance of thicker tissue sections and the modeling of multi-layered tissue organization integrated with MEAs for long-term recordings still remains a significant hurdle. Although researchers may resort to thinner tissue sections to model the brain, thicker sections of explanted tissue can better emulate the detailed multi-layered tissue organization of the *in vivo* brain, such as the mouse cortex, which is ~1 mm thick. The maintenance of intact, thick cultures, which are physiologically closer to the *in vivo* brain

than other *in vitro* models has obvious scientific merit and exciting potential applications such as the study of brain-machine interfaces *in vitro* that can more readily be translated to humans. The device described here permits electrical and optical interfacing with tissue that is more *in vivo*-like than what is possible with many common methodologies such as monolayer dissociated cultures and thin (100-400 μm) organotypic slice cultures.

Conclusions

The perfused pMEA tissue culture interface supported convectively enhanced mass transport of nutrients and intra-culture waste removal for long-term tissue maintenance with concurrent distributed electrical recordings and *in situ* culture imaging. Perfusion provided for a supply of fresh medium to the tissue and forced withdrawal of depleted medium, without leakage and evaporative losses. We achieved long-term adhesion of cultures to the perfusion pMEA substrate, thus enabling long-term electrophysiological recording and *in situ* imaging using live cell stains. Thick (≥ 500 μm) brain slice cultures and dissociated 3-D cell cultures in Matrigel were successfully cultured for a minimum of 1 and a maximum of 6 days *in vitro* using the perfused pMEA interface. This validated the utility of perfusion to keep cultures consistent, alive, thicker, and functionally more active over long periods of time –critical qualities for electrophysiology research. The maintenance-free culture feeding regimen by way of interstitial perfusion further allowed automated culturing, even for difficult to culture tissue models such as thick slices of explanted tissue. This reduced the experimental burden associated with manual media additions and aspirations, and the possibility for human error with respect to infection risks, while further enabling controllable on-demand electrical stimulation and microscopic imaging. The design and interfacing also allowed cultures to remain in the incubator throughout the duration of the experiment, enabling necessary control of environmental conditions for more consistent tissue outcomes.

Consistent, long-term maintenance of thick tissue preparations coupled with distributed recording, stimulation, and imaging are a powerful collection of qualities for electrophysiology research. This enables study of a wide range of normal processes, pathological conditions, and drug strategies which are currently hindered by short experiments, low experimental count, and poor reproducibility of results. The simple perfused pMEA interface described here presents an important step towards long-term recordings from *in vitro* cultures with greater physiological relevance and improved recording resolution.

Ethics statement

All experiments were in compliance with the Public Health Service (PHS) Policy on Humane Care and Use of Laboratory Animals, the Eighth Edition of the Guide for the Care and Use of Laboratory Animals, and the Animal Welfare Act. All use of animals and all procedures that used animals were reviewed and approved by the Georgia Institute of Technology Institutional Animal Care and Use Committee (protocol A10042).

Acknowledgments

I thank Michelle LaPlaca, Ph.D. and James Shoemaker for sharing cell culture equipment and brain tissue; Michelle Kuykendal for sharing fluorescent dyes and reagents; and Alex Calhoun, Ming-fai Fong, Jon Newman, and Riley Zeller-Townson for technical advice. Significant contributions by others to this work are listed in footnotes throughout the chapter.

CHAPTER 6

DISCUSSION

In this thesis, I have investigated features of primate EC spatial representation and performed layer-based analyses of EC activity to assess the timing and direction of information flow in relation to memory formation. The resulting gains in knowledge may be useful in designing mechanistic therapies to treat memory disorders. A qualified step toward the development of such therapies was made with the design and validation of a novel perfusion device for long-term electrical interfacing of large neuronal tissue constructs. In this chapter I reexamine the key results of the previous chapters and describe important questions that they raise. Future experiments to address these questions are also proposed.

Bioelectrical dynamics in the entorhinal cortex

The findings described in Chapters 2-4 represent advances in our understanding of the primate entorhinal cortex. While there is significant knowledge of the EC of rodents, this work represents a leap forward in our understanding of the EC of rhesus monkeys and will thus be very useful in understanding the human EC. Beyond the greater genomic similarity between monkeys and humans (compared to rodents and humans), the exploration of neuronal properties using visual experiments that are more relevant to how humans explore the world has been enlightening. The finding of grid cells in the monkey EC that respond to *locations in visual space* challenges the idea that grid cells represent the *location of the animal in physical space*. However, I pose that while the method of sampling the environment with saccadic eye movements is different from locomotion, the brain may utilize the EC for navigation in both cases (Figure 6.1). As information from all sensory systems reaches the

entorhinal cortex, grid cells likely either represent an integration of that sensory input for the main purpose of encoding locations in space or perhaps they more abstractly represent a map of sensory input onto a coordinate system. In the latter case, the implication is that grid cells may extend to other sensory domains. For example, if similar experiments were performed with auditory or olfactory input one may find neurons that encode an analogous coordinate system. It is of course difficult to envision the details of such representations, but some support for this idea has come from the finding of neurons in the rat MEC that represent time and distance in a periodic manner that is not phase-locked to any obvious network oscillation or periodic behavior (Kraus et al., 2012).

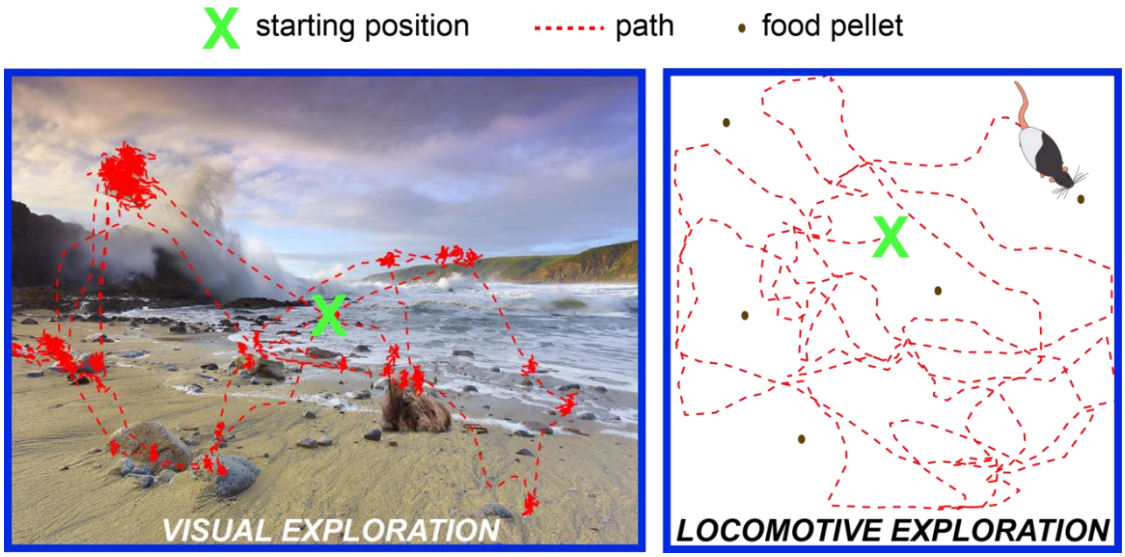

Figure 6.1 | Comparison of visual and locomotive exploration. A representation of gaze location when viewing an image is on the left and a diagram of a rat running around an enclosure is on the right (path adapted from (Hafting et al., 2005), http://www.ntnu.no/cbm/moser/gridcell). Both visual exploration and locomotive exploration can be described with movement trajectories (red dashed lines). Both methods of sampling the environment are used to obtain more detailed information at different locations, e.g. for investigating interesting objects (e.g. the bird, ox, and rocks). The chief difference is that viewing with saccadic eye movements permits skipping over regions of space to focus on particular objects of interest that have been noticed by peripheral vision systems (clusters of red lines correspond to individual fixation periods).

An interesting finding presented in Chapters 2 and 3 was that the firing rate of many of the spatially-responsive cells also reflected memory for images. For grid cells, this

conjunctive encoding followed an anatomical gradient (Figure 6.2). This demonstrates that mnemonic and spatial coding can be segregated, and also that individual neurons can multiplex coding for both mnemonic and spatial information. It will be interesting to explore these anatomical gradients in more detail with future experiments. Future studies can probe responses throughout more anterior locations that were not studied in this thesis and examine connections that might explain how conjunctive responses arise. For example, it would be important to know if neurons that are strictly 'memory' coding cells are more heavily connected with conjunctive grid-memory cells compared to strict 'space' cells (i.e. grid cells, border cells, and saccade direction cells. Furthermore, the conjunctive cells could be important for driving visual navigation according to novelty as proposed in Chapters 2 and 3; it will be necessary to record from more conjunctive cells, perhaps with navigation or visual search experiments designed to explicitly probe the neuronal correlates of different visual exploration strategies.

The results of the laminar analysis of the EC demonstrate that individual cortical layers play distinct functional roles in the formation of memories of visual information. This was apparent by examining layers individually and by looking at how signals in different layers influenced one another in time and frequency. By examining synchronous activity in the gamma-band (30-140 Hz) and above (up to 170 Hz), I found that layers I/II preferentially encode stimulus novelty, potentially answering the question, "Have I seen this before?" On the other hand, gamma-band activity in layers V/VI is not related to stimulus novelty, but is strongly related to the strength of the encoding of novel information. Layer III shares properties with layers I/II and layers V/VI, but with weaker modulation. Interestingly, when taking pairs of LFPs in different layers, it became clear that there are 3 sub-bands of activity that link the same regions and differentiate between task conditions.

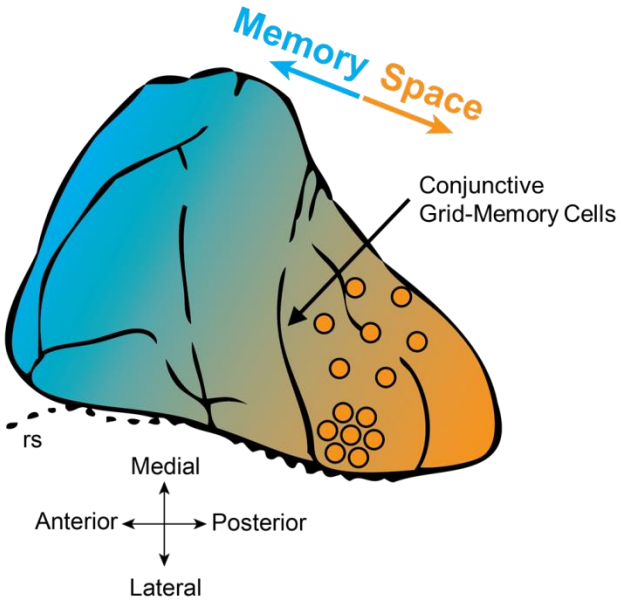

Figure 6.2 | Flat map of the macaque EC showing the memory-space gradient described in Chapter 2. Grid cells are at posterior locations and have increasing spacing with distance from the rhinal sulcus. Recognition memory responses were stronger at more anterior locations and grid cells were more likely to have conjunctive memory responses at more anterior locations within the posterior EC. Regional outlines in this figure were modified, with permission, from Insausti and Amaral, 2008.

The same 3 bands were seen in both monkeys tested with the same task condition relationships. Activity from about 70-140 Hz (high-gamma) was associated with novel stimulus viewing whereas activity from 30-70 Hz (low-gamma) and 140-170 Hz (ripple frequencies) was associated with repeat image viewing. Interestingly, the high- and low-gamma bands were associated with the same conditions proposed in Colgin et al., 2009 (Figure 6.3). Strongly encoded (subsequently well-remembered) images were correlated with increased gamma-band power transfer from deep to superficial layers and decreased power transfer from superficial to deep layers, suggesting that synchronization between hippocampal input and output, directed by the output, is important for memory formation. These effects are summarized in Figure 6.4.

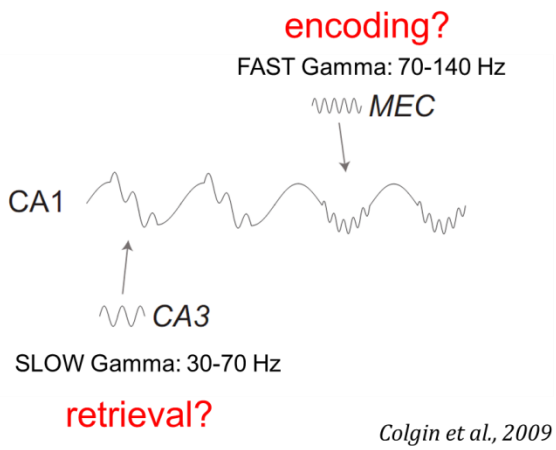

Figure 6.3 | Gamma-band sub-bands and information routing. Colgin et al., 2009 found that slow gamma couples CA1 and CA3 of the HPC and that fast gamma oscillations couple CA1 of the HPC and layer III of the medial entorhinal cortex (MEC). The authors did not perform experiments to test memory, but they proposed that the different frequencies could be associated with different memory processes. This was based on the reputation of the regions that they coupled: superficial layers of the EC received processed sensory information that is communicated to the HPC for memory encoding and that the HPC has been shown to contain cell assemblies that are activated during encoding and recall of episodic memories (Pastalkova et al., 2008). Thus slow gamma coupling within the HPC may be useful for retrieval and fast gamma coupling between superficial EC and the HPC may be useful for encoding. As described in Chapter 4, I found power transfer in slow and fast gamma-band frequencies that was indeed associated with stimulus recognition and the strength of encoding, respectively. Thus the findings of Chapter 4 may support the ideas proposed in Colgin et al., 2009. This figure was modified, with permission, from Colgin et al., 2009.

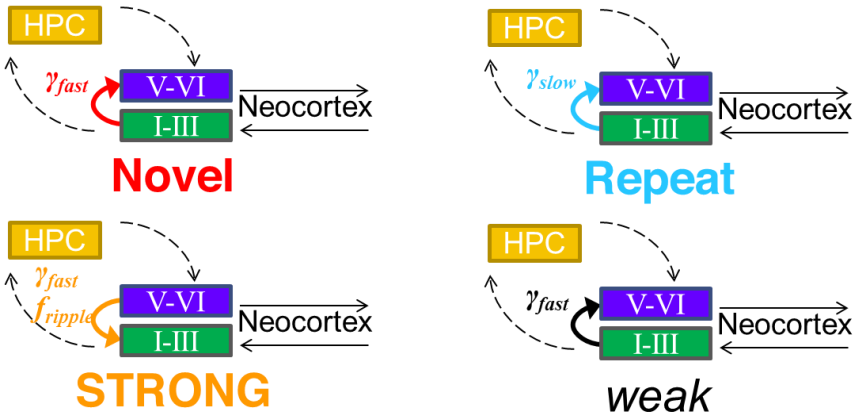

Figure 6.4 | Functional circuitry of recognition memory in the EC. I used microlesions and the CSD to classify layers of the EC. Gamma-band synchronization was modulated by novelty in the superficial layers and strength of encoding in the deep layers. GC analysis revealed distinct frequency bands and directions associated with different memory processes. As summarized here, image encoding may make use of a fast gamma sub-band and recognition may make use of a slow gamma sub-band for communication. Input from deep to superficial layers at fast gamma-band frequencies may inhibit activity in superficial layers allowing for selective transfer of information to the hippocampus and resulting in the encoding of strong memories; note that the fast gamma power transfer from superficial to deep layers may lead to weak encoding when it is excessive.

Taken together, the results integrate findings from many different *in vitro* and *in vivo* studies in a way that supports existing theories of EC function, i.e. that the rhinal cortices may provide a 'wall-of-inhibition' between the hippocampus and neocortex and that different synchronization frequencies are relevant for different mnemonic functions (Canto et al., 2008; de Curtis and Paré, 2004; Colgin et al., 2009; Chrobak and Buzsáki, 1994; Chrobak et al., 2000; Chrobak and Buzsáki, 1998b; Iijima et al., 1996; Koganezawa et al., 2008; van Haeften et al., 2003; Düzel et al., 2010). The results help to describe the range of normal brain activity of the EC in primates, which is known to be pathological in several devastating diseases such as Alzheimer's disease, temporal lobe epilepsy, and schizophrenia (Du et al., 1995; Braak and Braak, 1992; Arnold et al., 1991). In general, the results seem to suggest that neuronal activity should flow in a particular manner consistent with task demands, e.g. deep to superficial gamma-band activity transfer should be high during strong encoding, and when this activity is not present or flows in a different direction, e.g. excessive superficial to deep gamma-band power transfer, then poor performance (weak encoding) results.

Electrical interfacing and perfusion of brain tissue constructs

These population activity measures that were correlated with strength of recognition memory could be used as targets for emulation via neural implants to improve visuospatial learning and memory in disorders affecting the EC that cause impairments in these functions (Suthana et al., 2012; Berger et al., 2011). I propose that *in vitro* devices could be used to develop these neural implants, but that improved devices that can interface with more *in vivo* – like tissue may be necessary.

In Chapter 5, I described the design and development of a novel device for *in vitro* brain tissue perfusion and electrical interfacing. To the best of our knowledge, this device is

the first interstitial perfusion device with an embedded electrical interface. One clear advantage of using this device instead of current devices is that it allows for the maintenance of thicker tissue sections than can be maintained with existing methods (Potter and Demarse, 2001; Gähwiler et al., 1997). I also validated the ability of the tool to manipulate the activity of perfused neuronal cultures; significant modulation of high-frequency activity was induced with electrical stimulation. This finding suggests that the device may be amenable to studies of population activity such as multi-unit activity and field potentials. While field potentials have long been studied in isolated brain slices, they are typically recorded using only a small number of manually inserted electrodes. The interstitial perfusion MEA device enables such population activity studies to be performed on tissue slices or dissociated cultures (Leondopulos et al., 2012; Hales et al., 2012) in three dimensions with thicker tissue, more electrode sites, and over longer periods of time than traditional methods. Thus this device may provide *in vitro* bi-directional electrical interfacing with brain tissue that is more *in vivo* – like than what is currently possible. Being able to work with tissue that is more relevant to the *in vivo* brain should accelerate the neural implant development process.

Future directions for studying spatial representation and translational studies

The results presented in Chapters 2-4 suggest many avenues for future research into the function of the EC. In particular, the results of Chapter 2 pose many novel questions:

(1) To what extent is the visual grid cell representation egocentric or allocentric? To address this question, the same experiments described in Chapter 2 can be performed, but with modulated image size and location and/or allowing for head-movement and body movement. We have already begun to perform experiments with shifted image frames (Figure 6.5). In these experiments the image presentation frame is moved to look for any

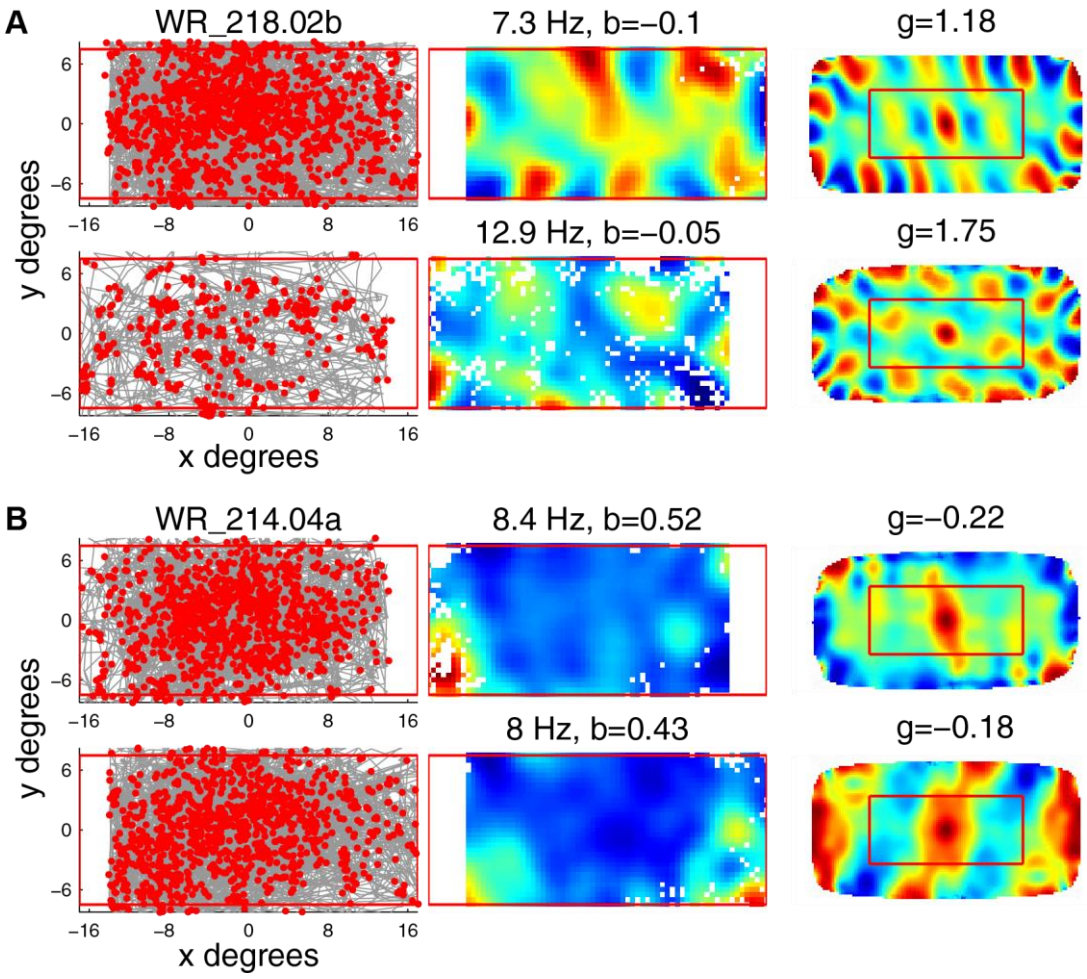

Figure 6.5 | EC neurons recorded in an image frame shifting experiment. Recordings from grid cells and border cells in experiments where the image frame shifts will be able to determine to what extent the grid representation is egocentric vs. allocentric. **A.** In this experiment, a grid cell was recorded from a new monkey (not used for Chapters 2, 3 or 4) while the image frame was shifted 2 degrees to the right (top row) and then 2 degrees to the left (bottom row). The plotting convention is the same as that introduced in Chapter 2, but with the red boxes outlining the maximum range of the stimuli (34 x 15 dva). **B.** Firing rate plots for a putative EC border cell recorded in the same task. True border cells are by definition allocentric and this neuron appears to have an allocentric representation of visual space, preferentially spiking near the image borders even after shifting the image frame. Data were collected by Miriam Meister, PhD and analyzed by NJK.

shift in the grid map. If the firing fields simply shift to match the image frame then the mapping has no egocentric qualities and is strictly allocentric. If there is less than a full shift then the mapping may be considered to have some egocentric qualities. As shown in Figure 6.5, a grid cell and border cell were recorded in a frame-shifting experiment. Both cells exhibit general spatial consistency in terms of spatial scale and autocorrelation. Interestingly,

both cells show an apparent shift along with the image frames, suggesting that they are representing visual space in an allocentric sense. Of particular interest is that these experiments have the potential to verify the existence of true visual border cells in the primate EC. Further data collection and a larger sample size will be required to assess the significance of the allocentric vs. egocentric qualities of neuronal firing in the EC.

(2) Do theories of spatial representation during locomotion (e.g. path integration) extend to visual exploration at a distance? To address this question, the visual paradigm could be redesigned to resemble what we typically think of as being navigation. Because grid cells are hypothesized to aid in navigation in locomoting rodents through path integration signals (McNaughton et al., 2006), it would be interesting to see if this applies to visual exploration as well. It is important to note that no experiment in rodents has explicitly tested this path integration hypothesis with respect to grid cells, though there is some support for this theory based on impaired performance on the Morris water maze task in rodents with lesions of the dorsolateral band of the entorhinal cortex (Steffenach et al., 2005). A visual search task (Chun and Phelps, 1999) could be used while grid cell activity is monitored. Performance on the task could be compared to that observed with disruption of grid cell activity by designer membrane receptor manipulation (Weible et al., 2011) or optogenetic or electrical stimulation (Couey et al., 2013; Diester et al., 2011; Suthana et al., 2012). If the grid cells are important for visual navigation, then performance should be degraded during disruption of grid cell activity.

(3) Does rate-modulation of grid cells by familiarity influence visual exploration? The conjunctive grid-memory cells could be a useful substrate for novelty-driven navigation such as in an optimal foraging mode of behavior. This analysis could be performed using the existing experimental data; however, a larger dataset of conjunctive grid-memory cells would

be useful (I have only recorded from 9 of these cells to date). The analysis could be designed to examine correlations between eye movement features such as distance between fixations and the firing rate of these conjunctive cells. As an example, first consider that visual exploration in free-viewing might be similar to foraging in visual search, whereby return to previously viewed locations is inhibited (Klein and MacInnes, 1999; Shariat Torbaghan et al., 2012; Wolfe and Danielson, 2012; Itti and Koch, 2001). If this is the case, one might expect that decreased firing rates of these conjunctive cells would be correlated with increased saccade distance.

(4) Are theta oscillations necessary for primate grid cells? The role of theta oscillations in grid cell pattern formation is still a hotly debated subject (Barry et al., 2012). Similar to the experiments of (Koenig et al., 2011; Brandon et al., 2011), theta oscillations could be disrupted by infusion of muscimol or lidocaine into the medial septum. If theta oscillations are required for grid cell pattern formation, I would expect to see a disruption in the rate maps during theta oscillation disruption.

(5) How does changing image content alter the spatial representation? The experiments in Chapter 2 were performed with continually changing image content. Rodent experiments with grid cell recordings typically involve a static environment where only the food content changes as the animals forage. Experiments recording from the same cells with blocks of static versus changing images could be used to compare stability in the two conditions.

(6) How does the EC spatial representation translate to views in 3-D? My experiments used a restricted 2-D reference frame that is quite different from what can be observed by the monkeys using their full range of eye, head, and body movements. In a truly natural setting with free movement, would the same grid cells represent locations of the animal in space, visual space, or a combination of both? Would other cells take over the new possible

representations? Ideally, experiments would be performed with freely moving monkeys. Experiments utilizing telemetry are quite difficult to perform; exploration of virtual environments may be a good alternative (Ekstrom et al., 2005). Researchers in the Buffalo lab have already begun to perform such experiments with a monkey foraging for virtual bananas (Figure 6.6).

Figure 6.6 | Navigation of virtual environments. Based on the findings reported in Chapter 2, a branch of research has sprouted in the Buffalo lab aimed at investigating activity patterns in the hippocampus and EC of monkeys exploring virtual 3-D environments with the aid of a joystick (see inset). The preliminary experiment design involves recording from the brains of monkeys while they are moving through the environment searching for virtual bananas to obtain a food reward. These experiments will be able to determine if there are neurons that respond to physical location in a virtual environment. Experiments were performed by Kiril Staikov and Drew Solyst.

Potential for designing treatments of disorders affecting the EC

Ultimately we want to be able to use our knowledge of the EC to help treat disorders that affect it. My results may lend themselves to therapeutic design; however, it's not clear how to translate the findings to devices that would have clinical use in humans, see Figure 6.7. For an example of knowledge of activity properties that could be translated, as described in Chapter 4, I found that excessive gamma-band (30-140 Hz) power in deep layers of the EC was associated with weak encoding during exploration of visual stimuli. It may be possible to reduce such undesirable activity in pathological tissue (and potentially normal

tissue as well) through neural implants. During the intended encoding of memories, implanted electrodes could be used to stimulate the deep layers of the EC in a randomized fashion that may promote asynchrony (Wagenaar et al., 2005a), see Figure 6.8. As depicted in Figure 6.8, stimulation parameters could be optimized through use of the in vitro testbed.

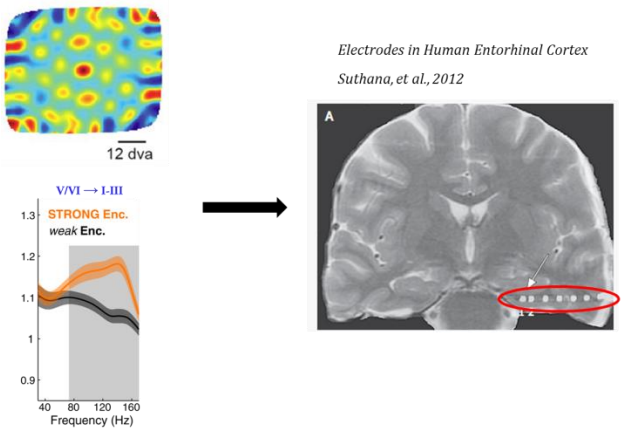

Figure 6.7 | Translation of knowledge of the EC into neural implants. Neural implants that make use of our understanding of bioelectrical properties like grid cells and directed connectivity could be designed to improve brain function. The image on the right was modified, with permission, from Suthana et al., 2012, Copyright Massachusetts Medical Society.

The stimulation could be triggered, e.g. with a user-operated switch or by head-mounted monitoring of eye movements, when the patient desires to encode information that is being sampled with the eyes or other sensory structures. I have built a low-cost stimulation system that was designed to study the ability to enhance memory formation with microstimulation of the EC (Appendix F). The ability to enhance memory performance with a small number of implanted electrodes in the EC holds much promise: a recent study showed significantly improved spatial memory in human epilepsy patients receiving deep-brain stimulation of the entorhinal cortex during a virtual navigation task (Suthana et al., 2012). We have received institutional approval and have begun work on studying the effects of stimulating the EC of monkeys in a manner similar to this study, see Figure 6.9. Experiments will be performed at Emory University in the laboratory of E. A. Buffalo, PhD.

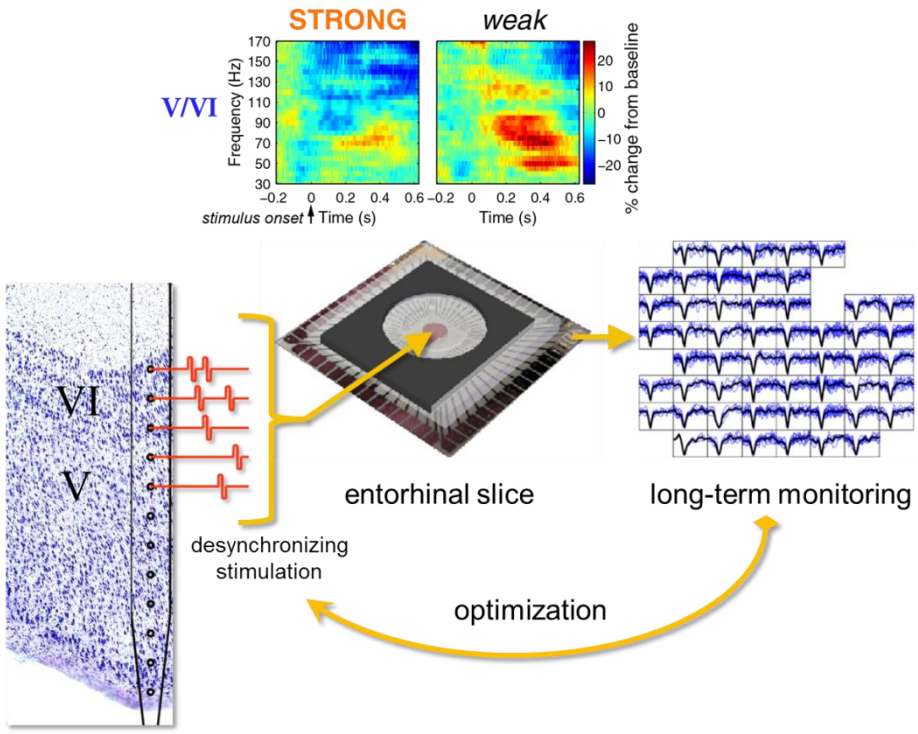

Figure 6.8 | Memory enhancement through promotion of asynchrony in EC deep layers. Considering the finding of increased synchronization in deep layers associated with weak memory formation, it may be useful to supply desynchronizing stimulation to the deep layers. Such a technique could be studied using the *in vitro* testbed, where the experimenter can fine-tune stimulation parameters with experiments lasting many days.

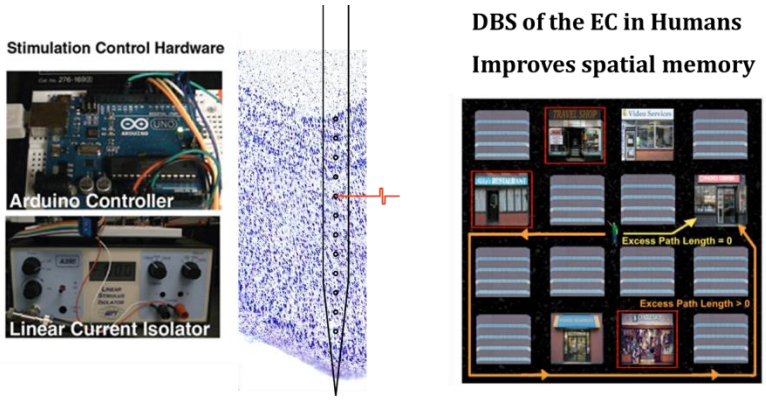

Figure 6.9 | Proposed memory enhancement experiments. Using the virtual environment (Figure 6.6) and a simple stimulation system that I've developed (on the left), we will be replicating a recent study performed in humans (depicted on the right) that found that stimulation of the EC could improve memory for virtual locations (Suthana et al., 2012). The cartoon of the implanted electrode array depicts a stimulus pulse applied to a single electrode site. The image on the right was modified, with permission, from Suthana et al., 2012, Copyright Massachusetts Medical Society.

Final thoughts

In this thesis I described the bioelectrical dynamics of the primate entorhinal cortex during visual stimulus encoding and recognition. The findings described in Chapter 4 contributed new knowledge but did not conflict in any obvious way with what was already known. The findings presented in Chapters 2 and 3, however, were placed largely in the context of rodent spatial representation experiments. This was because of the great potential benefit to creating a theory that reconciles these two paradigms: (1) a rodent moving around an enclosure and (2) a primate exploring visual space. There has been a great deal of effort put toward understanding the rodent spatial representation system and in that paradigm, neurons like grid cells and place cells are often reported to make up large percentages of the neuronal populations –these appear to be robust and consistently observable phenomena (Moser et al., 2008). However, as described in Chapter 1, place cells in the sense of the rodent paradigm have yet to be convincingly described in primates. Instead it appears that in primates, visual space is represented in analogous ways to locations of a rat. This brings forth the question, are the grid cell and place cell firing patterns as described in rodents epiphenomena of 'spatial view' -like cells operating under the same fundamental principles as in primates but with a wide field of view, as proposed by De Araujo et al., 2001?

It is not difficult to imagine that simply with a wide field of view and poor foveal acuity, for a rodent to truly 'fixate' on a region of space in the way that primates fixate on regions of visual space they may need to take advantage of sampling the local environment with olfactory and tactile sensors. This argument has been presented previously, perhaps most cogently in Rolls, Hippocampus 1999. Models of mnemonic processes are currently being built and revised with a strong focus on the neuronal representation of space in the hippocampal formation as described in rodents, often with only tenuous connections to

human physiology. If grid cells and place cells are critical for episodic memory formation in general and have been conserved through evolution such that they exist in humans, then the natural expectation, based on our knowledge of human physiology and ethology, is that these cells should be active during encoding of visual space, and perhaps in a more abstract sense, verbal communication and other experiences with other senses. As a highly visual, verbal, and social species, we spend most of our time collecting information and experiencing the world with the aid of sight and sound. If grid cells and place cells strictly encode the location of an animal in space then these cells would be mostly only relevant for the periods of our time when we walk or run from place to place –time periods that are typically devoid of some of the most memorable interactions and experiences of our lives. Indeed, being able to extrapolate theories of spatial representation in rodents to visual space (and potentially other abstract feature spaces) could have tremendous benefits in understanding learning and memory. If it is learned that the representation of physical space and remote space in the hippocampal formation are truly separate, then reconciling the separate neuronal processes will take some work. The findings presented here collectively represent a small step toward understanding how our brains form memories of complex visual information. Regardless of how this particular story develops, there is a fantastic amount of exciting research to be performed in order to understand how visual information and inputs from other senses are encoded in the brain to form memories.

As our understanding of the brain's involvement in functions such as memory advances, new doors are opened: from targets for treatments of diseases or enhancement of normal function to metacognitive knowledge that may help us work more effectively. Much work lies ahead of us, but this is certainly an exciting time to be involved in neuroscience and neuro-engineering. A novel device was described here that has potential for use as a tool for

studying brain structures like the EC and as an *in vitro* testbed for designing treatments for neurological diseases that the affect the EC and other brain areas. Continued collaboration between neuroscientists and engineers will act synergistically to further basic research and the development of clinical devices and procedures to improve human health.

APPENDIX A

AXIAL ARRAY USAGE AND MAINTENANCE

The axial array (from FHC, Inc. and NeuroNexus; Figure A.1) allowed the recording of signals from individual neurons and the field potentials of local neuronal groups. The array allowed recording from multiple layers of cortex and classification of layers by their current source density (CSD) profile, something that cannot easily be done with traditional microelectrodes because CSD estimates require knowledge of the exact physical distances between recoding sites.

On average, I could obtain about 10-20 recordings per array and record 100 or more units over all of those recordings. There were some initial challenges in getting these successful recordings. Finding a guide tube design that would effectively protect the array and allow penetration through the thick dura mater covering the brain took several iterations, see Figure A.2 for the final guide tube design. I had to find an effective means of sterilizing the array without doing damage to the array. Sterilization with ultraviolet light (germicidal UVC) for about 30 minutes (15 minutes applied to each side) has been effective over dozens of recordings and does not alter electrode impedance, whereas use of a Cetylcide-II® biocide decreased impedance with each use.

The array is manufactured by NeuroNexus Technologies and is composed of 12 iridium electrodes with gold leads imbedded in a polyimide strip that is mounted onto a tungsten microelectrode created by FHC, Inc. Each of the mounted contacts has a 30 micron diameter (707 μm^2 area) spaced at 150 microns starting at 500 microns from the tip of the tungsten electrode (Figure A.1). The 1.65 mm contact span is close to the about 2

mm width of the entorhinal cortex, which allowed recording across most of the layers of the entorhinal cortex in any given recording.

While others have used axial electrode arrays to record electrical activity in the primate brain, research has mostly been limited to recordings involving superficial penetrations such as in visual cortex. By way of the rigid tungsten electrode backbone and 10 cm length, the axial array solves the problem of performing axial recordings in deep brain structures. To reach the EC, the electrode must be moved through the entire dorsal-ventral extent of the brain. This was possible using the axial array and custom fixtures designed specifically for this work (see Appendix B).

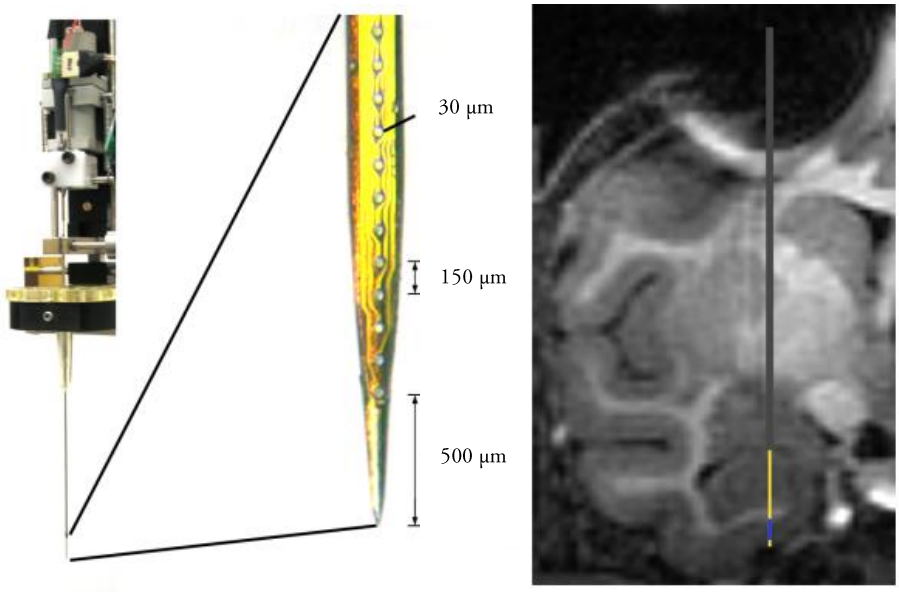

Figure A.1 | Axial array electrode used to record from the entorhinal cortex. The array has twelve 30 micron diameter contacts spaced at 150 microns along the shaft spanning (1.65 mm). The array is made by NeuroNexus and affixed to an expoxylite-insulated tungsten microelectrode. Contacts are addressed through a PCB (top left of the left-most image). On the right the array and guide tube are shown to scale at an approximate recording position. The blue line represents the range of the 12 contacts. (FHC, Inc., www.fh-co.com)

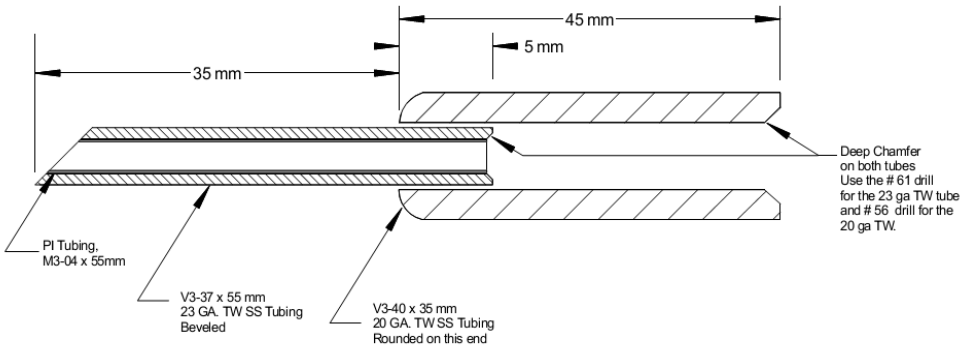

Figure A.2 | Telescoping guide cannula with protective polyimide liner. The 67 mm long portion of the array moves through the 23G tube with the protective polyimide liner. The 35 mm long upper part of the array is wider and can only move through the 20G tube. The tip of the array can thus move up to 22 mm past the bottom of the guide tube. These spatial restrictions posed multiple problems for deep penetrations that were only solved with the use of specialized adapters (see Appendix B).[10]

Important usage and handling considerations

1. Based on the Axial array design, the optimal guide tube dimensions are 45 mm 20 gauge tube with a 23G tube inserted 5 mm into the 20G tube and extending 35 mm.

2. The length of the top-most wide, 20G part of the guide tube should not be changed. It protects from any damage at the vulnerable connection joint with a 5 mm buffer zone.

3. The length of the thin guide tube provides 22 mm array travel past the end of the guide tube. Note that the FHC drive controller provides only 14 mm of travel.

4. The length of the thin guide tube must be long enough so that when the array is held by the drive it can be retracted past the tip at least 2 mm. This provides necessary protection for the array when penetrating the dura mater.

[10] Design created in collaboration with FHC, Inc. Drawing made by FHC, Inc.

APPENDIX B

IN VIVO PROBE POSITIONING ADAPTERS AND FIXTURES

Multiple devices were designed and used to aid in orienting and supporting the guide cannula and electrode array at desired coordinates for performing electrophysiological recordings. The devices provide simple solutions to several non-obvious problems that were encountered throughout the work in this thesis. Here I will describe 3 devices that were critically important and used in nearly all experiments: a guide tube holder, a positioning plate, and an angled penetration adapter. A rendered assembly of these parts is shown in Figure B.1.

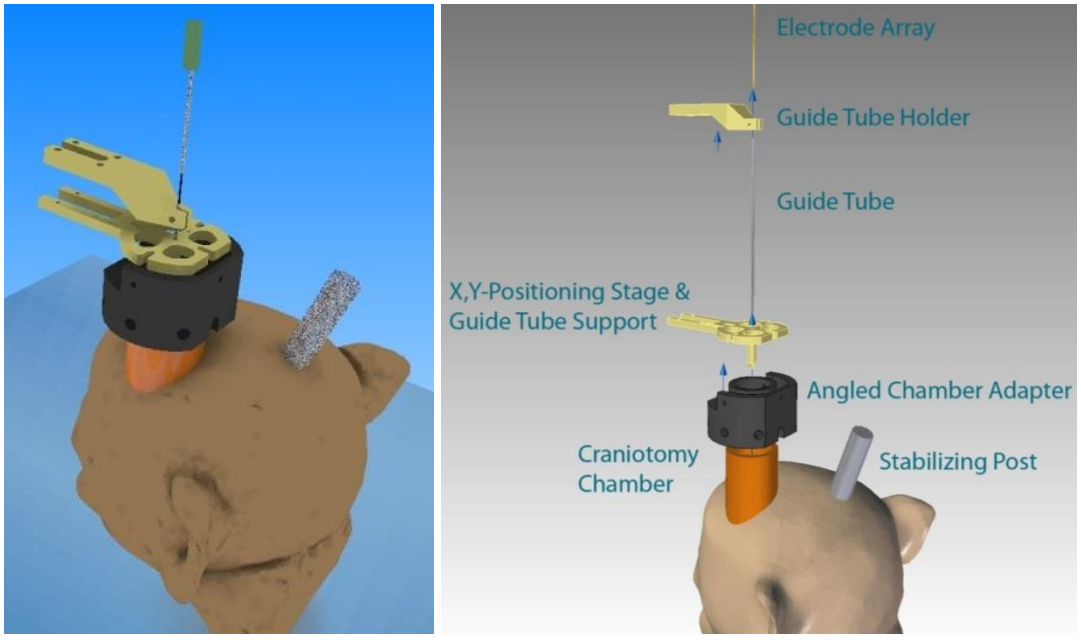

Figure B.1 | 3-D renderings of a monkey's head and positioning devices. The head was reconstructed from a T1-weighted MRI scan. The stabilizing head-post, recording chamber (orange), and probe positioning devices are assembled on the model. An exploded assembly is shown at the right. All parts are fitted onto the microdrive apparatus (not shown) that provides for both coarse and fine linear movement of the array.

A custom guide cannula support structure was created and 3-D printed with UV-cured FullCure720 material on an Objet Eden 250 printer (Figure B.2). The cannula holder was necessary to increase the maximum penetration depth in order to reach the ventral surface of the brain. Like the other parts described here, it would be difficult to accurately machine the small structures in the design and thus 3-D printing was the best fabrication solution.

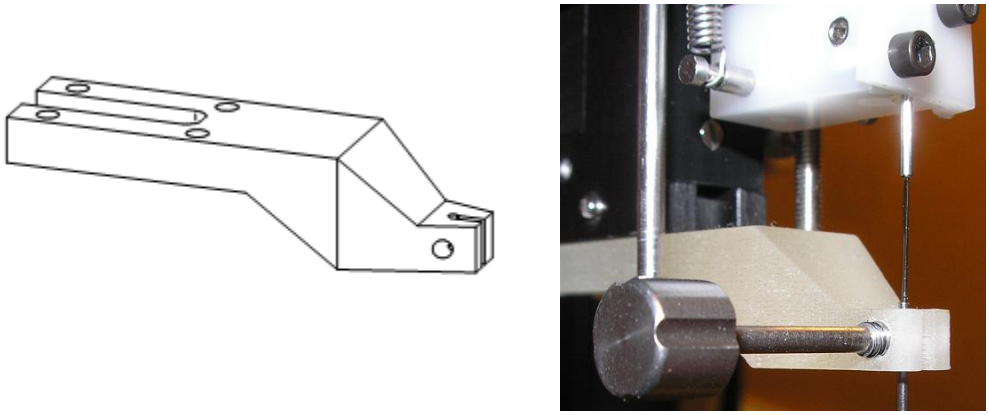

Figure B.2 | Custom step-down guide cannula support structure. The part was 3-D printed with FullCure720. The stainless steel guide tube is held in place by a stainless steel set screw. The step-down structure increases the maximum penetration depth.

A family of parts was designed and created with 3-D printing to permit angled penetrations allowing for insertion of the probe into the EC at locations that would have been impossible to reach with an adapter that simply fits directly on the craniotomy chamber (Figure B.3). Arbitrary angles were easily created after creation of an initial CAD design containing 2 orthogonal angle parameters. The top surface of the adapter rotates about the top center with respect to the chamber. Desired angles can be readily obtained from MRI scans and to create a new adapter, one simply needs to enter the desired angles; a range of about ±10 degrees for each angle is possible.

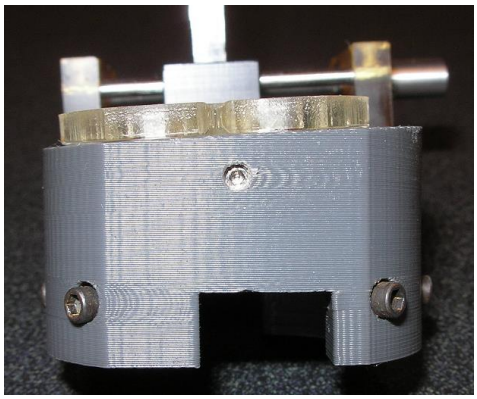

Figure B.3 | Custom angled penetration adapter. It was often necessary to perform angled penetrations to reach target structures. This was done with custom 3-D-printed chamber mounts. A generic design was created in Solid Edge that simply required 2 values to be entered: medial-lateral and anterior-posterior angles to quickly create needed mounts. The photograph shows a mount with a 3-degree angle. The design shown here was printed with ABS thermoplastic on a Stratasys Dimension printer, but much success was also had with FullCure720 on an Object Eden 250 printer.

The most crucial custom part that was used in all experiments was an XY positioning plate with guide tube support. The device comprised a single piece of material that was mounted on a two-degree-of-freedom XY stage, mounted onto the recording chamber. The key features of the device are two general flat regions, one for mounting to the XY stage, and another that is located over the chamber. There is a post extending perpendicular to the major area of the region over the chamber. The post itself consists of 'N' holes of any arbitrary length and diameter so that a cannula having up to 'N' stages can be inserted, where each deeper stage has a smaller diameter accommodated by the next hole. Structurally speaking, the device consists of the guide post, a cantilever beam, supported by the flat region over the chamber, which is itself essentially a cantilever beam supported at the point where it mounts to the XY stage and by any structures with which it overlaps. The devices used were made with FullCure720 on an Objet Eden 250 printer. Markings on the edges of the circular region allow the user to determine penetration placement.

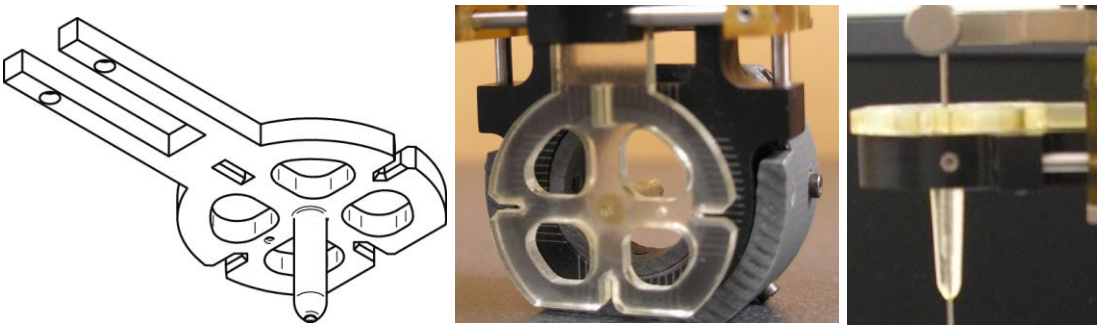

Figure B.4 | Guide tube support structure for deep penetrations and visualization. The device depicted here enabled the guide tube to be supported with the precision of 3-D printing. The EC projects to only about 5 x 14 mm on the positioning plane so the added support and precision was necessary to reach the target locations in the EC, at a distance of about 90 mm from the point where the set screw holds the guide tube in place. The device also allows visualization of penetrations and insertion of other tools such as swabs and optics through the 4 openings. Other advantages of this device over traditional positioning techniques are described in Table B.1.

The guide tube support allowed a cannula to be placed and supported at precise locations in a recording chamber. Other devices exist to perform this basic function, but this device improves upon current methods by adding additional support, allowing for deeper recording, and accommodating cannulae with multiple diameters. There are currently two methods used for guiding cannulae. Method 'A' implements a device inserted into a recording chamber with cylindrical holes called a "grid". The grid allows a cannula to be guided and supported at locations determined by the holes. Method 'B' implements a device with flat regions similar to the device being described, but with no guide post and only a single hole over the chamber region for guiding a cannula of a single diameter. Of note is that neither current device can accommodate N-stage diameter cannulae. As structures inserted into the brain become more complex, there will be an increased need for N-stage cannulae. To my knowledge, this device represents the first solution to that problem. A detailed comparison of the devices in methods A and B with the new device (C) with respect to five critically important criteria is shown in Table B.1 below.

Table B.1 | Comparison of novel positioning device to traditional methods

Method	Number of unique penetrations	Stability	Support for N-stage cannulae	Deepness of recording allowed	Visualization of penetration
A. Grid	Limited	Good	No	Deep	No
B. Plate	Unlimited	Poor	No	Deep, but less stable than with grid or tube	Yes
C. Novel Plate + Tube	Unlimited	Good	Yes	Deep	Yes

APPENDIX C

MICRODRIVE POSITION MONITORING

When recording deep in the brain, it is necessary to have high accuracy and precision in electrode placement. Each penetration is carefully planned with MRI scans and a structural atlas to reach the target structure while minimizing total damage as well as avoiding damage to important structures in the brain (e.g. the optic tract and lateral ventricle). Additionally, an estimate of recording position while lowering the probe with a microdrive is necessary for error correction and verification of reaching the target location. For acute experiments with probe insertion positions that may vary from day to day, penetration planning becomes cumbersome and introduces many opportunities for human error. Neurosurgical procedures in humans make use of sophisticated surgical planning and monitoring software and hardware that is currently prohibitively expensive for most research labs (e.g. the Brainsight system from Rogue Resolutions). Thus a simple piece of software was created to plan and monitor penetrations based on MRI images.

The software, comprising a single MATLAB script, drivemonitor.m, plots the estimated electrode position on the appropriate MRI slice after inputting user-defined calibration parameters (Figure C.1). The calibration needs to be performed only once by entering the appropriate parameters for the location of the reference point: the top center of the craniotomy chamber. The top of the chamber seems to be the best reference point when using mineral oil-based ointment and gadolinium solution to visualize the chamber on T1-weighted MRI (Figure C.1).

The script reads position data from the drive controller via RS-232 serial communication. Based on the entered values, the following will be plotted: the top of the chamber, the location of the dura mater, the end of the guide cannula, and the locations of each of the electrodes in a user-defined electrode array structure.

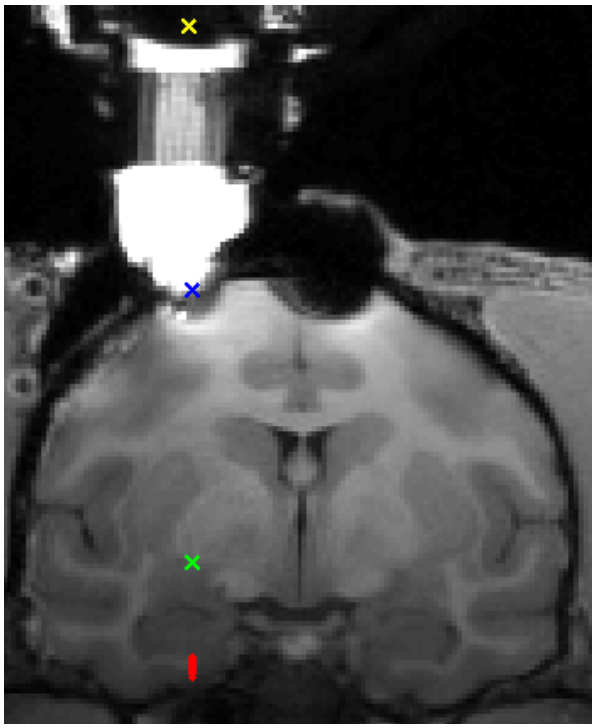

Figure C.1 | Display of estimated electrode position on T1-weighted MRI slice. A live display of the position of all electrode contacts (red) is generated in MATLAB through custom code for serial communication with the microdrive controller (FHC, Inc.). Yellow: top-center of chamber. Blue: location of top of dura mater. Green: tip of the steel guide cannula. Red: all electrode sites. Live zooming and panning is made possible through the MATLAB plotting interface, which is especially useful for zooming in on the 13 electrode sites in red.

APPENDIX D

TTL-DRIVEN FOOD REWARD DELIVERY SYSTEMS

This appendix describes in moderate detail the steps required to modify a peristaltic pump (specifically Cole Parmer model 7553-60) for automated food reward delivery. Three pumps have been successfully made using these steps and have been used to deliver reward to Rhesus Macaque monkeys while they are performing behavioral tasks interfaced with the CORTEX hardware/software system (www.cortex.salk.edu). The pumps are reliable; all pumps have been in use for 1-8 hours a day, over 200 days a year, for about 4 years, with no major problems. Much of the design was borrowed from a pump previously made by Bill Goolsby (bill.goolsby@emory.edu, Emory University School of Medicine). The principles could be used to modify other pumps/systems. Below are images of the outside of the finished product.

Figure D.1 | Exterior view of a finished reward delivery system.

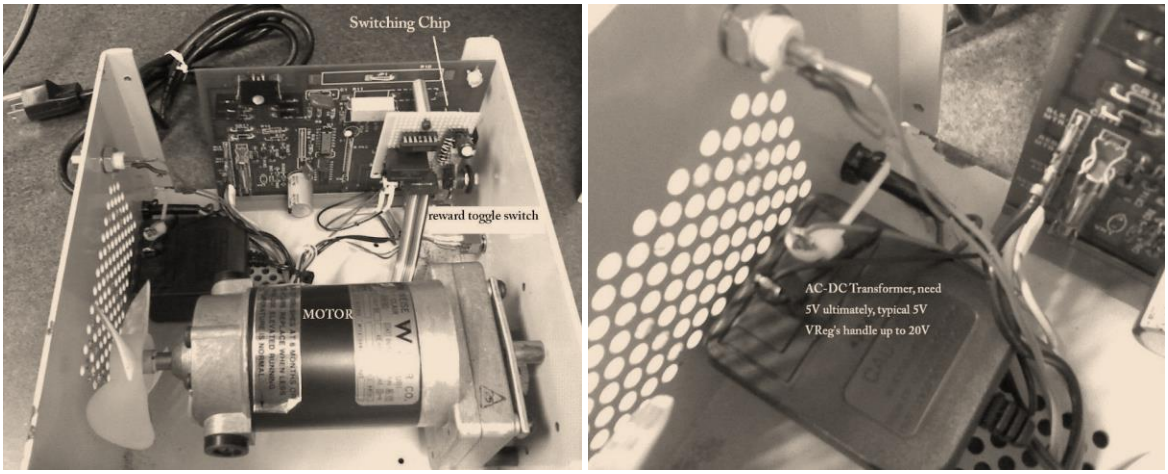

Figure D.2 | Interior view of peristaltic pump modified for reward delivery.

Setup Instructions

1) Acquire a pump (Cole Parmer model 7553-60) and peristaltic pump head.
2) To make the reward buzzer, acquire:
    a. Small hobby box to protect the electronics from fluids
    b. 5 V piezoelectric buzzer. These come in many different varieties, but the best I've found are Sonalert brand buzzers (these possess a pleasant sound and a baffle for manually adjusting volume if necessary).
    c. 10 kOhm potentiometer for the volume control
    d. Female BNC post
    e. A few inches of wire
3) Components to supply power to the switching circuit
    a. AC to DC transformer -you can probably use whatever you have laying around- you will ultimately need 5 V (supplied by the voltage regulator), check the manufacturer spec sheet to make sure you are within the tolerable input range - e.g. the 7805's that I used can handle up to 35 V input.

b. Standard NEMA 1-15 ¼" quick disconnect terminals to make a mechanical connection to the transformer blades (note: soldering to stainless steel is not typically done and the heat needed may damage the transformer).

4) Pump box interface components
    a. On-on toggle switch (for continuous vs. reward delivery)
    b. Female BNC adapter with insulation (the ground for the switching chip will be isolated from the pump/wall ground)
5) Switching chip components
    a. Prototyping board (wire-wrap or point to point soldering)
    b. Spacers to mount the board to the existing board
    c. 10-wire ribbon cable and IDC connectors
    d. LM7805 +5 V voltage regulator
    e. Inverting Schmitt trigger
    f. 5 V SPDT relay
    g. H11A1 optoisolator
    h. 1N4148 diode
    i. 2N3904 transistor
    j. Resistors (0.1, 1, 1.6, 10, 22, 100 kOhm)
    k. Capacitors (10 nF ceramic, 100 nF ceramic, 100 μF electrolytic)

After drilling the holes in the chassis for the BNC input and reward toggle switch, a good place to start is connecting the power supply. Connect the AC-DC transformer to the line power (mechanical connection) and secure to the pump box with mounting tape.

The circuit board needs to be removed and the pump speed circuit needs to be

severed with a razor blade (this is equivalent to setting the pump to a speed of 0). Run 2 wires from this severed connection to the switching board (reward pulses will temporarily switch the relay to the secondary position, which closes the connection and the pump runs at the speed determined by the variable resistor knob). You also need to remove the 100 μF capacitor and replace it with an RC circuit composed of a 22 kOhm resistor and a 10 μF electrolytic capacitor. Finally, you need to plan a mounting position for the switching chip and drill out mounting holes (in Figure D.3 below you can see the 2 nuts used to secure the spacers, upper left). The switching circuit is then made and connected. The schematic for the switching circuit is drawn in Figure D.4.

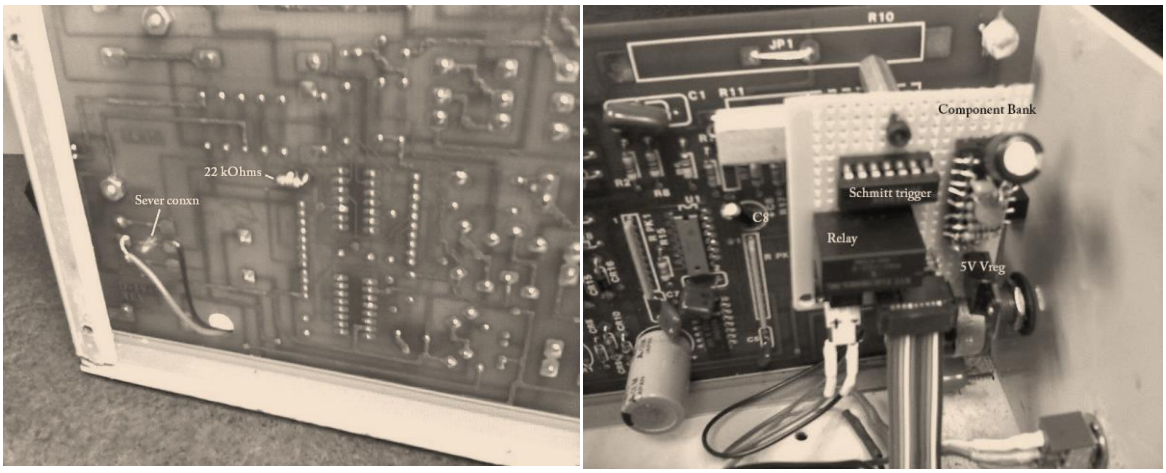

Figure D.3 | Modifications made to the pump control circuit. Left: the circuit is cut for insertion of the switch. Right: custom switching circuit is mounted to the PCB.

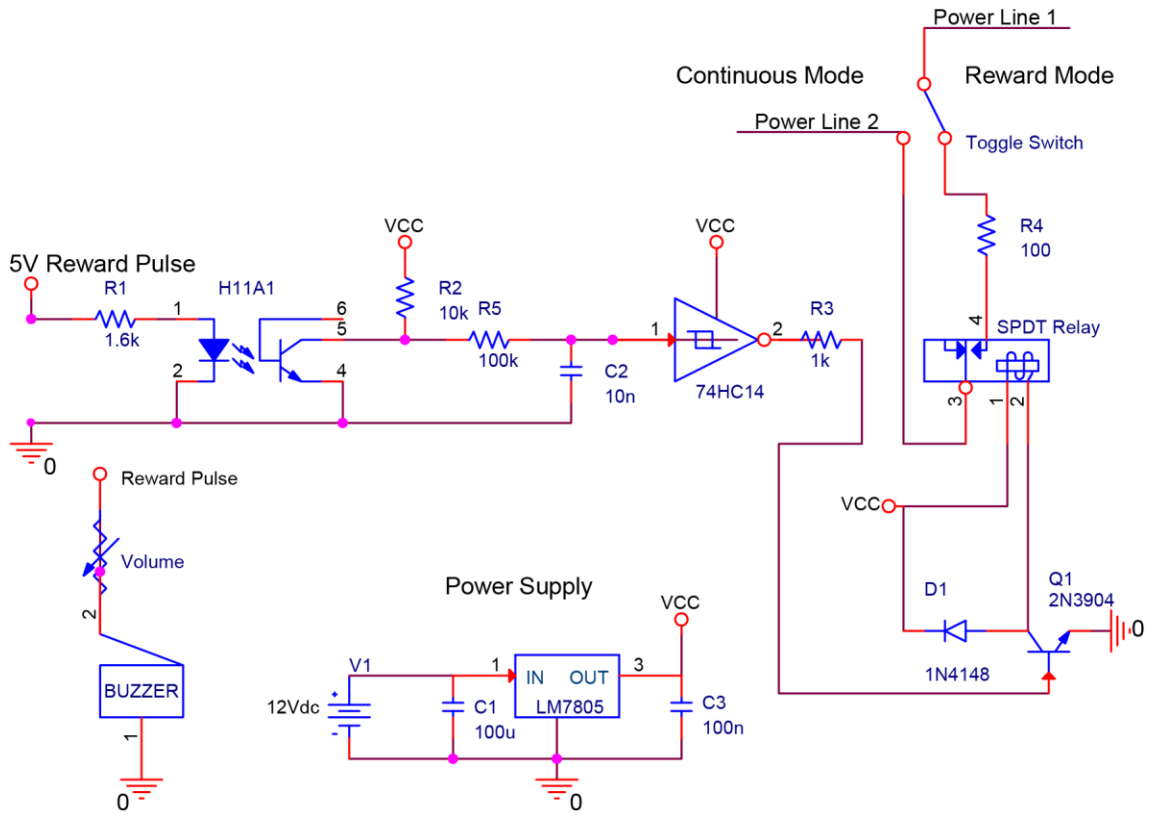

Figure D.4 | Circuit schematic for the switching circuit and reward buzzer.

Troubleshooting

1) The pump most likely will not work at all in reward mode if any part of the switching module is damaged. If it is not working at all, first check that the power supply is putting out the correct voltage and then begin examining individual components of the switching circuit.
2) If the pump is operating but not switching regularly, i.e. 'stuttering', check the following:
    a. Verify that the pump is not overheating. Some components may not function properly if too hot. Be sure to have the pump on a hard surface or raised up off of any soft surfaces.
    b. First check that the switching circuit is operating properly by listening for the

clicking noises in the relay. If it is clicking regularly, the problem is with something to the 'right' of the relay in the schematic, e.g. the connection to the 100 Ohm resistor or weak connections in the ON-ON toggle switch, or the motor itself.

i. Check the connections to the ON-ON switch, this is the last component before reaching the wires (pins 13 and 11 in the schematic) that, when closed, operate the motor.

ii. Check the two wires and other components that were soldered directly onto the green pump circuit board.

c. Check that the reward signal strength –if the wires leading to the back of the pump have poor connections, the input signal may irregularly cross threshold.

Digital Masterflex Pump Modification

A modern digital Masterflex pump (model 7528-10) can be modified to achieve the same result as the Cole Parmer model 7553-60 modification. See Figure D.5.

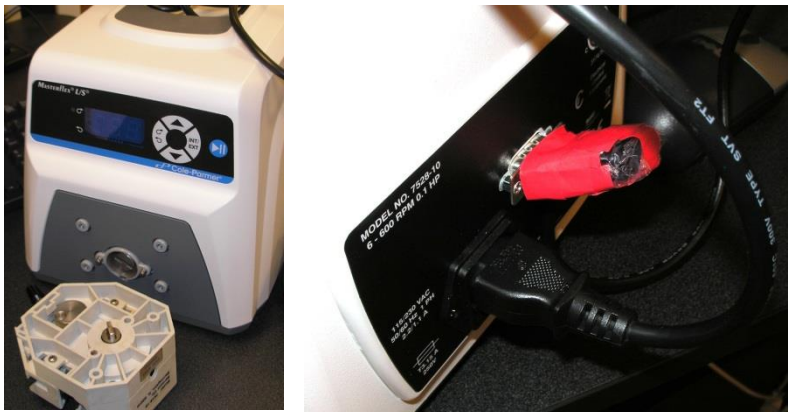

Figure D.5 | A modern digital Masterflex pump (model 7528-10) with reward circuit modification. Left: front of pump showing control panel and removed pump head. Right: Back of pump showing RS-232 + miniature low-signal relay modification (wrapped in protective red tape).

Setup instructions

The setup is very simple and is based on an easily-wired low-signal switch.

1) Obtain a low signal (3 V) double-throw non-latching single coil relay and a DB9 male connector. I used a Panasonic TXS2 DPDT 3 V relay, but only a single pole is needed.
2) Short pins 5 and 9 on the DB9 connector and connect pins 6 and 7 on the DB9 connector to the relay pole and the open end of the switch.
3) Connect the CORTEX reward signal pins to the + and – pins on the relay, using BNC attachments or other connectors for splitting the signal to the reward buzzer.

Operating instructions

1) The On/Off switch is in the back of the pump, though the pump can be left on at all times, provided there is sufficient clearance around the pump for adequate cooling.
2) The 'int/ext' button controls internal mode (like the 'continuous' switch on the older model pump modifications) vs. external mode (like the 'reward' mode on the older pumps). 'int' or 'ext' is displayed on the screen when changing modes.
3) The play/pause (|> / ||) button starts or stops the pump in continuous (int) mode.
4) To go into reward mode, you must press the int/ext button so that the display reads 'ext'.
5) The old pump modification can support 20 ms switching, but this pump operates reliably with 120 msec or longer pulses.
    a. By default, the CORTEX software sets the reward duration to 20 ms, but it can be configured to different times via the Run : Parameters : General menu, or using an external variable in the timing file.
    b. The default reward duration value could be changed in C:\c596\SOURCE\CONFIG\CPARAMS.C, followed by recompiling.

APPENDIX E

DATA REPLAY AND GAZE RE-CALIBRATION IN MATLAB

A MATLAB toolbox was created to visually replay experimental data, complete with a GUI for on-the-fly calibration of eye data and jumping to desired time points of the experiment. To use the program, it is necessary to set the file locations of the neuronal data and visual stimuli. It is also necessary to define the important time markers used in the experiment (this has been done for multiple different experiment designs). Many parameters have been made adjustable, such as playback rate, window size, and selections of specific data for plotting. Plotted on one side of the display are the stimuli and gaze locations (Figure E.1), neuronal activity is synchronously plotted on the other side of the display (Figure E.2). There is visual feedback (colored gaze locations where spikes occurred) and auditory feedback ('popping' sounds created using rectangular functions) for any neuron selectable through the GUI, allowing the researcher to identify spatial firing locations (i.e. for grid cells) as well as behavioral correlates of spiking (i.e. during particular parts of a task).

The recalibration capability is particularly useful for data where the behavior during the calibration part of the task was poor (with satisfactory behavior during the interesting parts of the task). In the following snapshot of the running program, the current gaze location is plotted in blue, and time periods where spikes have occurred were set to persist on the screen in red. The image intentionally obscures previous red locations and saccades are often plotted as variable-length chunks of time are used to check for spikes in order to permit a pseudo real-time display (dependent on the users' hardware).

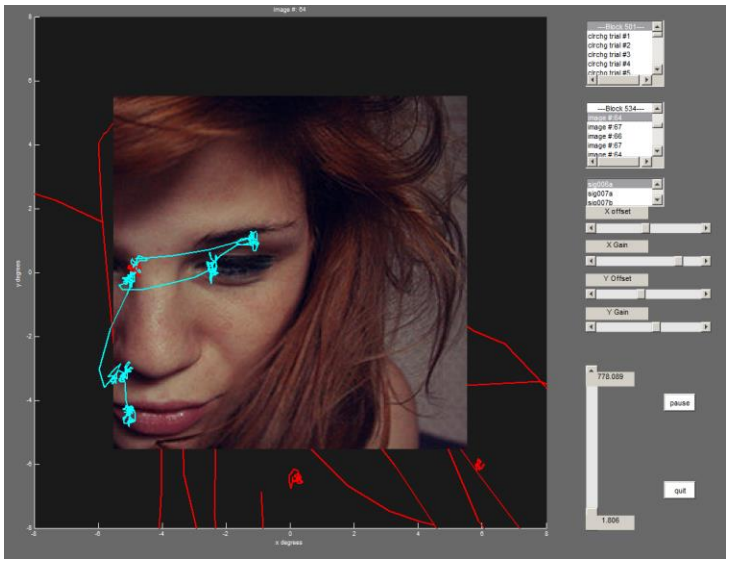

Figure E.1 | Screenshot of the data visualization program: stimuli and gaze locations. The left side of the GUI plots eye data and stimuli in pseudo real-time. A control panel is used for selecting task segments and altering eye tracking calibration. Cyan: current eye trace segment. Red: segments of eye data corresponding to times near the occurrence of spikes on the selected channel. Note that spikes from all previously examined time points (including time periods outside of image viewing trials) are retained on the display, but with the current image displayed on top.

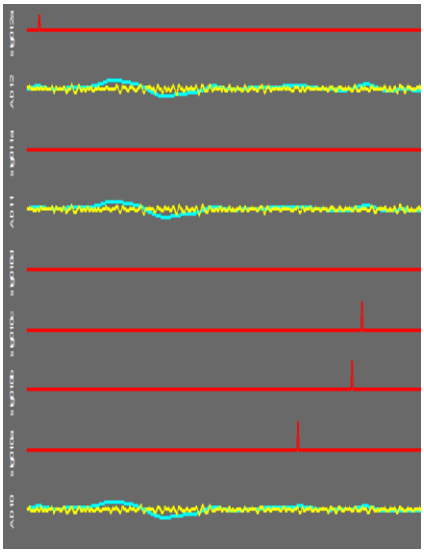

Figure E.2 | Screenshot of the data visualization program: neuronal activity. Neuronal activity is also plotted in false real-time for each channel recorded. Activity from 3 channels is plotted here in this screenshot. Spikes are in red near the filtered LFPs for the same channel. 4 units were recorded on the channel displayed at the bottom. Theta-band filtered LFPs are in blue and gamma-band filtered LFPs are in yellow, for each of 3 channels.

APPENDIX F

LOW-COST STIMULATION CONTROL SYSTEM

A simple and low-cost computer-controlled stimulation system was designed for electrical stimulation studies and for electrical microlesions for histological verification of recording sites. Building upon previous work in the Potter Lab (Rolston et al., 2009; Wagenaar and Potter, 2004; Wagenaar et al., 2004), I developed this custom stimulation system that delivers programmed current-controlled stimuli to electrode sites specified in software, see Figure F.1. The system is capable of: (1) immediate pre-programmed stimulus application (2-3 microseconds delay after reading a single digital input), (2) low-latency electrode switching (1.45 msec at 115200 baud transmission of ASCII string input) and (3) microsecond precision in the stimulus waveform (2-3 microsecond error). The system is low-cost (less than $1k), open source, and utilizes battery power and a USB interface, making it well-isolated, easy to use, and portable.

The system is capable of performing microlesions with the application of constant current. The system was tested in saline to verify that gas is formed at the recording sites selected (Figure F.1). One can expect to see localized damage at the lesion sites on histology (Figure F.1, right; (Townsend et al., 2002)). As described in Chapter 4, roughly 50 micron diameter lesions were made by applying 6 μA for 10 seconds. The lesioning experiments described in Chapter 4 were performed using a commercial system capable of testing impedances with the probe inserted in the brain to verify the connection with the electrode sites (NeuroNexus NIPod). However, the NIPod system is costly (~$6,000) and cannot perform custom stimulation experiments, only lesioning and impedance testing.

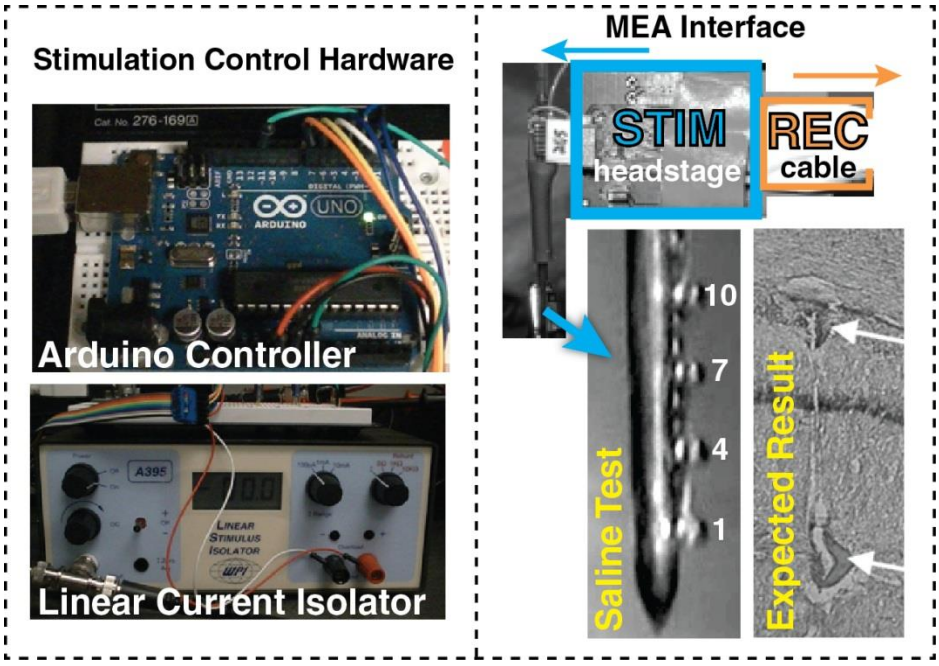

Figure F.1 | Custom stimulator, lesion generator. Based on previous work in the Potter Lab, I developed a custom low-latency stimulation and lesion generation system. **Left:** A battery-powered Arduino Uno microcontroller decodes commands from the USB port or optionally TTL-level inputs and both sends logic signals to a switching headstage to select the appropriate stimulation channel and sends out a PWM signal that, after appropriate analog filtering, gives a voltage command to a linear stimulus isolator (WPI 395; WPI, Inc.). The battery-powered stimulus isolator delivers current that is directed to the appropriate channel via the headstage. **Right:** A switching headstage (Rolston et al., 2009) connected to an axial array (Appendix A) can deliver stimulation to 1 of 16 channels at any given time. Signals can be simultaneously recorded through a cable connected to the headstage. Shown at the bottom is a photograph taken after applying lesioning current channels 1, 4, 7, and 10 in saline. To the right of this is what we expect to see with histology after DC current lesions (Townsend et al., 2002). Here, 2 sites in the rat hippocampus were lesioned (the damage is about 50 microns in diameter).

APPENDIX G

TISSUE CULTURING LID FABRICATION

Teflon lids were fabricated to hold FEP membranes for tissue cultures.

Instructions

1) The lid making process is initiated by obtaining virgin white Teflon tubing with 1.25" OD and 7/8" ID. The tubing shown in Figure G.1 was purchased from McMaster-Carr at about $25/foot.
2) The tubing should be transversely cut into 3/8" segments with a band saw. The band saw in the NeuroLab machine shop, Figure G.1, has a groove on the left that is exactly 5" from the blade center. Use steel parallel bars of known width to line up the 3/8" cut.

Figure G.1 | Teflon tubing is cut into 3/8 inch segments.

3) Power on the CNC mill (Figure G.2) and secure a vise on the mill table and parallelize to the x-axis using the spring-loaded edge finder bit and the mill as opposed to any other method -the cuts must be precise to make a good lid.
4) Load a reasonably sharp right-handed 3/8" endmill.

Figure G.2 | CNC Mill is used to cut lid diameters and O-ring slots.

6) Secure the 3-D printed jig (Figure G.3) in the vise and zero the x and y to the upper right corner. The jig was designed in Solid Edge and printed with an Objet Eden 250. Holes were designed for #6 screws. Here I tapped them to #6-32 threads/inch (tap #36) and used ½ inch screws. For all screws involved you will need a 7/64" Allen driver.

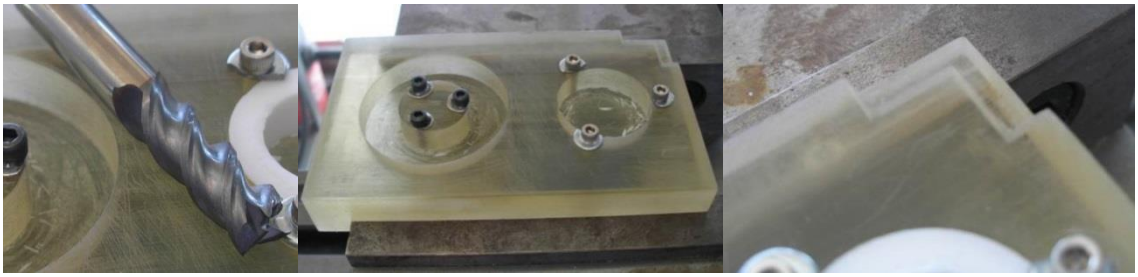

Figure G.3 | 3-D printed jig for diameter cutting. Left: 3/8" endmill used for cutting the Teflon tubing. Middle: The jig is clamped into the vise. **Right:** reference corner used for zeroing.

7) Place one of the cut pieces of tubing in the right side hole. Secure it by tightening the screws about ¼ - ½ turn. The screws were customized so that the lid can be tightened and removed quickly. To create these custom screws, #6 washers were cut down with wire cutters, sanded with a Dremel mounted on a vise, and glued to the screw heads with epoxy. See Figure G.4.

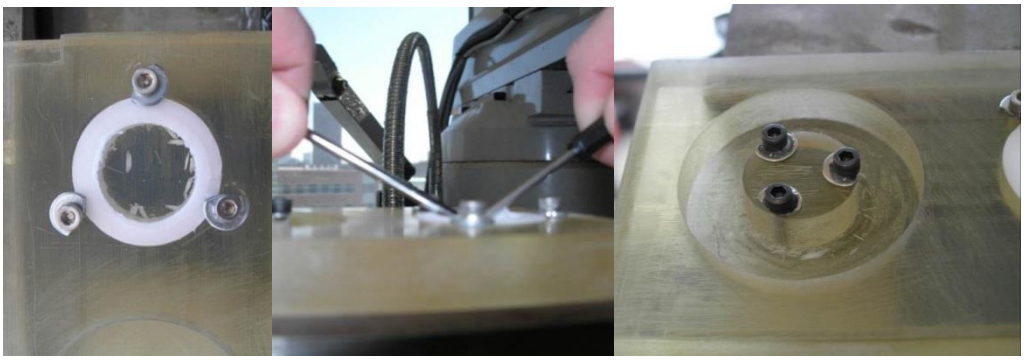

Figure G.4 | 3-D printed jig used to hold lids while cutting down to the correct inner and outer diameters.

8) When the ID is cut, you will turn back the screws, gently pry out the piece, and move it to the next stage on the left to have the OD cut. See Figure G.4.

9) The program to increase the ID to 0.96" and bring the OD to precisely 1.25" is LidIO.CNC, saved to the mill computer's hard drive. See Figure G.4.

10) After bringing many pieces of tubing to the correct diameter, you will load the metal jig (made by Jevin Scrivens) onto the vise, load the 10/16" width 3/8" diameter Woodruff keyseat cutter, and again zero to the upper right corner. See Figure G.5.

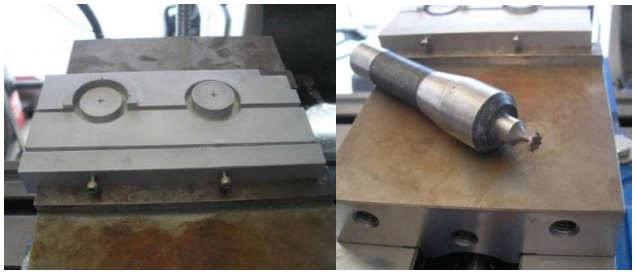

Figure G.5 | Jig used for cutting the O-ring grooves. Left: the jig is placed in the vise. **Right:** keyseat cutter used for cutting the grooves.

11) Run LidFinal.CNC to create the grooves for the outer and inner O-rings. You will need to check the first few by placing an inner O-ring and testing on an MEA as the groove will be lopsided if the origin was not properly calibrated.

REFERENCES

Ainsworth, M., Lee, S., Cunningham, M. O., Roopun, A. K., Traub, R. D., Kopell, N. J., and Whittington, M. A. (2011). Dual gamma rhythm generators control interlaminar synchrony in auditory cortex. *The Journal of neuroscience* 31, 17040–51.

Alonso, A., and García-Austt, E. (1987). Neuronal sources of theta rhythm in the entorhinal cortex of the rat. *Exp. Brain Res.* 67, 493–501.

De Araujo, I. E., Rolls, E. T., and Stringer, S. M. (2001). A view model which accounts for the spatial fields of hippocampal primate spatial view cells and rat place cells. *Hippocampus* 11, 699–706.

Arnold, S. E., Hyman, B. T., Van Hoesen, G. W., and Damasio, A. R. (1991). Some cytoarchitectural abnormalities of the entorhinal cortex in schizophrenia. *Archives of general psychiatry* 48, 625–32.

Bakker, R., Schubert, D., Levels, K., Bezgin, G., Bojak, I., and Kötter, R. (2009). Classification of cortical microcircuits based on micro-electrode-array data from slices of rat barrel cortex. *Neural Netw* 22, 1159–68.

Bakkum, D. J., Chao, Z. C., and Potter, S. M. (2008). Spatio-temporal electrical stimuli shape behavior of an embodied cortical network in a goal-directed learning task. *J. Neural Eng.* 5, 310–23.

Barry, C., Bush, D., O'Keefe, J., and Burgess, N. (2012). Models of grid cells and theta oscillations. *Nature* 488, E1–2; discussion E2–3.

Bartesaghi, R., Gessi, T., and Sperti, L. (1989). Electrophysiological analysis of the hippocampal projections to the entorhinal area. *Neuroscience* 30, 51–62.

Bartolomei, F., Khalil, M., Wendling, F., Sontheimer, A., Régis, J., Ranjeva, J.-P., Guye, M., and Chauvel, P. (2005). Entorhinal cortex involvement in human mesial temporal lobe epilepsy: an electrophysiologic and volumetric study. *Epilepsia* 46, 677–87.

Belluscio, M. A., Mizuseki, K., Schmidt, R., Kempter, R., and Buzsáki, G. (2012). Cross-frequency phase-phase coupling between θ and γ oscillations in the hippocampus. *J. Neurosci.* 32, 423–35.

Berdichevsky, Y., Sabolek, H., Levine, J. B., Staley, K. J., and Yarmush, M. L. (2009). Microfluidics and multielectrode array-compatible organotypic slice culture method. *J. Neurosci. Methods* 178, 59–64.

Berger, T. W., Hampson, R. E., Song, D., Goonawardena, A., Marmarelis, V. Z., and Deadwyler, S. a (2011). A cortical neural prosthesis for restoring and enhancing memory. *J. Neural Eng.* 8, 046017.

Blake, A. J., Rodgers, F. C., Bassuener, A., Hippensteel, J. A., Pearce, T. M., Pearce, T. R., Zarnowska, E. D., Pearce, R. a, and Williams, J. C. (2010). A microfluidic brain slice perfusion chamber for multisite recording using penetrating electrodes. *J. Neurosci. Methods* 189, 5–13.

Bliss, T. V. P., and Lomo, T. (1973). Long-lasting potentiation of synaptic transmission in the dentate area of the anaesthetized rabbit following stimulation of the perforant path. *J. Physiol.* 232, 331–356.

Boon, P., Vonck, K., De Herdt, V., Van Dycke, A., Goethals, M., Goossens, L., Van Zandijcke, M., De Smedt, T., Dewaele, I., Achten, R., et al. (2007). Deep Brain Stimulation in Patients with Refractory Temporal Lobe Epilepsy. *Epilepsia* 48, 1551–1560.

Boppart, S. A., Wheeler, B. C., and Wallace, C. S. (1992). A flexible perforated microelectrode array for extended neural recordings. *IEEE Trans Biomed Eng* 39, 37–42.

Bosman, C. A., Schoffelen, J.-M., Brunet, N., Oostenveld, R., Bastos, A. M., Womelsdorf, T., Rubehn, B., Stieglitz, T., De Weerd, P., and Fries, P. (2012). Attentional Stimulus Selection through Selective Synchronization between Monkey Visual Areas. *Neuron* 75, 875–88.

Braak, H., and Braak, E. (1996). Evolution of the neuropathology of Alzheimer's disease. *Acta Neurol. Scand.* 94, 3–12.

Braak, H., and Braak, E. (1992). The human entorhinal cortex: normal morphology and lamina-specific pathology in various diseases. *Neurosci. Res.* 15, 6–31.

Bragin, A., Wilson, C. L., Staba, R. J., Reddick, M., Fried, I., and Engel, J. (2002). Interictal high-frequency oscillations (80-500 Hz) in the human epileptic brain: entorhinal cortex. *Annals of neurology* 52, 407–15.

Brandon, M. P., Bogaard, A. R., Libby, C. P., Connerney, M. A., Gupta, K., and Hasselmo, M. E. (2011). Reduction of theta rhythm dissociates grid cell spatial periodicity from directional tuning. *Science* 332, 595–9.

Broersen, P. M. T. (2000). Finite sample criteria for autoregressive order selection. *IEEE Transactions on Signal Processing* 48, 3550–3558.

Brovelli, A., Ding, M., Ledberg, A., Chen, Y., Nakamura, R., and Bressler, S. L. (2004). Beta oscillations in a large-scale sensorimotor cortical network: directional influences revealed by Granger causality. *Proc. Natl. Acad. Sci. U. S. A.* 101, 9849–54.

Brozinsky, C. J., Yonelinas, A. P., Kroll, N. E. A., and Ranganath, C. (2005). Lag-sensitive repetition suppression effects in the anterior parahippocampal gyrus. *Hippocampus* 15, 557–61.

Brun, V. H., Solstad, T., Kjelstrup, K. B., Fyhn, M., Witter, M. P., Moser, E. I., and Moser, M.-B. (2008). Progressive increase in grid scale from dorsal to ventral medial entorhinal cortex. *Hippocampus* 18, 1200–12.

Buckmaster, C. A., Eichenbaum, H., Amaral, D. G., Suzuki, W. A., and Rapp, P. R. (2004). Entorhinal cortex lesions disrupt the relational organization of memory in monkeys. *The Journal of neuroscience* 24, 9811–25.

Buffalo, E. A. (1999). Dissociation Between the Effects of Damage to Perirhinal Cortex and Area TE. *Learn. Memory* 6, 572–599.

Buffalo, E. A. (2000). Perception and Recognition Memory in Monkeys Following Lesions of Area TE and Perirhinal Cortex. *Learn. Memory* 7, 375–382.

Buffalo, E. A., Fries, P., Landman, R., Buschman, T. J., and Desimone, R. (2011). Laminar differences in gamma and alpha coherence in the ventral stream. *Proc. Natl. Acad. Sci. U. S. A.*

Burgess, N., Barry, C., Keefe, J. O., and Al, B. E. T. (2007). An Oscillatory Interference Model of Grid Cell Firing. *Hippocampus* 812, 801–812.

Burgess, N., and O'Keefe, J. (2011). Models of place and grid cell firing and theta rhythmicity. *Curr. Opin. Neurobiol.* 21, 734–44.

Buzsáki, G. (1989). Two-stage model of memory trace formation: A role for "noisy" brain states. *Neuroscience* 31, 551–570.

Buzsáki, G., and Wang, X.-J. (2012). Mechanisms of gamma oscillations. *Ann. Rev. Neurosci.* 35, 203–25.

Canto, C. B., Wouterlood, F. G., and Witter, M. P. (2008). What does the anatomical organization of the entorhinal cortex tell us? *Neural Plast.* 2008, 381243.

Chan, A. M., Baker, J. M., Eskandar, E., Schomer, D., Ulbert, I., Marinkovic, K., Cash, S. S., and Halgren, E. (2011). First-pass selectivity for semantic categories in human anteroventral temporal lobe. *J. Neurosci.* 31, 18119–29.

Chelazzi, L., Ghirardi, M., Rossi, F., Strata, P., and Tempia, F. (1990). Spontaneous Saccades and Gaze-Holding Ability in the Pigmented Rat. II. Effects of Localized Cerebellar Lesions. *The European journal of neuroscience* 2, 1085–1094.

Chelazzi, L., Rossi, F., Tempia, F., Ghirardi, M., and Strata, P. (1989). Saccadic Eye Movements and Gaze Holding in the Head-Restrained Pigmented Rat. *The European journal of neuroscience* 1, 639–646.

Choi, Y., McClain, M. A., LaPlaca, M. C., Frazier, A. B., and Allen, M. G. (2007). Three dimensional MEMS microfluidic perfusion system for thick brain slice cultures. *Biomed Microdevices* 9, 7–13.

Chrobak, J. J., and Buzsáki, G. (1998a). Gamma oscillations in the entorhinal cortex of the freely behaving rat. *J. Neurosci.* 18, 388–98.

Chrobak, J. J., and Buzsáki, G. (1996). High-frequency oscillations in the output networks of the hippocampal-entorhinal axis of the freely behaving rat. *J. Neurosci.* 16, 3056–66.

Chrobak, J. J., and Buzsáki, G. (1998b). Operational dynamics in the hippocampal-entorhinal axis. *Neuroscience and biobehavioral reviews* 22, 303–10.

Chrobak, J. J., and Buzsáki, G. (1994). Selective activation of deep layer (V-VI) retrohippocampal cortical neurons during hippocampal sharp waves in the behaving rat. *J. Neurosci.* 14, 6160–70.

Chrobak, J. J., Lörincz, A, and Buzsáki, G. (2000). Physiological patterns in the hippocampo-entorhinal cortex system. *Hippocampus* 10, 457–65.

Chun, M. M., and Phelps, E. A. (1999). Memory deficits for implicit contextual information in amnesic subjects with hippocampal damage. *Nat. Neurosci.* 2, 844–7.

Colgin, L. L., Denninger, T., Fyhn, M., Hafting, T., Bonnevie, T., Jensen, O., Moser, M.-B., and Moser, E. I. (2009). Frequency of gamma oscillations routes flow of information in the hippocampus. *Nature* 462, 353–7.

Corkin, S. (2002). What's new with the amnesic patient H.M.? *Nature Rev. Neurosci.* 3, 153–60.

Couey, J. J., Witoelar, A., Zhang, S.-J., Zheng, K., Ye, J., Dunn, B., Czajkowski, R., Moser, M.-B., Moser, E. I., Roudi, Y., et al. (2013). Recurrent inhibitory circuitry as a mechanism for grid formation. *Nat. Neurosci.* 16, 318–24.

Cullen, D. K., Vukasinovic, J., Glezer, A., and Laplaca, M. C. (2007). Microfluidic engineered high cell density three-dimensional neural cultures. *J. Neural Eng.* 4, 159–72.

Cullen, D. K., Wolf, J. A., Vernekar, V. N., Vukasinovic, J., and LaPlaca, M. C. (2011). Neural tissue engineering and biohybridized microsystems for neurobiological investigation in vitro (Part 1). *Crit Rev Biomed Eng* 39, 201–40.

De Curtis, M., and Paré, D. (2004). The rhinal cortices: a wall of inhibition between the neocortex and the hippocampus. *Progress in neurobiology* 74, 101–10.

Dale, J., Kandil, F., Nishida, S., Ekstrom, A. D., Kahana, M. J., Caplan, J. B., Fields, T. A., Isham, E. A., Newman, E. L., and Fried, I. (2003). Cellular networks underlying human spatial navigation. *Nature* 425, 184–8.

Davidson, T. J., Kloosterman, F., and Wilson, M. A. (2009). Hippocampal replay of extended experience. *Neuron* 63, 497–507.

Deshmukh, S. S., and Knierim, J. J. (2011). Representation of non-spatial and spatial information in the lateral entorhinal cortex. *Frontiers in behavioral neuroscience* 5, 69.

Diester, I., Kaufman, M. T., Mogri, M., Pashaie, R., Goo, W., Yizhar, O., Ramakrishnan, C., Deisseroth, K., and Shenoy, K. V (2011). An optogenetic toolbox designed for primates. *Nat. Neurosci.* 14, 387–97.

Ding, M., Bressler, S. L., Yang, W., and Liang, H. (2000). Short-window spectral analysis of cortical event-related potentials by adaptive multivariate autoregressive modeling: data preprocessing, model validation, and variability assessment. *Biol. Cybern.* 83, 35–45.

Du, F., Eid, T., Lothman, E., Kohler, C., and Schwarcz, R. (1995). Preferential neuronal loss in layer III of the medial entorhinal cortex in rat models of temporal lobe epilepsy. *J. Neurosci.* 15, 6301–6313.

Düzel, E., Penny, W. D., and Burgess, N. (2010). Brain oscillations and memory. *Current opinion in neurobiology* 20, 143–9.

Egert, U., Okujeni, S., Nisch, W., Boven, K., Rudorf, R., Gottschlich, N., and Stett, A. (2006). Optimized Oxygen Availability and Signal-to-Noise Ratio in Brain Slice Recordings with Perforated Microelectrode Arrays. in MEA Meeting Proceedings, 174–177.

Eichenbaum, H., Sauvage, M., Fortin, N., Komorowski, R., and Lipton, P. (2012). Towards a functional organization of episodic memory in the medial temporal lobe. *Neuroscience and biobehavioral reviews* 36, 1597–608.

Eichenbaum, H., Yonelinas, A. P., and Ranganath, C. (2007). The medial temporal lobe and recognition memory. *Ann. Rev. Neurosci.* 30, 123–52.

Ekstrom, A. D., Caplan, J. B., Ho, E., Shattuck, K., Fried, I., and Kahana, M. J. (2005). Human hippocampal theta activity during virtual navigation. *Hippocampus* 15, 881–9.

Empson, R. M., and Heinemann, U. (1995). The perforant path projection to hippocampal area CA1 in the rat hippocampal-entorhinal cortex combined slice. *J. Physiol.* 484, 707–720.

Fell, J., Klaver, P., Lehnertz, K., Grunwald, T., Schaller, C., Elger, C. E., and Fernández, G. (2001). Human memory formation is accompanied by rhinal – hippocampal coupling and decoupling. 1–6.

Felleman, D. J., and Van Essen, D. C. (1991). Distributed hierarchical processing in the primate cerebral cortex. *Cereb. Cortex* 1, 1–47.

Ferrea, E., Maccione, A., Medrihan, L., Nieus, T., Ghezzi, D., Baldelli, P., Benfenati, F., and Berdondini, L. (2012). Large-scale, high-resolution electrophysiological imaging of field potentials in brain slices with microelectronic multielectrode arrays. *Front. Neural Circuits* 6.

Finch, D. M., Wong, E. E., Derian, E. L., and Babb, T. L. (1986). Neurophysiology of limbic system pathways in the rat: Projections from the subicular complex and hippocampus to the entorhinal cortex. *Brain Res.* 397, 205–213.

Finch, D., Tan, A., and Isokawa-Akesson, M. (1988). Feedforward inhibition of the rat entorhinal cortex and subicular complex. *J. Neurosci.* 8, 2213–2226.

Fisher, N. I. (1995). *Statistical Analysis of Circular Data.* Cambridge University Press.

Franke, F., Jäckel, D., Dragas, J., Müller, J., Radivojevic, M., Bakkum, D., and Hierlemann, A. (2012). High-density microelectrode array recordings and real-time spike sorting for closed-loop experiments: an emerging technology to study neural plasticity. *Front. Neural Circuits* 6.

Frey, U., Egert, U., Heer, F., Hafizovic, S., and Hierlemann, A. (2009). Microelectronic system for high-resolution mapping of extracellular electric fields applied to brain slices. *Biosensors Bioelectron.* 24, 2191–2198.

Fyhn, M., Molden, S., Witter, M. P., Moser, E. I., and Moser, M.-B. (2004). Spatial representation in the entorhinal cortex. *Science* 305, 1258–64.

Gähwiler, B. H., Capogna, M., Debanne, D., McKinney, R. A., and Thompson, S. M. (1997). Organotypic slice cultures: a technique has come of age. *Trends Neurosci* 20, 471–7.

Gähwiler, B. H., Thompson, S. M., and Muller, D. (2001). "Preparation and maintenance of organotypic slice cultures of CNS tissue.," in Current protocols in neuroscience.

Gelbard-Sagiv, H., Mukamel, R., Harel, M., Malach, R., and Fried, I. (2008). Internally generated reactivation of single neurons in human hippocampus during free recall. *Science* 322, 96–101.

Georges-François, P., Rolls, E. T., and Robertson, R. G. (1999). Spatial view cells in the primate hippocampus: allocentric view not head direction or eye position or place. *Cerebral Cortex (New York, N.Y. : 1991)* 9, 197–212.

Geweke, J. (1982). Measurement of Linear Dependence and Feedback between Multiple Time Series. *Journal of the American Statistical Association* 77, 304–313.

Gholmieh, G., Soussou, W., Han, M., Ahuja, A., Hsiao, M.-C., Song, D., Tanguay, A. R., and Berger, T. W. (2006). Custom-designed high-density conformal planar multielectrode arrays for brain slice electrophysiology. *J. Neurosci. Methods* 152, 116–29.

Girardeau, G., Benchenane, K., Wiener, S. I., Buzsáki, G., and Zugaro, M. B. (2009). Selective suppression of hippocampal ripples impairs spatial memory. *Nat. Neurosci.* 12, 1222–3.

Goedert, M., and Spillantini, M. G. (2006). A century of Alzheimer's disease. *Science* 314, 777–81.

Gomez-Isla, T., Price, J. L., McKeel Jr., D. W., Morris, J. C., Growdon, J. H., and Hyman, B. T. (1996). Profound Loss of Layer II Entorhinal Cortex Neurons Occurs in Very Mild Alzheimer''s Disease. *J. Neurosci.* 16, 4491–4500.

Granger, C. W. J. (1969). Investigating Causal Relations by Econometric Models and Cross-Spectral Methods. *Econometrica* 37, 424–38.

Gregoriou, G. G., Gotts, S. J., Zhou, H., and Desimone, R. (2009). High-frequency, long-range coupling between prefrontal and visual cortex during attention. *Science* 324, 1207–10.

Van Haeften, T., Baks-te-Bulte, L., Goede, P. H., Wouterlood, F. G., and Witter, M. P. (2003). Morphological and numerical analysis of synaptic interactions between neurons in deep and superficial layers of the entorhinal cortex of the rat. *Hippocampus* 13, 943–52.

Hafting, T., Fyhn, M., Bonnevie, T., Moser, M.-B., and Moser, E. I. (2008). Hippocampus-independent phase precession in entorhinal grid cells. *Nature* 453, 1248–52.

Hafting, T., Fyhn, M., Molden, S., Moser, M.-B., and Moser, E. I. (2005). Microstructure of a spatial map in the entorhinal cortex. *Nature* 436, 801–6.

Hales, C. M., Zeller-Townson, R., Newman, J. P., Shoemaker, J. T., Killian, N. J., and Potter, S. M. (2012). Stimulus-evoked high frequency oscillations are present in neuronal networks on microelectrode arrays. *Front. Neural Circuits* 6, 29.

Herculano-Houzel, S., Mota, B., and Lent, R. (2006). Cellular scaling rules for rodent brains. *Proc. Natl. Acad. Sci. U. S. A.* 103, 12138–43.

Huang, Y., Williams, J. C., and Johnson, S. M. (2012). Brain slice on a chip: opportunities and challenges of applying microfluidic technology to intact tissues. *Lab Chip* 12, 2103–17.

Humphrey, N. K. (1972). “Interest” and “pleasure”: two determinants of a monkey’s visual preferences. *Perception*.

Iijima, T., Witter, M. P., Ichikawa, M., Tominaga, T., Kajiwara, R., and Matsumoto, G. (1996). Entorhinal-Hippocampal Interactions Revealed by Real-Time Imaging. *Science* 272, 1176–1179.

Insausti, R., and Amaral, D. G. (2008). Entorhinal cortex of the monkey: IV. Topographical and laminar organization of cortical afferents. *J. Comp. Neurol.* 509, 608–41.

Irons, H. R., Cullen, D. K., Shapiro, N. P., Lambert, N. A., Lee, R. H., and Laplaca, M. C. (2008). Three-dimensional neural constructs: a novel platform for neurophysiological investigation. *J. Neural Eng.* 5, 333–41.

Ison, M. J., Mormann, F., Cerf, M., Koch, C., Fried, I., and Quiroga, R. Q. (2011). Selectivity of pyramidal cells and interneurons in the human medial temporal lobe. *J. Neurophysiol.* 106, 1713–21.

Itti, L., and Koch, C. (2001). Computational modelling of visual attention. *Nature Rev. Neurosci.* 2, 194–203.

Itti, L., Koch, C., and Niebur, E. (1998). A model of saliency-based visual attention for rapid scene analysis. *IEEE Transactions on Pattern Analysis and Machine Intelligence* 20, 1254–1259.

Jackson, J., Goutagny, R., and Williams, S. (2011). Fast and Slow Gamma Rhythms Are Intrinsically and Independently Generated in the Subiculum. *J. Neurosci.* 31, 12104–12117.

Jacobs, J., Kahana, M. J., Ekstrom, A. D., Mollison, M. V, and Fried, I. (2010). A sense of direction in human entorhinal cortex. *Proc. Natl. Acad. Sci. U. S. A.* 107, 6487–92.

Jones, I. L., Livi, P., Lewandowska, M. K., Fiscella, M., Roscic, B., and Hierlemann, A. (2011). The potential of microelectrode arrays and microelectronics for biomedical research and diagnostics. *Anal Bioanal Chem* 399, 2313–29.

Jones, R. S. G. (1993). Entorhinal-hippocampal connections: a speculative view of their function. *Trends Neurosci.* 16, 58–64.

Jones, R. S., and Heinemann, U. (1988). Synaptic and intrinsic responses of medical entorhinal cortical cells in normal and magnesium-free medium in vitro. *J Neurophysiol* 59, 1476–1496.

Jung, M., Wiener, S., and McNaughton, B. (1994). Comparison of spatial firing characteristics of units in dorsal and ventral hippocampus of the rat. *J. Neurosci.* 14, 7347–7356.

Jutras, M. J., and Buffalo, E. A. (2010). Recognition memory signals in the macaque hippocampus. *Proc. Natl. Acad. Sci. U. S. A.* 107, 401–6.

Jutras, M. J., Fries, P., and Buffalo, E. A. (2009). Gamma-band synchronization in the macaque hippocampus and memory formation. *J. Neurosci.* 29, 12521–31.

Kay, L. M. (2003). Two species of gamma oscillations in the olfactory bulb: dependence on behavioral state and synaptic interactions. *Journal of integrative neuroscience* 2, 31–44.

Killian, N. J., Jutras, M. J., and Buffalo, E. A. (2012). A map of visual space in the primate entorhinal cortex. *Nature* 491, 761–4.

Kjelstrup, K. B., Solstad, T., Brun, V. H., Hafting, T., Leutgeb, S., Witter, M. P., Moser, E. I., and Moser, M.-B. (2008). Finite scale of spatial representation in the hippocampus. *Science* 321, 140–3.

Klein, R. M., and MacInnes, W. J. (1999). Inhibition of Return is a Foraging Facilitator in Visual Search. *Psychol. Sci.* 10, 346–352.

Knake, S., Wang, C. M., Ulbert, I., Schomer, D. L., and Halgren, E. (2007). Specific increase of human entorhinal population synaptic and neuronal activity during retrieval. *NeuroImage* 37, 618–22.

Koenig, J., Linder, A. N., Leutgeb, J. K., and Leutgeb, S. (2011). The spatial periodicity of grid cells is not sustained during reduced theta oscillations. *Science* 332, 592–5.

Koganezawa, N., Taguchi, A., Tominaga, T., Ohara, S., Tsutsui, K.-I., Witter, M. P., and Iijima, T. (2008). Significance of the deep layers of entorhinal cortex for transfer of both perirhinal and amygdala inputs to the hippocampus. *Neuroscience Research* 61, 172–81.

Kraus, B. J., Brandon, M. P., Connerney, M. A., Robinson, R. J., Eriksson, S., Libby, C. P., White, J. A., Hasselmo, M. E., and Eichenbaum, H. (2012). Medial entorhinal cortical neurons exhibit temporally-modulated firing patterns during stationary treadmill running. in Society for Neuroscience Online Abstracts (New Orleans, LA).

Kreiman, G., Fried, I., and Koch, C. (2002). Single-neuron correlates of subjective vision in the human medial temporal lobe. *Proc. Natl. Acad. Sci. U. S. A.* 99, 8378–83.

Krupic, J., Burgess, N., and O'Keefe, J. (2012). Neural representations of location composed of spatially periodic bands. *Science* 337, 853–7.

Kumar, S. S., and Buckmaster, P. S. (2006). Hyperexcitability, interneurons, and loss of GABAergic synapses in entorhinal cortex in a model of temporal lobe epilepsy. *J. Neurosci.* 26, 4613–23.

Langston, R. F., Ainge, J. A., Couey, J. J., Canto, C. B., Bjerknes, T. L., Witter, M. P., Moser, E. I., and Moser, M.-B. (2010). Development of the spatial representation system in the rat. *Science* 328, 1576–80.

Leonard, B., Amaral, D., Squire, L., and Zola-Morgan, S. (1995). Transient memory impairment in monkeys with bilateral lesions of the entorhinal cortex. *J. Neurosci.* 15, 5637–5659.

Leondopulos, S. S., Boehler, M. D., Wheeler, B. C., and Brewer, G. J. (2012). Chronic stimulation of cultured neuronal networks boosts low-frequency oscillatory activity at theta and gamma with spikes phase-locked to gamma frequencies. *Journal of Neural Engineering* 9, 026015.

Leuthardt, E. C., Schalk, G., Wolpaw, J. R., Ojemann, J. G., and Moran, D. W. (2004). A brain-computer interface using electrocorticographic signals in humans. *J. Neural Eng.* 1, 63–71.

Levick, J. R. (1987). Flow through interstitium and other fibrous matrices. *Q J Exp Physiol* 72, 409–437.

Lubenov, E. V, and Siapas, A. G. (2009). Hippocampal theta oscillations are travelling waves. *Nature* 459, 534–9.

Malenka, R. C., and Bear, M. F. (2004). LTP and LTD: an embarrassment of riches. *Neuron* 44, 5–21.

Manns, J. R., Stark, C. E., and Squire, L. R. (2000). The visual paired-comparison task as a measure of declarative memory. *Proc. Natl. Acad. Sci. U. S. A.* 97, 12375–9.

Maris, E., and Oostenveld, R. (2007). Nonparametric statistical testing of EEG- and MEG-data. *J. Neurosci. Methods* 164, 177–90.

Matsumura, N., Nishijo, H., Tamura, R., Eifuku, S., Endo, S., and Ono, T. (1999). Spatial- and task-dependent neuronal responses during real and virtual translocation in the monkey hippocampal formation. *J. Neurosci.* 19, 2381–93.

Maurer, A. P., VanRhoads, S. R., Sutherland, G. R., Lipa, P., and McNaughton, B. L. (2005). Self-motion and the origin of differential spatial scaling along the septo-temporal axis of the hippocampus. *Hippocampus* 15, 841–52.

McMahon, D. B. T., and Olson, C. R. (2007). Repetition suppression in monkey inferotemporal cortex: relation to behavioral priming. *J. Neurophysiol.* 97, 3532–43.

McNaughton, B. L., Battaglia, F. P., Jensen, O., Moser, E. I., and Moser, M.-B. (2006). Path integration and the neural basis of the "cognitive map". *Nature Rev. Neurosci.* 7, 663–78.

Meunier, M., Bachevalier, J., Mishkin, M., and Murray, E. A. (1993). Effects on visual recognition of combined and separate ablations of the entorhinal and perirhinal cortex in rhesus monkeys. *J. Neurosci.* 13, 5418–32.

Miller, E. K., Gochin, P. M., and Gross, C. G. (1993). Suppression of visual responses of neurons in inferior temporal cortex of the awake macaque by addition of a second stimulus. *Brain Res.* 616, 25–9.

Mizuseki, K., Sirota, A., Pastalkova, E., and Buzsáki, G. (2009). Theta oscillations provide temporal windows for local circuit computation in the entorhinal-hippocampal loop. *Neuron* 64, 267–80.

Moser, E. I., Kropff, E., and Moser, M.-B. (2008). Place cells, grid cells, and the brain's spatial representation system. *Ann. Rev. Neurosci.* 31, 69–89.

Musick, K., Khatami, D., and Wheeler, B. C. (2009). Three-dimensional micro-electrode array for recording dissociated neuronal cultures. *Lab Chip* 9, 2036–42.

Naya, Y., and Suzuki, W. A. (2011). Integrating What and When Across the Primate Medial Temporal Lobe. *Science* 333, 773–776.

O'Keefe, J., and Dostrovsky, J. (1971). The hippocampus as a spatial map: Preliminary evidence from unit activity in the freely-moving rat. *Brain Res.* 34, 171 – 175.

De Oliveira, S. C., Thiele, A., and Hoffmann, K.-P. (1997). Synchronization of Neuronal Activity during Stimulus Expectation in a Direction Discrimination Task. *J. Neurosci.* 17, 9248–9260.

Ono, T., Nakamura, K., Nishijo, H., and Eifuku, S. (1993). Monkey hippocampal neurons related to spatial and nonspatial functions. *J. Neurophysiol.* 70, 1516–1529.

Oostenveld, R., Fries, P., Maris, E., and Schoffelen, J.-M. (2011). FieldTrip: Open source software for advanced analysis of MEG, EEG, and invasive electrophysiological data. *Comput Intell Neurosci* 2011, 156869.

Pare, D., deCurtis, M., and Llinas, R. (1992). Role of the hippocampal-entorhinal loop in temporal lobe epilepsy: extra- and intracellular study in the isolated guinea pig brain in vitro. *J. Neurosci.* 12, 1867–1881.

Parikh, H., Marzullo, T. C., and Kipke, D. R. (2009). Lower layers in the motor cortex are more effective targets for penetrating microelectrodes in cortical prostheses. *J. Neural Eng.* 6, 026004.

Passeraub, P. A., Almeida, A. C., and Thakor, N. V (2003). Design , Microfabrication and Analysis of a Microfuidic Chamber for the Perfusion of Brain Tissue Slices. *Biomed Microdevices* 5, 147–155.

Pastalkova, E., Itskov, V., Amarasingham, A., and Buzsáki, G. (2008). Internally generated cell assembly sequences in the rat hippocampus. *Science* 321, 1322–7.

Paxinos, G., and Watson, C. (2007). *The Rat Brain In Stereotaxic Coordinates*. Academic Press.

Pedreira, C., Mormann, F., Kraskov, A., Cerf, M., Fried, I., Koch, C., and Quiroga, R. Q. (2010). Responses of human medial temporal lobe neurons are modulated by stimulus repetition. *J. Neurophysiol.* 103, 97–107.

Pesaran, B., Nelson, M. J., and Andersen, R.A. (2010). A relative position code for saccades in dorsal premotor cortex. *J. Neurosci.* 30, 6527–37.

Pettersen, K. H., Devor, A., Ulbert, I., Dale, A. M., and Einevoll, G. T. (2006). Current-source density estimation based on inversion of electrostatic forward solution: effects of finite extent of neuronal activity and conductivity discontinuities. *J. Neurosci. Methods* 154, 116–33.

Potter, S. M., and Demarse, T. B. (2001). A new approach to neural cell culture for long-term studies. *J. Neurosci. Methods* 110, 17 – 24.

Rajaraman, S., Choi, S., Mcclain, M. A., Ross, J. D., Laplaca, M. C., and Allen, M. G. (2011). Metal-Transfer-Micromolded Three-Dimensional Brain-Slice Recordings. *J Microelectromech Syst* 20, 396–409.

Rambani, K., Vukasinovic, J., Glezer, A., and Potter, S. M. (2009). Culturing thick brain slices: an interstitial 3D microperfusion system for enhanced viability. *J. Neurosci. Methods* 180, 243–54.

Robertson, R. G., Rolls, E. T., Georges-François, P., and Panzeri, S. (1999). Head direction cells in the primate pre-subiculum. *Hippocampus* 9, 206–19.

Rolls, E. T. (1999). Spatial view cells and the representation of place in the primate hippocampus. *Hippocampus* 9, 467–80.

Rolls, E. T., and Cowey, A. (1970). Topography of the retina and striate cortex and its relationship to visual acuity in rhesus monkeys and squirrel monkeys. *Experimental brain research.*10, 298–310.

Rolls, E. T., and O'Mara, S. M. (1995). View-responsive neurons in the primate hippocampal complex. *Hippocampus* 5, 409–24.

Rolls, E. T., Treves, A., Robertson, R. G., Georges-Francois, P., and Panzeri, S. (1998). Information About Spatial View in an Ensemble of Primate Hippocampal Cells. *J Neurophysiol* 79, 1797–1813.

Rolston, J. D., Gross, R. E., and Potter, S. M. (2009). A low-cost multielectrode system for data acquisition enabling real-time closed-loop processing with rapid recovery from stimulation artifacts. *Frontiers in Neuroengineering* 2, 12.

Sahakian, B. J., Morris, R. G., Evenden, J. L., Heald, A., Levy, R., Philpot, M., and Robbins, T. W. (1988). A Comparative Study of Visuospatial Memory and Learning in Alzheimer-Type Dementia and Parkinson'S Disease. *Brain* 111, 695–718.

Saleem, K. S., and Logothetis, N. K. (2007). *A Combined MRI and Histology Atlas of the Rhesus Monkey Brain in Stereotaxic Coordinates*. London: Academic Press.

Sargolini, F., Fyhn, M., Hafting, T., McNaughton, B. L., Witter, M. P., Moser, M.-B., and Moser, E. I. (2006). Conjunctive representation of position, direction, and velocity in entorhinal cortex. *Science* 312, 758–62.

Scott, A., Weir, K., Easton, C., Huynh, W., Moody, W. J., and Folch, A. (2013). A microfluidic microelectrode array for simultaneous electrophysiology, chemical stimulation, and imaging of brain slices. *Lab Chip* 13, 527–35.

Shariat Torbaghan, S., Yazdi, D., Mirpour, K., and Bisley, J. W. (2012). Inhibition of return in a visual foraging task in non-human subjects. *Vision Res.* 74, 2–9.

Siegel, R. M., Raffi, M., Phinney, R. E., Turner, J. A, and Jandó, G. (2003). Functional architecture of eye position gain fields in visual association cortex of behaving monkey. *J. Neurophysiol.* 90, 1279–94.

Skaggs, W. E., McNaughton, B. L., Permenter, M., Archibeque, M., Vogt, J., Amaral, D. G., and Barnes, C. a (2007). EEG sharp waves and sparse ensemble unit activity in the macaque hippocampus. *J. Neurophysiol.* 98, 898–910.

Solstad, T., Boccara, C. N., Kropff, E., Moser, M.-B., and Moser, E. I. (2008). Representation of geometric borders in the entorhinal cortex. *Science* 322, 1865–8.

Steffenach, H.-A., Witter, M., Moser, M.-B., and Moser, E. I. (2005). Spatial memory in the rat requires the dorsolateral band of the entorhinal cortex. *Neuron* 45, 301–13.

Stett, A., Rudorf, R., Stein, B., Egert, U., Boven, K., Gottschlich, N., and Nisch, W. (2005). Perforated polyimide microelectrode arrays for single-cell and tissue recording. in MST Kongress.

Stewart, M., and Fox, S. E. (1991). Hippocampal theta activity in monkeys. *Brain Res.* 538, 59–63.

Stoppini, L., Buchs, P. A., and Muller, D. (1991). A simple method for organotypic cultures of nervous tissue. *J. Neurosci. Methods* 37, 173–82.

Stoppini, L., Duport, S., Corre, P., and Corrèges, P. (1997). A new extracellular multirecording system for electrophysiological studies: application to hippocampal organotypic cultures. *J. Neurosci. Methods* 72, 23–33.

Sun, W., and Dan, Y. (2009). Layer-specific network oscillation and spatiotemporal receptive field in the visual cortex. *Proc. Natl. Acad. Sci. U. S. A.* 106, 17986–91.

Suthana, N., Haneef, Z., Stern, J., Mukamel, R., Behnke, E., Knowlton, B., Fried, I., Dlouhy, B. J., and Rao, R. C. (2012). Memory enhancement and deep-brain stimulation of the entorhinal area. *The New England Journal of Medicine* 366, 502–10.

Suzuki, W. A., and Amaral, D. G. (1994). Topographic organization of the reciprocal connections between the monkey entorhinal cortex and the perirhinal and parahippocampal cortices. *J. Neurosci.* 14, 1856–77.

Suzuki, W. A., Miller, E. K., and Desimone, R. (1997). Object and place memory in the macaque entorhinal cortex. *J Neurophysiol* 78, 1062–1081.

Tahvildari, B., and Alonso, A. (2005). Morphological and electrophysiological properties of lateral entorhinal cortex layers II and III principal neurons. *J. Comp. Neurol.* 491, 123–40.

Takeuchi, D., Hirabayashi, T., Tamura, K., and Miyashita, Y. (2011). Reversal of interlaminar signal between sensory and memory processing in monkey temporal cortex. *Science* 331, 1443–7.

Tamura, R., Ono, T., Fukuda, M., and Nakamura, K. (1992). Spatial responsiveness of monkey hippocampal neurons to various visual and auditory stimuli. *Hippocampus* 2, 307–22.

Taube, J. S., Muller, R. U., and Ranck, J. B. (1990). Head-direction cells recorded from the postsubiculum in freely moving rats. I. Description and quantitative analysis. *J. Neurosci.* 10, 420–35.

Thiagarajan, T. C., Lebedev, M. A., Nicolelis, M. A., and Plenz, D. (2010). Coherence Potentials : Loss-Less , All-or-None Network Events in the Cortex. *PLoS Biol.* 8.

Thiébaud, P., De Rooij, N. F., Koudelka-Hep, M., and Stoppini, L. (1997). Microelectrode arrays for electrophysiological monitoring of hippocampal organotypic slice cultures. *IEEE Trans Biomed Eng* 44, 1159–63.

Thomson, D. J. (1982). Spectrum estimation and harmonic analysis. *Proc IEEE Inst Electr Electron Eng* 70, 1055–1096.

Townsend, G., Peloquin, P., Kloosterman, F., Hetke, J. F., and Leung, L. S. (2002). Recording and marking with silicon multichannel electrodes. *Brain Res. Brain Res. Protoc.* 9, 122–9.

Tseng, P., Cameron, I. G. M., Munoz, D. P., and Itti, L. (2009). Quantifying center bias of observers in free viewing of dynamic natural scenes. *Journal of Vision* 9, 1–16.

Ulanovsky, N., and Moss, C. F. (2007). Hippocampal cellular and network activity in freely moving echolocating bats. *Nat. Neurosci.* 10, 224–33.

Velasco, M., Velasco, F., and Velasco, A. L. (2001). Centromedian-thalamic and hippocampal electrical stimulation for the control of intractable epileptic seizures. *Journal of clinical neurophysiology* 18, 495–513.

Vukasinovic, J., Cullen, D. K., LaPlaca, M. C., and Glezer, A. (2009). A microperfused incubator for tissue mimetic 3D cultures. *Biomed. Microdevices* 11, 1155–65.

De Waele, S., and Broersen, P. M. T. (2003). Order selection for vector autoregressive models. *IEEE Transactions on Signal Processing* 51, 427–433.

Wagenaar, D. A., Madhavan, R., Pine, J., and Potter, S. M. (2005a). Controlling Bursting in Cortical Cultures with Closed-Loop Multi-Electrode Stimulation. *J. Neurosci.* 25, 680 – 688.

Wagenaar, D. A., Pine, J., and Potter, S. M. (2004). Effective parameters for stimulation of dissociated cultures using multi-electrode arrays. *J. Neurosci. Methods* 138, 27–37.

Wagenaar, D. A., and Potter, S. M. (2004). A versatile all-channel stimulator for electrode arrays , with real-time control. *J. Neural Eng.* 1, 39–45.

Wagenaar, D. A., and Potter, S. M. (2002). Real-time multi-channel stimulus artifact suppression by local curve fitting. *J. Neurosci. Methods* 120, 113–120.

Wagenaar, D., Demarse, T. B., and Potter, S. M. (2005b). MeaBench: A toolset for multi-electrode data acquisition and on-line analysis. *Proc. 2nd Int. IEEE EMBS Conf. Neural Eng.*, 518–521.

Wang, Z., and Klein, R. M. (2010). Searching for inhibition of return in visual search: a review. *Vision Res.* 50, 220–8.

Weible, A. P., Rowland, D. C., Dickinson, J., Roth, B. L., and Kentros, C. G. (2011). Transgenically-targeted increase in the activity of medial entorhinal layer II neurons induces reversible field expansion and remapping of CA1 place cells. in Society for Neuroscience Online Abstracts.

Wilson, F. A., and Goldman-Rakic, P. S. (1994). Viewing preferences of rhesus monkeys related to memory for complex pictures, colours and faces. *Behav. Brain Res.* 60, 79–89.

Witter, M. P., and Amaral, D. G. (1991). Entorhinal cortex of the monkey: V. Projections to the dentate gyrus, hippocampus, and subicular complex. *J. Comp. Neurol.* 307, 437–59.

Witter, M. P., Wouterlood, F. G., Naber, P. A., and Van Haeften, T. (2000). Anatomical organization of the parahippocampal-hippocampal network. *Ann. N. Y. Acad. Sci.* 911, 1–24.

Wolfe, J. M., and Danielson, J. (2012). Visual Foraging Behavior: When are the berries riper on the other side of the screen? *Journal of Vision* 12, 265–265.

Xiang, J. Z., and Brown, M. W. (1998). Differential neuronal encoding of novelty, familiarity and recency in regions of the anterior temporal lobe. *Neuropharmacology* 37, 657–76.

Yartsev, M. M., Witter, M. P., and Ulanovsky, N. (2011). Grid cells without theta oscillations in the entorhinal cortex of bats. *Nature* 479, 103–107.

Yazdan-Shahmorad, A., Lehmkuhle, M. J., Gage, G. J., Marzullo, T. C., Parikh, H., Miriani, R. M., and Kipke, D. R. (2011). Estimation of electrode location in a rat motor cortex by laminar analysis of electrophysiology and intracortical electrical stimulation. *J. Neural Eng.* 8, 046018.

Zhang, Y., Chen, Y., Bressler, S. L., and Ding, M. (2008). Response preparation and inhibition: the role of the cortical sensorimotor beta rhythm. *Neuroscience* 156, 238–46.

Zoccolan, D., Graham, B. J., and Cox, D. D. (2010). A self-calibrating, camera-based eye tracker for the recording of rodent eye movements. *Front. Neurosci.* 4, 193.

Zola, S. M., Squire, L. R., Teng, E., Stefanacci, L., Buffalo, E. A., and Clark, R. E. (2000). Impaired recognition memory in monkeys after damage limited to the hippocampal region. *J. Neurosci.* 20, 451–63.

Zola, S.M., Squire, L. R., Amaral, D. G., and Suzuki, W. A. (1989). Lesions of perirhinal and parahippocampal cortex that spare the amygdala and hippocampal formation produce severe memory impairment. *J. Neurosci.* 9, 4355–70.

VITA

Nathan J. Killian

Nathan Killian was born and raised in Mexico, Missouri where he attended public schools. He received a B.S. in Biomedical Engineering from Washington University in St. Louis, St. Louis, Missouri in 2007 before coming to Georgia Tech to pursue a doctorate in Bioengineering. After completion of his Ph.D. work, he will be working as a post-doctoral fellow in the Department of Neurosurgery at Massachusetts General Hospital – Harvard Medical School to assist in the development of a thalamic visual prosthesis, a device that may restore sight to the blind.